

---

ORIGIN AND CHARACTERIZATION OF DISKS  
SUBSTRUCTURES, AND THEIR RELATION TO  
STELLAR HOSTS

NICOLAS KURTOVIC

---

HEIDELBERG, 2023



Dissertation  
submitted to the  
Combined Faculty of Mathematics, Engineering and Natural Sciences  
of Heidelberg University, Germany  
for the degree of  
Doctor of Natural Sciences

Put forward by  
M.Sc. NICOLAS KURTOVIC  
born in Santiago, Chile

Oral examination: July 12th, 2023



---

ORIGIN AND CHARACTERIZATION OF DISKS  
SUBSTRUCTURES, AND THEIR RELATION TO  
STELLAR HOSTS

---

REFEREES:

PROF. DR. PAOLA PINILLA

PROF. DR. ANDREAS QUIRRENBACH



## **Abstract**

Planets are formed from the gas and dust content available in planet-forming disks around young stars, creating substructures in their density, thermal, and chemical distribution. Characterizing those substructures can provide constraints on the planet-formation potential of each disk.

To improve our understanding of how planets are formed around the stars that are the most common in our galaxy, very low mass stars and binary stars, I studied high spatial resolution observations of dust and gas emission from these objects. To maximize information recovery, I analyzed these datasets with visibility-based methods.

The results demonstrate that substructured emission in the dust continuum is present in all spatially resolved disks around very low mass stars, which could be explained by ongoing planet formation. In circumbinary disks, the combination of hydro-models and observations suggest that measuring the eccentricity gradient as a function of radii can be used as a tracer for the presence of Saturn-like planets embedded in the disks. On the other hand, for multiple disk systems, I showed the feasibility of recovering the orbital motion of young objects through the relative movement of their disks, which is crucial to interpreting the emission substructures.



## Zusammenfassung

Planeten entstehen aus dem Gas- und Staubbudget, das in planetenbildenden Scheiben um junge Sterne vorhanden ist, wodurch sich Substrukturen in ihrer Dichte, thermischen und chemischen Verteilung bilden. Die Charakterisierung dieser Substrukturen kann Restriktionen für das Potential für Planetenentstehung jeder Scheibe liefern.

Um unser Verständnis dafür zu verbessern, wie Planeten um jene Sterne gebildet werden, die besonders häufig in unserer Galaxie vorkommen, nämlich Sterne mit sehr geringer Masse und Doppelsterne, habe ich hochauflösende Beobachtungen von Staub- und Gasemissionen dieser Objekte untersucht. Um die Informationsgewinnung zu maximieren, analysierte ich die Datensätze mit Methoden im visibility-space.

Die Ergebnisse zeigen, dass strukturierte Emission im Staubkontinuum in allen räumlich aufgelösten Scheiben um sehr massearme Sterne vorhanden ist, was durch fortlaufende Planetenbildung erklärt werden könnte. In zirkumbinären Scheiben deutet die Kombination von Hydromodellen und Beobachtungen darauf hin, dass die Messung des Exzentrizitätsgradienten als Funktion des Scheibenradius als Tracer für das Vorkommen von Saturn-ähnlichen Planeten in den Scheiben verwendet werden kann. Andererseits zeigte ich für multiple Scheibensysteme die Machbarkeit, die Orbitbewegung der jungen Sterne durch die relative Bewegung ihrer jeweiligen Scheiben zu rekonstruieren, was entscheidend dafür ist, die Substrukturen ihrer Emission zu interpretieren.



## Resumen

Los planetas se forman a partir del gas y polvo existente en discos formadores de planetas alrededor de estrellas jóvenes, creando subestructuras en su distribución de densidad, temperatura, y química. La caracterización de estas subestructuras puede proporcionar límites sobre el potencial de formación planetaria de cada disco.

Para entender cómo se forman los planetas alrededor de las estrellas más comunes en nuestra galaxia, las estrellas de muy baja masa y las estrellas binarias, estudié observaciones de alta resolución espacial de la emisión de polvo y gas en estos objetos. Para maximizar la recuperación de información, analicé estos conjuntos de datos con métodos basados en el análisis de las visibilidades.

Los resultados demuestran que las subestructuras en la emisión de continuo del polvo están presentes en todos los discos alrededor de estrellas de muy baja masa que están espacialmente resueltos, y podrían explicarse por la formación de planetas. En discos circumbinarios, la combinación de modelos hidrodinámicos y observaciones sugiere que medir el gradiente de excentricidad como función de radio se puede utilizar como un trazador de la presencia de planetas similares a Saturno en el disco. Por otro lado, para sistemas con múltiples discos, demostré la viabilidad de recuperar el movimiento orbital de las estrellas jóvenes a través del movimiento relativo de sus discos, lo que es crucial para interpretar las subestructuras de emisión.



*Abajo lo viejo. Arriba el núcleo*



<b>LIST OF FIGURES</b> . . . . .	<b>5</b>
<b>LIST OF TABLES</b> . . . . .	<b>9</b>
<b>1 An introduction to planet formation and its observability</b>	<b>11</b>
1.1 Thesis goal and outline . . . . .	11
1.2 In the path of life: Planetary Systems . . . . .	12
1.3 Disks and planet formation . . . . .	15
1.3.1 Structure and substructures of a disk . . . . .	16
1.4 Observations of thermal dust continuum substructures . . . . .	23
1.4.1 Frequency rate of substructure-detection . . . . .	23
1.4.2 The relation between continuum brightness, mass density, and temperature . . . . .	25
1.5 Observations of molecular gas line emission . . . . .	27
1.5.1 Channel maps of molecular emission . . . . .	28
1.5.2 Integrated maps . . . . .	30
1.6 The impact of stellar mass in a planet-forming disk . . . . .	34
1.7 The impact of stellar-multiplicity in a planet-forming disk . . . . .	36
1.7.1 Internal binary-companion . . . . .	36
1.7.2 External binary-companion . . . . .	37
<b>2 Observational considerations</b>	<b>41</b>
2.1 Interferometric observations . . . . .	41
2.1.1 Observing planet-forming disks in the sky . . . . .	41
2.1.2 Brightness and visibilities . . . . .	42
2.1.3 Recovering the brightness distribution from the sampled visibilities . . . . .	45
2.2 Generating simulated observations . . . . .	51
2.2.1 Challenges when comparing physical models to observations . . . . .	51
2.2.2 The SIMIO-continuum package . . . . .	53
<b>3 Planet formation in very low mass stars</b>	<b>57</b>
3.1 Introduction . . . . .	57
3.2 Target selection . . . . .	59
3.3 Observations . . . . .	60
3.4 Morphology of the continuum emission . . . . .	63
3.4.1 Rings and cavities in CIDA1, MHO6, and J0433 . . . . .	69

3.4.2	Dust disk masses . . . . .	70
3.5	Molecular emission from $^{12}\text{CO}$ and $^{13}\text{CO}$ . . . . .	71
3.5.1	Lines detection . . . . .	71
3.5.2	Radial gas profiles . . . . .	72
3.5.3	Keplerian rotation of CO emission . . . . .	73
3.6	Occurrence rate of substructures . . . . .	73
3.7	Origin of dust continuum rings and cavities . . . . .	74
3.7.1	Detected structures coincide with possible CO iceline location . . . . .	75
3.7.2	CIDA1 . . . . .	77
3.7.3	J0433 . . . . .	77
3.7.4	MHO6 . . . . .	78
3.8	Comparison of dust size-luminosity relation with previous studies . . . . .	80
3.9	J0415 dust radial extent . . . . .	83
3.10	Gas to dust size ratio . . . . .	83
3.11	MHO6 kinematics . . . . .	86
3.11.1	Analysis of the velocity map . . . . .	86
3.11.2	Modeling of the gas visibilities . . . . .	88
3.12	Summary . . . . .	90
3.13	Additional content . . . . .	92
<b>4</b>	<b>Planet formation in a circumbinary disk</b>	<b>103</b>
4.1	Clues about planet formation in circumbinary systems . . . . .	103
4.2	An interesting case-study: CS Cha . . . . .	104
4.3	ALMA Observations . . . . .	106
4.4	Observational results . . . . .	108
4.4.1	Circumbinary disk: Dust continuum emission physical properties . . . . .	108
4.4.2	No detection of emission near CSCha B . . . . .	110
4.4.3	Dust morphology from the visibility fitting . . . . .	111
4.4.4	The $^{12}\text{CO}$ molecular line emission . . . . .	116
4.5	Hydrodynamical simulations . . . . .	120
4.5.1	Setup: Circumbinary disk with FARGO3D . . . . .	120
4.5.2	Disk evolution with no planet . . . . .	125
4.5.3	Disk evolution with a Saturn-like planet . . . . .	127
4.6	Non-detection of CSCha B . . . . .	129
4.7	A Saturn-like planet is consistent with the morphology of the CSCha disk . . . . .	130
4.8	Cavity edge and ring morphology . . . . .	134
4.9	Summary . . . . .	135
4.10	Additional content . . . . .	136
<b>5</b>	<b>Planet formation in an interacting multiple stellar system: RW Aur</b>	<b>141</b>
5.1	The impact of dynamical interactions on the disks of young binary disk systems . . . . .	141
5.2	Observations . . . . .	144
5.3	Dust continuum emission of RWAur . . . . .	146
5.3.1	Parametric visibility modeling . . . . .	147
5.3.2	RW Aur B orbit: With ALMA astrometry . . . . .	150
5.3.3	RW Aur B orbit: Excluding ALMA astrometry . . . . .	153

5.3.4	RWAur A inner disk geometry . . . . .	154
5.4	Molecular 12CO line emission of RWAur . . . . .	158
5.5	The RWAur system is in a gravitationally bound orbit . . . . .	162
5.5.1	Astrometry with ALMA . . . . .	165
5.6	Summary . . . . .	167
5.7	Additional content . . . . .	168
5.7.1	Dust continuum parametric models . . . . .	168
5.7.2	Orbital solutions excluding the ALMA data . . . . .	168
5.7.3	RWAur CO isotopologues emission . . . . .	170
<b>6</b>	<b>Summary and Future Prospects</b>	<b>173</b>
6.1	Summary of my thesis . . . . .	173
6.2	Future Prospects . . . . .	175
6.2.1	Maximizing information recovery from gas observations through visibility modeling . . . . .	175
6.2.2	Astrometry of binary disks with ALMA . . . . .	175
6.2.3	Disks rotation as a probe for the origin of substructures . . . . .	177
	<b>Bibliography</b>	<b>182</b>



## List of Figures

---

1.1	Exoplanet orbital period compared to the host stellar mass, for the confirmed exoplanet population through transits or radial velocities. . . . .	14
1.2	Stages of (low-mass) star and planet formation, from <a href="#">Öberg &amp; Bergin (2021)</a> . . . . .	16
1.3	An illustration of the spatial distribution of the disk material, over a plane parallel to the disk midplane. . . . .	17
1.4	Dust continuum emission gallery showing disks with substructures. . . . .	21
1.5	Collection of mechanisms that can induce substructures in the density distribution of a planet-forming disk. Figure credit to <a href="#">Bae et al. (2022)</a> . . . . .	22
1.6	The $M_{\star} - M_d$ relation for disks observed in nearby SFR. . . . .	24
1.7	Image representations of the molecular emission line $^{12}\text{CO}$ in the transition J:2-1, from the disk around HD163296. . . . .	29
1.8	Artifact substructure in the $M_0$ and $M_{peak}$ for the $^{13}\text{CO}$ J:2-1 emission of the disk HD163296. . . . .	31
1.9	Comparison of integrating line emission with and without masking. . . . .	34
1.10	Strength of radial drift against disk age, for a $0.1 M_{\odot}$ and $1.0 M_{\odot}$ host star. . . . .	36
1.11	The $^{12}\text{CO}$ J:2-1 emission of AS 205 is compared to the gas morphology in a simulation of a parabolic fly-by. . . . .	38
2.1	Sky angular extent comparison of the Moon, Jupiter, and the Neptune orbit at 150 pc. . . . .	43
2.2	Example of the steps followed by the CLEAN algorithm. . . . .	46
2.3	An example of the workflow followed by the observation and reconstruction of an interferometric dataset. . . . .	48
2.4	Example of the relation between visibility coverage, PSF structure, angular resolution, and robust weighting, for generating CLEAN images of the RU Lup disk. . . . .	49
2.5	The 0.87 mm dust continuum emission of the CS Cha system, imaged with CLEAN and different robust parameters. . . . .	51
2.6	Examples of generating synthetic observations using SIMIO. . . . .	54
3.1	ALMA Observations of the disks around VLMS in Taurus. . . . .	61
3.2	Spatial distribution of the Taurus sample the extinction map background compiled by <a href="#">Schlafly et al. (2014)</a> . . . . .	62
3.3	Visibility modeling versus continuum observations of the sample. . . . .	64

List of Figures

3.4	Azimuthally averaged radial profiles of the VLMS dust and gas emission. . .	68
3.5	Dust mass compared to stellar mass for the Taurus disks. . . . .	71
3.6	Temperature profile compared to estimated ice-line locations. . . . .	76
3.7	Size luminosity relation in the Taurus SFR . . . . .	81
3.8	Gas to dust size ratio as a function of dust mass. . . . .	84
3.9	MHO 6 Brightness temperature profile measured from CO emission. . . . .	89
3.10	Surface height of MHO 6. . . . .	89
3.11	Spectral profile of the $^{12}\text{CO}$ and $^{13}\text{CO}$ in our sample. The gray line denotes the 0Jy level. . . . .	95
3.12	Keplerian fitting of $^{12}\text{CO}$ and $^{13}\text{CO}$ with eddy. The grid shows the best surface recovered with eddy, extending up to the distance of the mask for the fitting. . . . .	95
3.13	Position velocity diagram of the gas emission. . . . .	96
3.14	Channel maps of the CO emission of CIDA 1 . . . . .	97
3.15	Channel maps of the CO emission of MHO 6. . . . .	98
3.16	Channel maps of the CO emission of J0433. . . . .	99
3.17	Channel maps of the CO emission of CIDA 7 . . . . .	100
3.18	Channel maps of the CO emission of J0420. . . . .	101
3.19	Channel maps of the CO emission of J0415. . . . .	101
4.1	Detection of CS Cha B with several instruments over a time period of about 20 yr. . . . .	105
4.2	Reconstructed images of CS Cha dust continuum emission and $^{12}\text{CO}$ . . . . .	108
4.3	The non-detection of CS Cha B in the high-sensitivity millimeter emission images of CS Cha. . . . .	111
4.4	Best solution for the dust continuum emission generated using the Model 2e, which considers two eccentricities for the disk components. . . . .	115
4.5	CS Cha gas emission and kinematics. . . . .	117
4.6	Gas surface density after 100 000 binary orbits for each simulation. . . . .	123
4.7	Eccentricity and semi-major axis for the cavity ( $e_{\text{cav}}, a_{\text{cav}}$ ) as a function of time in binary orbits. . . . .	126
4.8	Eccentricity and semi-major axis for the peak density ring ( $e_{\text{peak}}, a_{\text{peak}}$ ) as a function of time in binary orbits. . . . .	127
4.9	Planets' semi-major axis and eccentricity as a function of time (in binary orbits). . . . .	128
4.10	Comparison of azimuthally averaged radial profiles of CS Cha. . . . .	133
4.11	Schematic profile of the components considered in CS Cha parametric visibility modeling. . . . .	136
4.12	$^{12}\text{CO}$ Channel maps of CS Cha, generated with a robust parameter of 0.0. . . . .	137
4.13	Best solutions for the dust continuum emission generated with the Models 2g, 3g and 4g. . . . .	138
5.1	Dust continuum emission of RW Aur, from the LB1 observation. . . . .	145
5.2	Dust continuum and $^{12}\text{CO}$ azimuthally averaged profiles from the CLEAN images. . . . .	155
5.3	Best parametric models and residuals for the dust continuum emission. . . . .	156
5.4	Orbital solutions found from ALMA and historical astrometry. . . . .	156

5.5	Normalized probability density distribution for some of the orbital parameters of RW Aur B around RW Aur A. . . . .	157
5.6	Warped visibility model for RW Aur A dust continuum emission. . . . .	157
5.7	$^{12}\text{CO}$ emission images at different spatial scales. . . . .	159
5.8	Position velocity diagram along the major axis of the disks, calculated from the LB $^{12}\text{CO}$ cube. . . . .	161
5.9	Same as Figure 5.5, but showing the solutions when excluding the ALMA astrometry. . . . .	169
5.10	Blueshifted and redshifted molecular line emission of $^{12}\text{CO}$ , relative to RW Aur A systemic velocity. . . . .	170
5.11	Integrated maps of $^{13}\text{CO}$ and $\text{C}^{18}\text{O}$ molecular line emission. . . . .	170
6.1	Expected Keplerian motion at different radii over HD163296, in a period of 10 yrs. . . . .	176
6.2	Detectability of asymmetries rotating at 1 au from the central star, with ALMA. . . . .	178



## List of Tables

---

3.1	Stellar properties of the VLMS. . . . .	59
3.2	Best parameters from parametric visibility modeling . . . . .	67
3.3	Continuum and CO radial extension for each VLMS disk. . . . .	69
3.4	Summary of ALMA observations. . . . .	93
3.5	Continuum imaging summary. . . . .	94
3.6	$^{12}\text{CO}$ and $^{13}\text{CO}$ imaging summary. . . . .	94
4.1	Best parameters from the parametric visibility modeling of CS Cha dust continuum emission. . . . .	113
4.2	Best parameters from the kinematic fitting with <code>eddy</code> to the image generated with a robust parameter of 0.0 . . . . .	120
4.3	Disk properties from the hydro-simulations. . . . .	124
5.1	Observation log of the RW Aur observations by ALMA. . . . .	143
5.2	Dust continuum emission properties obtained with parametric visibility modeling. . . . .	148
5.3	Highest likelihood orbital solution, and $1\sigma$ deviation for the orbital parameters of RW Aur B around RW Aur A. . . . .	153
5.4	Geometry and inner disk properties of RW Aur A, as measured by an MCMC fitting described in Sect. 5.3.4. . . . .	154
5.5	Best fit parameters for the visibility modeling of the dust continuum emission. The pixel size was 4 mas. . . . .	169



# 1

## An introduction to planet formation and its observability

---

### 1.1 Thesis goal and outline

In this work, I characterize the impact of stellar multiplicity and low stellar mass on the substructures of disks around such objects. The ultimate goal of this characterization is to deepen our understanding of how planets are formed in those systems. I will combine two approaches: a) Observations of young planet-forming's material, chemical, and temperature distributions to analyze their morphology and physical conditions. b) Discuss the observations in the context of numerical simulations or theoretical predictions of planet formation.

My contributions to the planet-formation field are summarized in the following chapters, encompassing a fraction of the work I did over my doctoral studies. The content is organized as follows:

- In the present **Chapter 1**, I explore the basic concepts, definitions, and current understanding of the planet formation field. I also discuss the observational properties of planet-forming disks.
- The observability of planet-forming disks at millimeter wavelengths is considerably dependent on a technique known as interferometry. In **Chapter 2**, I explain the necessary concepts to understand this technique within the context of planet formation.
- Very low mass stars are the most common type of star in our galaxy. I explore the conditions for planet formation around them in **Chapter 3** by analyzing a group of young stars in the Taurus Star Forming Region.
- The majority of the stars in our galaxy belong to a binary system (or even higher stellar multiplicity system). The n-body interaction between

planetary systems, the host star, and the companion star can modify the conditions for planet formation and evolution. To understand how planet formation operates in multiple-stellar systems, **Chapter 4** presents an analysis of a planet-forming disk around two stars, also known as a circumbinary disk.

- I continue exploring the effect of stellar multiplicity in the formation of planetary systems in **Chapter 5**, this time by analyzing a system where two stars are tidally interacting and perturbing each other disk.
- Finally, in **Chapter 6**, I explore the future of planet formation research and summarize the findings of the works presented in the previous chapters.

## 1.2 In the path of life: Planetary Systems

*In the following paragraphs, I express my understanding and interpretation of the existence of life, and it should only be considered as a thought exercise to explain the motivation for my work.*

The existence of life in our universe is a fascinating outcome of combining the laws of physics and letting them interact for gigayears periods. In our own Solar System, the conditions for life were particularly favorable on Earth's surface, allowing life to thrive and evolve into complex and diverse individuals, communities, and ecosystems. The initial conditions for the origin of life, and its development, are still being researched at the time of writing this work. Nevertheless, the presence of life on Earth is proof that our universe can generate and sustain it. This leads to rephrasing the follow-up question "Does life exist outside of Earth" into a more probabilistic tone: "What is the spatial density of life in the universe?"

To constrain the spatial density of life in the universe, we need to set some definitions and conditions for life's existence and development. Life, as we know it, is an emergent property of complex self-contained organisms that interact with their environment by exchanging mass and energy, ultimately lowering their entropy or keeping it constant. The mechanisms that allow these processes are usually related to the interplay of different atoms and molecules, and thus as a first approximation, we can consider that the basis of life belongs to microscopic scales.

Within our galaxy, planetary bodies are the ideal environment for life, as the medium’s composition, temperature, and density are appropriate for the physical processes and chemical reactions involved in sustaining the life forms we know of. Therefore, studying these objects becomes crucial to understanding when and where life could exist. Our own Solar System is rich in diversity of planetary-type bodies, with a wide range of masses covering from gas giant and sub-giant planets to several rocky planets, moon systems, asteroids, and comets, with some being more favorable for the existence of known life than others. An essential consideration when studying planets is that almost all of them began their existence together with the Sun, in a process known as “planet formation”.

The detection of planetary bodies orbiting around other stars has demonstrated that the planet formation process was not unique to the Solar System. To the 10th of April of 2023, **5332** exoplanets have been confirmed around other stars (based on the NASA Exoplanet Archive), with a large fraction of them being detected through the transits or radial velocities methods, which allow for determining the size or mass of the planet, respectively. In Figure 1.1, I show the population of confirmed exoplanets by comparing their orbital periods against their host stellar mass. Given that most of the detection methods are based on measuring changes in the light emitted by the host star, they are biased towards detecting short-period exoplanets around solar-type objects.

Despite the observational biases and challenges, there is evidence that planet-formation has happened around stars of a wide range of masses, even for objects with the minimum mass required for stable hydrogen-burning cores ( $\approx 0.08 M_{\odot}$ ). These detections support the idea that planet formation could be ubiquitous around low and moderate mass stars, which is promising for detecting life elsewhere than the Solar System. Indeed, if planets are the places with the highest likelihood of hosting life in our universe, and planetary systems are a frequent outcome of the star-formation process, it means that the number of places where life could develop could be of a similar order of magnitude to the number of stars.

As a human civilization, we are still in the very early stages of understanding what kinds of planetary systems exist in the universe, including their properties and potential for life. Considering that planets acquire most of their mass and composition during the formation stages, comprehending how planet formation works is crucial to understand the processes that lead to

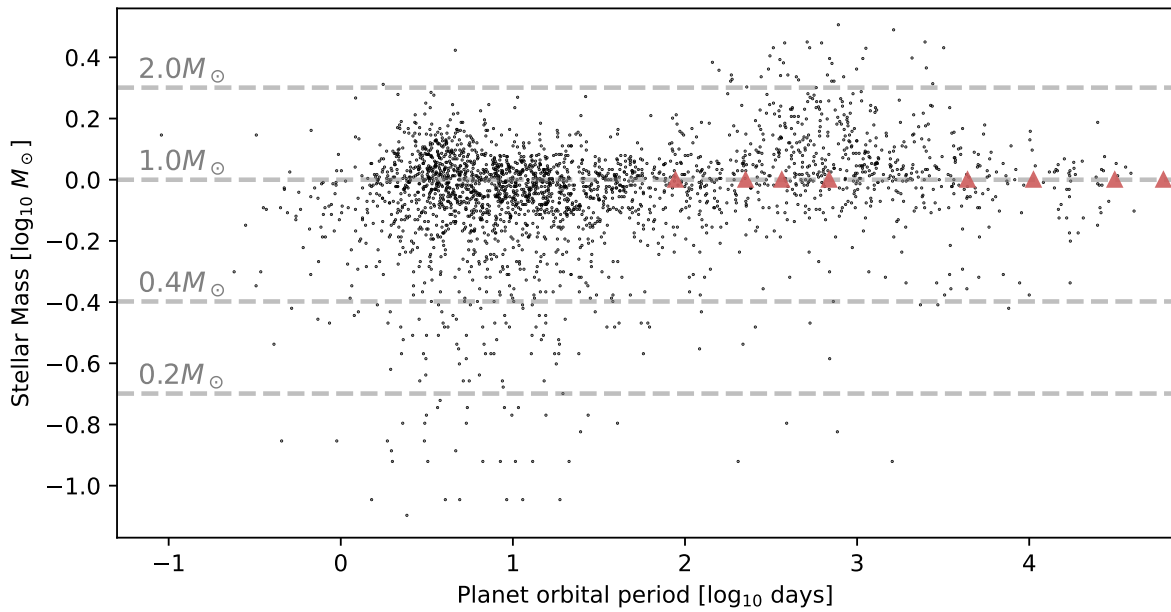


**Figure 1.1:** Exoplanet orbital period compared to the host stellar mass, for the confirmed exoplanet population. Dashed lines show constant stellar mass values. A total of 2561 planets are shown in this plot. I excluded planets detected through direct imaging or microlensing, as they do not always allow for precise determination of stellar mass, planet mass, and planet orbital period. The exoplanets were filtered to show those with orbital periods smaller than 200 yrs and stellar masses lower than  $4 M_{\odot}$ . The red triangles represent the planets of the Solar System. The data was obtained from the NASA Exoplanet Archive on the 18th of April, 2023.

the origin and evolution of life and of our own.

### 1.3 Disks and planet formation

There is a general consensus that planets are formed from the gas and dust present in disks surrounding young stars (e.g. Williams & Cremin, 1968; Safronov, 1972; Coradini et al., 1981; Mizuno et al., 1988; Ruden, 1999; Weidenschilling, 2000; Papaloizou & Terquem, 2006; Espaillat et al., 2014; Andrews, 2020). This idea has been around for centuries (with the first discussions being proposed by Immanuel Kant and Pierre-Simon Laplace in 1755 and 1796), and only recently we have been able to test star-formation and planet-formation theories through observations and numerical simulations.

Circumstellar disks are a natural outcome of the conservation of momentum after the collapse of the initial molecular cloud, which is exemplified in Figure 1.2, extracted from Öberg & Bergin (2021). Disks around young stars were first identified by the excess infrared emission from these objects, which was interpreted as being extended material around the star (Strom et al., 1989; Skrutskie et al., 1990). Ever since, additional observations started showing evidence of millimeter dust continuum and gas emission coming from disk-like structures in young stars (e.g. Beckwith et al., 1990; Dutrey et al., 1996; Mannings & Sargent, 1997). Historically, disks have been known as *protoplanetary disks*, as they were thought to precede the formation of planets. However, as shown in the following sections, modern observations suggest that planet formation may have already started at very early stages of these systems. Therefore, in this thesis, I will refer to the disks around young stars as “*planet-forming disks*”.

Despite understanding the basics of where (planet-forming disks) and when (within the lifetime of a disk) the planets are formed around newborn stars, there are many open questions about how exactly planets form within those disks. For instance, what is the role of different mechanisms driving the formation of planets, from micrometer dust to megameter-sized bodies? How do the initial disk properties influence the architecture and composition of the planets it will form? What are the specific timescales for planet formation in different planet-forming disk regions? As in most scientific topics of current active research, none of these questions has a simple, unique answer. In the case of planet-forming disks, those answers will depend on the mechanisms driving the evolution of the disks themselves, as the disks and the forming planets are intricately related.

As it will be shown in the following Sections, the evolution of the material

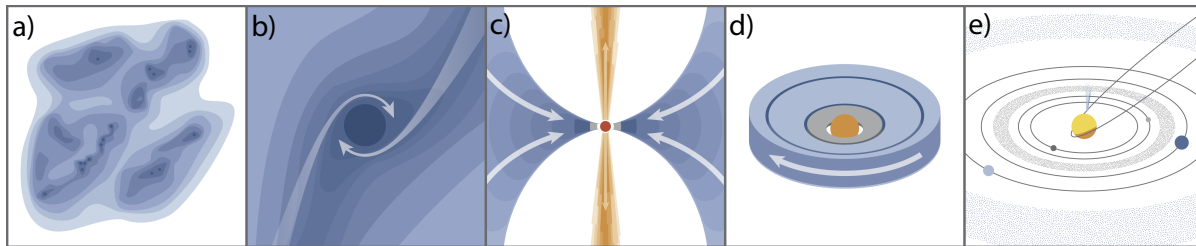


**Figure 1.2:** Stages of (low-mass) star and planet formation, from Öberg & Bergin (2021).

**a)** The gas and dust are initially contained in molecular clouds, which can become cold due to efficient energy loss through radiation. Eventually, the combination of high density and low temperatures leads them to collapse under their own gravity, forming dense cores of material. **b)** As the material falls onto the core, the conservation of angular momentum increases the rotational speed. The center of the core becomes the birthplace of a star. **c)** A star has been born and continues accreting material through an accretion disk. Outflows of material can be ejected from the central regions of the disk, which contribute to clearing the surrounding material envelope. **d)** The envelope material has been dispersed, and the forming star is still the host of a circumstellar disk composed of gas and dust. The timescale for hosting a disk changes from system to system, but it is usually within a period of  $< 1\text{ Myr}$  to  $20\text{ Myr}$ . **e)** The material of the disk has the potential to become a planetary system.

of a disk will be strongly related to the mass of the central star and also to interactions with a gravitational perturber, such as a binary star. In this work, the question I will explore is: **What is the impact different stellar masses or companions have on the planet formation potential of each disk?** And I will do so driven by state-of-the-art high spatial resolution observations of the disks material.

### 1.3.1 Structure and substructures of a disk

To begin understanding how planets are formed, we need to understand the distribution of the material in a disk and identify the observable signatures related to planet formation. On the axis perpendicular to a disk midplane (to which I will usually refer as the vertical axis), the structure of a disk will be an equilibrium between gravity contributing to flattening the gas and dust content toward the midplane, and the gas turbulence and pressure support expanding it into higher elevation layers. The equilibrium distribution is exemplified in the diagram shown in Figure 1.3.

Initially, the disk inherits its material from the interstellar medium, and thus it will mainly contain dust in micrometer-sized grains. Under the right conditions, these grains will interact, growing to millimeter, centimeter, or larger sized objects. Unlike the gas component, the dust grains do not have

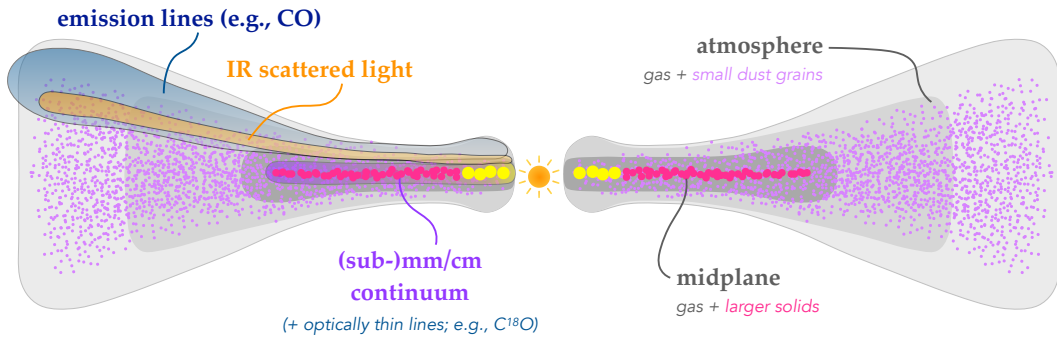


**Figure 1.3:** An illustration of the spatial distribution of the disk material, over a plane parallel to the disk midplane.

The grey shaded regions represent the distribution of the gas content. The small purple dots represent the small dust grains, while larger yellow and dark-pink dots represent millimeter-centimeter sized dust grains, at different temperatures. Different observational tracers, such as molecular emission or thermal continuum emission, will observe different regions of the disk. Figure from Andrews (2020).

gaseous pressure support, but the interaction with the surrounding gas can still modify the dust spatial distribution through drag. The interaction between a dust particle and the gas is commonly characterized by the Stokes number  $St$  (deeper discussion on this subject is summarized in Testi et al., 2014), which is defined as:

$$St = \Omega_K \tau_s, \quad (1.1)$$

where  $\Omega_K$  is the Keplerian orbital period, and  $\tau_s$  is the “stopping time” of a particle of mass  $m$  and speed  $v$  subject to a drag force  $F$ , defined as  $\tau_s = m v / F$ . The value of  $St$  is adimensional and positive. For objects with  $St \ll 1$ , their movement will be completely coupled to the gas, as the time it takes a drag force  $F$  to equal the movement of the particle to the movement of the gas is very small. For particles with  $St \approx 1$  to  $St \gg 1$ , their movement will be partially decoupled to completely decoupled, respectively, and thus they will settle towards the midplane of the disk (e.g., Tanaka et al., 2005). The different components of a disk: gas, small grains, and large grains, will be spatially segregated as a function of elevation from the midplane. Such differentiation means that different observational tracers, such as molecular light emission, stellar scattered light from small dust particles, or thermal continuum emission from millimeter-sized grains, will come from different disk regions, as shown in Figure 1.3, extracted from Andrews (2020).

Over the azimuthal direction, the gas component can modify the velocity of a dust particle and thus also its trajectory around the star. Even though dust and gas will orbit the star with nearly Keplerian velocities, the difference between having or not having pressure support will make them have slightly different orbital velocities. In the midplane of the disk, the azimuthal velocity of the gas is described as:

$$v_{\text{gas}} = \underbrace{\sqrt{\frac{GM_{\star}}{r}}}_{\text{Keplerian component}} + \underbrace{\frac{1}{\rho_{\text{gas}}} \frac{dP}{dr}}_{\text{Pressure support}}, \quad (1.2)$$

where  $G$  is the gravitational constant,  $M_{\star}$  is the mass of the star,  $r$  is the distance of the gas parcel to the star,  $\rho_{\text{gas}}$  is the gas density,  $dP/dr$  is the gas pressure gradient, and we have assumed that the disk mass is negligible compared to  $M_{\star}$ . As a thought exercise, let us think about a disk with a gas density profile following a monotonically decreasing power law as a function of disk radii. The gas pressure would be at its highest at the center of the disk, with a negative pressure gradient over radii. As the pressure is decreasing, and since  $1/\rho_{\text{gas}}$  is positive, the contribution of the pressure support results in  $v_{\text{gas}} < v_{\text{kep}}$ , thus, slightly sub-Keplerian.

Different from the gas, the rotational speed of solid particles is purely Keplerian (dust does not have pressure support). This is particularly important for the particles with  $\text{St} \approx 1$ , as their velocity will be continuously decreased by the drag of the sub-Keplerian gas. By reducing their angular momentum, the periastron or the particle's orbit is also reduced, and this process continues until the particle has drifted to the central star region. This is known as dust "radial drift", and represents one of the main challenges to planet formation, because the timescale of radial drift can be much shorter than that of grain growth (Whipple, 1972; Adachi et al., 1976; Weidenschilling, 1977; Nakagawa et al., 1981; Takeuchi & Lin, 2002).

Let us also consider the opposite radial pressure profile case, where the pressure locally increases with increasing radii. The pressure gradient would then become positive, and therefore locally we have that  $v_{\text{gas}} > v_{\text{kep}}$ , thus, slightly super-Keplerian. In this case, the drag force on the dust particles would increase their angular momentum. Generally speaking, the drag due to the non-Keplerian velocity of the gas produces a drift to the particles in the direction toward the local gas pressure maxima.

In [Pinilla et al. \(2012b\)](#), it was shown that local pressure maxima in the pressure profile could “trap” dust particles at a certain radii, which provides the necessary conditions for dust particle growth. Thus, even though radial drift tends to concentrate the dust particles closer to the disk center (the global pressure maxima), local pressure maxima can prevent disks from being completely depleted from solid material. Recent observations at high angular resolution of the dust and gas component have provided evidence to support both the existence of radial drift and mechanisms stopping it. For example, smaller disk sizes are commonly observed when tracing larger particle sizes (e.g., [Macías et al., 2021](#)), while size ratios  $R_{\text{dust}}/R_{\text{gas}} < 1$  are ubiquitously observed at millimeter wavelengths (e.g. [Ansdell et al., 2018](#); [Long et al., 2022](#)), where  $R_{\text{dust}}$  is the radial size of the dust content, and  $R_{\text{gas}}$  is the radius of the gas content<sup>1</sup>. From thermochemical simulations with dust evolution, [Trapman et al. \(2019\)](#) showed that detections of  $R_{\text{dust}}/R_{\text{gas}} < 0.25$  are an unambiguous sign of dust evolution due to radial drift, which has also been observed in several disks (e.g., [Facchini et al., 2019](#); [Flaherty et al., 2020](#); [Martinez-Brunner et al., 2022](#)), including those that will be shown in Chapter 3.

Local pressure maxima can produce regions where dust and gas accumulate, thus producing local deviations from a smooth profile in the mass density distribution. For consistency throughout this work, those deviations from smoothness will be referred to as “disk substructures”, on the understanding that the primary structure of the material around the star is the disk-like morphology, and thus *sub*-morphologies inside the disk are *sub*-structures. Nonetheless, the words “structure” or “substructure” are interchangeably used in the literature without leading to confusion. One of the first identifications of a substructured disk came from unresolved observations tracing the spectral energy distribution (SED) of TW Hya ([Calvet et al., 2002](#)), the closest disk to Earth at 51 pc. Nowadays, our observational facilities allow us to observe disks at very high spatial resolution, and substructures are routinely observed in disks of over  $\approx 0.5$  Myr of age (see [Andrews, 2020](#)). A gallery with examples of substructured dust continuum emission at millimeter wavelengths<sup>2</sup> is shown in Figure 1.4, which compiles images of observations

---

<sup>1</sup>The measurement of disk sizes is an active area of research. The size is usually estimated from a distance that encloses a certain percent of the total flux. This topic will be revisited in Chapter 3

<sup>2</sup>To a first approximation, the millimeter continuum emission traces the location of millimeter-sized particles. This depends on the grains’ opacity, which is still a subject of active study.

that I have calibrated, analyzed, or both, over my graduate studies. As shown in the image, substructures are observed for disks of a wide range of sizes.

Additionally to being potential places for planet formation, disk substructures can also be a consequence of already existing planets perturbing the density profile of the disk, as it will be covered more extensively in the following subsections. Thus, substructures become a “chicken-egg” problem, as substructures and planets can be the consequence and origin of the other.

The detection of a substructure cannot be immediately linked to future or ongoing planet formation, because of the large diversity of physical mechanisms and disk properties that can also leave their imprints in the disk as substructures in the density distribution. To mention some of them in a non-exhaustive list of mechanisms, substructures can be related to the interaction of the dust and gas in the disk, to the magneto-hydrodynamical evolution of the disk, to the accretion mechanisms, interaction with the external environment through inflows/outflows of material or photoevaporation, among many others. A considerable fraction of these processes are summarized in Figure 1.5, extracted from the review chapter of [Bae et al. \(2022\)](#). Additionally, many mechanisms related to hydro- or magneto-instabilities are summarized in [Lesur et al. \(2022\)](#). Identifying substructures and understanding their origin is, thus, key to revealing their role in tracing and/or forming planets.

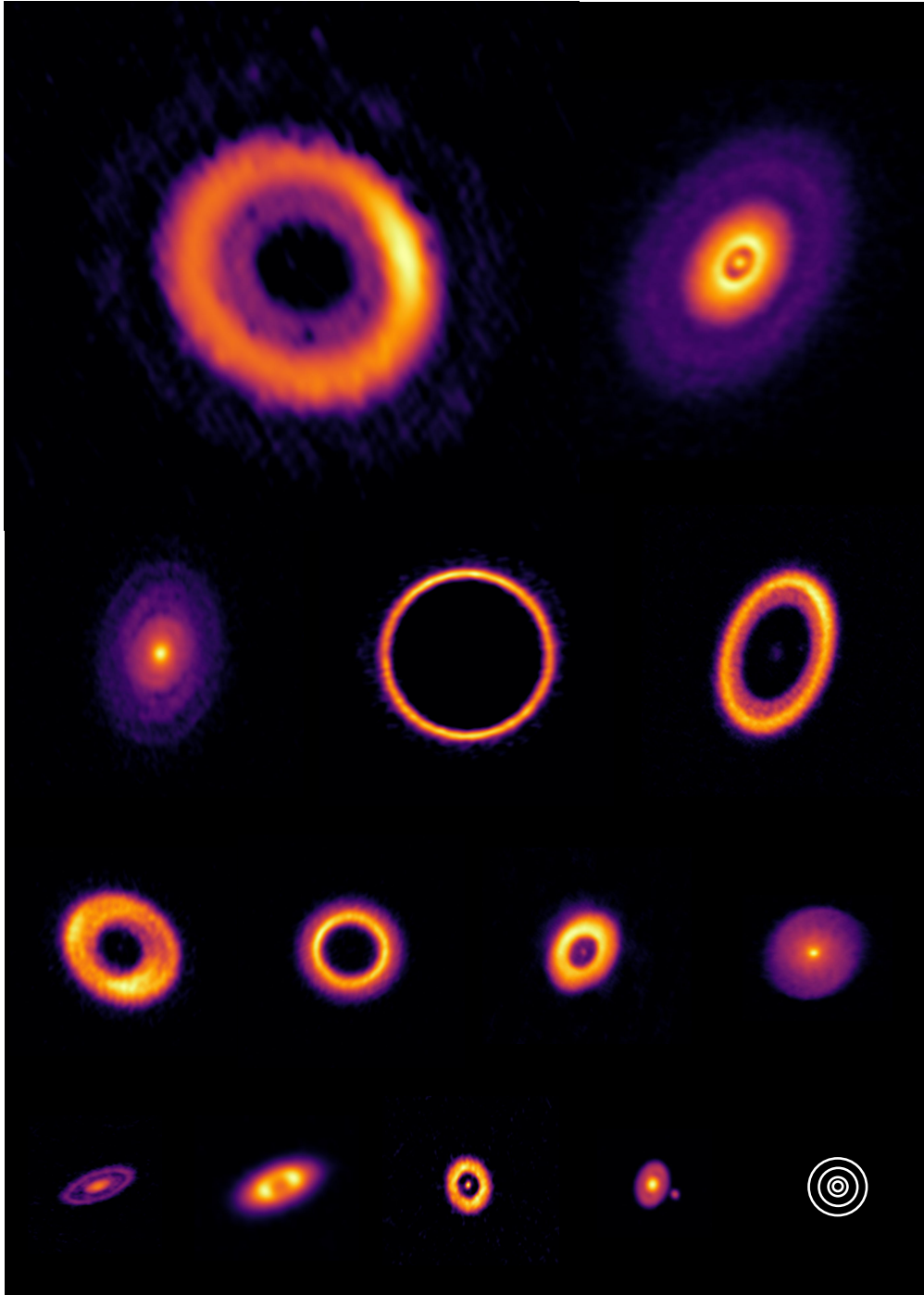


**Figure 1.4:** Dust continuum emission gallery showing disks with substructures. Brighter color means higher brightness temperature. All the disks shown in this gallery have been part of works where I have participated calibrating and/or analyzing this data. From top to bottom and left to right: LkHa 330 (Pinilla et al., 2022b), RX J1615 (Benisty et al, in prep.), WaOph 6 (Brown-Sevilla et al., 2021), J1604 (Kurtovic et al., in prep), PDS 70 (Benisty et al., 2021), CQ Tau (Wölfer et al., 2021), CS Cha (Kurtovic et al., 2022), HD 100546 (Pyerin et al., 2021), AS205 N (Kurtovic et al., 2018), AS205 S (Kurtovic et al., 2018), CIDA 1 (Pinilla et al., 2021), HT Lup A-B (Kurtovic et al., 2018). White concentric circles represent the size of the orbits of Jupiter, Saturn, Uranus and Neptune around the Sun. All disks are at the same spatial scale.

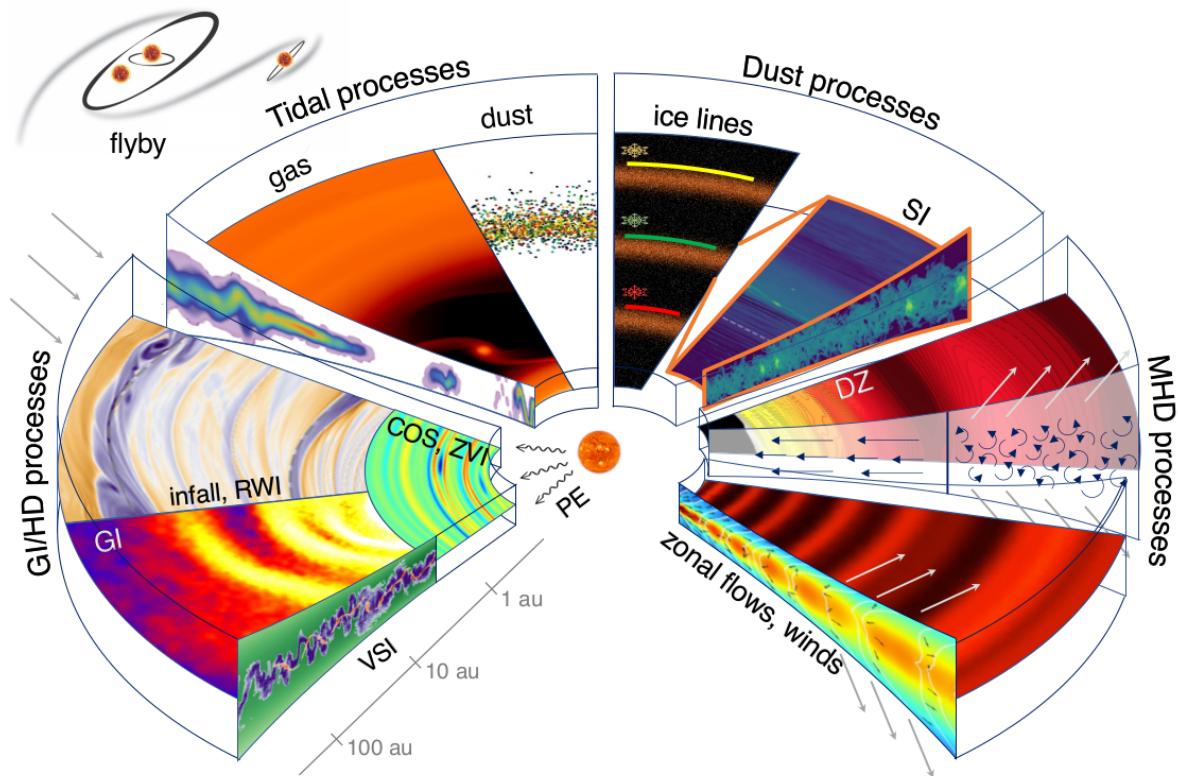


**Figure 1.5:** Collection of mechanisms that can induce substructures in the density distribution of a planet-forming disk. Figure credit to [Bae et al. \(2022\)](#). From left to right, in clock-wise direction, processes shown are Gravitational Instability (GI, [Toomre, 1964](#); [Kratte & Lodato, 2016](#)), hydrodynamical processes (HD) such as the Vertical Shear Instability (VSI, [Urpin & Brandenburg, 1998](#); [Arlt & Urpin, 2004](#); [Nelson et al., 2013](#); [Barraza-Alfaro et al., 2021](#)), Rossby-wave Instability (RWI, [Lovelace et al., 1999](#)), infall of material (e.g., [Bae et al., 2015](#); [Kuznetsova et al., 2022](#)), Convection Overstability ([Klahr & Hubbard, 2014](#)), Zombie-vortex Instability (ZVI, [Barranco & Marcus, 2005](#)), internal photoevaporation ([Clarke et al., 2001](#); [Alexander et al., 2014](#); [Gárate et al., 2021](#)), tidal processes related to internal planets (e.g., [Pinilla et al., 2012a](#); [Bae & Zhu, 2018a,b](#)) or companions (e.g., [Lubow, 1991](#); [Artymowicz & Lubow, 1994](#); [Miranda & Lai, 2015](#); [Cuello et al., 2019](#)), molecular icefronts or icelines producing a phase transition in the disk properties (e.g., [Zhang et al., 2015](#)), Streaming Instability (SI, [Youdin & Goodman, 2005](#); [Johansen & Youdin, 2007](#); [Gonzalez et al., 2017](#)), and Magneto-hydrodynamic processes (MHD) such as the Magnetorotational Instability ([Balbus & Hawley, 1991](#)), the deadzone ([Gammie, 1996](#); [Flock et al., 2015](#)), zonal flows (e.g., [Johansen et al., 2009](#)). Further discussion on hydro- and MHD-related processes that can lead to substructures is given in ([Lesur et al., 2022](#)).

## 1.4 Observations of thermal dust continuum substructures

Detecting newborn planets through direct imaging has been challenging to our current instruments (e.g., [Brown-Sevilla et al., 2021](#)). Thus, we rely on finding them through their imprints in the disk material, such as the substructures produced by planet-disk interactions.

### 1.4.1 Frequency rate of substructure-detection

The frequency rate for detection of substructures in the thermal dust continuum emission of planet-forming disks has increased dramatically since the beginning of operations of ALMA extended baselines, as they have provided the capacity for observing disks in nearby star-forming regions (SFR) with  $2 \sim 5$  au resolution (a deeper discussion on the role of angular resolution in observations of disks can be found in Chapter 2). Ever since the first observation of several axisymmetric substructures in the dust emission of the disk around HL Tau ([ALMA Partnership et al., 2015](#)), several other works started showing the presence of ring-like morphologies (e.g. [Andrews et al., 2016](#)), crescent-like structures (e.g. [van der Marel et al., 2013](#); [Casassus et al., 2015](#)), and even spirals (e.g. [Pérez et al., 2016](#); [Dong et al., 2018](#)). Motivated by the increasing number of detection of substructures in disks around Class II objects, the community started targeting larger samples of disks to test the frequency rate and type of substructures for different disks. These observations at very high angular resolution targeted bright extended sources to optimize the substructure detection rate, which at the time was unconstrained. Surveys such as DSHARP ([Andrews et al., 2018](#)) and high-resolution ODISEA ([Cieza et al., 2021](#)) showed that whenever a bright disk was observed at high enough spatial resolution, substructures in the dust emission would be detected. A similar result was obtained by [Long et al. \(2018\)](#) with a survey of the Taurus SFR, where with moderate spatial resolution, the team could detect rings in the disks that were well spatially resolved.

Although detecting substructures is an excellent opportunity to constrain planet formation, there are many observational biases towards detecting substructures in bright extended disks, mainly due to the sensitivity and angular resolution of our observational facilities. Therefore, the substructure frequency rate still needs to be better constrained in the most compact and faint disks. In Figure 1.6, the stellar mass ( $M_\star$ ) to disk mass ( $M_d$ ) relation

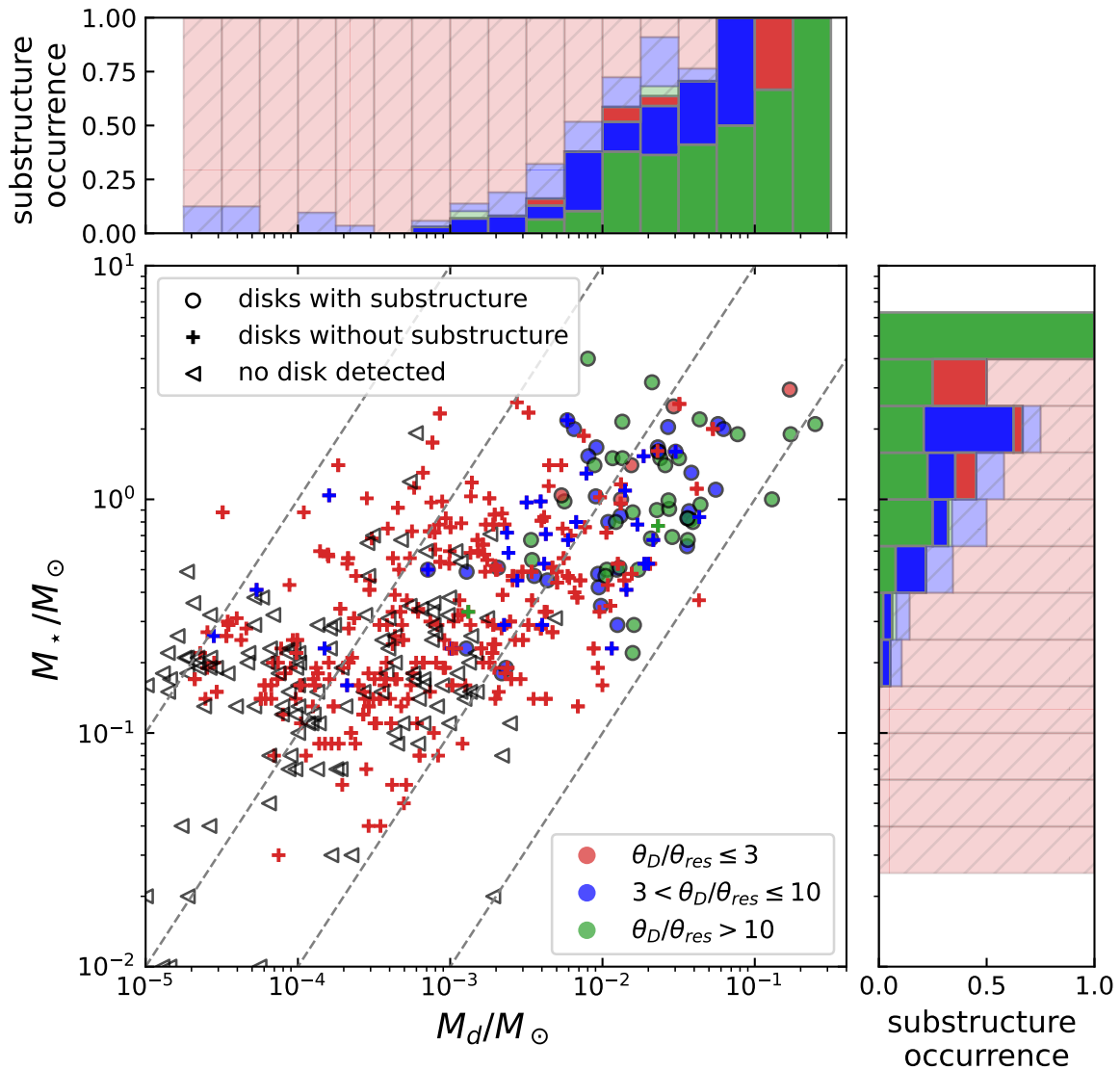


**Figure 1.6:** The  $M_\star - M_d$  relation for disks observed in nearby SFR. The different symbols and colors represent the detection of substructures and the angular resolution of the observation. High angular resolution observations are biased towards brighter disks (higher  $M_d$ ) around solar-type hosts, with the substructure occurrence rate being largely unconstrained for low mass stars and low mass disks. Figure credits to [Bae et al. \(2022\)](#).

is shown for disks observed in the nearby SFR (extracted from [Bae et al., 2022](#)), showing that frequency rate of substructures is mostly unconstrained in disks around lower mass stellar hosts, despite being the most common environment for planetary systems in the galaxy (see Chapter 3). Targeting these systems with enough angular resolution and sensitivity to characterize their disks' structure is considerably more expensive in exposure time than in the bright sources.

### 1.4.2 The relation between continuum brightness, mass density, and temperature

Recovering the mass density distribution of a planet-forming disk is key to studying its potential for planet-formation. However, this is a challenging quantity to determine directly. The main component of a disk is gas contained as cold molecular Hydrogen and Helium, which compose about 98% of a disk mass. Both elements, however, are unobservable with our current facilities. Only the remaining 2% of a disk mass is contained in heavier elements, which are easier to observe. In this section, I will focus on the observability of solid grains, which are the basis for the formation of planets.

The solids are composed mainly of combinations of various ices, carbonaceous materials, and silicates, as determined by combined observations of the Interstellar Medium, planet-forming disks, and laboratory experiments (e.g. [Sandford, 1996](#); [Jäger et al., 2008](#); [Keller et al., 2008](#); [Watson et al., 2009](#)). These grains can emit thermal continuum radiation, which allows them to be detectable over a wide range of wavelengths.

#### A first approximation

For simplicity, let us assume a small disk volume containing a fixed grain size distribution. Under the assumption that the grains are in equilibrium temperature, we can describe their specific intensity emission using the Planck equation:

$$I_\nu = B_\nu(T_{\text{phys}}) \cdot (1 - \exp(-\tau_\nu)), \quad (1.3)$$

where  $B_\nu(T_{\text{phys}})$  is the specific intensity given by the Planck equation for a black body with a temperature  $T_{\text{phys}}$  (the abbreviation for physical temperature) at a frequency  $\nu$ , and  $\tau_\nu$  is the specific optical depth defined as:

$$\tau_\nu = \kappa_\nu \cdot \Sigma(\vec{r}), \quad (1.4)$$

where  $\kappa_\nu$  is the opacity of the grains at the frequency  $\nu$ , and  $\Sigma(\vec{r})$  is the grains density at the coordinate given by  $\vec{r}$ , where the small volume is located. For an axisymmetric disk, we can consider  $\vec{r} = (r, \theta, z)$  in polar coordinates.

Following this description, if we assume that the dust continuum emission comes from an optically thin volume ( $\tau_\nu \ll 1$ ), then we can approximate

Equation 1.3 and 1.4 into:

$$I_\nu \approx \kappa_\nu \cdot B_\nu(T_{\text{phys}}) \cdot \Sigma(\vec{r}), \quad (1.5)$$

which after integrating over the whole disk, returns the relation between observed flux and disk dust mass  $M_{\text{dust}}$ :

$$M_{\text{dust}} = \frac{d^2 F_\nu}{\kappa_\nu B_\nu(T_{\text{phys}})}, \quad (1.6)$$

where  $F_\nu$  is the measured flux from the whole disk, as observed at a distance  $d$ . The simple relation given by Equation 1.6 gives a first approximation into the dust content of a whole disk as a function of  $(\kappa_\nu, T_{\text{phys}}, d, F_\nu)$ . Although  $d$  and  $F_\nu$  can be directly measured with observations, the values for  $T_{\text{phys}}$  and  $\kappa_\nu$  need some additional assumptions.

In the case of observations at millimeter wavelengths, it has become standard to assume that the emission is coming from the midplane of the disk with a constant  $T_{\text{phys}} = 20\text{ K}$ . Under this assumption, a linear proportionality exists between  $M_{\text{dust}}$  and  $F_\nu$  for a constant  $\nu$ , allowing for a simple and quick comparison for observations of disks, even if they are spatially unresolved. Some modifications can be made to the value of  $T_{\text{phys}}$  to make Equation 1.6 more accurate, as in Andrews et al. (2013), where they use a  $T_{\text{phys}}$  that is dependent on the luminosity of the star  $L_\star$ . For observations at high angular resolution, where the distribution of  $I_\nu$  is recovered as a function of radial distance from the star, the Equation 1.6 can also be modified such that the integral of Equation 1.5 considers a  $T_{\text{phys}}$  that is a function of radii.

Another assumption to calculate Equation 1.6 comes from the value of  $\kappa_\nu$ . In the first approximation to convert  $F_\nu$  into  $M_{\text{dust}}$  with the assumption of  $T_{\text{phys}} = 20\text{ K}$ , it has become standard to use the description  $\kappa_\nu = 2.3(\nu/230\text{ GHz})^{0.4}\text{ cm}^2\text{ g}^{-1}$ , which was proposed by Andrews & Williams (2005). For the typical observations at 1.3 mm wavelengths, this value becomes  $\kappa_{1.3\text{ mm}} = 2.3$ .

### A more realistic consideration

The first approximation from the previous section to relate  $M_{\text{dust}}$  with  $F_\nu$  was based on assuming a constant  $T_{\text{phys}}$ , and a value for  $\kappa_\nu$  which followed a single power law referenced at 230 GHz (1.3 mm). In reality, neither of those quantities is constant over the whole disk. Although better approximations

for  $T_{\text{phys}}$  can be considered, the value of  $\kappa_\nu$  needs to be modeled considering the contribution of different grain species.

By considering measurements from laboratory experiments over the opacity of different materials as a function of  $\nu$ , more accurate opacities can be calculated for different grain sizes. Currently, the two dominant opacities description as a function of grain sizes came from the works presented by [Ricci et al. \(2010\)](#) and [Birnstiel et al. \(2018\)](#), also known as the ‘‘Ricci’’ and ‘‘DSHARP’’ opacities. Applying these opacities to study observations of  $I_\nu$  still requires additional assumptions, such as assuming a functional description for the grain size distribution as a function of disk azimuth and radii. This is an active research topic which goes beyond the scope of this work. For a more complete discussion, I refer the reader to ([Miotello et al., 2022](#)).

### Brightness temperature and optical depth

So far I have focused on recovering  $M_{\text{dust}}$  from optically thin  $\tau_\nu$  observations. However, for the opposite scenario where  $\tau_\nu$  is optically thick, we could use spatially resolved observations of  $I_\nu$  to recover  $T_{\text{phys}}$ . Let us assume that  $\tau_\nu \gg 1$ , such that Equation 1.3 becomes  $I_\nu \approx B_\nu(T_b)$ , where the temperature  $T_b$  is called ‘‘brightness temperature’’, and represents the temperature that an optically thick black body requires to match  $I_\nu$ . We can also rewrite Equation 1.3 with the brightness temperature:

$$B_\nu(T_b) = B_\nu(T_{\text{phys}}) (1 - \exp(-\tau_\nu)), \quad (1.7)$$

which allows to establish relations between  $T_b$ ,  $T_{\text{phys}}$  and  $\tau_\nu$ . For example, if we assume a value for  $T_{\text{phys}}$ , we can use the measurement of  $T_b$  to estimate the optical depth of the observed region:

$$\tau_\nu = -\ln \left( 1 - \frac{T_b}{T_{\text{phys}}} \right), \quad (1.8)$$

enabling a first-order testing for the optically thin or optically thick scenarios.

## 1.5 Observations of molecular gas line emission

Cold molecular hydrogen and helium are unobservable with our current facilities. Therefore, observations of the disk’s gas rely on gas tracers such as molecular emission lines. The frequency-dependency of the intensity of

molecular emission lines is much stronger than that of the dust continuum emission, as the vibrational modes of molecules only emit light in very specific energy transitions. We can use this characteristic to our advantage, as the Doppler effect due to gas movement will redshift or blueshift the emission of a molecular line. An example of a molecular line observation is shown in Figure 1.7, extracted from (Bae et al., 2022).

Molecular emission will primarily come from the regions where the molecule is present. Due to the variations of density, temperature, and radiation field over the disk radii and elevation from the midplane, different molecular species will exist in the gas phase over different disk regions (see Henning et al., 1993; Dutrey et al., 2014). This chemical structure represents an opportunity to explore the physical conditions of the disk at different elevations and radial distances by observing different molecular lines. In the following, I describe the characteristics of the most common image representations of observations of molecular emission lines.

### 1.5.1 Channel maps of molecular emission

Molecular vibrational lines are emitted at known specific wavelengths. The wavelength where the line emission is detected can be shifted by the velocity of the gas relative to the observer through the Doppler effect. We can connect the gas velocity to the frequency shift of the emission line by simply using that:

$$v_{los} = c \left( \frac{\lambda_{\text{obs}} - \lambda_{\text{line}}}{\lambda_{\text{line}}} \right), \quad (1.9)$$

where  $c$  is the speed of light in vacuum, and  $v_{los}$  is the velocity of a gas parcel in our line of sight, with the emission of the gas parcel being detected at  $\lambda_{\text{obs}}$ , with an emission wavelength at rest of  $\lambda_{\text{line}}$ . If we observe over a narrow wavelength range  $\Delta\lambda$  centered at  $\lambda_{\text{obs}}$ , we will effectively be observing all the gas that is moving at  $v_{\text{obs}}$  in the line of sight, within a certain range  $\Delta v$ . Such image is called a “channel map”, as it traces the gas component for a single frequency (or wavelength) channel.

These channels can be interchangeably defined by wavelength or frequency. In the context of a specific emission line, they can also be defined by velocity. Over a single channel (thus, a fixed velocity), the detected gas will have the morphology of an isovelocity curve, which for rotating disks has a charac-

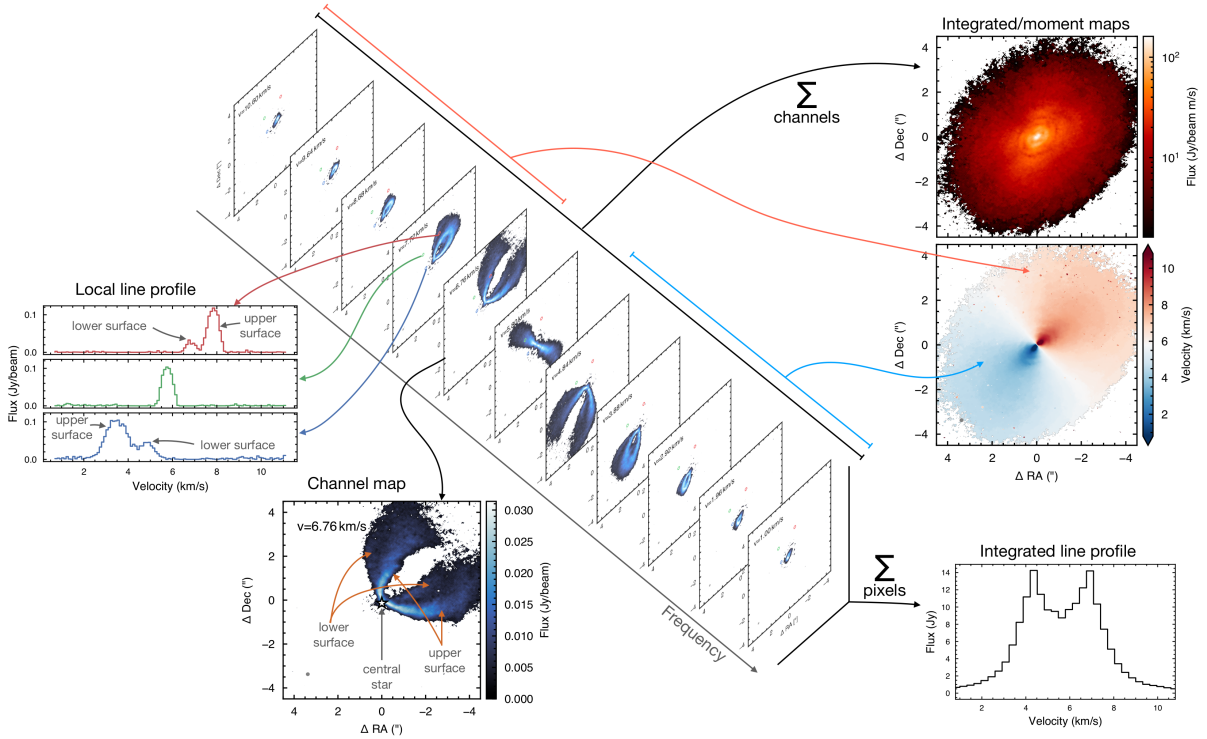


**Figure 1.7:** Image representations of the molecular emission line  $^{12}\text{CO}$  in the transition J:2-1, from the disk around HD163296. The channel maps of the molecular line are shown in the middle panels as a function of frequency. Each pixel in the cube contains the spectra at the pixel location, as shown in the Local line profiles. For high spatial resolution, high spectral resolution, and high signal-to-noise ratio, the single images of the channel maps can distinguish between different emission layers. When integrating the channel maps over frequency, it’s possible to recover intensity integrated and kinematic maps, as shown in the upper right panels. When integrating over the spatial coordinates, we can recover the integrated line profile as a function of frequency. The data shown in this Figure was also shown in Isella et al. (2016) and Isella et al. (2018). Figure from Pinte et al. (2022).

teristic shape known as the “butterfly pattern” (see Horne & Marsh, 1986; Beckwith & Sargent, 1993; Dutrey et al., 1994, 1998; Dartois et al., 2003; Isella et al., 2007; Rosenfeld et al., 2013; Dutrey et al., 2014). This pattern is shown in the middle panels of Figure 1.7 for channels with different frequencies (velocities).

The projected velocity of the gas  $v_{los}$  allows us to recover the 3D-structure of the gas velocity, by considering the contribution of each independent axis:

$$v_{los} = v_r \sin(\theta) \sin(i) + v_\theta \cos(\theta) \sin(i) + v_z \sin(\theta) \cos(i), \quad (1.10)$$

where  $(v_r, v_\theta, v_z)$  are the velocities in cylindrical coordinates,  $\theta$  is the azimuthal angle over the disk, measured counter-clockwise from the north axis,

which coincides with the major axis of the disk, and  $i$  is the inclination of the disk. For a perfectly Keplerian disk, the velocities  $v_r$  and  $v_z$  become 0, and thus the isovelocity curve becomes a function of the tuple  $(\theta, i, PA)$ , with the position angle  $PA$  being the angle between the north axis and the ascending node<sup>3</sup>.

### 1.5.2 Integrated maps

In spatially-resolved and frequency-resolved observations of disks, the channel maps contain the 3D projected information of the gas (2D for space, 1D for velocity). In order to analyze the data, it is convenient to integrate the channel maps over the velocity axis, creating the “integrated maps”. In the following, I describe the integrated maps utilized in my work:

#### Integrated and peak brightness

Let us consider  $I_{k,(i,j)}$  as the intensity of the pixel in the coordinates  $(i,j)$  in the channel number  $k$ . By summing the emission over the velocity axis, we recover the “Moment 0” map of the emission, or integrated brightness map, which is calculated as:

$$M_{0,(i,j)} = \sum_k^N I_{k,(i,j)}, \quad (1.11)$$

where  $k$  is the channel map number, with a total of  $N$  channel maps. The  $M_0$  image contains the total flux of the source, allowing for a first-order estimation of brightness morphology and the size of the emitting region. The emission of molecular lines commonly originates from two different vertical layers. Both contributions are combined when calculating a moment map, which complicates the interpretation of observed structures in the  $M_0$  image, especially over different azimuthal angles  $\theta$ . Depending on the disk inclination and elevation of the emitting layers, substructure can be observed in the  $M_0$ , such as an “X” shaped substructure which originates from those regions where the emission of the front and back layer of a disk is detected, as shown in Figure 1.8. Although the “X” shape has a radiative origin, it does not trace a physical change in the disk temperature or density.

Alternatively to integrating the flux for different velocities, it is common to

---

<sup>3</sup>This is equivalent to saying that the  $PA$  is defined as the angle between north and the semi-major axis in the redshifted side of the disk.

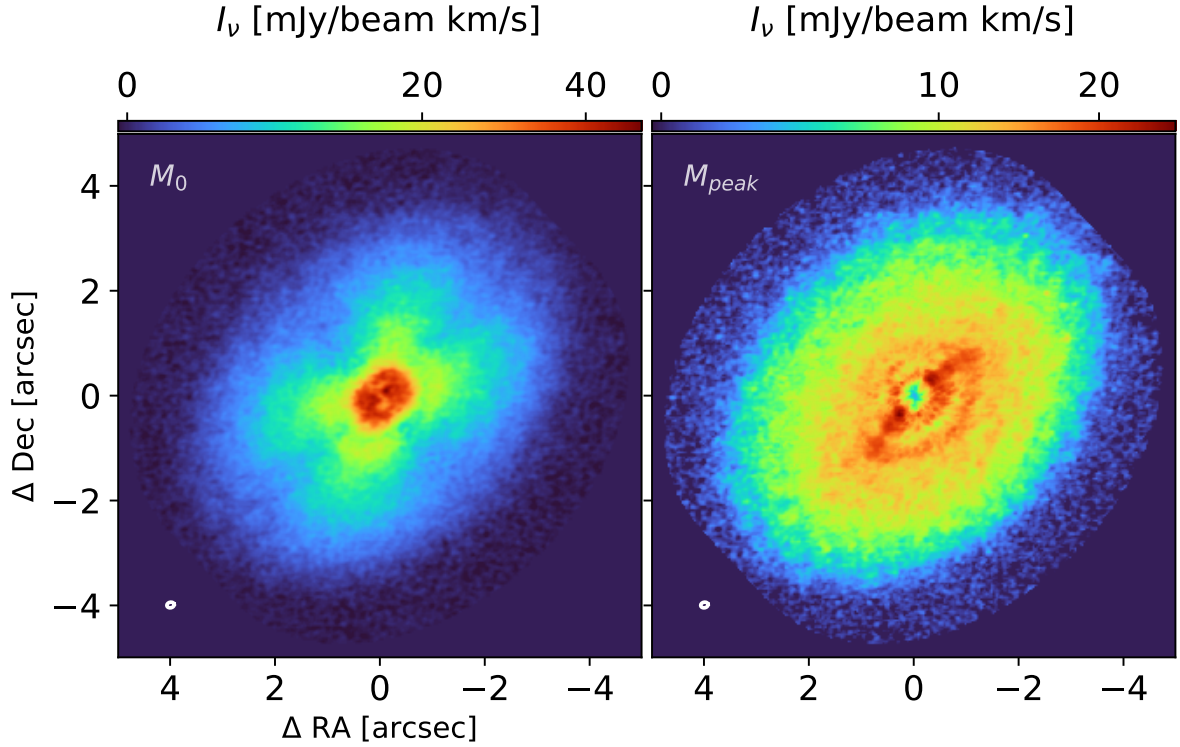


**Figure 1.8:** Artifact substructure in the  $M_0$  and  $M_{peak}$  for the  $^{13}\text{CO}$  J:2-1 emission of the disk HD163296. The color map has been chosen to emphasize the structure of the emission. In the  $M_0$  map, an “X” shaped structure can be observed, which is symmetric over reflection relative to the minor axis of the disk. The  $M_{peak}$  shows a central cavity, and a linear-like overbrightness structure over the major axis, spanning about  $1/3$  of the disk radii. This data was published as part of the MAPS ALMA Large Program (Öberg et al., 2021) and were calculated using a Keplerian mask.

recover the peak brightness of each pixel in the peak brightness map  $M_{peak}$ , which can be related to a brightness temperature  $T_b$  by following a similar approach to the one explained in Section 1.4.2 (under the assumption that the gas emission is in local thermodynamic equilibrium). The peak brightness of each pixel usually originates from the front layer of the disk. Therefore, we can use  $M_{peak}$  to trace the elevation of the emitting layers and recover their brightness temperature profile as a function of radii (e.g., Pinte et al., 2018; Law et al., 2021; Paneque-Carreño et al., 2022; Law et al., 2022a,b).

Different approaches can be considered for calculating  $M_{peak}$ . The simplest of them is the moment 8 map ( $M_8$ ), which returns the peak brightness for each pixel. More sophisticated approaches include fitting quadratic functions or Gaussian components spectrum of each pixel, which allows recovering “super-frequency resolution” information (e.g., Teague & Foreman-Mackey, 2018a;

Casassus & Pérez, 2019). It should be considered, however, that all of the methods mentioned above are affected by image reconstruction artifacts and beam convolution. In the right panel of Figure 1.8, I show the  $M_{\text{peak}}$  of the  $^{13}\text{CO}$  J:2-1 emission from the disk HD163296. A cavity can be observed at the disk center, suggesting that  $I_\nu$  decreases as a function of radii, while a linear-like substructure shows overbrightness along the major axis of the front emitting layer. Both substructures are not physical in origin, as the image reconstruction of the channel maps originates them. This is important to remember when calculating emission line properties, such as the brightness temperature.

### Velocity maps

Similar to the  $M_0$  map, we can create a  $M_1$  map as an intensity-weighted velocity integrated map, such that each pixel  $(i, j)$  has a value of:

$$M_{1,(i,j)} = \sum_k^N \frac{I_{k,(i,j)} v_{los,k}}{M_{0,(i,j)}}. \quad (1.12)$$

The  $M_1$ , however, has a similar problem to the  $M_0$ , where the combination of information from two different emitting layers complicates the interpretation of the results. Instead, we can calculate the velocity at peak brightness map  $M_{vpb}$ , commonly calculated together with  $M_{\text{peak}}$ , by saving the  $v_{los}$  associated with the peak brightness. The  $M_{vpb}$  will trace the velocity of the emitting layer recovered by  $M_{\text{peak}}$ , and thus it becomes useful for estimating  $(v_r, v_\theta, v_z)$ . When  $M_{vpb}$  is well spatially resolved, we can use it to estimate the mass of the central host star. Over this thesis, I will commonly do this through the package `eddy` (Teague, 2019).

### Emission masking

Computing the integrated maps requires collapsing the channels over the velocity axis, thus combining the information of  $N$  images into a single one. It should be considered, however, that the brightness of every pixel has an uncertainty  $\mu$  associated. As a thought exercise, let us think about the emission of a single pixel at the coordinates  $(i, j)$ . For a perfect reconstructed image, the emission of the pixel in every channel can be described as a linear combination of the disk emission plus the uncertainty of the measurement,

such that:

$$I_{k,(i,j)} = D_{k,(i,j)} + X(0, \mu^2), \quad (1.13)$$

where  $D_{k,(i,j)}$  is the emission from the disk at the channel  $k$  in the pixel  $(i, j)$ , and  $X(0, \mu^2)$  is a normal random variable centered at 0 with a standard deviation of  $\mu$ , representing the uncertainty associated to each channel. When we sum over  $k$  to create the integrated maps, as in Equation 1.11, we add the contribution from the disk  $D_k$  and the contribution from the noise represented by  $X$ . For example, for  $N$  channels, the integrated brightness of the pixel becomes:

$$I_{(i,j)} = D_{(i,j)} + X(0, N \cdot \mu^2), \quad (1.14)$$

where  $D_{(i,j)} = \sum_k^N D_{k,(i,j)}$  is the total contribution of the disk emission to the pixel  $(i, j)$ . In this calculation, we have used that the sum of  $N$  times  $X(0, \mu^2)$  is also a normally distributed random variable, which is centered at 0 and has a standard deviation equal to the square root of the sum of the individual deviations:

$$X(0, N \cdot \mu^2) = N \cdot X(0, \mu^2). \quad (1.15)$$

Therefore, the  $M_0$  will have a brightness uncertainty per pixel equal to  $\sqrt{N}\mu$ , which is  $\sqrt{N}$  higher than the uncertainty of a single channel. Observations of planet-forming disks typically span at minimum about  $10 \text{ km s}^{-1}$ , which at velocity resolutions of  $0.1 \text{ km s}^{-1}$  would return emission distributed in over  $N = 100$  channels. Directly adding all of them into an integrated map would result in a sensitivity loss of a factor of 10, which is equal to acquiring an observation  $\times 100$  shorter in exposure time.

A partial solution to this problem comes from only integrating the regions where emission is expected. In the case of disks, this can be done through “Keplerian masks”, which follow the disk region corresponding to the isoveLOCITY curve for a given disk geometry (inc, PA), stellar mass  $M_\star$ , and elevation of the emitting surface. An example of this masking is shown in Figure 1.9, where the  $M_0$  resulting from integrating with and without a mask are compared. Each pixel’s uncertainty will depend on the number of channels included in the mask. Even with Keplerian masking, the inner disk regions are still considering a very high number of channels, which decreases the

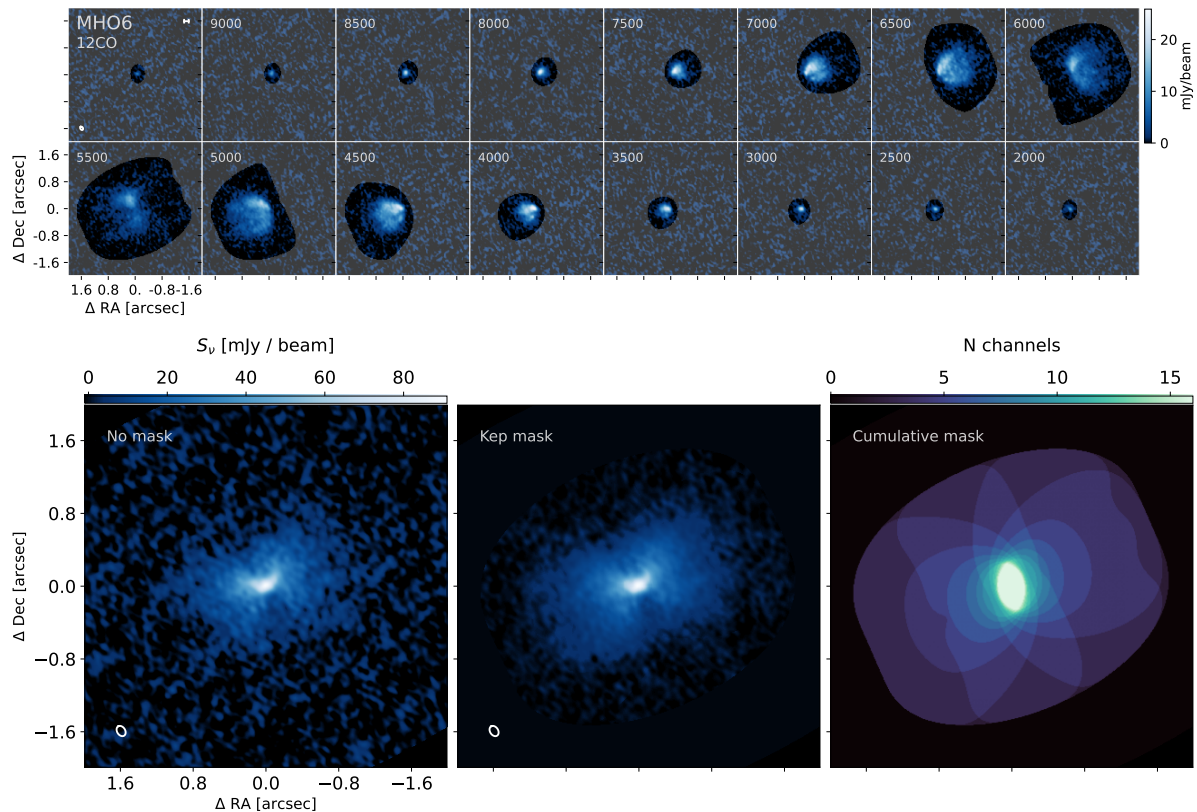


**Figure 1.9:** Comparison of integrating line emission with and without masking. The channel maps of the  $^{12}\text{CO}$  J:2-1 emission of MHO 6 are shown in the upper panels, with the unshaded region showing the Keplerian masked pixels. The three large panels in the bottom row show the  $M_0$  calculated without applying any masking in the left, the  $M_0$  calculated with Keplerian masking in the middle, and the number of channels where each pixel is included in the Keplerian mask in the right. The total number of added channels is 16, all of them are shown in the upper rows. This dataset will be presented in more detail in Chapter 3.

sensitivity of detection in the  $M_0$ .

## 1.6 The impact of stellar mass in a planet-forming disk

Disk-like structures have been detected in objects ranging from Brown-Dwarf (BDs) masses to Intermediate Mass Stars (IMS, e.g., Pinilla et al., 2017c, 2022b). The evolution of the material in those disks is strongly dependent on the properties of the host star, particularly on the stellar mass and luminosity, as they will determine the radiation field, the orbital timescales of a disk, and the strength of radial drift (e.g., Pinilla et al., 2022a), which is dependent on the stellar parameters following  $v_{\text{drift}} \propto L_{\star}^{1/4} / \sqrt{M_{\star}}$  (Pinilla et al., 2013).

The disks around BDs and very low mass stars (VLMS) are particularly in-

teresting, as these objects are the most frequent outcome of the star-formation process (Scholz et al., 2012; Mužić et al., 2019). Circumstellar disks around them have been identified from the near-infrared to centimeter wavelength (e.g., Luhman, 2006; Klein et al., 2003; Scholz et al., 2006, 2007; Ricci et al., 2012; Daemgen et al., 2016; van der Plas et al., 2016; Ricci et al., 2017b,a; Sanchis et al., 2020; Hashimoto et al., 2021), which tend to be more compact and lower in dust mass when compared to disks around T-Tauri stars (e.g., Pinilla et al., 2017c; Ward-Duong et al., 2018; Hendl et al., 2017, 2020; Long et al., 2022). The typical millimeter fluxes of such disks suggest that they have a dust content of only a few Earth masses, or lower, thus challenging the formation of giant planets through core or pebble accretion (Liu et al., 2020), in contrast to the detections of such objects around VLMS (e.g. Morales et al., 2019).

The dust evolution in the disks around BDs and VLMS will be strongly dominated by radial drift, which is stronger than in disks around solar-type objects at all stages of a disk evolution. This is shown in Figure 1.10 from Pinilla (2022), where the evolution of the radial drift is estimated considering the evolution of the stellar luminosity as a function of age. Because the disks in VLMS are more compact, colder, and have a lower mass, determining how these disks overcome the dust radial drift is an active topic of research.

Millimeter-sized particles have been detected in BD and VLMS disks through measurements of the spectral index (Ricci et al., 2014; Pinilla et al., 2017c), which are only possible to explain when radial drift is significantly reduced by the presence of strong pressure bumps (Pinilla et al., 2013). The presence of pressure bumps could produce substructures, such as rings, gaps, spiral arms, and lopsided asymmetries, with different amplitude, contrasts, and locations depending on the origin of the pressure variations (e.g., Pinilla & Youdin, 2017; Andrews, 2020). The occurrence rate of substructures in disks around VLMS will be tested in Chapter 2, where millimeter observations at high angular resolution of a small sample of disks in the Taurus SFR are shown.

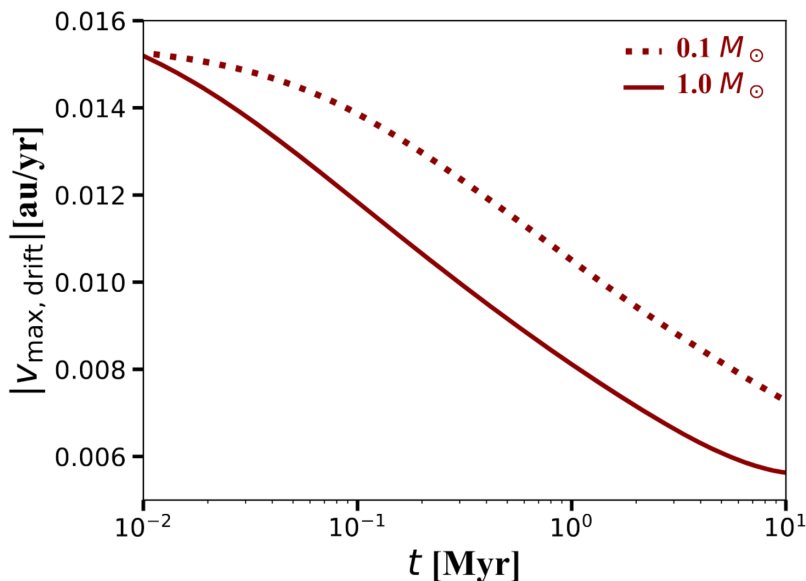


**Figure 1.10:** Strength of radial drift against disk age, for a  $0.1 M_{\odot}$  and  $1.0 M_{\odot}$  host star. Figure extracted from [Pinilla \(2022\)](#).

## 1.7 The impact of stellar-multiplicity in a planet-forming disk

The tidal forces resulting from a companion-disk interaction can perturb the material distribution of a disk, thus impacting the disk evolution and its planet-formation potential (e.g., [Clarke & Pringle, 1993](#); [Bate, 2018](#)). We can separate the companion-disk interactions into two different families: a) Interactions where the companion star is close to the primary star, such that there is material orbiting both of them, known as a circumbinary disk, and b) interactions between an external companion and the circumstellar disk of the primary star. We will name these two cases as the internal and external companion cases. In the following, I briefly describe each scenario:

### 1.7.1 Internal binary-companion

In a circumbinary disk scenario, the binary stars will gravitationally interact with the disk material, exchanging energy and angular momentum through resonant torques ([Goldreich & Tremaine, 1979](#); [Artymowicz et al., 1991](#); [Goldreich & Sari, 2003](#)). These tidal forces are expected to carve a central cavity in the disks, where the material density is severely reduced ([Artymowicz & Lubow, 1994](#); [Miranda & Lai, 2015](#)).

Hydrodynamic simulations of circumbinary disks have shown that disks become eccentric due to dynamical instabilities, and the binaries will produce a significant depletion of material in the center of the disk, usually referred to as a cavity. The properties of this cavity will be dependent on the binaries and the disk itself (see [Lubow, 1991](#); [MacFadyen & Milosavljević, 2008](#); [Thun et al., 2017](#); [Hirsh et al., 2020](#); [Muñoz & Lithwick, 2020](#); [Ragusa et al., 2020](#)). The change in the density profile will also affect the disk pressure profile, thus triggering a dust trap that can stop the dust radial drift. These cavities have been observed at millimeter wavelengths (e.g., [Smallwood et al., 2021](#); [Long et al., 2021](#)). Due to the well-defined effect of the binaries over their circumbinary disks, searching for deviations from the expected cavity size, eccentricity, or disk axisymmetry, can provide clues about the additional mechanisms shaping the disk morphology. In Chapter 4, we will explore the substructures of the circumbinary disk around CS Cha, using the deviations from expected morphology as a tracer for planet formation.

### 1.7.2 External binary-companion

Dynamical interactions between young stellar systems significantly impact their planet formation environment. Binaries are known to truncate the disks of their companions (e.g. [Papaloizou & Pringle, 1977](#); [Artymowicz & Lubow, 1994](#); [Manara et al., 2019](#); [Rota et al., 2022](#)), disrupt the disk material into highly eccentric or unbound orbits (e.g. [Rodriguez et al., 2018](#)), and modify the material distribution over the disk, generating spirals, arc-like structures, and inducing warps (e.g. [Zapata et al., 2020](#); [Nealon et al., 2020](#)). An example of an observation of a tidally-induced substructure is shown in Figure 1.11, where the emission of the system AS 205 is compared remarkably similar to an independent numerical simulation for the gas distribution in a system undergoing a parabolic fly-by interaction ([Kurtovic et al., 2018](#); [Cuello et al., 2019](#)).

Close encounters in highly eccentric systems or unbound fly-bys are more common at the early stages of stellar and disk formation ([Pfalzner & Kaczmarek, 2013](#); [Bate, 2018](#)), and those interactions generate structures that only last for a short astronomical time (scales of thousands of years, e.g., [Cuello et al., 2019](#)). However, the consequences of those encounters can be catastrophic for the disk and its potential planetary system. A few systems have been observed to have interacted recently with a companion, such as HV Tau

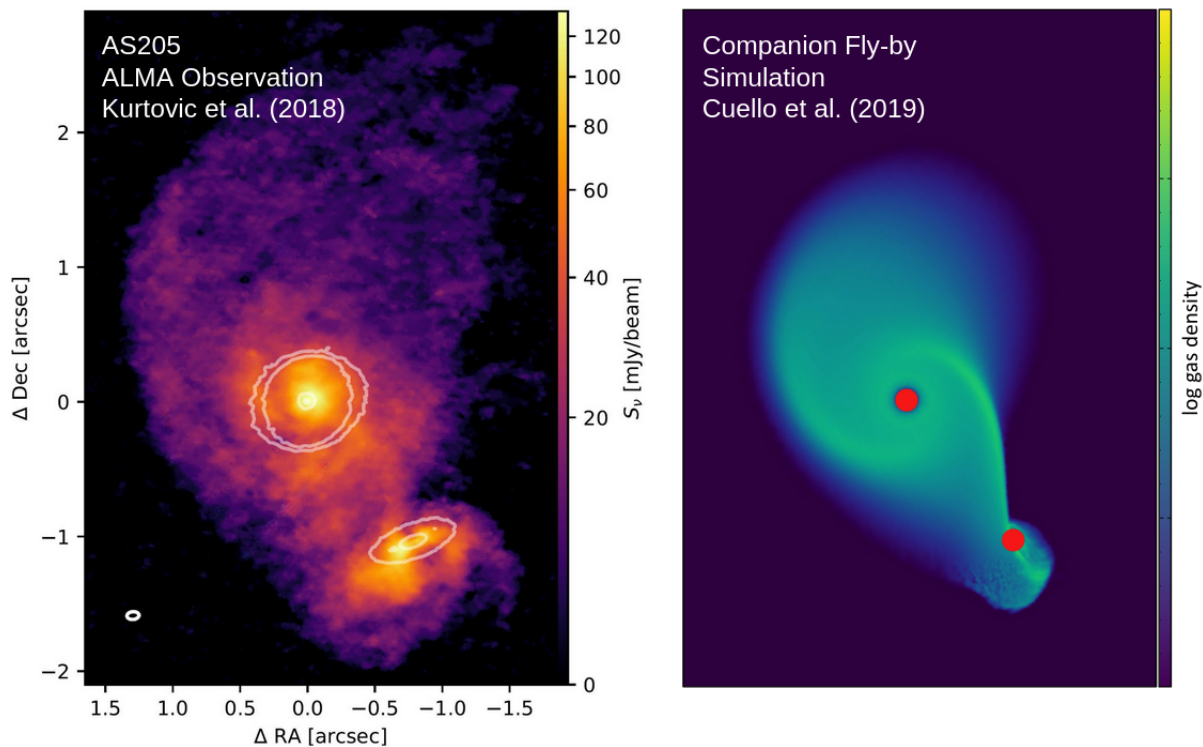


**Figure 1.11:** The image shown in the left panel comes from Kurtovic et al. (2018), while the simulation of the right panel is a rotated and scaled numerical model from Cuello et al. (2019).

with DO Tau (Winter et al., 2018), FU Ori (Takami et al., 2018), BHB2007-11 (Alves et al., 2019), AS 205 (Kurtovic et al., 2018), SR24 (Mayama et al., 2010; Fernández-López et al., 2017; Weber et al., 2023), UX Tau (Zapata et al., 2020), Z CMa (Dong et al., 2022), and RW Aur (Rodriguez et al., 2018).

The impact of a companion on a circumstellar disk will be dependent on the orientation of the orbit relative to the disk plane and the closest distance at interaction (e.g., Cuello et al., 2019). Therefore, to fully understand how the substructures of multiple stellar systems are related to the interaction between the stars, it is crucial to characterize the orbit of the binaries. In Chapter 5, I will discuss the recovery of astrometric information using ALMA observations and parametric visibility modeling to explain the observed structures in the system RW Aur, and the nature of the interaction between the stars.





# 2

## Observational considerations

---

Observations of the light emitted by planet-forming disks is our primary tool to understand the processes related to planet formation. Therefore, properly characterizing our techniques, methods, and instruments is needed to understand our observational limitations and maximize information recovery. In this chapter, I discuss some of the observational and numerical methods used in my research and present them within the context of planet formation. The material discussed in this chapter is partially based on the research presented in Kurtovic (currently under review, submitted to JOSS).

### 2.1 Interferometric observations

#### 2.1.1 Observing planet-forming disks in the sky

Young circumstellar disks, where planet-formation is actively ongoing, are found around young stellar objects (ages of  $< 20$  Myr). Unfortunately, there are not many of them in the immediate solar vicinity. The brightest and nearest planet-forming disks to Earth are located around TW Hya (the closest, at 54 pc), V4046 Sgr (71 pc), and HD 163296 (101 pc), with distances from GAIA DR3 ([Gaia Collaboration et al., 2021](#)). The remaining thousands of known young circumstellar disks are located farther than 100 pc, with typical distances ranging between 120 pc to 180 pc for nearby Star Forming Regions (SFR) such as Lupus, Taurus, Chameleon, or Upper Scorpius.

The large distance between Earth and the nearby SFR makes observations of young stellar systems challenging, mainly due to their small angular extent over the sky-plane. To put their sizes into perspective, let us compare them to the orbits of the planets in our own Solar System. The giants Jupiter, Saturn, Uranus, and Neptune are located at roughly 5 au, 10 au, 20 au and

30 au from the Sun. If we placed a replica of the Solar System in one of the nearby SFR ( $\approx 150$  pc), the angular size in the sky-plane for the diameter of each orbit would become about 66 mas, 130 mas, 260 mas and 400 mas. In Figure 2.1, I show a size comparison between the Moon and Jupiter, as we see them in the sky, and the orbit of Neptune at 150 pc.

An observation typically needs at least three resolution elements over a region of interest to distinguish between a substructure and its surroundings. For example, to observe the planet-formation environment at 5 au from the young stellar object, an angular resolution of approximately 10 milliarcseconds would be required for stars located at a distance of 150 parsecs. Similarly, studying planet formation in the inner regions, within the first 1 astronomical unit, would require angular resolutions of 1-2 milliarcseconds.

What size should we build a telescope to observe with those angular resolutions? We can approximate the angular resolution of a telescope as  $\theta_t \approx \frac{\lambda}{D_t}$ , where  $D_t$  is the telescope's diameter and  $\lambda$  is the observed wavelength. Thus, to observe the 1 mm emission coming from dust grains in a planet-forming disk, we would need a telescope of  $D_t \approx 20$  km to reach the resolution of  $\theta_t = 10$  mas, which is unfeasible to build as a single structure on Earth surface (a more detailed description for the resolution of an observation is given in Section 2.1.3).

Instead of a single dish telescope, we can combine smaller antennas to synthesize a telescope of the size of the antenna separation through the interferometry technique. While this technique can potentially enable us to achieve arbitrarily small angular extents, it comes with additional data recording and analysis challenges. In the following section, I will outline the basic definitions for understanding interferometric observations of planet-forming disks.

### 2.1.2 Brightness and visibilities

In the observational study of an astronomical source, the main observable goal is the recovery of the sky brightness distribution  $I = I(l, m)$ . Here,  $I : (\mathbb{R}, \mathbb{R}) \rightarrow \mathbb{R}$  is the function that returns the brightness of a source in the sky coordinates  $(l, m)$ , which are two orthogonal axes defined as  $l = \sin((\alpha - \alpha_0) \cos \delta)$  and  $m = \sin(\delta - \delta_0)$ , where  $(\alpha, \delta)$  are the Right ascension and Declination coordinates, and  $(\alpha_0, \delta_0)$  is the phase center of the observation. For small angular extents, such as those spanned by planet-forming disks, the  $(l, m)$  coordinates can be considered Cartesian coordinates, and thus we will typically show them as



**Figure 2.1:** In the left panel, a comparison of the angular size of the Moon and Jupiter in the Earth sky. In the right panel, the size in the sky of a Neptune orbit at 150 pc is compared to Jupiter. Moon image credits to Gregory H. Revera, obtained from Wikimedia Commons. Jupiter image credits to NASA/Brian0918, obtained from Wikipedia Commons.

$(\Delta\alpha, \Delta\delta)$  relative to an arbitrary center. By knowing  $I(l, m)$  for every  $(l, m)$  of interest, we can start setting constraints over the physical processes that originated such brightness distribution.

Observing  $I(l, m)$  with high angular resolution at millimeter wavelengths is only possible with interferometers. For simplicity, let us consider an interferometer as an instrument that combines the light from two or more antennas<sup>4</sup> by creating an interference pattern. Unlike optical or near-infrared cameras, which sample  $I(l, m)$  directly through pixel grids, an interferometer does not sample  $I$ . For all intents and purposes of this thesis, and under the definition and assumptions previously established for  $I$ , an interferometer samples the two-dimensional Fourier transform of  $I$ , given by:

$$V_\lambda(u, v) = \int \int I_\lambda(l, m) e^{-2\pi i(ul+vm)} dl dm, \quad (2.1)$$

where  $(u, v)$  are spatial frequencies measured in units of observed wavelength ( $\lambda$ ) given by the projected distance between the antennas composing the interferometer. In the following, I will drop the use of the  $\lambda$  index, but  $V$  and  $I$  should always be considered for a specific wavelength or wavelength range. The function  $V : (\mathbb{R}, \mathbb{R}) \rightarrow \mathbb{C}$  is called the visibility function, and it returns a complex number for every pair  $(u, v)$ , thus  $V = \text{Re}(V) + \text{Im}(V)$ .

---

<sup>4</sup>Historically, single antenna interferometers have been designed and built for specific purposes, such as the sea interferometer (Bolton & Slee, 1953). Such applications are outside of the scope and interest of this thesis.

Both  $\text{Re}(V)$  and  $\text{Im}(V)$  are commonly measured in the same brightness units as  $I$ . A detailed theoretical discussion on the mathematical origin of equation 2.1 can be found in [Thompson et al. \(2017\)](#).

Each pair of antennas will measure  $V$  in a single pair of spatial frequency  $(u_n, v_n)$ , with  $n$  the index of the antenna pair and both  $u_n$  and  $v_n$  constant for a fixed time. Following this definition, we can think of antenna pairs as being tuned to measure a specific two-dimensional spatial frequency, which is determined by the position of the antennas over the Earth's surface and the elevation of the observed source over the horizon.

In principle, only two antennas are needed to create an interferometer. This interferometer would only be sensible to structures with angular scales comparable to  $\lambda/D$ , and only in the axis parallel to the baseline. Such measurement is not useful if one wants to recover the two-dimensional  $I(l, m)$ . Adding additional antennas makes more pairs available for combination, and each one will measure the brightness of a given  $(u_n, v_n)$ . From now on, we will refer to the set of measurements where the visibility function was sampled  $\{V(u_n, v_n)\}_{n=0}^N$  as the **visibilities**, where  $N$  is the number of samplings taken during the observation. The closest antenna pair in projected distance will set the smaller spatial frequency sampled  $(u, v)_{\min}$ . Similarly, antennas located farther away will have a larger projected distance, and thus they will give the maximum value sampled spatial frequency  $(u, v)_{\max}$ . The values for  $(u, v)_{\min}$  and  $(u, v)_{\max}$  define the visibility range or visibility coverage, which is the region of the visibility space that is sampled by the baselines of an observation. It is common in the literature to find discussions about the quality of the visibility coverage, which refers to the density of measurements in a specific region of the spatial frequency plane.

Interferometers act as a spatial filter through the discrete measurement of the values of  $V$ . Let us think about a planet-forming disk in the sky, whose maximum angular extent is  $1''$ , meaning if we fix the origin of the coordinate system at the center of the disk, then  $I(l, m) = 0$  for any  $\sqrt{l^2 + m^2} > 0.5''$ . We are also interested in reaching an angular resolution of  $0.02''$  (or 20 mas), because a given physical process becomes observable at such resolution. To study  $I$  within those boundaries, we need to measure  $V$  over spatial frequencies sensible to scales from  $1''$  to  $0.02''$ . For an observation at 1.3 mm wavelengths, the  $0.02''$  resolution is obtained with an antenna pair with a baseline of approximately 14 km, while the  $1''$  is achieved with antenna baselines of about 260 m. Thus, to recover  $I(l, m)$  over the range of interest, we

will need baselines spanning from at minimum 260 m, to 14 km. Currently, the ALMA antenna configuration C-10 is the only one that can achieve those requirements.

For a given observation, each baseline given by an antenna pair will have an uncertainty associated with its visibility measurement. The physical origin of this noise can range from atmospheric effects to instrumental thermal noise. Thus, for each  $V_n = V(u_n, v_n)$ , we can associate a weight defined as  $w_n = 1/\sigma_n^2$ , where  $\sigma_n$  is the root-mean-square (rms) deviation of the measurement.

### 2.1.3 Recovering the brightness distribution from the sampled visibilities

In principle, recovering  $I(l, m)$  over a range of  $(l, m)$  of interest should be as simple as taking the inverse Fourier transform of the visibilities. However, our interferometers observe a discrete sample of  $V$  and not a continuous description. Therefore, interferometers can only recover an incompletely sampled  $V$ , and to get to  $I$ , we will need to make assumptions over the values in those spatial frequencies  $(u, v)$  where  $V$  was not measured. Given this fundamental issue, most methods for recovering  $I$  rely on constructing a model for the sky brightness distribution ( $I_m$ ). The model image  $I_m$  is typically derived by minimizing metrics such as  $\chi^2$ , entropy, or residual amplitude. In the following, I describe the two methods used in my work.

#### The CLEAN algorithm

One of the most accepted algorithms to construct  $I_m$  is called the CLEAN algorithm (Högbom, 1974; Clark, 1980). In a few steps, the algorithm works as follows:

1. Take the inverse Fourier transform of the visibilities under the assumption that the value of the visibility function for every spatial frequency not measured is 0. This produces an image representation of the visibilities with a certain number of pixels and pixel angular size called the “dirty image”.
2. Identify the pixel with the highest brightness in the image, estimate a point source based on this brightness, and save it in a “CLEAN model” image.

## 2 Observational considerations

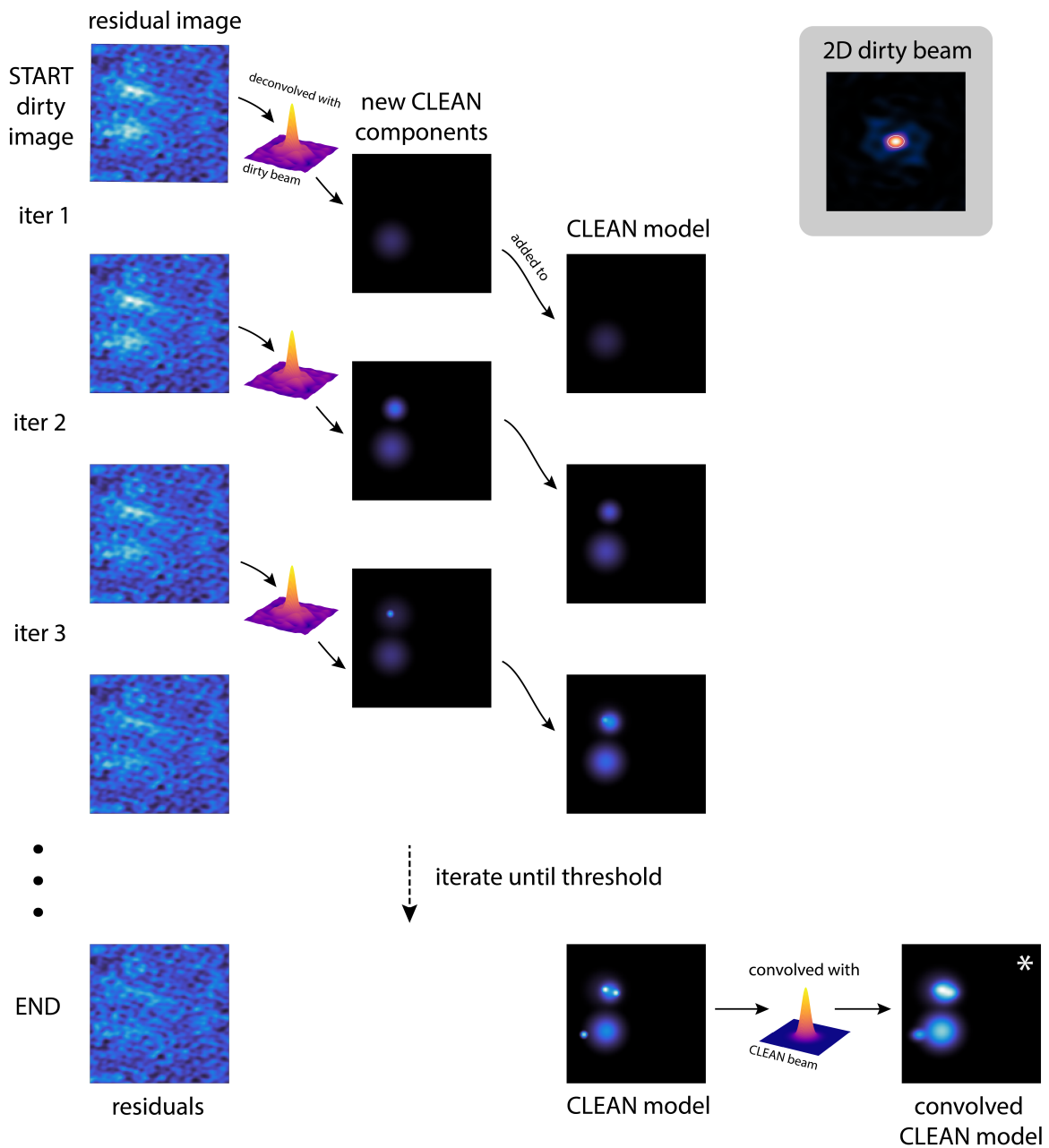


**Figure 2.2:** Example of the steps followed by the CLEAN algorithm. Figure from [Czekala et al. \(2021\)](#).

3. Calculate the visibilities of the CLEAN model and subtract them from the observed visibilities to obtain the "residual visibilities".
4. Repeat step 1 with the residual visibilities, cumulatively adding components to the model image until the highest brightness reaches a certain threshold, usually set relative to the observation signal-to-noise ratio.

The resulting CLEAN model is our  $I_m$ , which is similar to obtaining a model by minimizing  $\chi^2$  (Schwarz, 1978). This model, however, can contain spatial brightness variations of higher frequencies than those covered by the visibility range because the scale for brightness variation corresponds to the pixel size (as seen in the panel (d) of Figure 2.3). Therefore, the CLEAN model image is convolved with a Gaussian representative of the resolution of the observation, to erase artificial spatial variations that are not constrained by the baselines. This convolved model is then added to the inverse Fourier transform image of the residual visibilities (the residuals image), which creates the CLEAN image. This process is illustrated in Figure 2.2, extracted from Czekala et al. (2021).

Over the years since the first publication of the CLEAN algorithm, several changes have been introduced to make it useful in a broader range of applications. These modifications are considered in the CLEAN algorithm implementation found in the CASA software (McMullin et al., 2007), and some relevant parameters in the context of this thesis are described below:

- *multiscale*: Instead of subtracting delta functions represented by point sources in step 2, we can also subtract Gaussian sources (as in 2.2). The width of these Gaussians is fixed for each iteration of the algorithm, and we will refer to that set of Gaussian widths as the “multiscales” set.
- *smallscalebias*: The algorithm preference between adding point sources or Gaussians to the CLEAN model can be modified through the “smallscalebias” parameter.
- *gain*: The amplitude of the flux subtracted in step 2 can be limited to more conservative values to avoid including artifacts in the CLEAN model. The “gain” parameter controls this amplitude

An example of a model reconstructed from a synthetic observation is shown in Figure 2.3, where a ring is reconstructed starting from the incomplete visibility sampling. The advantage of this algorithm is that it can be applied to any set of data, such as the continuum emission or the gas emission of a protoplanetary disk. Each image is created based solely on the information available on the given visibilities.

To calculate the representative Gaussian for convolving the CLEAN model, we need to determine the minimum spatial size that a given visibility range can recover. To accomplish this, we use the inverse Fourier transform of a

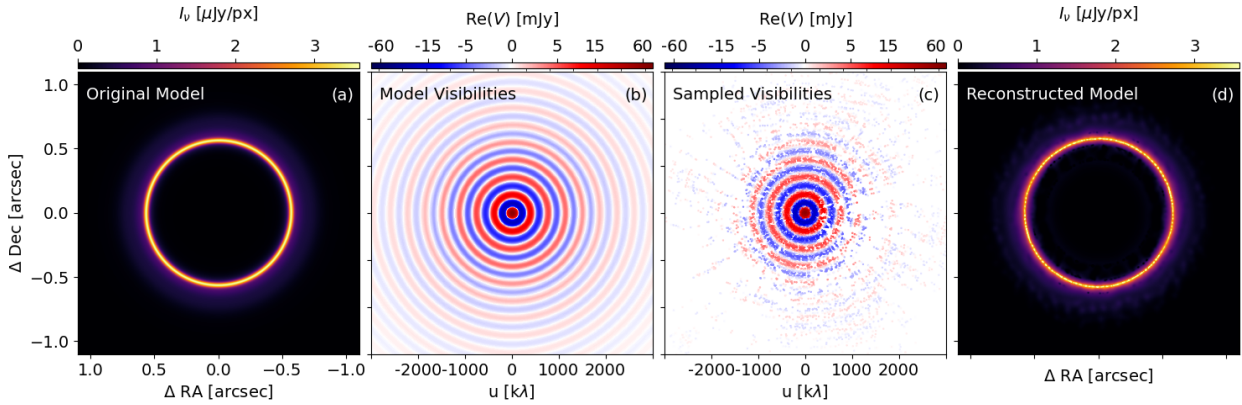


**Figure 2.3:** An example of the workflow followed by the observation and reconstruction of an interferometric dataset. A brightness distribution at a fixed wavelength in the sky plane (in panel (a)) has a Fourier representation shown in panel (b). Interferometers obtain an incomplete sample of the visibility function (shown in (c)), which is used to reconstruct a model of the brightness distribution. In panel (d), the model was reconstructed using the CLEAN algorithm, and it shows the high spatial frequency variations that originate from cleaning with discrete point or Gaussian sources.

synthetic visibility set that matches the observations in  $(u, v)$  coordinates but has a constant value for the measured visibilities. This synthetic set simulates an observation of a point source located at the phase center of the observation. The resulting inverse Fourier transform indicates the spatial brightness spread of a point source over the  $(l, m)$  coordinates, and this image is known as the Point Spread Function (PSF) image. When using the CLEAN algorithm for image reconstruction, it is not possible to differentiate between two point sources that are closer together than the size of the central peak of the PSF. Therefore, we approximate the width of the PSF with the full width at half maximum (FWHM) of a Gaussian function, which determines the resolution of the image. For interferometers, this approach estimates the angular resolution  $\theta_D$ .

When reconstructing images through the CLEAN algorithm, the weights of the visibilities can be considered to bias the reconstruction towards the shortest or longest baselines, thus changing the sensitivity to larger or more compact spatial scales. Assigning weights based on  $w_n$  will typically bias an observation to shorter baselines, typically with lower rms, resulting in a larger PSF and lower angular resolution. This choice is known as natural weight. Similarly, assigning the same weight to all measurements will bias the observation towards longer baselines, reducing the PSF size and increasing the angular resolution, also known as uniform weight. The choice of weighting is

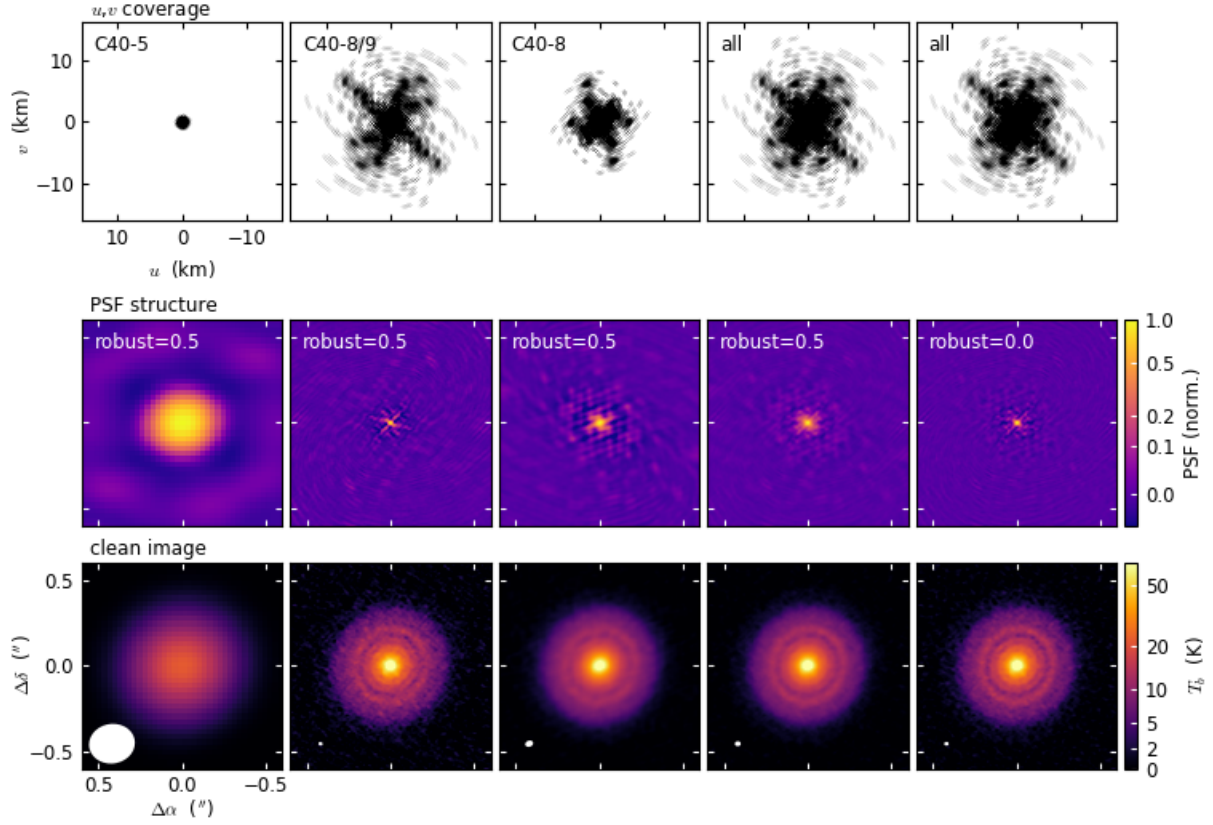


**Figure 2.4:** Example of the relation between visibility coverage, PSF structure, angular resolution, and robust weighting, for generating CLEAN images of the RU Lup disk. The upper row panels shows the visibility coverage recovered from ALMA observations with different antenna configurations. The PSF of these visibility coverages is shown in the middle row panels, with the chosen robust value specified in the top left corner. The lower row shows the resulting CLEAN image from each visibility set, with the beam shown in the lower left corner. This image was extracted from [Andrews et al. \(2018\)](#).

controlled through the *robust* parameter, which can be set to 2 or -2 for natural or uniform weight, respectively, but can also take any value in between. An example of the relation between the visibility coverage of an observation, the PSF shape, and the resulting CLEAN image is shown in Figure 2.4 with the disk RU Lup, which was extracted from [Andrews et al. \(2018\)](#).

### Parametric visibility modeling

Given the visibilities of an observation, we can attempt to recover  $I_m$  by describing it with a combination parametric functions, so that:

$$I_m = I_m(\alpha_m, (l, m)), \quad (2.2)$$

where  $\alpha_m$  is a set of values for the parameters that describe  $I_m$ . To find the optimal values for the set  $\alpha_m$ , we can calculate the Fourier transform of  $I_m$  in the same  $(u, v)$  coordinates covered by a specific observation (let us call the model visibilities  $V_m$ ), and minimize the residuals between the model visibilities and the observed visibilities. This optimization is commonly performed through minimization of  $\chi^2$  with linear methods or Markov Chain Monte Carlo.

Compared to CLEAN, there are three main advantages to using parametric visibility modeling to construct an  $I_m$ .

- The parametric function works as a prior for the morphology of the source emission. For example, planet-forming disks are expected to follow Keplerian rotation around the star and usually show axisymmetric structures. By describing them with functions more appropriate to their morphology, such as rings, we can better reproduce their shape as a function of  $(l, m)$ , compared to describing them with delta functions and circular Gaussians.
- In the context of disks, recovering parameters such as the disk size, inclination, position angle, or deviation from a smooth profile can be done directly from  $\alpha_m$  or through the comparison between  $V_m$  and the observed visibilities. Such information is not a direct output of the CLEAN model.
- Parametric functions can recover faint extended emission that the CLEAN algorithm would leave in its residuals. As the model reconstruction of CLEAN depends on the individual signal-to-noise ratio of each angular resolution element, it cannot reproduce structures with peak emission that fall below the single resolution element sensitivity.

Despite the multiple advantages of parametric visibility modeling to recover  $I$ , it also has disadvantages compared to CLEAN. The main advantage is also its main limitation, as  $I_m$  can only take the shape of the given functions described by the parameters in  $\alpha_m$ . If  $I$  has an emission not considered in the  $\alpha_m$ , then it will not be well represented by  $I_m$ , and structured residuals will be observed. Thus, describing very complex structures can quickly become prohibitive due to the high number of free parameters, and non-linear perturbations or turbulent structures are too complex to be included in  $\alpha_m$ . In those cases, recovering  $I$  with CLEAN is a better alternative.

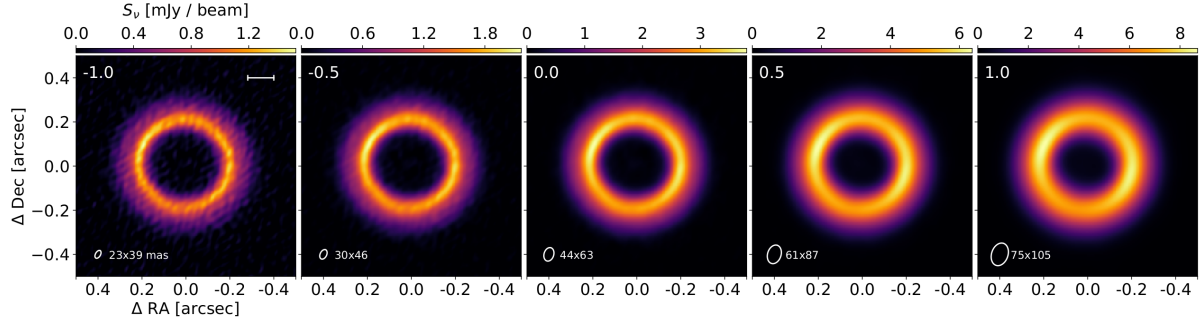


**Figure 2.5:** The 0.87 mm dust continuum emission of the CS Cha system, imaged with CLEAN and different robust parameters. The robust parameter used to reconstruct each image is shown in the upper left corner of each panel. The lower left corner shows the size of the FWHM of each beam. All images come from the same visibilities. This source is presented in deeper detail in Chapter 4.

Another feature of visibility modeling is the capacity for recovering “super-resolution” features in the visibilities. Due to the different weighting options of CLEAN, and its limitation on the sensitivity per angular resolution element, there are structures in  $I$  which are not represented in the CLEAN image. The image reconstruction through CLEAN can strongly depend on the choice of reconstruction parameters, particularly on the robust value. Through the convolution with a Gaussian resulting from a weighted average of the visibilities, the CLEAN algorithm can effectively erase information of substructures that is available in the visibilities, as shown in Figure 2.5, where the rightmost panels do not show the radial brightness structure of the ring. Those features can be recovered through parametric modeling, as shown in Chapters 3, 4, and 5.

## 2.2 Generating simulated observations

### 2.2.1 Challenges when comparing physical models to observations

Interpreting high angular resolution observations requires direct comparison with the output of physical models. For instance, hydro-dynamical models can be used to constrain the mass of candidate planets shaping observed structures (e.g. Zhang et al., 2018; Pérez et al., 2019; Bae et al., 2021), the consequences of considering hydro-fluid instabilities (e.g. Barraza-Alfaro et al., 2021), or the impact of photoevaporation in the disks (e.g. Gárate et al., 2021), among many others also mentioned in Chapter 1. The most direct way to test those models is to either compare them to existing obser-

vations or to predict how future observations would show the signatures of each phenomenon. Creating a synthetic observation of the physical model is a crucial step in any of those scenarios.

A physical model can be used to generate observable predictions through running radiative transfer algorithms (e.g., RADMC-3D [Dullemond et al., 2012](#)), which generate synthetic images of the model at a specific wavelength. Those images can be used as a pixelated representation of  $I$ . The resolution of those images will depend on the simulation resolution, and therefore it can be set as arbitrarily small as physically and computationally possible. After the radiative transfer model has been generated, the question is how much of that image can be recovered if observed by an interferometer, such as ALMA.

To go from a model image to a synthetic observation, we need to include the observational considerations given by the finite spatial and frequency resolution. The most simple procedure to create a synthetic observation is to emulate the last step of the CLEAN imaging algorithm, which convolves the model with a Gaussian representative of the PSF width. By doing so, the information in spatial scales smaller than the beam size is effectively erased, allowing a direct comparison with an ALMA image generated with the CLEAN image. Although this method is quick and straightforward, it overlooks the fact that the beam size is not uniquely determined for an observation (as discussed in Section 2.1.3), and therefore the convolution with a Gaussian beam could artificially smooth information in spatial scales covered by the visibilities. Another limitation comes from ignoring all the factors involved in interferometric imaging, such as the visibility coverage and decisions over the model reconstruction. Overall, obtaining a synthetic observation by convolving with a Gaussian should only be considered a quick first approximation.

A more robust way to generate a synthetic observation is to calculate the visibilities of the model image, and reconstruct it as if it had been observed. For ALMA, this can be done with the task `simobserve` and `simanalyze` from the CASA software, which allows the user to set any antenna configuration, object position in the sky, exposure time, and frequency bandwidth. This approach is ideal for simulating very specific observations, generating a set of visibilities that can later be studied as an actual observation. However, the complexity can quickly scale when it has to be compared with existing observations composed of multiple execution blocks, multiple antenna configurations, or data from multiple ALMA cycles.

Matching every observational detail in `simobserve` to emulate an existing observation is challenging. This problem becomes even more complicated when combining several observations to generate the image to be compared. An example of this problem is the attempt to compare a simulation to the planet-forming disk TW Hya, which has been observed multiple times by different ALMA Projects, resulting in several dataset configurations, exposure times, frequency bandwidth, and therefore different  $uv$ -coverage. In [Huang et al. \(2018a\)](#), the authors combined data from 9 different projects to study the millimeter emission of TW Hya, and just on ALMA Band 7 the authors have 17 different epochs, each one of them with a certain number of antennas and baselines, observing TW Hya at different latitudes, with varying times of exposure, resulting in 17 different  $uv$ -coverages that would need to be simulated with `simobserve` and concatenated afterward. Such a task becomes too time-consuming to be attempted, especially for projects trying to compare with multiple sources.

### 2.2.2 The SIMIO-continuum package

To facilitate the connection between simulated models and observations, a collection of routines and algorithms has been put together and offered to the community as SIMIO-continuum, or SIMIO for short. Unlike `simobserve`, which can create a new observational setup based on the user inputs, SIMIO is designed to compare with archival observations, mimicking their observational setup, effectively comparing each model to an existing observation. This python-based package aims to be as easy to use for non-observers as doing a Gaussian convolution but incorporating the robustness of generating images as if they were actual interferometric observations.

A key component of SIMIO are the *templates*, which are archival ALMA observations of millimeter continuum emission to be used as reference. Each one of those observations contains one or more antenna arrays, a specific total integration time, frequency bandwidth, etc., which translate into a particular sampling of the visibility plane. SIMIO takes the visibility coverage and replaces the observed visibilities with the visibilities of an input model. This way, SIMIO returns a visibility set with the exact observational setup of the template, but with the synthetic model as the observed object in the sky.

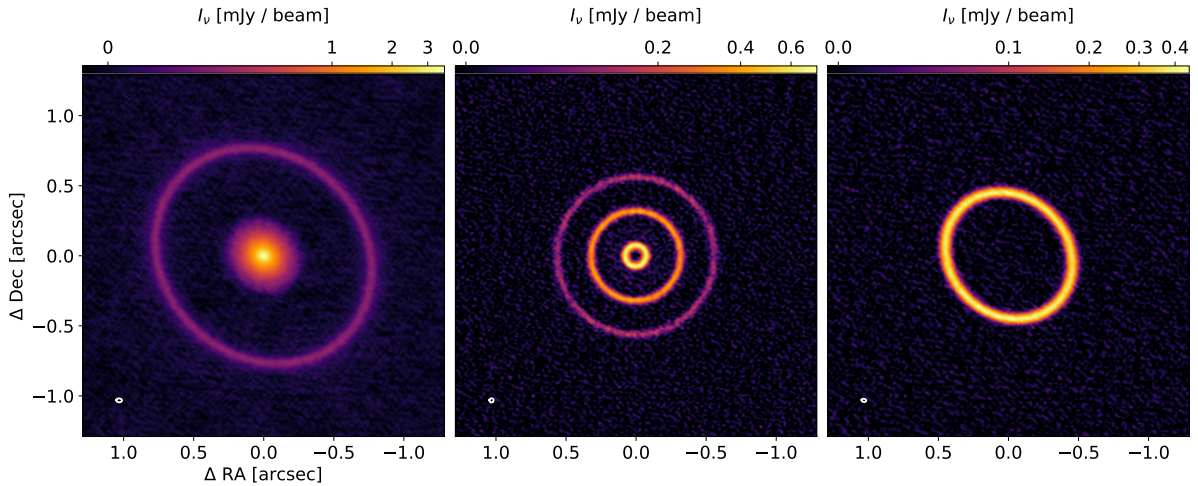


**Figure 2.6:** Examples of generating synthetic observations using SIMIO. The images shown in here are part of works that will be published in Gárate et al. (in review), and Delage et al. (in prep.).

## Templates

SIMIO replaces an observation’s data with a model’s visibilities, effectively mimicking all the observational setups. To decrease the data volume of ALMA observations and allow SIMIO to run on a personal computer, the templates available for SIMIO have been averaged in time (30 s time-binning) and frequency (1 channel per spectral window), similar to Andrews et al. (2021). Such binning is not necessary for a customized template, which can be easily created maintaining the original frequency resolution and exposure time of an observation. The most updated list of publicly available templates can be found on my webpage<sup>5</sup>. The functions have been tested for single-pointing observations and only continuum emission.

## Fourier Transform

SIMIO computes the Fourier transform of a model based on the visibility coverage or the template observation. This is done with the CASA software task `ft`. SIMIO also allows for visibility handling to change a source inclination, position angle, distance from Earth, and the addition of thermal noise.

<sup>5</sup>[www.nicolaskurtovic.com](http://www.nicolaskurtovic.com)

## Examples of using SIMIO

The package SIMIO-continuum has already been used in published works (e.g., [Pinilla et al., 2022b](#); [Garrido-Deutelmöser et al., 2023](#)), and also by some other works which at the time of writing this work are in review or in preparation (Gárate et al., in review; Delage et al., in prep.). In [Figure 2.6](#), I show images generated from synthetic observations made with SIMIO. Although the public version of SIMIO only works with dust continuum observations, it can also be adapted to work with frequency-dependent gas observations, as shown in [Chapter 3](#).



# 3

## Planet formation in very low mass stars

---

This chapter is an adapted version of the the published research article “*Size and structures of disks around very low mass stars in the Taurus star-forming region*” (Kurtovic et al., 2021), and the article in preparation “*Recovering the gas properties of a planet-forming disk through parametric visibility-modeling.*” (Kurtovic & Pinilla, in preparation).

### 3.1 Introduction

M-dwarfs and Brown-Dwarfs (from now on referred to as BD) are the most frequent outcome of the cloud collapse during the star formation process (e.g., Scholz et al., 2012; Mužić et al., 2019). Additionally, exoplanet discoveries suggest that short-period planets ( $< 50$  days) are detected more frequently around M-dwarfs than around FGK stars (Mulders et al., 2015; Hardegree-Ullman et al., 2019), with even a few giant planets discovered around BDs and very low mass stars ( $\lesssim 0.1 M_{\odot}$ , VLMS, e.g., Morales et al., 2019). Such detections imply that planets of a large range of masses can form around these objects, although it remains an open question if these massive objects form as binary companions of the BDs and very low mass stars (VLMS) or as planets. The high occurrence rate of M-dwarfs and planets around them means that the most likely environment for planet formation could be around low mass stars, hence the importance of understanding their planet-forming disks.

In Chapter 1, I mentioned that the disks around M-dwarfs are typically more compact than those around Solar-type stars. However, it remains unclear if their compact sizes are due to the lack of pressure bumps or due to the lack of angular resolution to detect rings and gaps in these disks (the scale of a radial pressure bump cannot be smaller than one local scale height, e.g.,

Dullemond et al., 2018). Before publishing the work shown in this Chapter in Kurtovic et al. (2021), most of the observational knowledge about substructures came from bright (and probably massive) disks, such as the DSHARP or ODISEA sample (Andrews et al., 2018; Cieza et al., 2021). Therefore, observing compact disks around VLMS became key to setting constraints over the potential for planet-formation around these objects.

In Pinilla et al. (2018b), the authors reported the lowest mass star with a resolved large dust cavity (radius  $\sim 20$  au) that had been detected to that date, in the disk around the M4.5 star CIDA 1. In the context of planets creating such a cavity, a high planet-to-stellar mass ratio is needed to open a gap and trap particles in disks around VLMS because, in these cases, the disk scale height at a given location is higher than in moderate or high mass stars (Pinilla et al., 2017c; Sinclair et al., 2020). In a typical disk around a VLMS as CIDA 1, at least a Saturn-mass planet is needed to open a gap in the disk, which challenges the understanding of substructures and the common idea that planets are responsible for their formation since these disks around VLMS and BDs may not have enough mass to form such massive planets (although they may originate from gravitational instability if the disks were much denser in their early stages, e.g., Mercer & Stamatellos, 2020).

Based on the previous CIDA 1 observations, we selected a sample of five disks to observe with ALMA at a resolution of  $0.1''$  in the Taurus star-forming region, whose properties are similar to CIDA 1. Specifically, these disks around low mass stars are more massive compared to other disks with hosts in the same stellar regime. These observations included  $^{12}\text{CO}$  and  $^{13}\text{CO}$  and aimed to estimate how common substructures are around VLMS. Given that radial drift is expected to be very efficient in these disks, they are excellent laboratories to search for evidence of this mechanism by testing the difference between the radial extent of the gas and dust (Trapman et al., 2019).

The following chapter analyzes the observations of the selected VLMS in the Taurus SFR, focusing on the properties of their structures and their disk sizes. The rotation and structure of the gas emission are also analyzed to recover information about the host star.

2MASS	Used Name	Spectral Type	$M_\star$ [ $M_\odot$ ]	$T_{\text{eff}}$ [K]	$L_\star$ [ $L_\odot$ ]	dist (DR2) [pc]	dist (DR3) [pc]
J04141760+2806096	CIDA 1	M4.5	0.19	3197	0.20	135.7	134.6
J04322210+1827426	MHO 6	M5.0	0.17	3125	0.06	141.9	145.6
J04334465+2615005	J0433	M5.2	0.15	3098	0.12	173.3	161.8
J04422101+2520343	CIDA 7	M5.1	0.15	3111	0.08	136.2	140.7
J04202555+2700355	J0420	M5.25	0.14	3091	0.07	170.4	165.7
J04155799+2746175	J0415	M5.2	0.15	3098	0.05	135.7	133.2

**Table 3.1:** Stellar properties of the VLMS. Source properties used in this work. Spectral Type,  $T_{\text{eff}}$ , and  $L_\odot$  comes from [Herczeg & Hillenbrand \(2014\)](#). Stellar masses derived following the method presented in [Pascucci et al. \(2016\)](#), using distances inferred from Gaia DR2 ([Gaia Collaboration et al., 2018](#)).

## 3.2 Target selection

This work includes the 0.87 mm emission of the VLMS in Taurus that had been observed at high angular resolution until 2020, which are six young stars summarized in Table 3.1. While the disk around CIDA 1 had already been published in [Pinilla et al. \(2018b\)](#), my work in [Kurtovic et al. \(2021\)](#) reanalyzed the data to compare all the disks with the same methodologies. The remaining five sources had not been published before.

The previously unpublished observations of very low mass stars in the Taurus star-forming region were obtained as part of a small survey at high angular resolution with ALMA. The sample was selected to optimize the chances of finding substructures. The criteria used to select the targets were as follows: (1) the targets must have been previously observed and detected by either SMA or ALMA in millimeter wavelengths (based on the observations by [Andrews et al. \(2013\)](#) and [Ward-Duong et al. \(2018\)](#), respectively); (2) the stellar mass must be in the range  $\sim 0.1 - 0.2 M_\odot$ ; and (3) the millimeter brightness of the disk must be high relative to the stellar mass when compared to other sources in the same mass range. The last condition comes from observations of the  $L_{\text{mm}} - M_\star$  relation of transition disks and disks with substructures ([Pinilla et al., 2020](#)), which shows that those disks usually have higher millimeter brightness compared to others with stellar hosts of a similar mass. From the list of targets that fulfilled the conditions, the selected disks were preferred due to their lower optical extinction, which would improve the detection of the  $^{12}\text{CO}$  emission from the disks.

### 3.3 Observations

The target properties used in this study (shown in Table 3.1) were taken from [Herczeg & Hillenbrand \(2014\)](#), with stellar masses derived following the method described in [Pascucci et al. \(2016\)](#), using distances inferred from Gaia DR2 ([Gaia Collaboration et al., 2018](#)). The distances in parsecs were calculated as the inverse of the parallax. After the publication of [Kurtovic et al. \(2021\)](#), the GAIA collaboration updated the parallax value of our sources in the publication of the GAIA DR3 [Gaia Collaboration et al. \(2021\)](#). The distances from DR3 are also shown in Table 3.1, and the difference relative to DR2 is small enough such that the analysis in the following sections is not affected. The spatial distribution of our sample in the Taurus optical extinction map is shown in Figure 3.2, where the location of the stars is compared against a reddening map from [Schlafly et al. \(2014\)](#) of the Taurus star-forming region. The reddening values for the sources are 0.61 for CIDA 1, 0.48 for MHO 6, 0.51 for J0433, 0.50 for CIDA 7, 1.38 for J0420, and 0.44 for J0415.

The targets MHO 6, J0433, CIDA 7, J0420, and J0415 were observed with ALMA at 0.87 mm (Band 7) as part of the project 2018.1.00310.S (PI: P. Pinilla), during Cycle 6, with the spectral setup configured to observe in four spectral windows centered at 331.3, 333.3, 344.0, and 345.8 GHz, with two of them centered on observing dust continuum emission, and two observing molecular line emission from  $^{12}\text{CO}$  ( $J = 3 - 2$ ) and  $^{13}\text{CO}$  ( $J = 3 - 2$ ). The frequency resolution for  $^{12}\text{CO}$  was 244.1 kHz per channel; while for  $^{13}\text{CO}$  and the continuum, it was 976.6 kHz. The most extended antenna configuration used was C43-8, providing an angular resolution of  $0.08''$  at best. Some of our sources had archival data from ALMA project 2012.1.00743.S (PI: G. van der Plas) and 2016.1.01511.S (PI: J. Patience), with observations of  $^{12}\text{CO}$  and dust continuum, which were also included in the self-calibration and analysis. The archival Band 7 data of CIDA 1 was observed by the project 2015.1.00934.S (PI: L. Ricci) published in [Pinilla et al. \(2018b\)](#), and in this work, I combined it with 2016.1.01511.S (PI: J. Patience). A summary of the observation details and the data considered for each target are shown in Table 3.4.

The raw datasets were calibrated by applying the ALMA pipeline using the CASA version specified for each project ([McMullin et al., 2007](#)). Then, The software CASA v5.6.2 was used for the subsequent data handling and imaging. The dust continuum emission was extracted from every source by

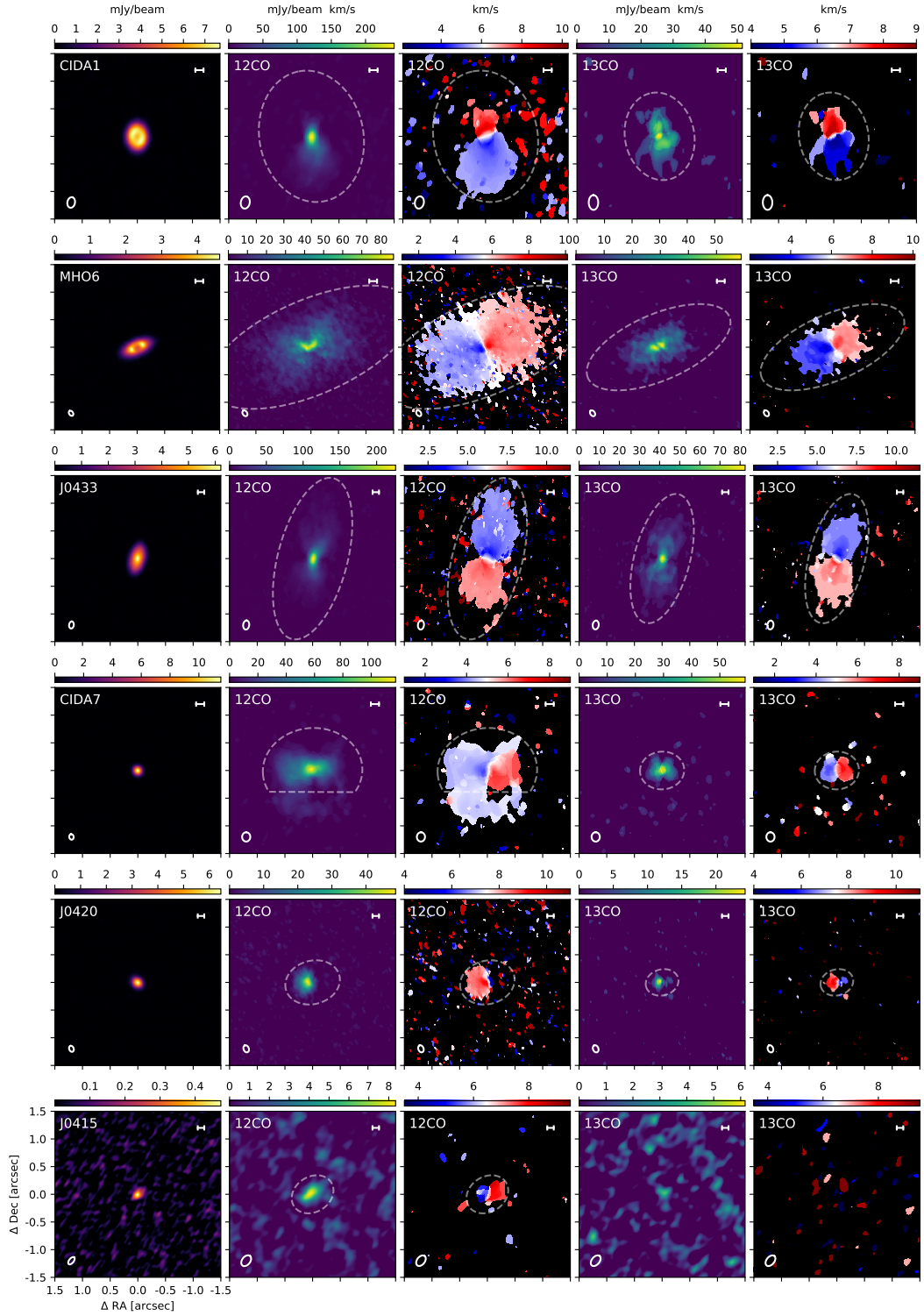


**Figure 3.1:** ALMA Observations of the disks around VLMS in Taurus. From left to right: The dust continuum emission,  $^{12}\text{CO}$  moments 0 and 1, and  $^{13}\text{CO}$  moments 0 and 1. All boxes are  $3.0''$  in size. The scale bar represents 20 au. The white ellipses show the synthesized beam. Dashed lines show the region used to calculate the radial profiles. A zoomed-in version of the continuum images can be found in Figure 3.3.

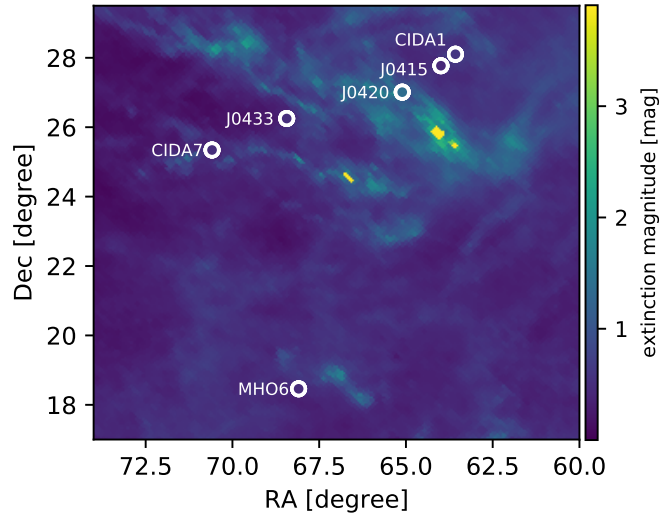


**Figure 3.2:** Spatial distribution of the Taurus sample the extinction map background compiled by [Schlafly et al. \(2014\)](#).

flagging the channels closer than  $25 \text{ km s}^{-1}$  to the targeted molecular lines. To reduce the data volume, the data was averaged over time (6 s intervals) and channels (with a width of 125 MHz). Before combining all available observations for each source, the centroid position of the emission was determined by fitting a Gaussian using the `imfit` task and shifted using `fixvis` and `fixplanets` tasks to the centroid of the observations of extended baselines, shown in Table 3.5. To confirm a consistent flux calibration by ALMA, the emission amplitude in different executions was compared. I found a discrepancy of 12% in the fourth compact observation of J0433 (2018-11-24), which was rescaled to match all the others.

To boost the signal-to-noise ratio (S/N) of each source, I performed self-calibration of the datasets in two steps: First, I combined the compact configuration observations and performed self-calibration. Second, I combined those self-calibrated observations with the extended configuration observations and self-calibrated them again. Phase calibrations were applied until the improvement on the S/N was below  $\sim 5\%$ , and only one amplitude calibration was applied in each step. The overall S/N improvement was between  $1.5 \sim 4.0$ , depending on the source. The only source where self-calibration was not possible was J0415, because the initial S/N of 9 needed to be higher for improvements. The final continuum images were generated using a Briggs robust parameter of 0.0 for CIDA 1, and 0.5 for the remaining sources. The image properties are summarized in Table 3.5.

All the dust continuum emission calibration steps, including centroid shifting, flux calibration, and self-calibration tables, were then applied to the molecular line emission channels. The continuum emission was subtracted using the `uvcontsub` task, and the images were generated using a robust parameter of 1. In MHO 6, J0420, and J0415, visibility tapering was applied to increase the S/N of the gas images. For MHO 6, I used a visibility tapering of 0.13" on the  $^{12}\text{CO}$ ; while for CIDA 7 and J0415, I applied a visibility tapering of 0.1" in both molecular line images. I made all the scripts for self-calibration and imaging available online <sup>6</sup>.

The final images of the dust continuum, moment 0, and moment 1 of the  $^{12}\text{CO}$  and  $^{13}\text{CO}$  (when detected) are shown in Figure 3.1, and the velocity channel maps are in Appendix 3.13. The details of the dust continuum and CO images can be found in the additional content Section 3.13, summarized in Table 3.5 and 3.6, respectively.

### 3.4 Morphology of the continuum emission

Our sources are spatially compact (radius of 0.1"  $\sim$  0.3"), and both their radial extent and substructures have sizes comparable to the synthesized beam shape. To avoid image reconstruction biases, I recovered the deprojected brightness profile of the sources in the visibility plane through parametric modeling. The continuum visibilities were extracted from the self-calibrated measurement set, the central frequency of each channel was used to convert the visibility coordinates to wavelength units. I started by modeling every source with a central Gaussian profile, and then the complexity of the profile was increased if the residuals suggested it. I also guided the parametrization of the profiles based on the best fitting from `frank` (Jennings et al., 2020), which fits a nonparametric 1D radial brightness profile in the visibilities, using Gaussian processes. For CIDA 7, J0420, and J0415, the function that describes their brightness profile is a centrally peaked Gaussian profile, following an intensity given by:

$$I_g(r) = f_1 \exp\left(-\frac{r^2}{2\sigma_1^2}\right), \quad (3.1)$$

where  $I_g$  is the Gaussian intensity profile of the source as a function of the

---

<sup>6</sup> [https://github.com/nicokurtovic/VLMS\\_ALMA\\_2018.1.00310.S](https://github.com/nicokurtovic/VLMS_ALMA_2018.1.00310.S)

### 3 Planet formation in very low mass stars

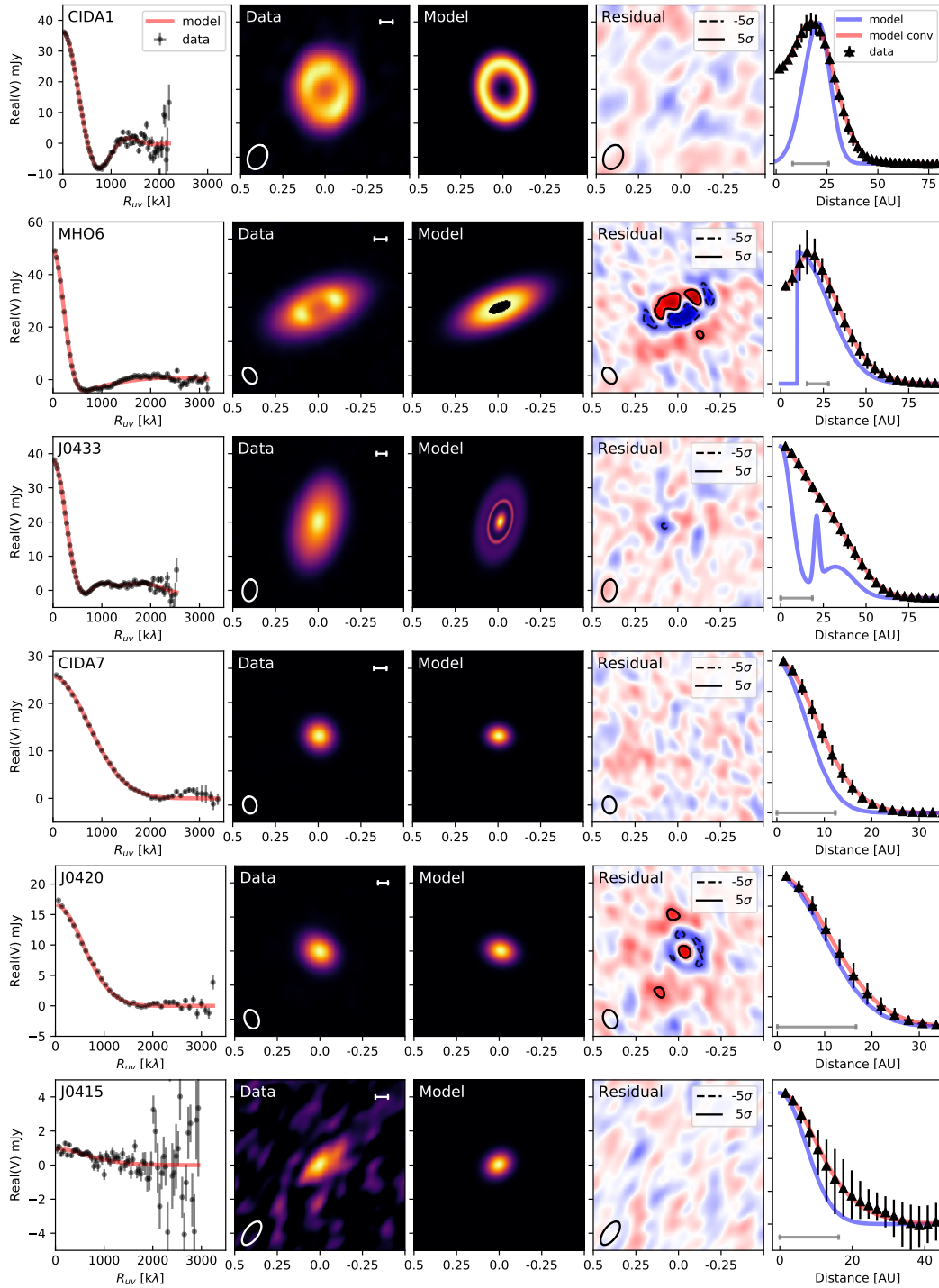


**Figure 3.3:** Visibility modeling versus continuum observations of the sample.

From left to right: (1) Real part of the visibilities after centering and deprojecting the data versus the best fit model of the continuum data, (2) continuum emission of our sources where the scale bar represents a 10 au distance, (3) model image, (4) residual map, (5) and normalized, azimuthally-averaged radial profile calculated from the CLEAN images, compare to the parametric model profile without beam convolution (purple solid line) and after convolution (red solid line). In the right most plots, the gray scale shows the beam major axis FWHM.

radius  $r$ .

The disks around CIDA 1 and MHO 6, were modeled with a radially asymmetric Gaussian ring or a broken Gaussian from hereafter, where the inner and outer width of the ring can differ. This profile is motivated by results of radially asymmetric accumulation of particles in pressure bumps (see e.g., [Pinilla et al., 2015, 2017b](#)). Such radially broken Gaussian profiles have been used to describe the morphology of different rings in transition disks and disks with substructures (e.g., [Pinilla et al., 2018](#); [Huang et al., 2020](#)), which is the same model used in [Pinilla et al. \(2018b\)](#) to model CIDA 1. The intensity profile is given by a ring as follows:

$$I_{\text{bg}}(r) = \begin{cases} f_1 \exp\left(-\frac{(r-r_1)^2}{2\sigma_1^2}\right) & \text{for } r \leq r_1 \\ f_1 \exp\left(-\frac{(r-r_1)^2}{2\sigma_2^2}\right) & \text{for } r > r_1 \end{cases}, \quad (3.2)$$

where  $I_{\text{bg}}$  is the broken Gaussian intensity profile as a function of the radius,  $r_1$  is the radial location of the ring peak intensity, and  $\sigma_{1,2}$  are the Gaussian widths for the inner and outer sides of the ring, respectively.

Finally, for J0433, the profile is the sum of a centrally peaked Gaussian profile and two symmetric Gaussian rings, as suggested by **frank**. It is also the profile that creates the lowest amount of residuals from our experiments, such as the single Gaussian, Gaussian ring, and broken Gaussian ring. The intensity profile is

$$I_{\text{J0433}}(r) = \sum_{i=1}^3 f_i \exp\left(-\frac{(r-r_i)^2}{2\sigma_i^2}\right), \quad (3.3)$$

where  $r_{i=1} = 0$ , so the first Gaussian is peaked at the center.

The visibilities of each profile were computed by combining each model with a spatial offset ( $\delta_{\text{RA}}$ ,  $\delta_{\text{Dec}}$ ), inclination (inc), and position angle (PA). Therefore, each model has four more free parameters in addition to those that describe the intensity profile. The Fourier transform and the  $\chi^2$  calculation were carried out with the **galarío** package ([Tazzari et al., 2018](#)). The pixel size used in the models is 1 mas, which is several times smaller than the smallest resolvable scale of the observations. The  $\chi^2$  was scaled up by a factor of

2.667 since *CASA* does not account for the effective channel width, introduced by Hanning smoothing, when it averages the weights during data binning. An uniform prior probability distribution was adopted over a wide parameter range, such that walkers would only be initially restricted by geometric considerations ( $\text{inc} \in [0, 90]$  ,  $\text{PA} \in [0, 180]$ ,  $\sigma \geq 0$ ).

	CIDA 1	MHO 6	J0433	CIDA 7	J0420	J0415	unit
$\delta_{\text{RA}}$	$-0.18^{+0.09}_{-0.14}$	$3.84^{+0.15}_{-0.09}$	$3.73^{+0.07}_{-0.09}$	$-1.18^{+0.06}_{-0.06}$	$2.87^{+0.08}_{-0.09}$	$-4.19^{+4.04}_{-2.68}$	mas
$\delta_{\text{Dec}}$	$-5.16^{+0.11}_{-0.20}$	$-2.69^{+0.11}_{-0.07}$	$-3.91^{+0.19}_{-0.04}$	$-0.06^{+0.06}_{-0.06}$	$-4.42^{+0.07}_{-0.10}$	$0.28^{+3.32}_{-4.24}$	mas
inc	$38.2^{+0.15}_{-0.06}$	$64.56^{+0.06}_{-0.01}$	$57.62^{+0.01}_{-0.12}$	$31.35^{+0.30}_{-0.28}$	$38.24^{+0.26}_{-0.24}$	$34.96^{+1.21}_{-28.18}$	deg
PA	$11.2^{+0.18}_{-0.16}$	$113.55^{+0.04}_{-0.05}$	$165.26^{+0.03}_{-0.11}$	$85.95^{+0.53}_{-0.47}$	$74.83^{+0.42}_{-0.38}$	$125.55^{+22.13}_{-79.22}$	deg
$f_1$	$10.25^{+0.01}_{-0.01}$	$10.45^{+0.01}_{-0.01}$	$10.76^{+0.06}_{-0.01}$	$11.00^{+0.01}_{-0.01}$	$10.63^{+0.01}_{-0.01}$	$9.45^{+0.08}_{-0.03}$	$\log_{10}(\text{Jy/sr})$
$r_1$	$153.63^{+1.69}_{-1.88}$	$68.64^{+0.17}_{-0.03}$	—	—	—	—	mas
$\sigma_1$	$54.35^{+1.69}_{-1.72}$	$0.001^{+0.05}_{-0.001}$	$36.46^{+0.43}_{-4.61}$	$45.05^{+0.08}_{-0.07}$	$57.69^{+0.11}_{-0.11}$	$53.09^{+0.45}_{-8.60}$	mas
$f_2$	—	—	$10.39^{+0.01}_{-0.22}$	—	—	—	$\log_{10}(\text{Jy/sr})$
$r_2$	—	—	$121.48^{+0.58}_{-5.99}$	—	—	—	mas
$\sigma_2$	$41.92^{+1.15}_{-0.97}$	$129.20^{+0.21}_{-0.08}$	$8.36^{+8.59}_{-0.12}$	—	—	—	mas
$f_3$	—	—	$10.08^{+0.01}_{-0.01}$	—	—	—	$\log_{10}(\text{Jy/sr})$
$r_3$	—	—	$184.67^{+1.77}_{-3.85}$	—	—	—	mas
$\sigma_3$	—	—	$60.76^{+1.85}_{-0.81}$	—	—	—	mas
$F_{0.87\text{mm}}$	$36.08 \pm 0.17$	$49.05 \pm 0.15$	$37.52 \pm 0.1$	$25.52 \pm 0.10$	$16.50 \pm 0.05$	$0.95 \pm 0.19$	mJy

**Table 3.2:** Best parameters from parametric visibility modeling

The parameters are described in Equations (3.1), (3.2), and (3.3). “mas” stands for milliarcsecond. The resulting  $F_{0.87\text{mm}}$  of each model is given in the last row (the measured  $F_{0.87\text{mm}}$  from the data is in Table 3.5).

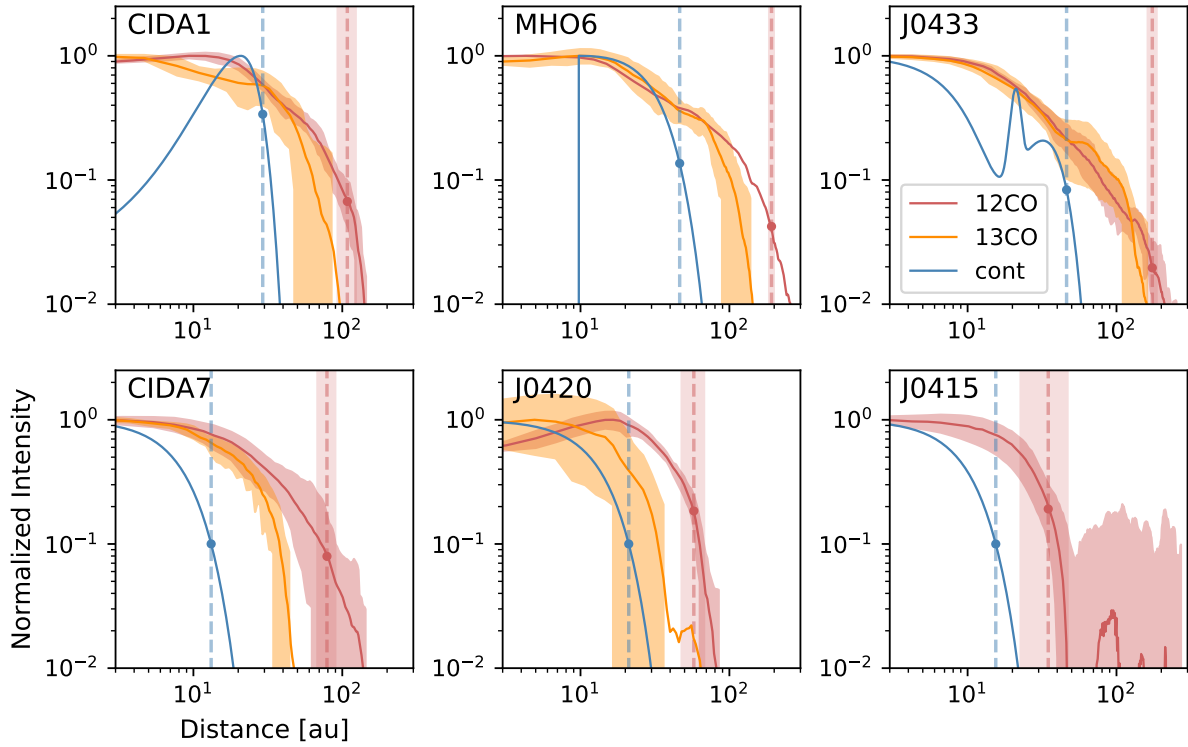


**Figure 3.4:** Azimuthally averaged radial profiles of the VLMS dust and gas emission. Each curve is normalized to the peak, and the shaded region represents the 68% dispersion at each radii. The orange and red solid curves correspond to the average intensity profile for the gas profiles of the deprojected images, while the blue solid line corresponds to the best  $\chi^2$  solution from the visibility fit of the dust continuum. The dashed vertical line denotes the position and  $1\sigma$  error of the  $R_{90}$  radius for the dust (blue) and the gas (red).

I used a Monte Carlo Markov chain (MCMC) routine based on the `emcee` package (Foreman-Mackey et al., 2013a) to sample the posterior probability distribution of each parameter space. Furthermore, I ran more than 250000 steps after converging to find the most likely set of parameters and the error bars, taken from the 16th and 84th percentile.

The results for each parameter are shown in Table 3.2, while in Fig. 3.3 the models are shown with and without beam convolution (right most panel). The visibilities and radial profile were deprojected using the best inclination and position angle. The residual image was generated in `CASA` using the same parameters and procedure used for the observations, from a measurement set with its visibilities calculated by subtracting the best model from the data. At the moment of the publication of this work, my package `SIMIO` was not yet finished, but a similar workflow was used to generate the synthetic observations.

	$R_{\%}$	$R_{\text{dust}}$ [au]	$R_{12\text{CO}}$ [au] ( $R_{\text{gas}}$ )	$R_{13\text{CO}}$ [au]	$R_{\text{gas}} / R_{\text{dust}}$
CIDA 1	68	$24.57^{+0.03}_{-0.04}$	$73.7 \pm 15.0$	$47.4 \pm 6.8$	$3.0 \pm 0.6$
	90	$29.22^{+0.07}_{-0.09}$	$108.1 \pm 15.0$	$68.5 \pm 6.8$	$3.7 \pm 0.5$
MHO 6	68	$34.18^{+0.01}_{-0.05}$	$130.7 \pm 7.0$	$78.5 \pm 7.1$	$3.8 \pm 0.2$
	90	$46.36^{+0.01}_{-0.07}$	$191.9 \pm 7.0$	$113.0 \pm 7.1$	$4.1 \pm 0.2$
J0433	68	$36.58^{+0.11}_{-0.01}$	$114.6 \pm 11.9$	$92.2 \pm 11.7$	$3.1 \pm 0.3$
	90	$46.22^{+0.08}_{-0.07}$	$174.0 \pm 11.9$	$125.5 \pm 11.7$	$3.8 \pm 0.3$
CIDA 7	68	$9.26^{+0.02}_{-0.02}$	$55.1 \pm 10.8$	$19.6 \pm 10.9$	$6.0 \pm 1.2$
	90	$13.16^{+0.02}_{-0.02}$	$78.9 \pm 10.8$		$6.0 \pm 0.8$
J0420	68	$14.84^{+0.03}_{-0.03}$	$43.1 \pm 9.9$	$23.3 \pm 9.8$	$2.9 \pm 0.7$
	90	$21.09^{+0.04}_{-0.04}$	$57.7 \pm 9.9$	$32.2 \pm 9.8$	$2.7 \pm 0.5$
J0415	68	$10.87^{+1.78}_{-0.15}$	$26.4 \pm 12.1$	—	$2.4 \pm 1.2$
	90	$15.46^{+2.53}_{-0.22}$	$34.8 \pm 12.1$	—	$2.3 \pm 0.9$

**Table 3.3:** Continuum and CO radial extension for each VLMS disk.

Uncertainties for continuum comes from the walkers distribution in each MCMC. Gas radii uncertainties were calculated from the synthesized beam radius of each image.

The radial profile recovered from the parametric visibility modeling was used to measure the dust continuum emission radii ( $R_{\text{dust}}$ ) that encloses 68% and 90% of the total flux (the dust  $R_{68}$  and  $R_{90}$ , respectively). The 16th and 84th percentile on the  $R_{68}$  and  $R_{90}$  was calculated by computing radial profiles of the set of parameters sampled by the walkers. The results are shown in Table 3.3 and in Figure 3.4. The continuum emission extends up to 46 au in the biggest disks, MHO 6, and J0433, while the sample also has the smallest (13 au) and the dimmest ( $\sim 1$  mJy) Taurus disks ever resolved in 0.87 mm emission, CIDA 7, and J0415, respectively.

### 3.4.1 Rings and cavities in CIDA1, MHO6, and J0433

The observations show evidence of ring structures in three out of six disks of the sample. At the current resolution, CIDA 1 and MHO 6 show a single ring and a cavity, which are well described by a broken Gaussian profile. In CIDA 1, the inner side of the Gaussian is more extended than the outer side,

which is similar to the results obtained in [Pinilla et al. \(2018b\)](#). The ratio between the widths of the inner side and the outer side is 1.2, and the peak of the ring emission is located at 21 au.

For MHO 6, there is a azimuthal asymmetry in the north side of the ring, which peaks radially at 10 au. The inner side of the ring converges to  $\sigma = 0$  au, with a narrow error margin. To ensure that the result was not being affected by numerical biases related to the pixel size, another MCMC was run with a pixel size of 0.4 mas (about 0.057 au), and the same result was recovered consistently for each parameter. Even though this steep transition could suggest an unresolved inner side of the ring, the best model is also driven by the non-axisymmetric emission of the disk, which becomes clear when looking at the residuals (see [Fig. 3.3](#)). The contrast of these asymmetries is about 5% of the peak amplitude of the ring, meaning that most of the emission is still well described by a radially axisymmetric ring.

For J0433, the best model finds two rings located at 21 and 32 au, with gaps at 16 and 25 au. The brightness ratio between the first ring and first gap is about 4.4; whereas, the contrast is 1.2 between the second gap and ring. Since the brightness ratio fades at the  $1\sigma$  error (as seen in [Figure 3.4](#)), it cannot be excluded that the second ring is an extension of the outer side of the first ring.

### 3.4.2 Dust disk masses

Under the assumption that the dust continuum emission is optically thin, dust mass of the disks can be calculated by following [Hildebrand \(1983\)](#):

$$M_{\text{dust}} \approx \frac{d^2 F_\nu}{\kappa_\nu B_\nu(T)}, \quad (3.4)$$

where  $d$  is the distance in parsecs (given in [Table 3.1](#), taken from Gaia DR2),  $\kappa_\nu$  is the mass absorption coefficient, and  $B_\nu(T)$  is the Planck function. For  $\kappa_\nu$ , I assumed the standard opacity law  $\kappa_\nu = 2.3 \text{ cm}^2 \text{ g}^{-1} (\nu/230 \text{ GHz})^{0.4}$  ([Andrews et al., 2013](#)), while the temperature was assumed constant at  $T_{\text{dust}} = 20 \text{ K}$  (e.g., [Ansdell et al., 2016](#); [Pinilla et al., 2018b](#)), as discussed in [Chapter 1](#). The uncertainty of the dust mass was estimated by taking the 10% uncertainty in the flux calibration. Our results for each source are compiled in [Table 3.5](#) and shown compared with the disk dust mass in the Taurus region in the [Figure 3.5](#). The lowest dust mass estimate was ob-

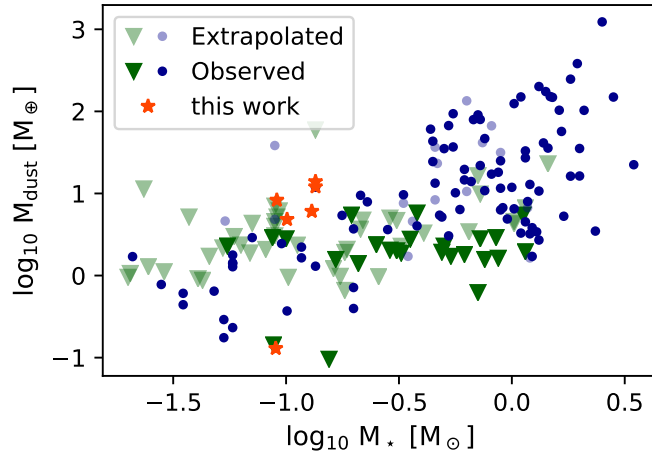


**Figure 3.5:** Dust mass compared to stellar mass for the Taurus disks.

The  $M_d$  was computed using distances inferred from Gaia DR2, assuming a 20K disk temperature and using the most updated value of  $F_{0.87\text{mm}}$  from Andrews et al. (2013), Tripathi et al. (2017), and Ward-Duong et al. (2018). Sources where  $F_{0.87\text{mm}}$  was extrapolated from a  $F_{1.3\text{mm}}$  measurement are plotted in faded colors (see Table 2 in Andrews et al., 2013), while direct measurements from SMA or ALMA are plotted in darker colors. Green triangles denotes upper limits, and the VLMS studied in this work are plotted as orange stars.

tained for J0415, with only  $0.22 \pm 0.02 M_{\oplus}$  (about  $2.1 \pm 0.2 M_{\text{Mars}}$ ), while the most massive dust disk was detected in J0433 with  $14.32 \pm 1.43 M_{\oplus}$ . It is important to notice that these masses should be considered lower limits, as the emission at 0.87 mm wavelengths is most likely optically thick. The main purpose of obtaining this dust mass value is recovering a distance-corrected measurement of the brightness that can be used to compare to other disks.

## 3.5 Molecular emission from $^{12}\text{CO}$ and $^{13}\text{CO}$

### 3.5.1 Lines detection

Both molecular lines were detected in all of the sources, except for J0415, where only  $^{12}\text{CO}$  is detected. As shown in Figures 3.1 and 3.3, the angular resolution of  $\sim 90\text{mas}$  was just enough to resolve the dust continuum and gas emission of this source, but the limited sensitivity did not allow us to constrain the geometric parameters as in the other systems. The spectral profiles of  $^{12}\text{CO}$  and  $^{13}\text{CO}$  for each source, shown in Figure 3.11, were obtained with the CASA 5.6.2 software by placing an elliptical mask in the region where emission was detected. The errorbars represent the standard deviation of the noise, measured from the channels without emission.

For the two smooth sources, CIDA 7 and J0420, there is considerable cloud absorption in the  $^{12}\text{CO}$  emission. The western side of J0420 is completely absorbed, while its rotational pattern is recovered in the  $^{13}\text{CO}$  (see Figures 3.1 and 3.18). On the other hand, in CIDA 7, an extended asymmetric emission is observed in the south region, with a velocity range of at least  $0.8 \text{ km s}^{-1}$  (it was detected in two velocity channels). The contribution of this emission is not significant to the total flux of the gas emission, and it was not detected in  $^{13}\text{CO}$ . Although the S/N did not allow us to accurately recover geometric parameters from the gas emission, the PA obtained from the dust continuum emission is in good agreement with the orientation of the major axis in the rotation pattern.

In the sources with detected substructures, both J0433 and CIDA 1 are affected by cloud contamination. For CIDA 1, the side most affected by extinction is the north side, while the same is true for the south side of J0433 (row 1 and 3 of Figure 3.1). The least cloud-contaminated source is MHO 6 disk (also seen in Figure 3.2), which is the brightest and more extended disk in CO emission of our sample. A characterization of the magnitude of the cloud contamination is shown in the Section 3.11.

### 3.5.2 Radial gas profiles

The inclinations and position angles obtained from the continuum fitting were used to deproject the distances from the central star in the moment 0 images, which were used to calculate the azimuthally averaged radial profiles of the  $^{12}\text{CO}$  and  $^{13}\text{CO}$  emission. The vertical structure was neglected in this calculation, as the available tools at the time of this research did not allow for a robust estimation of the emission surface height. Later tests between flat and flared emission surfaces show mostly consistent results, and the flat emission structure does not change the results of this work. In CIDA 1, J0433, and J0420, the profiles were calculated from the side that is less affected by cloud contamination. In CIDA 7, the contribution of the asymmetric emission in the south is negligible, but nevertheless it was not taken into account to recover the disk emission profile (see masking in Figure 3.1). The gas  $R_{68}$  and  $R_{90}$  radii that encloses 68% and 90% of the flux are shown in Table 3.3 and Fig. 3.4.

As discussed in Section 3.8, the brightness in dust continuum and gas emission of J0415 are much lower than expected from previous SMA observations

(Andrews et al., 2013). The low S/N of the detection prevented us from applying self-calibration, and so the sensitivity is two times worse than in the other VLMS disks. Therefore, the radial profile of the  $^{12}\text{CO}$  emission was calculated from an image generated by only considering the channels in the velocity range with line detection, without applying clipping at  $3\sigma$ .

### 3.5.3 Keplerian rotation of CO emission

Although the rotational pattern is recovered for all the disks in the sample in both CO isotopologues (with the exception of the  $^{13}\text{CO}$  in J0415), the strong cloud contamination and low S/N of the images prevented reliably recovering the dynamical mass from the sources. The only system where the cloud contamination does not completely extincts the emission in the central velocity channels is MHO 6, where a good spatial is obtained of both lines. The analysis of MHO 6 emission is described in Section 3.11.

To have a referential value for the stellar hosts mass, I used CASA5.6 to get the position velocity diagrams (PV diagram from hereafter) along the major axis of each source, based on the position angle obtained from the continuum visibility modeling. The only exception is J0415, whose PV diagram was obtained along the east-west axis. The PV diagrams are shown in Figure 3.13.

## 3.6 Occurrence rate of substructures

Obvious substructures are only detected in the brightest disks of our sample (CIDA 1, MHO 6, and J0433), which are also the most radially extended disks in gas and dust emission. The existence of strong dust traps located at larger radial distances from the star is most likely the reason for this observational result, as the dust is allowed to stay for longer timescales in the outer disk, thereby increasing the emitting area. On the other hand, our limited angular resolution only allowed us to detect substructures in the most extended disks.

This direct detection of substructures in 50% of our sample does not represent the occurrence rate of substructures in all disks around VLMS, as our sample is biased towards the brightest disks and our spatial resolution is limited. Therefore, our observations only allowed us to directly detect deviations from a simple Gaussian profile in the disks where the extent of the emission is consistently larger than the synthesized beam size.

CIDA 7 and J0420 are a good example of the limitations that our datasets have when detecting substructures. Even though I was unable to confirm the existence of dust substructures in these systems, the visibility profile in Fig. 3.3 of CIDA 7 shows some structure which is not described by a Gaussian profile, while the residual image of J0420 suggests that there might be more substructured dust emission that is not described by a single centrally peaked Gaussian in these disks. Higher angular resolution and sensitivity are needed to confidently characterize them. Given that these two disks are not totally dust depleted, the expected efficient radial drift must have been counteracted by a dust trapping mechanism. The compactness of these disks suggest that the dust trap is located so close to the star that our resolution did not allow us to detect it. In theory, any pressure bumps cannot be smaller than the local pressure scale height, which implies that if they are located closer to their star, their radial extent is smaller than our current resolution. CIDA 7 and J0420 are good candidates to be targeted by deep observations with ALMA in the most extended antenna configuration, allowing us to detect substructures of  $\leq 2$  au in size at the distance of these targets, which is six and ten times smaller than the dust  $R_{68}$  of those disks, respectively. Future observations will test if even the very small disks around VLMS are able to generate dust traps, as it is observed in the massive and extended ones.

For J0415, our visibility coverage and sensitivity resolves the emission, and the centrally peaked Gaussian model does not leave any significant residual. Higher sensitivity is needed in order to discern deviations from the Gaussian profile (see Figure 3.3).

### 3.7 Origin of dust continuum rings and cavities

All the detected substructures in our sample resemble ring-like emission. MHO 6 is the only disk displaying what could be a hint of non-axisymmetric dust emission in the residuals at our current sensitivity. Rings structures are the most common type of substructure in moderate and massive stars, as shown by surveys such as DSHARP (Andrews et al., 2018; Huang et al., 2018b), Taurus survey at 1.3 mm (Long et al., 2018), the ODISEA survey in Ophiuchus (Cieza et al., 2021), and a similar trend is found for extended disks around VLMS.

### 3.7.1 Detected structures coincide with possible CO iceline location

The iceline of each volatile marks the location in the disk where that volatile transitions from being mostly gas-phase to being frozen out on dust grains. It is possible that this phenomena could induce ring-like substructures in the dust continuum emission by changing the dust opacity and grain collisional fragmentation and growth rates (e.g., [Okuzumi et al., 2016](#)). To investigate if any of the iceline locations of the major volatiles coincide with the location of our gaps, the midplane temperature of our disks was calculated by following [Kenyon & Hartmann \(1987\)](#), where, for an irradiated flared disk, the temperature was parametrized as:

$$T(r) = T_{\star} \left( \frac{R_{\star}}{r} \right)^{1/2} \phi_{\text{fl}}^{1/4}, \quad (3.5)$$

with  $r$  is the distance from the star,  $T_{\star}$  and  $R_{\star}$  are the star temperature and radius, respectively, and  $\phi_{\text{fl}}$  is the flaring angle, which in this work is assumed to be equal to 0.05 ([Dullemond & Dominik, 2004](#)). The stellar radius  $R_{\star}$  was measured from the stellar luminosity  $L_{\star}$  by assuming black body emission and spherical symmetry ( $L_{\star} = 4\pi R_{\star}^2 \sigma_{sb} T_{\star}^4$ , with  $\sigma_{sb}$  the Stefan-Boltzmann constant). As a first approximation, the contribution of accretion luminosity is ignored in the calculations of the stellar luminosity (further discussed in [Long et al., 2018](#)). If the stellar radius is replaced in Equation (3.5), the distance  $r_i$  at which the temperature  $T_i$  is reached, given a star of fixed luminosity  $L_{\star}$ , is obtained by following:

$$r_i = \frac{L_{\star}^{1/2}}{T_i^2} \cdot \left( \frac{\phi_{\text{fl}}}{4\pi\sigma_{sb}} \right)^{1/2}. \quad (3.6)$$

The two coldest icelines presented in [Zhang et al. \(2015\)](#) are considered, which are the CO with a sublimation temperature of  $\sim 20 \sim 28$  K (I took the lower limit 20 K from [Öberg et al. \(2011\)](#) for direct comparison with [Long et al. \(2018\)](#)), and the N<sub>2</sub> iceline, which goes from  $\sim 12 \sim 15$  K. The iceline location was calculated for each star using the parameters shown in Table 3.1, and the results are shown in Figure 3.6.

In the right panel of Figure 3.6, the positions of the detected substructures are displayed as a function of the root of stellar luminosity. Most of the substructures detected lie within the region where the CO iceline is identified. However, the role that the CO iceline plays in the morphology of our disk

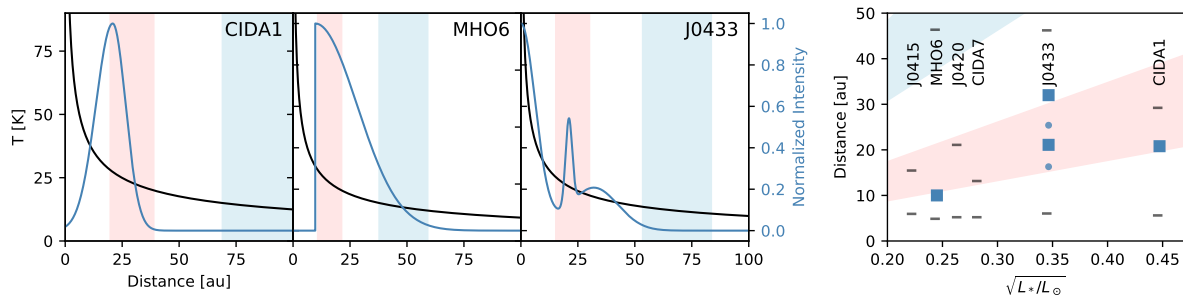


**Figure 3.6:** Temperature profile compared to estimated ice-line locations.

Left panels: Temperature profile of the midplane is obtained from equation (3.5) and plotted with a black curve. The blue curve shows the best radial profile obtained from the continuum visibility modeling, which was normalized to the peak emission. Vertical red and light blue shaded regions show the possible locations of the CO (light red) and  $N_2$  (light blue) icelines. Right panel: Disk radius is shown versus the square root of stellar luminosity ( $\sqrt{L_\star}$ ). The shaded regions show the iceline location for CO (light red) and  $N_2$  (light blue), obtained from equation (3.6). The peak location of the modeled continuum emission rings are shown in squares, while the gap locations of J0433 are shown with dots. The lower line in each target marks half of the theoretical resolution given by the longest baseline for each dataset, as measured from the center, and the upper line marks the continuum  $R_{90}$ .

is not conclusive from our datasets. Even if we neglect the uncertainties introduced by the stellar parameters and the disk temperature, it is not clear if the structures that were generated by an iceline would result in a ring peaked at the iceline position or in a gap (Pinilla et al., 2017a; van der Marel et al., 2018).

In Pinilla et al. (2017c), they found that icelines do not strongly change the gas density in those locations, nor can they carve a dust cavity as the ones detected in MHO6 and CIDA1. Given that the peak of the rings detected in these disks are located very close to the position of the CO iceline, we cannot rule out the possibility that the iceline played a role in triggering the mechanism that is carving the cavity. In J0433, both peaks and gaps are found at the region (or close) where the CO iceline could be located. Given the radial compactness of the disks in our sample, the limited angular resolution, and the wide radial range covered by the CO iceline location, it is also possible that the substructures coincide with the iceline just by chance, in the same way that other surveys of substructures have not found a strong correlation between the position of substructures and iceline location (e.g., Long et al., 2018). Additional deeper observations of the CO isotopologues could allow a better constrained modeling of the temperature of radial and vertical profile of these disks, thus providing better evidence for the role the

iceline plays on the substructures detected.

### 3.7.2 CIDA1

Our modeling of the cavity in CIDA 1 gives similar results to those found in [Pinilla et al. \(2018b\)](#), thus in [Kurtovic et al. \(2021\)](#) I did not explore new possibilities for its cavity origin. At the time of the publication of this work, finding that the inner side of the ring was wider than the outer side was opposite to what we expected from the physical motivation of using this model, which accounts for the timescale of grain growth from micrometer to millimeter particles in dust traps ([Pinilla et al., 2017b, 2018b](#)). In [Kurtovic et al. \(2021\)](#), we considered the possibility is that there is unresolved emission inside the main ring, and the inner side of the Gaussian is blending with it. This unresolved emission could come from an inner disk, which could only be tested with observations at higher angular resolution. In [Pinilla et al. \(2021\)](#), using new observations obtained with ALMA, we confirmed this hypothesis.

### 3.7.3 J0433

If the gaps of the dust continuum emission are assumed to be generated by a planet-disk interaction, we can use the width of the gap to estimate the mass of this gap-carving planet, under the assumption that this single planet is located at the position of the gap, and the ring is peaked at the local pressure maxima of the gas. In this scenario, if the physical parameters of the disk are kept constant, a more massive planet would create a wider gap (e.g., [Fung et al., 2014](#); [Kanagawa et al., 2015](#); [Rosotti et al., 2016](#)).

A similar procedure as [Long et al. \(2018\)](#) was used for a crude estimate of the mass of the planet in the first J0433 gap. In this approach, the distance between the gap and ring scales with the Hill radius of the planet:

$$R_{\text{Hill}} = r_p (M_p / (3 M_\star))^{1/3}, \quad (3.7)$$

where  $r_p$  is the location of the planet (the location of the gap coincides with the location of the planet, as the planet is carving the gap),  $M_p$  is the mass of the planet, and  $M_\star$  is the mass of the host star. By considering the distance between the gap and ring to be  $5 R_{\text{Hill}}$  (conservative upper limit for the gap width carved by a planet in [Dodson-Robinson & Salyk, 2011](#)), and considering that our best model gives  $r_{\text{ring}} - r_{\text{gap}} = 5 \text{ au}$  for the first ring, then the approximate mass of the planet would be  $M_p \sim 0.1 M_{\text{Jup}}$ .

This calculation has a large uncertainty depending on the type of simulation. For instance, [Dodson-Robinson & Salyk \(2011\)](#) estimated a maximum of  $4R_{\text{Hill}}$  between the planet location and the ring position, while [Pinilla et al. \(2012a\)](#) estimated  $7R_{\text{Hill}}$  for planets as massive as Jupiter. Taking these two limits ( $4R_{\text{Hill}}$  and  $7R_{\text{Hill}}$ ), the estimated planet mass becomes  $M_p = 0.11_{-0.07}^{+0.10} M_{\text{Jup}}$ . In this calculation, we did not account for the physical conditions of the disk, such as turbulence or temperature, nor did we consider the minimum mass to open a gap in the disk. Therefore, it only gives a crude estimate for the order of magnitude of a single planet carving the gap. A future analysis should consider higher angular resolution observations to better constrain the gap-ring morphology as well as dedicated hydro-simulations to estimate the planet candidate mass.

### 3.7.4 MHO6

In MHO 6, the modeling indicates the existence of a central cavity that is slightly asymmetric. Several processes in protoplanetary disks could create this type of an inner cavity, such as photoevaporation due to stellar irradiation (e.g., [Alexander & Armitage, 2007](#); [Owen et al., 2012](#); [Owen & Kollmeier, 2019](#)), companions (e.g., [Price et al., 2018](#)), a planet-disk interaction (e.g., [Rice et al., 2006](#); [Zhu et al., 2011](#)), and dead zones (e.g., [Flock et al., 2015](#)). In the following, each one of these scenarios is discussed for the MHO 6 cavity.

**Photoevaporation:** The 10au dust cavity and the low accretion rate ( $5 \times 10^{-11} M_{\odot} \text{yr}^{-1}$  estimated from a UV excess in [Herczeg & Hillenbrand, 2008](#)) are in agreement with the predicted evolution for a very low mass star ( $0.1 M_{\odot}$ ) having its material stripped away by a photoevaporative flow ([Owen et al., 2012](#)). However, there is no clear evidence of a gas depleted cavity in the  $^{12}\text{CO}$  emission or  $^{13}\text{CO}$  emission, as shown by the modeling in Section 3.11, which could be due to the high optical depth of the CO isotopologues. A follow-up with dedicated VLMS photoevaporation models and higher angular resolution of this target in different molecular lines would be able to characterize the impact of this mechanism in the cavity detect.

**Companion:** Binary companions produce cavities in circumbinary disks, with sizes in the range of 3 – 5 times the binary semi-major axis, depending on the mass ratio, the eccentricity, and the disk viscosity ([Artymowicz & Lubow,](#)

1994; Miranda et al., 2017; Ragusa et al., 2017). They also produce quasi-periodic variations in the accretion rate (Muñoz & Lai, 2016). If MHO 6 was a circumbinary disk, the location of this companion could not be farther out than  $\sim 3$  au ( $\sim 20$  mas) from the primary star. However, previous independent observations of MHO 6 have not found any evidence of multiplicity in this system (Briceño et al., 1998; Kraus & Hillenbrand, 2007; Herczeg & Hillenbrand, 2014, the latest reference identified companions in its survey as late-type as M0.0). A spectroscopic follow-up with radial velocities, given the high inclination of the system, could be useful to constrain the upper mass limit of a companion in the close inner region.

**Embedded planets:** The planet population around very low mass stars spans a wide range of masses, where even giant planets have been detected (e.g., Morales et al., 2019, a  $0.46 M_{\text{Jup}}$  around a  $0.1 M_{\odot}$  VLMS), meaning that protoplanetary disks around VLMS probably have the potential to create such objects. If we make a simple calculation following the opening gap criterium introduced by Crida et al. (2006), the approximate mass needed for a single planet to open a gap and explain the cavity observed in MHO 6 is 1 or  $0.6 M_{\text{Saturn}}$  ( $0.18$  and  $0.3 M_{\text{Jup}}$ ), located at  $\sim 7$  au for  $\alpha = 10^{-3}$  and  $\alpha = 10^{-4}$ , respectively. If we assume a gas to dust ratio of 100, a disk mass of  $\sim 12.6 M_{\text{Saturn}}$  or  $\approx 3.8 M_{\text{Jup}}$  is estimated, given the dust mass obtained in Section 3.4.2. This means that the cavity opening planet is  $< 10\%$  of the current estimated mass of the disk. This implies that this type of potential single planet could have formed within the disk of MHO 6, although the possibility of multiple planets being responsible of this central cavity cannot be excluded.

**Dead zone:** A dead zone is a low-ionized region at the disk midplane, where the dense environment blocks the high energy radiation, suppressing the magneto-rotation instability and, therefore, the angular momentum transport. It has been shown that the presence of dead zones can open gaps and cavities by forming gas pressure bumps at the outer edge of the dead zones, where dust trapping is efficient (e.g., Regály et al., 2012; Flock et al., 2015). In Pinilla et al. (2016), they predicted that cavities formed by dead zones alone would have millimeter- and micrometer-sized particles concentrated at the peak of the gas density. As a result, the radial location of the ring in millimeter wavelengths and scatter light would be the same. If we neglect

temperature effects, the images suggest that the peak of  $^{13}\text{CO}$  is closer to the star than the millimeter peak. If we considered the  $^{13}\text{CO}$  as an optically thin line at mostly constant temperature, the micrometer-sized particles would peak closer to the star as well. In the dead zone scenario, [Pinilla et al. \(2016\)](#) also predict a strong gas depletion in the outer parts of the disk, further out from the dust trap, which is not currently seen in the observations of  $^{13}\text{CO}$ . If a magneto-hydrodynamical wind is included in the models together with a dead zone, the observational diagnostics are very similar to planets. One step forward to try to disentangle between these models is to image this disk in scattered light and search for potential planets in the cavity. However, these disks are too faint to image given the limitations of current telescopes in the optical and near-infrared.

To summarize, the formation of the cavity observed in MHO 6 could be explained by one or a combination of the mechanisms discussed above. Several observational efforts can be done to disentangle these possibilities, such as a better estimate of the star accretion rate, a deeper search for planets or companions in its cavity in the optical and infrared wavelengths as well as imaging the disk in this regime, and very deep and higher angular resolution observations of molecular lines.

### 3.8 Comparison of dust size-luminosity relation with previous studies

All the sources in this work had observed or estimated 0.87 mm fluxes, and a subset also had their dust continuum  $R_{68}$  measured with previous visibility modeling. In the following, I compare and discuss the measurements with previous results, including the VLMS in the study of a size-luminosity relation.

**Flux:** J0415 was observed using the Submillimeter Array (SMA) at a wavelength of 1.3 mm, with a reported flux density of  $12.6 \pm 1.4$  mJy in [Andrews et al. \(2013\)](#), where they extrapolated this measurement to 0.87 mm using  $F_\nu \propto \nu^\alpha$ , with  $\alpha = 2.4 \pm 0.5$ , thus obtaining  $F_{0.87\text{mm}} = 32.9 \pm 15.2$  mJy. Although for all our other five sources, the extrapolations from the SMA flux measurements are consistent within the error range, the flux at 0.87 mm received from J0415 is approximately 35 times dimmer than expected, as observed independently by two different ALMA projects. A possible explanation could be a sudden change in millimeter flux due to flares, as it has been

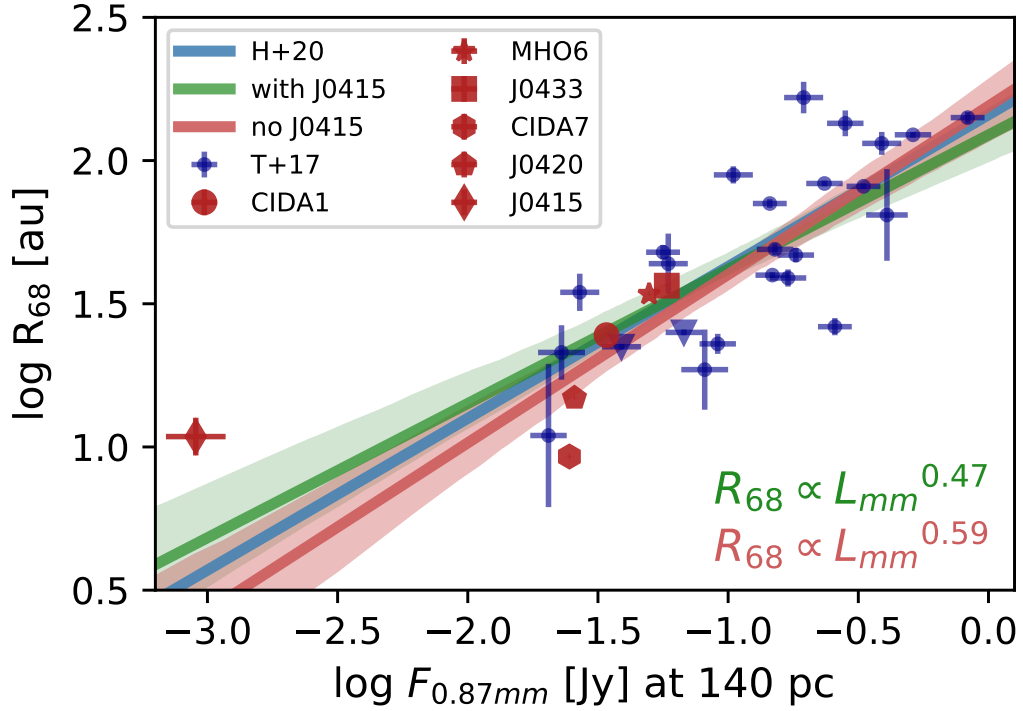


**Figure 3.7:** Size luminosity relation in the Taurus SFR

Relation between  $\log(R_{68})$  and  $\log(F_{0.87\text{mm}})$ . The points in blue are from [Tripathi et al. \(2017\)](#), with distances scaled to 140pc using distances inferred from Gaia DR2, similar to [Andrews et al. \(2018a\)](#). The solid line in blue is the linear regression found by [Hendler et al. \(2020\)](#) (abbreviated as H+20), fitting the data from [Tripathi et al. \(2017\)](#). The VLMS from this work are shown in red. The bests linear regression fits and their 68% confidence intervals are plotted in red when J0415 is excluded from the fit, and in green when all points are considered.

observed in low mass stars (e.g., [MacGregor et al., 2018](#)). Future observations at 1.3 mm should solve this discrepancy with the SMA results.

**Dust  $R_{68}$ :** The radius enclosing 68% of the dust continuum emission ( $R_{68}$ ) was previously estimated for MHO 6 and J0433, using visibility modeling on SMA 340 GHz observations. In [Tripathi et al. \(2017\)](#) and [Andrews et al. \(2018a\)](#), they estimated a value of  $R_{68} = 36.9^{+8.5}_{-5.7}$  au for MHO 6 ( $0.26''^{+0.06}_{-0.04}$ ), and  $R_{68} = 58.9^{+6.9}_{-8.7}$  au for J0433 ( $0.34''^{+0.04}_{-0.05}$ ), which are consistent with the values measured by this work. Both are slightly overestimated (1.6 times for J0433) compared to the values of this work due to the considerably lower angular resolution of SMA observations compared to ALMA ( $0.86'' \times 0.80''$  for MHO 6 and  $0.61'' \times 0.52''$  for J0433).

**The size-luminosity relation:** We combined our VLMS measurements with the Taurus sample observed with the SMA at 340GHz from [Tripathi et al. \(2017\)](#) to compare with the recent analysis by [Hendler et al. \(2020\)](#), where they obtained a relation of  $R_{68} \propto L_{\text{mm}}^{0.53}$  for the Taurus star-forming region. For comparison purposes with this study, I followed the same approach by using the Bayesian linear regression, described in [Kelly \(2007\)](#), which was implemented in the python package `linmix` (publicly available in github, see [Meyers, 2015](#)), to fit a linear relation between  $R_{68}$  and  $L_{\text{mm}}$  following:

$$\log_{10}(R_{68}) = \alpha + \beta \log_{10}(L_{\text{mm}}), \quad (3.8)$$

where  $\alpha$  and  $\beta$  are the regression coefficients. Our best fit was calculated by using the median value of the last 200000 steps after convergence. We find that including our VLMS sample does not statistically change the previous result. However, the inclusion of J0415 changes the steepness of this relation in about  $1\sigma$ . When considering J0415 as part of the fitting data, then the relation recovered is  $\alpha = 2.09 \pm 0.09$ ,  $\beta = 0.47 \pm 0.08$ . By excluding J0415 from the fitting, the result is  $\alpha = 2.19 \pm 0.10$ ,  $\beta = 0.59 \pm 0.10$ . Both relations are close to the  $1\sigma$  limit of each other, and they also overlap with the previous calculation from [Hendler et al. \(2020\)](#), as shown in Figure 3.7. The relations' intrinsic scatter from the linear regression are  $\sigma_{\text{scatter}} = 0.231 \pm 0.041$  and  $\sigma_{\text{scatter}} = 0.217 \pm 0.040$ , respectively. Therefore, including J0415 does not significantly increase the scatter.

The difference in the steepness of the recovered relations is not statistically significant from what was previously found. However, it is not completely clear if the same single power law relation between the millimeter luminosity and the size of the disks holds along the whole luminosity range. Given that J0415 is the only source with its size measured in the  $\sim 1$  mJy brightness range, it is unknown if disks have some mechanisms to remain extended even when they are low in dust content (thus flattening the relation between size and luminosity in the low luminosity regime), or if a J0415-extended dust size is part of the relation scatter that is also observed in bright disks. To understand if J0415 is an outlier and to test if the power law behavior of the  $R_{68} - L_{\text{mm}}$  relation flattens or holds at the low brightness regime, we need more deep observations at a high angular resolution of disks with  $F_{0.87\text{mm}} < 10\text{mJy}$ . This could be achieved by observing each source from several tens of minutes to a few hours in ALMA Band 7.

### 3.9 J0415 dust radial extent

Although CIDA 7 has a dust content of at least  $\sim 27$  times higher than J0415, it remains an open question as to how both can have a similar size (see Table 3.3). This result could be due to weaker dust traps in J0415 compared to those in CIDA 7, thus CIDA 7 can trap the dust more efficiently.

Alternatively, if the  $M_{\text{gas}}$  of the disk is very low, the millimeter grains would have a high Stokes number and radial drift would become negligible. In Pinilla et al. (2017c), they explored this scenario with a disk of 60 au in radius around a BD of  $0.05M_{\odot}$ . When  $M_{\text{gas}} = 2 \cdot 10^{-2} M_{\text{Jup}}$ , diffusion and drift still depleted the disk from millimeter particles; however, when  $M_{\text{gas}} = 2 \cdot 10^{-3} M_{\text{Jup}}$ , the millimeter grains were decoupled from the gas, and they could remain in the disk for longer timescales. For J0415, if we assume a dust to gas ratio of 1/100, we obtain  $M_{\text{gas}} \approx 4 \cdot 10^{-2} M_{\text{Jup}}$ , which does not seem to be low enough for a complete dust-gas decouple to occur. Additional observations are needed in order to characterize its gas radial density profile and to test this possibility.

Finally, it has been proposed that dust grains could be growing in a fractal manner, such that large aggregates would avoid radial drift by maintaining a low Stokes number (Kataoka et al., 2013). This scenario can be distinguished from the compact millimeter grains by measuring the opacity index  $\beta$  between the 1 mm and 3 mm emission (Kataoka et al., 2014). Those observations, however, would require a very high sensitivity with enough angular resolution to spatially resolve the radial profile of J0415.

### 3.10 Gas to dust size ratio

Four of the six disks in this sample show a ratio between the  $R_{90,\text{gas}}$  and  $R_{90,\text{dust}}$  that is very close to or above 4.0, which is similar to the ratio measured in CX Tau (Facchini et al., 2019) (ratio of  $3.9 \pm 0.5$  at  $R_{90}$ ), as compared in Figure 3.8. These values, however, are conservative measurements of radii ratios for the sources with strong cloud contamination (all the sources in our sample, except for MHO 6), and so they should be considered as a lower limit. As it can be seen in the velocity channel maps in Figures 3.14, 3.16, 3.17, 3.18, and 3.19, the channels that are less affected by cloud contamination are the highest velocity channels, which are closer to the star. As soon as the emission gets radially extended in the channels closer to the central velocity,

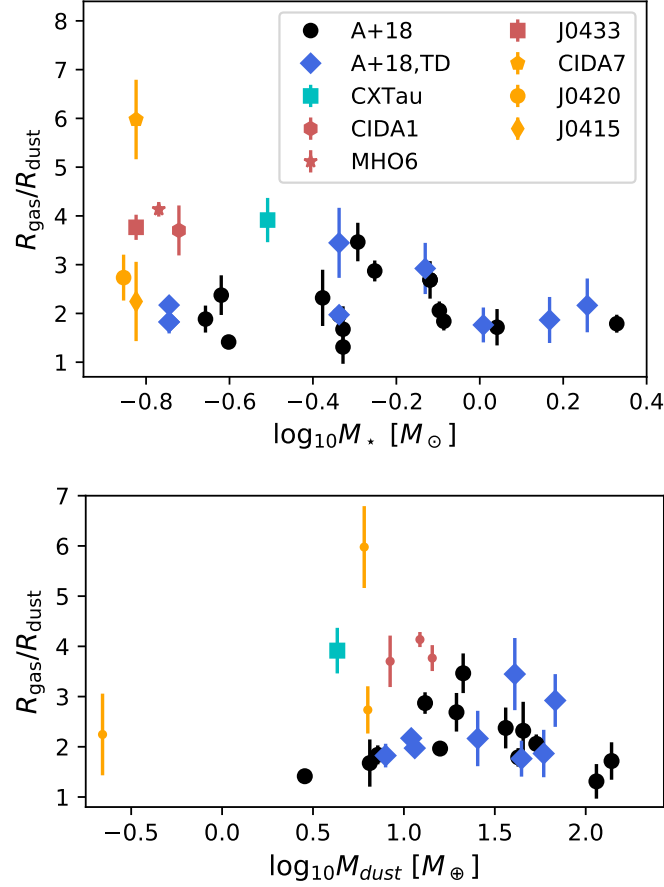


**Figure 3.8:** Gas to dust size ratio as a function of dust mass.

Upper panel:  $R_{\text{gas}}/R_{\text{dust}}$  as a function of the stellar mass of the disks in the Lupus star-forming region (SFR) reported in [Ansdell et al. \(2018\)](#) (abbreviated as A+18), CX Tau ([Facchini et al., 2019](#)), and the targets reported in [Kurtovic et al. \(2021\)](#). For CX Tau, I took the  $R_{90}$  radii of the dust and gas. The VLMS of this work are shown in red for the sources with a substructure, and they are in yellow for the smooth sources, with the values from Table 3.3. Ratios from the Lupus SFR by [Ansdell et al. \(2018\)](#) were calculated from  $R_{90}$  and a different color was used for disks identified as transition disks (TD). Lower panel:  $R_{\text{gas}}/R_{\text{dust}}$  of the same targets, but compared to the dust mass of the disks. The dust mass was calculated from Equation (3.4) under the assumption that  $T = 20$  K for the whole disk midplane, with distances from GAIA DR2.

the cloud extinction becomes so high that we cannot see the disk emission anymore. The integrated flux moment 0 images and the gas emission are then biased towards the compact emission located close to the star, underestimating the  $R_{\text{gas}}$  measurement. This effect is particularly strong in J0420 and J0415, as they are the dimmest sources in this work, and J0420 also has the highest extinction (see Fig. 3.2).

The observations show that it is common for bright disks around VLMS to have a gas radial extension of  $> 3$  times the millimeter dust radial extension, which is consistent with the efficient radial drift expected for millimeter-sized grains in VLMS disks (Pinilla et al., 2013; Zhu et al., 2018). In fact, recent thermo-chemical modeling including dust evolution by Trapman et al. (2019, 2020) shows that ratios of  $R_{\text{gas}}/R_{\text{dust}} > 4$  cannot be solely explained by effects of optical depths; additionally, in those cases, radial drift is required to explain the gas and dust size difference. Despite the limited sensitivity and cloud contamination, these disks are still very close and even above that limit. Although similar ratios have been observed in sources with a moderate stellar mass ( $\sim 0.5 M_{\odot}$ , see Ansdell et al., 2018), as shown in the upper panel of Figure 3.8, the direct comparison between our works is hindered by the data differences, such as in the sensitivity and angular resolution, and also by the different approaches used to obtain the gas and dust radii: The continuum radial extension in this work was calculated from the visibilities rather than the images, and no Keplerian masking was applied in the flux integrated gas images. A larger disk sample was analyzed by Long et al. (2022), including the VLMS presented in this work, and no consistent trend between  $R_{\text{gas}}/R_{\text{dust}}$  and  $M_{\star}$  was found, which means that radial drift is not the only mechanism shaping the disks sizes.

According to Trapman et al. (2019) and Trapman et al. (2020), they expect more massive disks to have a higher  $R_{\text{gas}}/R_{\text{dust}}$  ratio, driven by a larger observed  $R_{\text{gas}}$  due to the greater total CO content, and also because the higher dust content would produce a more efficient grain growth and inward radial drift. However, this trend is not observed in the lower panel of Figure 3.8. Apparently, a decreasing radii ratio is obtained towards higher dust mass disks, which could be the result of an efficient radial drift in disks around VLMS, and the linear relation between  $\log(M_{\star}) - \log M_{\text{dust}}$ . This supports the idea that smaller disks result from a fast radial drift (Long et al., 2019) due to their inability to trap dust in the outer regions, while more massive disks are more capable of creating dust traps farther away from the central

star.

CIDA 7 stands out in our sample as having the most extreme  $R_{\text{gas}}/R_{\text{dust}}$  ratio, with the gas being six times more extended than the dust, which is well beyond the ratio limit of 4 from [Trapman et al. \(2019\)](#). This confirms that radial drift is responsible for the compact size of this source. However, it is not completely dust depleted, so radial drift has been counteracted by another mechanism, or a combination of them. The southern non-Keplerian emission detected in this system (in the velocity channels 4.4 and 4.8 km s<sup>-1</sup> from [Fig. 3.17](#) and [3.1](#)) was masked when measuring the  $R_{90,\text{gas}}$ , so the ratio of six is between the disk rotating gas and the dust size recovered from the model. I was unable to determine the origin of this extended emission in the south, as it is only detected in two different channels and it does not appear to be axisymmetric. A multiwavelength follow-up, with high sensitivity and angular resolution, might be required to understand the nature of this emission, as it could be explained by several different mechanisms, such as winds, outflows, interactions with external companions, an interaction with the surrounding cloud and envelope, among others.

The lowest gas-to-dust size ratio in our sample, measured in J0415, is likely due to the combined effects of lower than expected brightness, a low sensitivity due to our inability to apply self-calibration, and the extinction due to cloud contamination. Although I was unable to confidently recover the gas radius, the observations set a lower limit for its radial extension, thus confirming that in this very low disk mass regime the gas emission is still more extended than dust emission. A more precise measurement of the gas radius requires a combination of deeper observations of lines less affected by the surrounding cloud and envelope as well as line modeling.

## 3.11 MHO6 kinematics

### 3.11.1 Analysis of the velocity map

Given that MHO6 is the only disk with the gas emission detected across the whole velocity range, it is a good candidate for the dynamical mass measurement of its star. As described in [Section 3.3](#), I used `CASA` to generate the moment 1 image from the velocity maps; in addition, I also generated velocity integrated images using the python package `bettermoments` ([Teague & Foreman-Mackey, 2018b](#)), with a quadratic and Gaussian method, and

also by varying the root mean square (RMS) clipping limit. The Keplerian rotation of these images was modeled using the package `eddy` (Teague, 2019), with different models considering the stellar mass ( $M_\star$ ), the central velocity (VLSR), the flaring parameter ( $\psi$ ), the position angle (PA), and the source center ( $x_0, y_0$ ) as fixed or free parameters. The fitting was performed inside an elliptical masked region, extending up to  $0.9''$  in the  $^{12}\text{CO}$  emission, and up to  $0.6''$  in the  $^{13}\text{CO}$ . Each image was modeled separately.

Depending on the free parameters used (e.g., fixing the PA or allowing the fitting of vertical structure) and also on the velocity integrated image used, the stellar mass recovered would vary in the range of  $0.16 \sim 0.24 M_\odot$ , which is consistent with a stellar mass derived from evolutionary models ( $0.09 - 0.20 M_\odot$  Kraus & Hillenbrand, 2009; Herczeg & Hillenbrand, 2014; Ward-Duong et al., 2018). However, it is important to note that all the models and images would leave residuals, which span two times the channel velocity widths and are also strongly structured, as shown in Figure 3.12, which were computed by clipping the emission in each channel at the  $3\sigma$  level.

Although our observations have enough spatial resolution to resolve the vertical structure in some of our disks (as seen in Figure 3.1 as a cone-like emission in the  $^{12}\text{CO}$  moment 0 of MHO 6 and J0433), the low S/N did not allow us to differentiate between the emission coming from the back side of the disk from that of the front side, in the image. The integrated velocity map contains the emission of both sides as if they were the same, and thus parameters such as  $M_\star$  or  $\psi$  from  $Z(r, \psi) \propto r^\psi$  could not be recovered reliably. This issue is not an exclusive problem in VLMS disks, but it applies to all the gas measurements with a high angular resolution and poor S/N. Future approaches to accurately recover  $M_\star$  should consider more robust methods, such as visibility modeling (similar to the `DiskJockey` code from Czekala et al., 2015). See also Section 3.11.

MHO 6 is a good candidate to further study the kinematics, substructures, and the physics of planet formation in VLMS. Its brightness allows high S/N observations at high angular resolution with non-prohibitive integration times. Combining the datasets presented in this paper, plus an observation of  $\geq 5$  hr of time on source with ALMA using long baseline configurations should have enough resolution and sensitivity to precisely characterize the kinematics of the CO isotopologues, as previously done with disks around T-Tauri and Herbig stars (e.g., Pinte et al., 2019; Teague et al., 2019).

### 3.11.2 Modeling of the gas visibilities

The gas emission from MHO 6 is spatially resolved in  $^{12}\text{CO}$  and  $^{13}\text{CO}$ . However, the sensitivity per individual channel does not allow disentangling the emission from the front and back layer in the image plane or determining the height of the emitting layers. This information is contained in the observation, as suggested by the structured residuals from subtracting the best eddy model.

To take advantage of the underlying Keplerian rotation of the disk, I modeled the emission of MHO 6 in the visibilities. The results explained in the following paragraphs are still in preparation for publication, but a summary goes as follows:

- The front and back emission layers are described by the same emission height by construction, following an exponentially tapered power-law profile. Due to the low brightness of the back emission layer, its height cannot be constrained independently to the 3 sigma level.
- The disk's temperature is also modeled as an exponentially tapered power-law.
- The stellar mass, disk inclination, position angle, and disk center are left as free parameters.

The parametric visibility modeling of the visibilities was run through an MCMC, similar to the methodology taken in the dust continuum emission. The results for the brightness temperature profile of the CO isotopologues are shown in Figure 3.9. The elevation of the emitting layer is shown in Figure 3.10, where we also compare it with other bright disks that have been published in Law et al. (2021, 2022a,b). The disk around MHO 6 has one of the most elevated emission surfaces within the first 50 au, as expected from very low mass stars (Pinilla, 2022). Additionally, we confirmed the central star's mass is  $0.15 M_{\odot}$ , and the estimates of  $R_{68}$  and  $R_{90}$  are consistent with the estimates from the moment 0, despite the additional considerations of elevated surfaces.

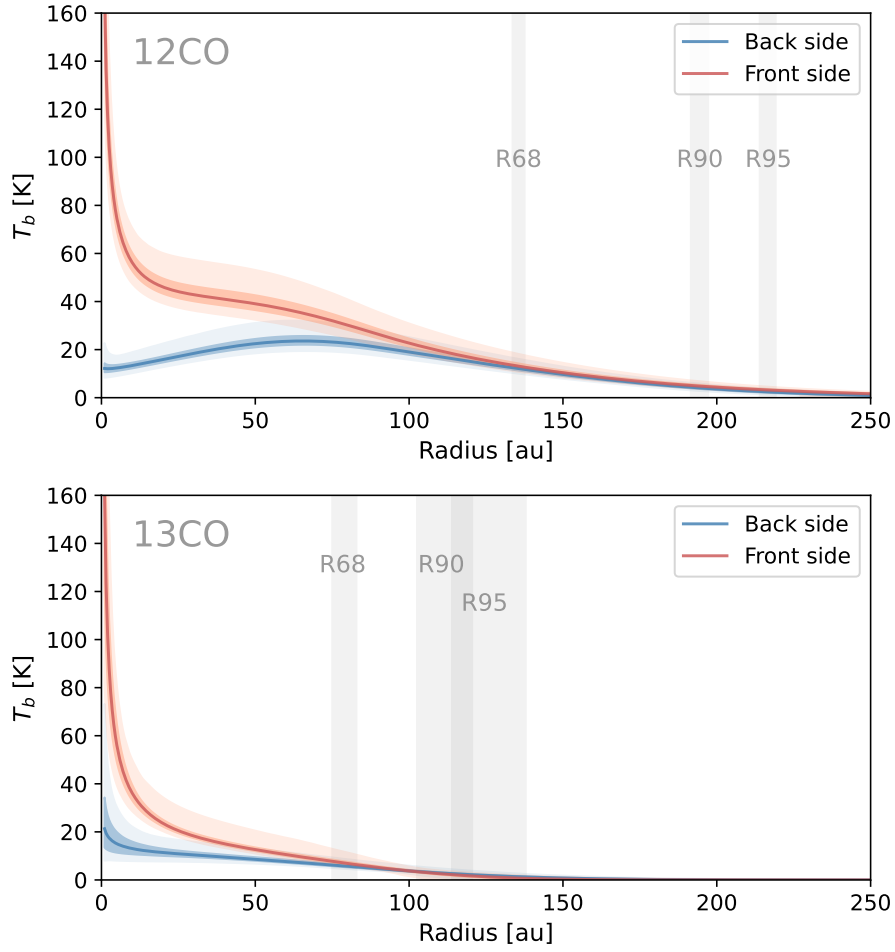


**Figure 3.9:** MHO 6 Brightness temperature profile measured from CO emission. The  $^{12}\text{CO}$  and  $^{13}\text{CO}$  emission are shown in the upper and lower panel, respectively.

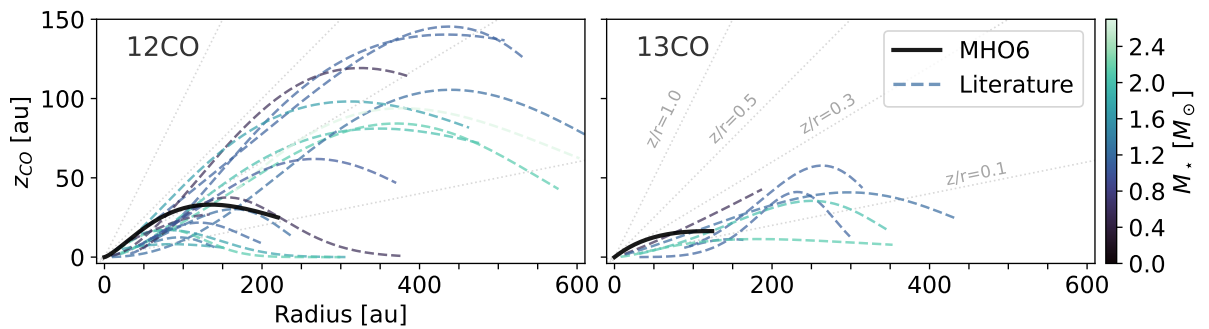


**Figure 3.10:** For comparison, the fitted surfaces of  $^{12}\text{CO}$  and  $^{13}\text{CO}$  emission from Law et al. (2021, 2022a,b) are also shown over their fitting range. MHO 6 is shown until its  $R_{95\%}$ .

### 3.12 Summary

To understand the process of planet formation in VLMS and compare it with our current knowledge of planet formation in solar type stars, we observed and studied a sample of the brightest disks around VLMS in Taurus, at a  $0.1''$  resolution and at a 0.87 mm wavelength. This sample is composed of CIDA 1, MHO 6, J0433, CIDA 7, J0420, and J0415 (2MASS names in Section 3.3). Here I summarize our main conclusions as follows.

- **Detection rate of substructures:** Millimeter dust substructures were directly detected in only 50% of the targets in the sample. Our results suggest that the detection of substructures in disks around VLMS is limited by angular resolution and sensitivity, since the dust radial extent is very small and these disks are also very faint. Deep, high angular resolution observations over a non-brightness biased sample of VLMS should confirm the ubiquity of substructures in these disks.
- **Substructured disks:** Substructures were detected in CIDA 1, MHO 6, and J0433; with the latest two being new detections. These three disks are the brightest and largest in our sample. They all have axisymmetric ring-like substructures, and only MHO 6 shows a weak asymmetry of amplitude less than 5% of the peak brightness. Both CIDA 1 and MHO 6 show central cavities in their emission. Under the assumption that a planet-disk interaction is the origin of the MHO 6 cavity, then a Saturn-mass planet ( $0.3 M_{\text{Jup}}$ ) is needed (as in the case of CIDA 1 [Pinilla et al., 2018b](#)). This planet should be located around 7 au. However, other mechanisms that can explain the origin of this cavity are not excluded, such as multiple planets, a dead zone, a binary companion, or photoevaporation. Our visibility modeling of J0433 suggests that this disk could have two rings located at 21 and 32 au. However, the separation between both is only measured at the  $1\sigma$  confidence. A planet of  $\sim 0.1 M_{\text{Jup}}$  in mass could explain the first gap-ring. These substructures were detected within the region where the CO iceline could be located. The temperature profile and emission height of the CO isotopologues can be studied from these observations, and this is already work in progress. Those results will help to determine if the iceline played any role in triggering or maintaining the substructures observed, or if any deviations from Keplerian motion are detected.

- **Smooth disks:** The dust disks in CIDA 7, J0420, and J0415 are the less radially extended, less massive disks of the sample. With an angular resolution of  $0.1''$ , these disks are well described by a single Gaussian radial profile, which I used to measure their sizes. CIDA 7 is the most compact of them, with an  $R_{90} = 13.16$  au, which is similar to the 15.46 au from J0415. Yet, the dust mass estimate suggests that CIDA 7 is about  $\times 27$  more massive. In J0420, the residual continuum image shows some structured non-axisymmetric emission with  $5\sigma$  peaks. However, this emission is very low in contrast to the smooth emission, which is over  $300\sigma$  at its peak. Higher angular resolution observations are needed to describe the potential substructures in these disks .
- **Size-luminosity relation:** The disks in the sample follow a similar relation between  $L_{\text{mm}} - R_{68}$  as the one found for bright disks in the same star-forming region (see [Hendler et al., 2020](#)). However, the single measurement of a disk size in the low luminosity regime (J0415) needs to be complemented with deeper additional observations of other sources with a low stellar mass and low disk brightness. These measurements will help us understand the behavior of the size-luminosity relation across the whole range of disk sizes, enabling us to test if a single power law describes it.
- **Evidence of efficient radial drift:** When considering the dust and gas radii as the location where 90% of the emission is enclosed, four out of six disks in the sample show a ratio between  $R_{\text{gas}}/R_{\text{dust}}$  above 3.5. This is expected for disks where radial drift is depleting the dust. The most extreme case of high  $R_{\text{gas}}/R_{\text{dust}}$  in our VLMS is observed in CIDA 7, with a value of six. This very high  $R_{\text{gas}}/R_{\text{dust}}$  ratio suggests that strong radial drift is at play ([Trapman et al., 2019](#)), raising the question about how this disk remains massive in dust.

Overall, this study suggests that the disks around VLMS follow similar trends as those that have been observed in disks around higher mass stars, based on this sample of bright disks. Notably, these observations do not exclude giant planet formation as an explanation for the substructures detected.

### 3.13 Additional content

A summary of the observation log is provided in Table 3.4. The difference for configurations “Compact” and “Extended” denotes the stage at which I started its self-calibration based on the spatial extension of the antenna array, see Section 3.3. The properties of the dust continuum emission images and gas emission datacube are shown in Table 3.5 and 3.6, respectively. The channel maps of the  $^{12}\text{CO}$  and  $^{13}\text{CO}$  are also shown below, together with the integrated flux and the eddy fit to MHO 6.

Source	Program ID	Obs. Date	Exp. time (min)	N° Antennas	Baselines (m)	Configuration
CIDA 1	2015.1.00934.S	2016-08-12	47.68	38	15 - 1462	Compact
	2016.1.01511.S	2017-07-06	4.23	42	17 - 2647	Compact
MHO 6	2012.1.00743.S	2013-11-19	4.66	28	17 - 1284	Compact
		2014-07-27	2.71	33	24 - 820	Compact
	2018.1.00310.S	2019-08-21	47.15	45	41 - 3189	Extended
J0433	2012.1.00743.S	2013-11-17	2.80	29	17 - 1284	Compact
		2014-07-27	2.27	33	24 - 820	Compact
	2018.1.00310.S	2018-11-20	12.98	47	15 - 1398	Compact
		2018-11-24	12.98	46	15 - 1261	Compact
		2019-08-13	26.61	43	41 - 3144	Extended
		2019-08-13	10.45	43	41 - 3144	Extended
CIDA 7	2018.1.00310.S	2018-11-13	12.48	47	15 - 1398	Compact
		2019-08-24	26.04	47	41 - 3396	Compact
		2019-08-24	26.04	47	41 - 3638	Extended
J0420	2012.1.00743.S	2013-11-19	4.66	26	17 - 1284	Compact
		2014-07-27	2.27	33	24 - 820	Compact
	2018.1.00310.S	2018-10-30	12.98	48	15 - 1398	Compact
		2018-11-13	12.98	47	15 - 1398	Compact
		2019-08-12	27.22	47	41 - 3638	Extended
		2019-08-13	27.22	43	41 - 3144	Extended
		2019-09-18	27.25	41	15 - 3638	Extended
J0415	2016.1.01511.S	2015-09-20	4.8	42	15 - 3189	Extended
	2018.1.00310.S	2019-09-20	27.88	45	15 - 3189	Extended

**Table 3.4:** Summary of ALMA observations.

Source	RA (ICRS)	Dec (ICRS)	Beam (mas $\times$ mas, deg)	Peak $I_\nu$ (mJy beam $^{-1}$ )	RMS noise (mJy beam $^{-1}$ )	$F_{0.87\text{mm}}$ (mJy)	$M_{\text{dust}}$ ( $M_\oplus$ )
CIDA 1	04:14:17.620	+28:06:09.289	150 $\times$ 111, -24	5.48	0.064	36.3 $\pm$ 0.1	8.40 $\pm$ 0.84
MHO 6	04:32:22.128	+18:27:42.286	104 $\times$ 72, 35	4.62	0.025	48.40 $\pm$ 0.15	12.25 $\pm$ 1.23
J0433	04:33:44.670	+26:15:00.080	128 $\times$ 86, -8	6.21	0.024	37.93 $\pm$ 0.12	14.32 $\pm$ 1.43
CIDA 7	04:42:21.022	+25:20:33.996	101 $\times$ 80, 10	11.53	0.029	25.96 $\pm$ 0.10	6.05 $\pm$ 0.61
J0420	04:20:25.581	+27:00:35.242	113 $\times$ 82, 22	6.45	0.021	17.35 $\pm$ 0.05	6.33 $\pm$ 0.63
J0415	04:15:58.016	+27:46:16.811	161 $\times$ 78, -36	0.44	0.052	0.96 $\pm$ 0.29	0.22 $\pm$ 0.02

**Table 3.5:** Continuum imaging summary.

Source	Ch. width (km s $^{-1}$ )	Detection LSRK (km s $^{-1}$ )	Beam (mas $\times$ mas, deg)	Peak $I_\nu$ (mJy beam $^{-1}$ km s $^{-1}$ )	RMS noise (mJy beam $^{-1}$ )	Flux (Jy)
CIDA 1 $^{12}\text{CO}$	0.20	1.7 - 11.1	268 $\times$ 173, 1	91.2	4.0	0.725
$^{13}\text{CO}$	1.00	2.0 - 9.1	118 $\times$ 83, 36	21.6	1.3	0.215
MHO 6 $^{12}\text{CO}$	0.25	0.65 - 10.1	115 $\times$ 81, 35	33.8	2.0	3.179
$^{13}\text{CO}$	0.90	2.0 - 9.1	118 $\times$ 83, 36	21.6	1.3	1.061
J0433 $^{12}\text{CO}$	0.35	0.7 - 11.2	165 $\times$ 110, -7	72.7	2.2	1.241
$^{13}\text{CO}$	1.0	1.0- 11.0	159 $\times$ 110, -8	22.7	1.3	0.618
CIDA 7 $^{12}\text{CO}$	0.4	0.8 - 8.4	168 $\times$ 148, -1	61.9	2.6	1.065
$^{13}\text{CO}$	1.0	3.0 - 8.0	170 $\times$ 149, 0	22.8	1.6	0.160
J0420 $^{12}\text{CO}$	0.45	7.75 - 10.9	135 $\times$ 98, 23	35.1	1.5	0.224
$^{13}\text{CO}$	0.90	5.5 - 10.9	133 $\times$ 96, 22	8.2	1.0	0.038
J0415 $^{12}\text{CO}$	0.8	4.4 - 8.4	216 $\times$ 142, -38	32.1	3.8	0.020
$^{13}\text{CO}$	1.0	—	222 $\times$ 141, -40	—	2.6	<0.004

**Table 3.6:**  $^{12}\text{CO}$  and  $^{13}\text{CO}$  imaging summary.

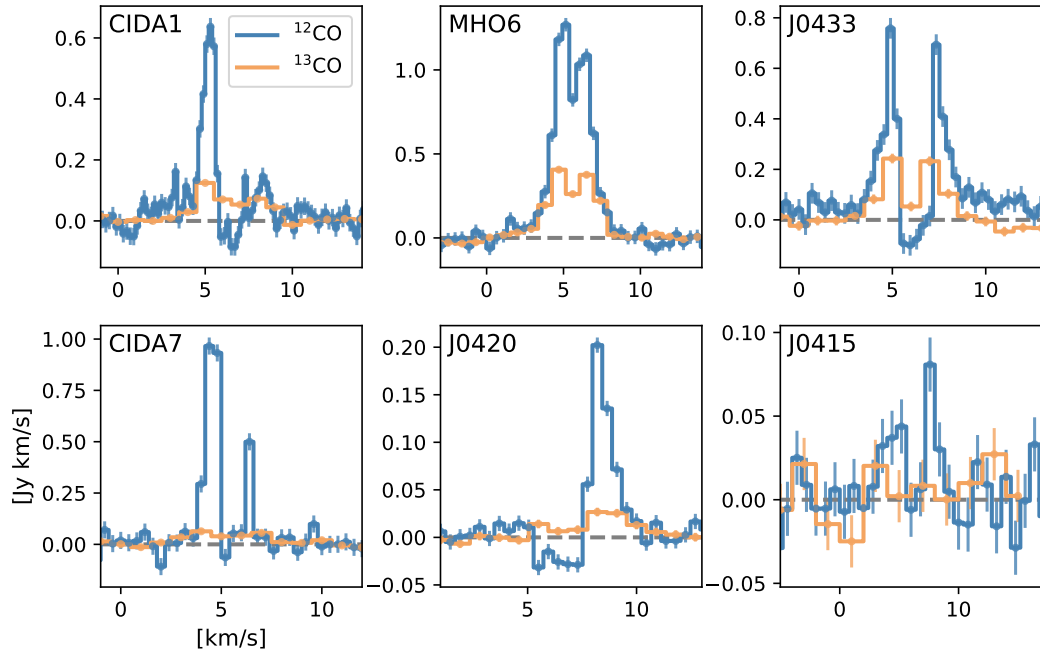


**Figure 3.11:** Spectral profile of the  $^{12}\text{CO}$  and  $^{13}\text{CO}$  in our sample. The gray line denotes the 0 Jy level.

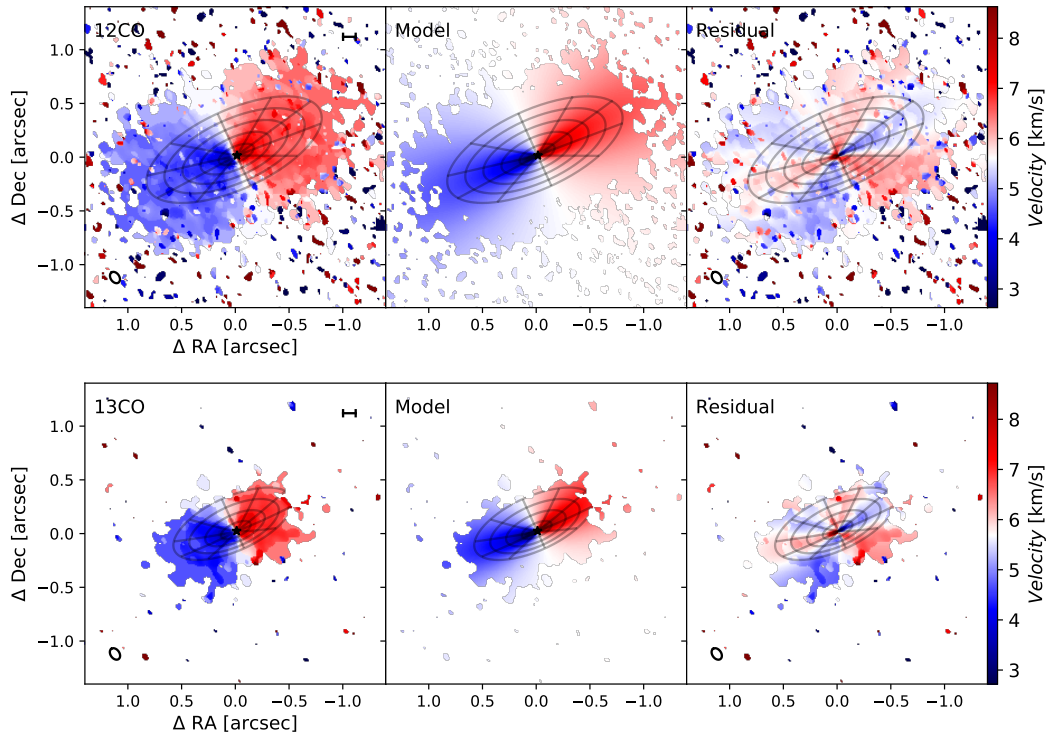


**Figure 3.12:** Keplerian fitting of  $^{12}\text{CO}$  and  $^{13}\text{CO}$  with eddy. The grid shows the best surface recovered with eddy, extending up to the distance of the mask for the fitting.

### 3 Planet formation in very low mass stars

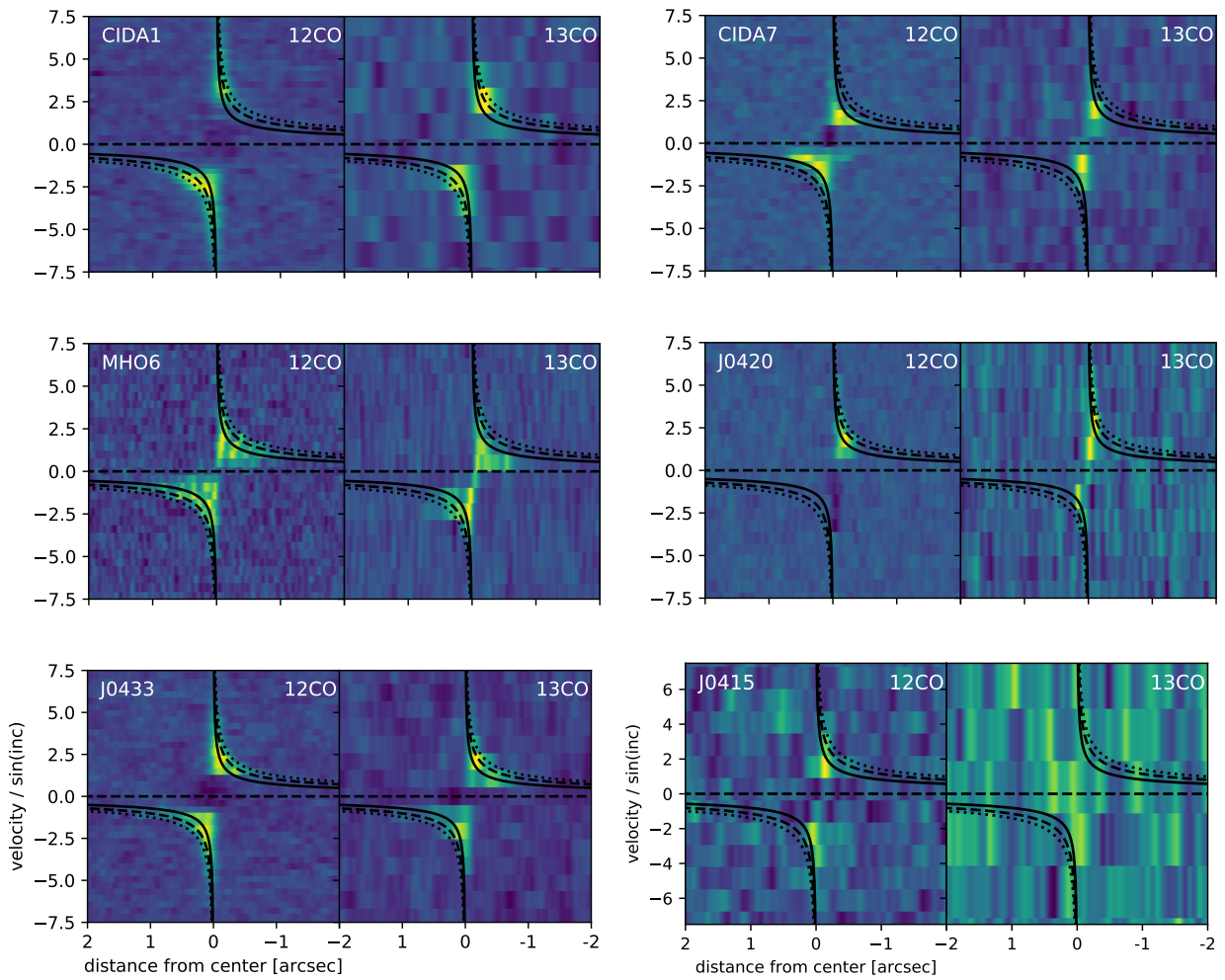


**Figure 3.13:** Position velocity diagram of the gas emission. The  $^{12}\text{CO}$  and  $^{13}\text{CO}$  are shown in the left and right, respectively. The lines show the Keplerian rotation for 0.1, 0.2 and 0.3  $M_{\odot}$ .

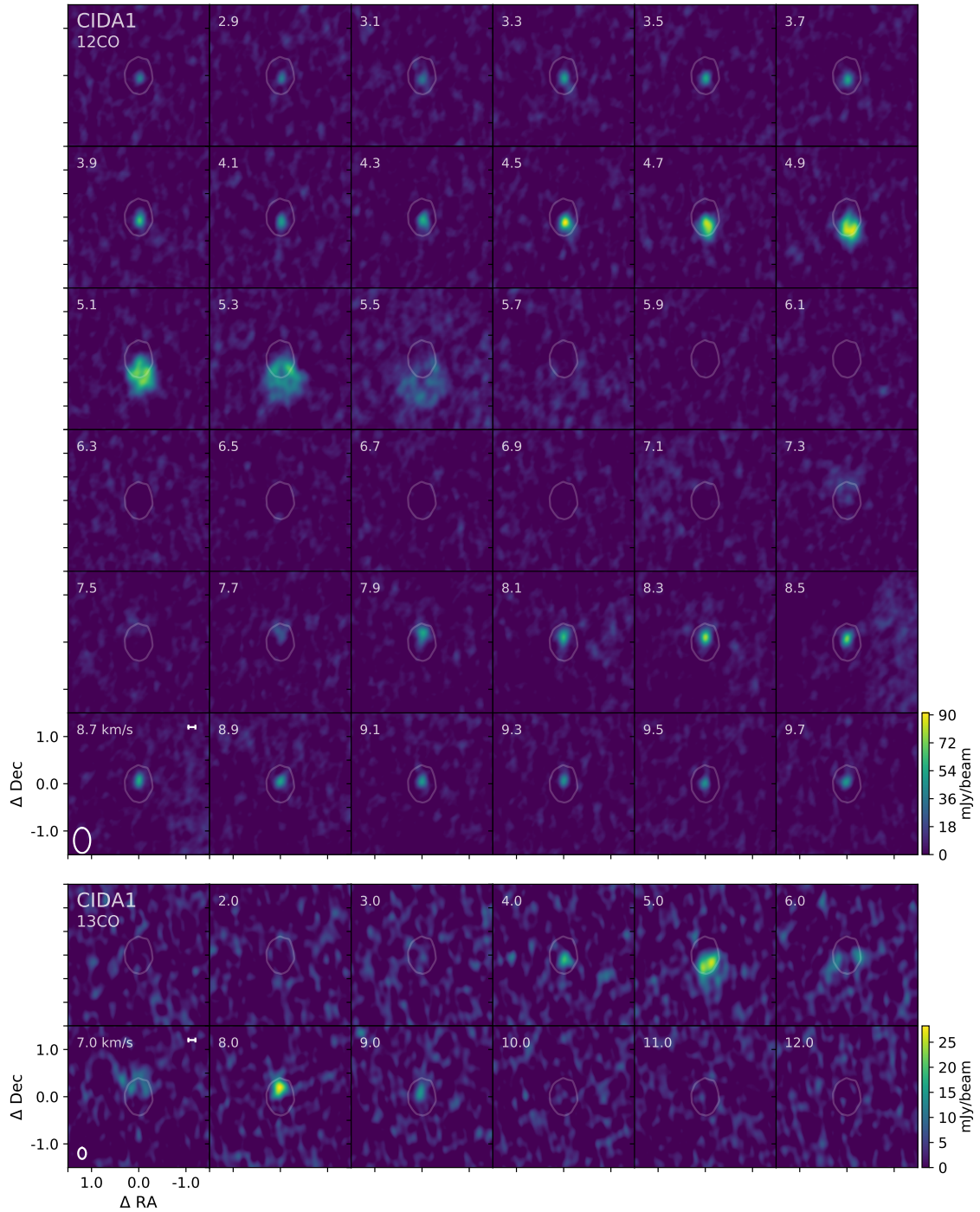


**Figure 3.14:** Channel maps of the CO emission of CIDA 1

The  $^{12}\text{CO}$  channel maps are shown in the top, and  $^{13}\text{CO}$  channel maps are shown in the bottom. Each square is 3.0" in width and height, centered at the same position as the dust continuum image. The contour level traces the  $5\sigma$  emission in the continuum image. The scale bar in the lower left panel is 20 au in size, and the beam size is found in the lower left corner of the same panel. Central velocities in km/s of each channel are given in the upper left corner of each panel.

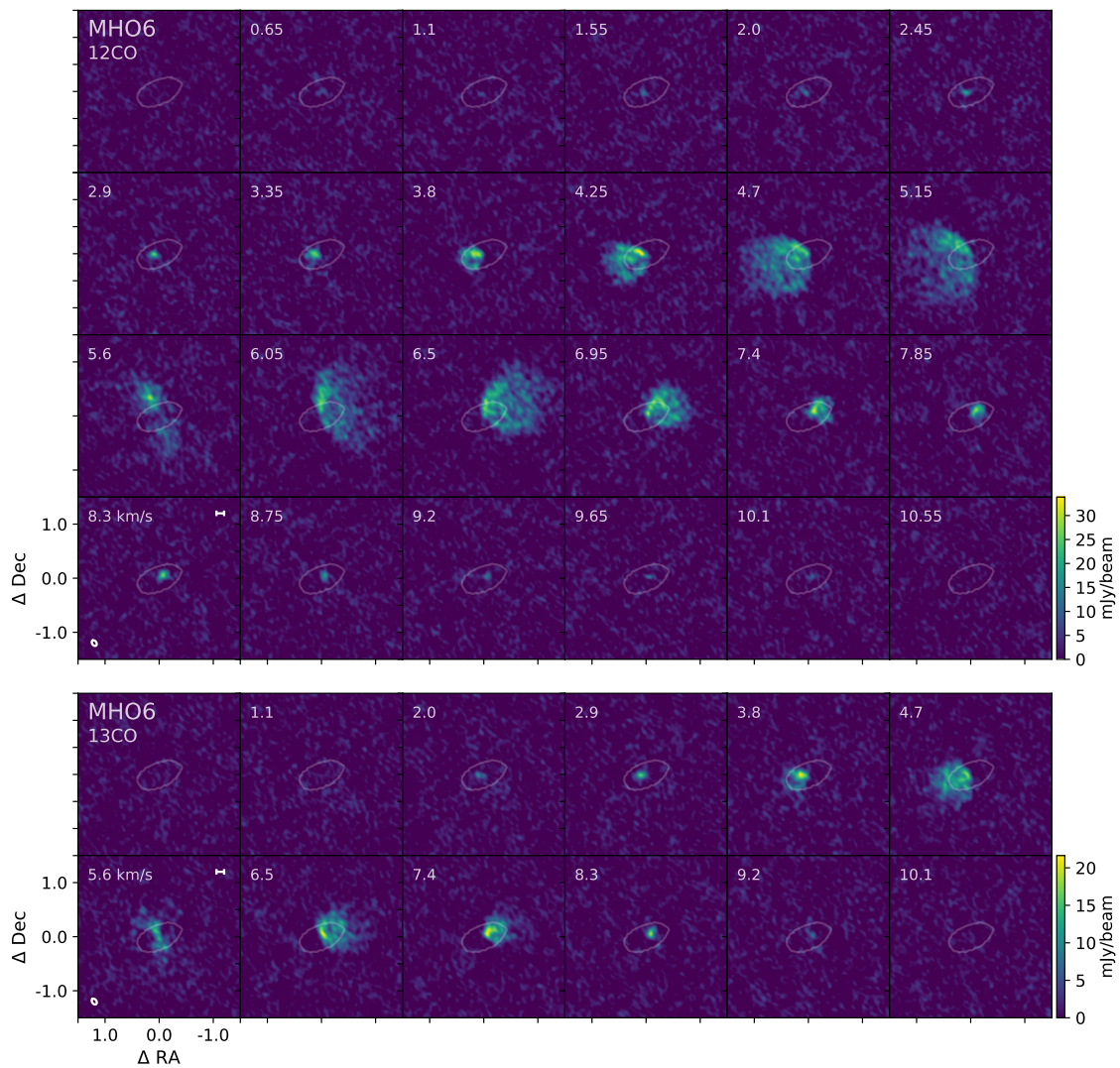


**Figure 3.15:** Channel maps of the CO emission of MHO 6.  
Image details are the same as for Figure 3.14.

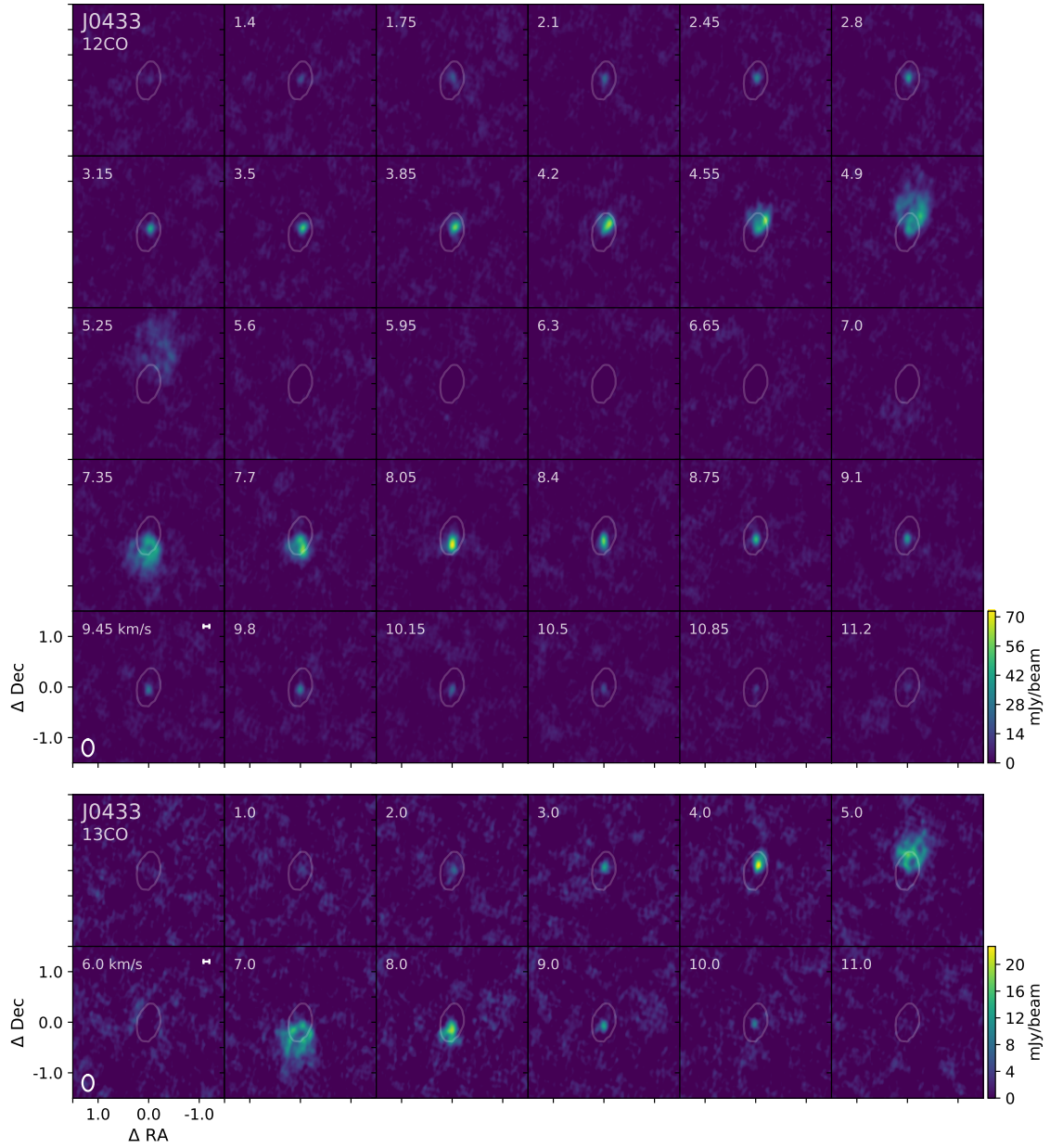


**Figure 3.16:** Channel maps of the CO emission of J0433. Image details are the same as for Figure 3.14.

### 3 Planet formation in very low mass stars

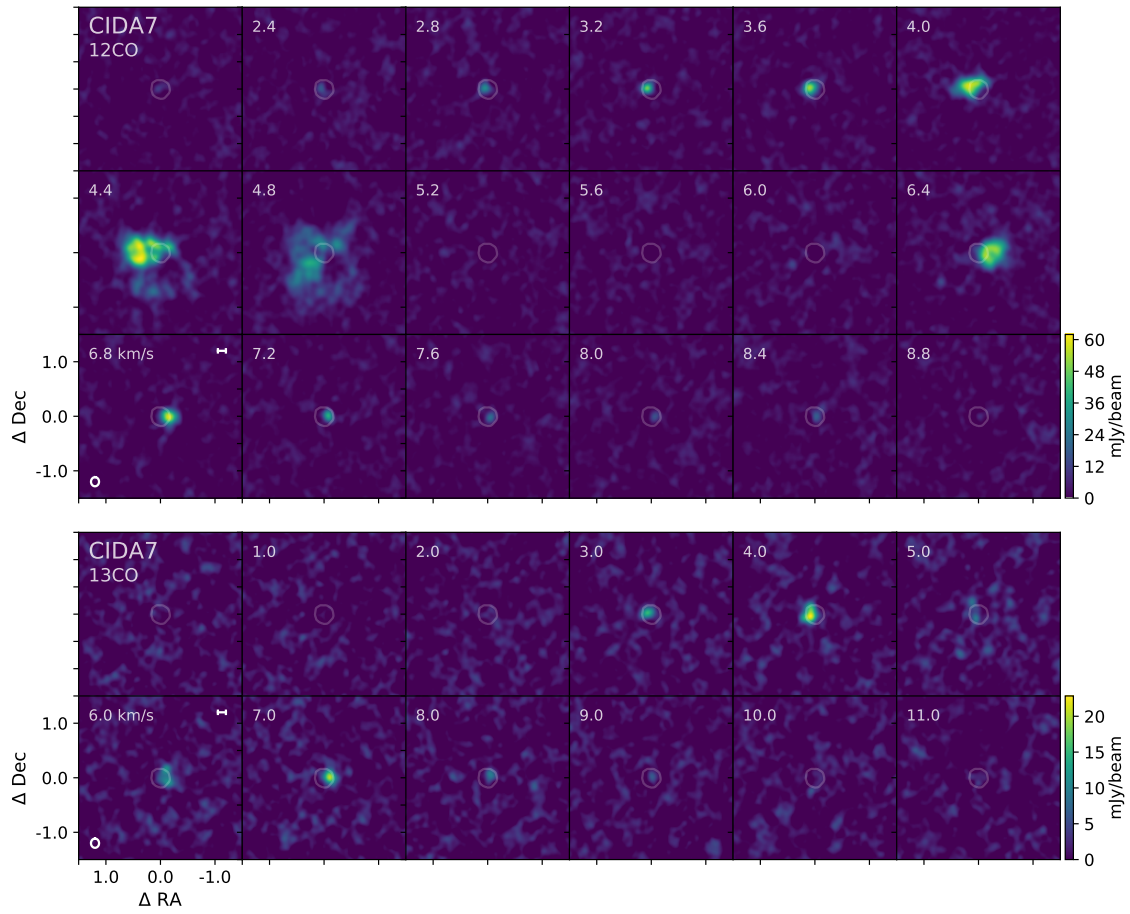


**Figure 3.17:** Channel maps of the CO emission of CIDA 7  
Image details are the same as for Figure 3.14.

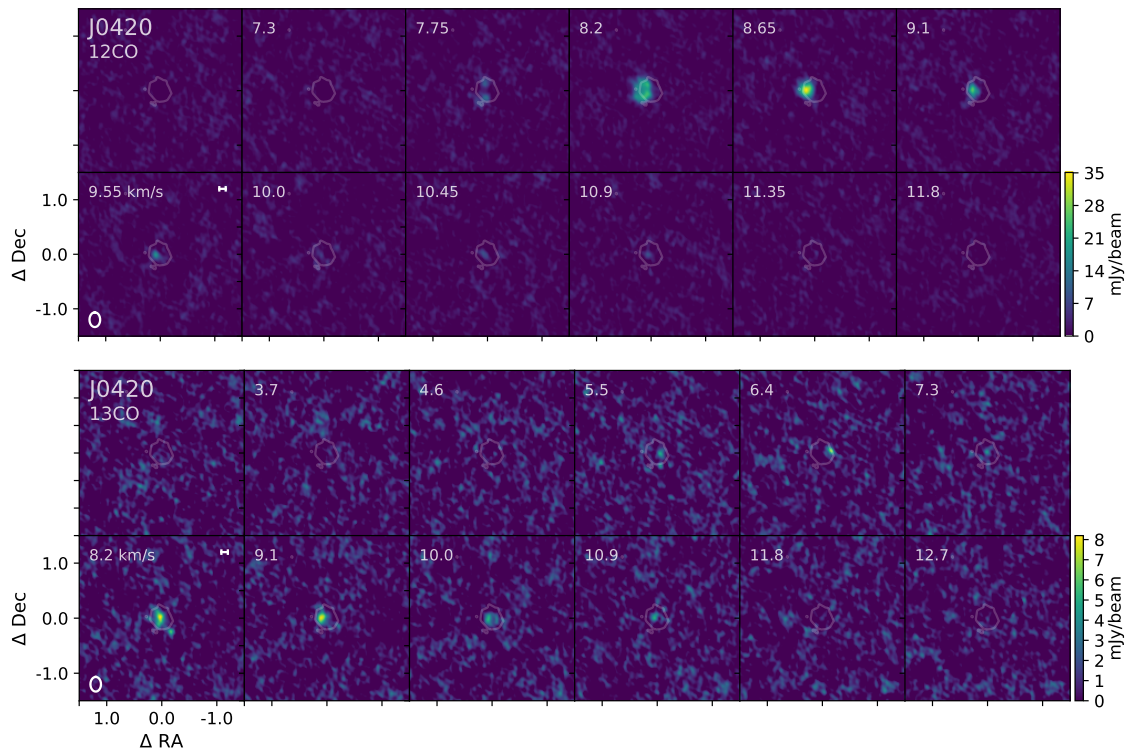


**Figure 3.18:** Channel maps of the CO emission of J0420. Image details are the same as for Figure 3.14.

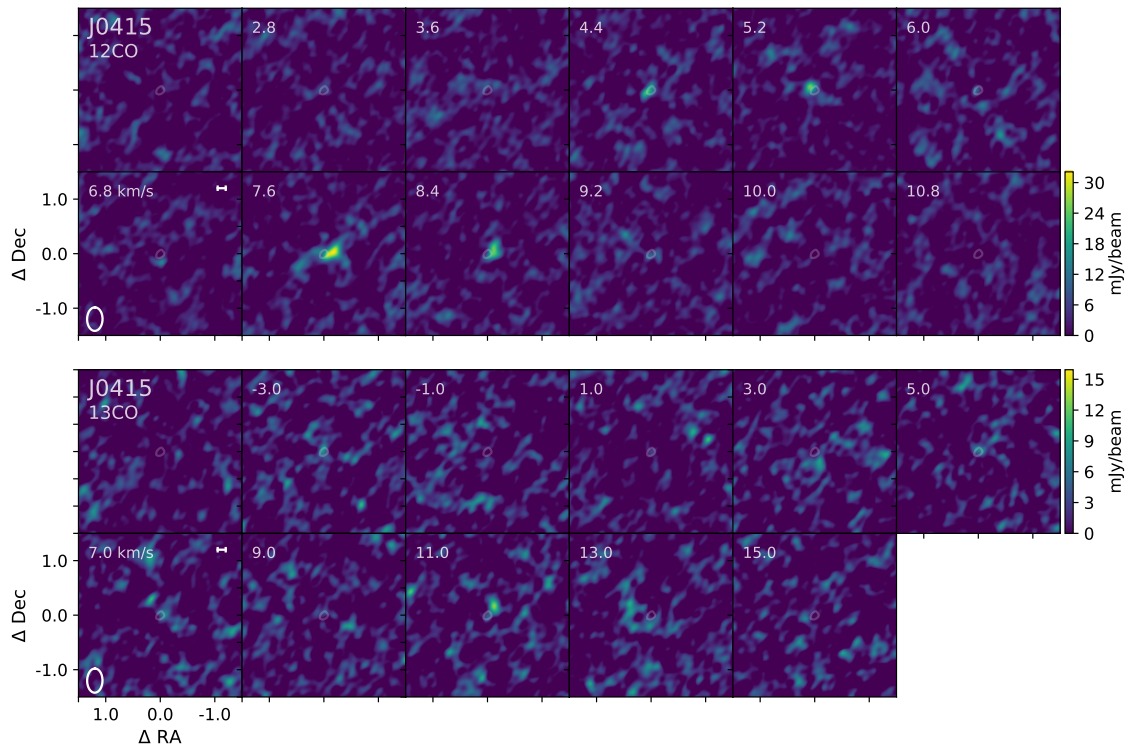


**Figure 3.19:** Channel maps of the CO emission of J0415. Image details are the same as for Figure 3.14.



# 4

## Planet formation in a circumbinary disk

---

This chapter is an adapted version of the the published research article “*The morphology of CS Cha circumbinary disk suggesting the existence of a Saturn-mass planet*”, published in [Kurtovic et al. \(2022\)](#).

### 4.1 Clues about planet formation in circumbinary systems

Over the last decade, space telescopes such as Kepler and the Transiting Exoplanet Survey Satellite (TESS) have successfully detected several planets in circumbinary orbits, which are also known as P-type orbit planets (see [Doyle et al., 2011](#); [Kostov et al., 2020](#)). These planets have been found to share some orbital properties, such as:

1. Most of them are located close to the inner dynamical stability limit ([Dvorak, 1986](#); [Holman & Wiegert, 1999](#); [Martin, 2019](#))
2. ii) their orbits are mostly coplanar and of low eccentricity, with a planet occurrence rate similar to single stellar systems ([Armstrong et al., 2014](#); [Martin & Triaud, 2014](#))

As these common characteristics cannot be explained as simply observational biases ([Martin & Triaud, 2014](#)), there could be evidence for common formation mechanisms at play for these planets.

Due to the interaction between the two central stars, not all the regions of a circumbinary disk are suitable for planet formation. Tidal forces are expected to carve a central cavity in the disks, where the material density is severely reduced ([Artymowicz & Lubow, 1994](#); [Miranda & Lai, 2015](#)), and oscillations in the eccentricity of the orbits make extremely challenging to have planetesimal and pebble accretion in the regions close or within the dynamical stability limit ([Paardekooper et al., 2012](#); [Pierens et al., 2020](#)).

Consequently, the detection of several planets in the edge of that region suggests that the planets were formed farther away, and later migrated to the location where they can now be observed (Pierens & Nelson, 2007; Meschiari, 2012; Kley & Haghighipour, 2014; Thun & Kley, 2018).

Hydrodynamic simulations of circumbinary disks have shown that disks become eccentric due to dynamical instabilities, and the properties of the cavity will be dependent on the binaries and disk itself (see Lubow, 1991; MacFadyen & Milosavljević, 2008; Thun et al., 2017; Hirsh et al., 2020; Muñoz & Lithwick, 2020; Ragusa et al., 2020). The inclusion of a planet can disrupt this behavior, as the gap opened by a planet can shield the outer disk from the action of the binaries, allowing it to become more circular (Kley et al., 2019; Penzlin et al., 2021). Therefore, the study of a disk kinematics and structures of a young circumbinary disk could either hint at or exclude the presence of such planets.

## 4.2 An interesting case-study: CS Cha

A particularly interesting multiple stellar system is CS Cha, a spectroscopic binary with a period of at least 7 yr (Guenther et al., 2007; Nguyen et al., 2012) and a member of Chameleon I association, with an estimated age of  $4.5 \pm 1.5$  Myr (Luhman, 2007). CS Cha is located at 169 pc estimated from the inverse of the parallax of GAIA EDR3 (Gaia Collaboration et al., 2016, 2021), and the combined luminosity of the binary is estimated to be  $L_{\star} = 1.45 L_{\odot}$  (Manara et al., 2014). The system is known to host a circumbinary disk, which was first identified from its spectral energy distribution (SED) due to an excess in the infrared wavelengths (Gauvin & Strom, 1992), and later detected at 1.3 mm wavelength (Henning et al., 1993). The system was cataloged as a transition disk due to its SED shape, which was modeled early on as a disk with a central cavity (Espaillat et al., 2007). Over the last two decades, there have been several attempts to measure the cavity size and ring location, mainly through its SED (Espaillat et al., 2007; Kim et al., 2009; Espaillat et al., 2011; Ribas et al., 2016), with the latest estimations being  $R_{\text{cav}} = 18_{-5}^{+6}$  au. Recent observations with the Spectro-Polarimetric High-contrast Exoplanet REsearch (*SPHERE*) at the Very Large Telescope (*VLT*) made it possible to spatially resolve the disk scattered light, demonstrating that if there is a cavity in scattered light emission (small micron-sized grains), it must be within the coronagraph hidden region, setting an upper limit of

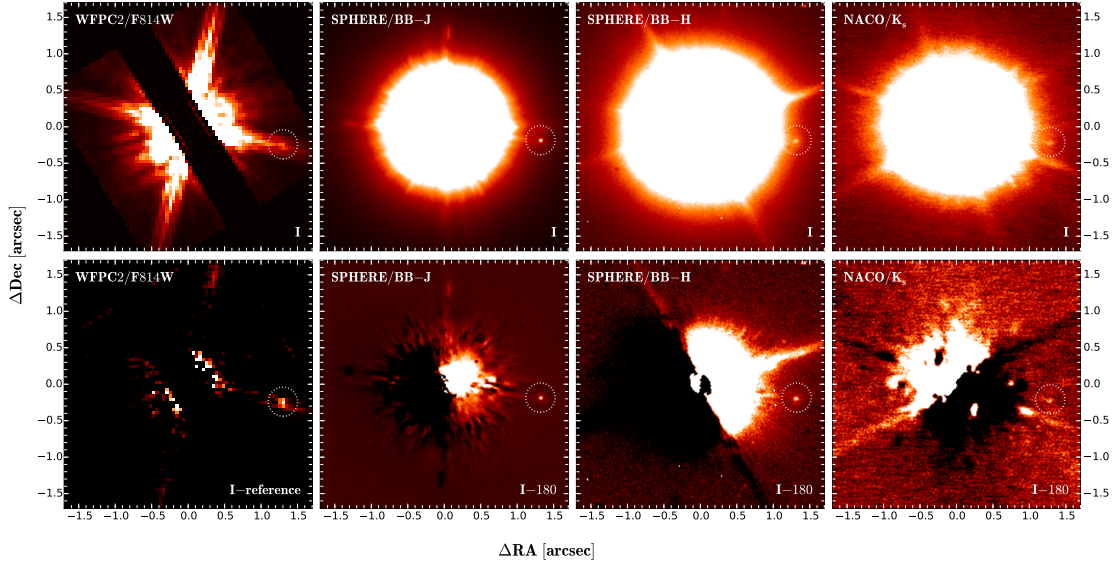


**Figure 4.1:** Detection of CS Cha B with several instruments over a time period of about 20 yr.

Image from [Ginski et al. \(2018\)](#).

15.6 au ([Ginski et al., 2018](#)). Finally, the modeling of interferometric data of the millimeter dust continuum emission with a 1D radial profile, suggests that the disk has a ring-like shape with its peak located at  $204 \pm 7$  mas ( $34.5 \pm 1.2$  au) ([Norfolk et al., 2021](#)).

Combined observations of NAOS-CONICA (*NACO*) at the VLT, SPHERE (at VLT), and the Hubble Space Telescope (*HST*), have allowed the identification of an apparent co-moving companion located at  $\approx 1.3''$  ( $\approx 220$  au) of projected distance to the CS Cha binaries ([Ginski et al., 2018](#)), shown in Figure 4.1. Initially, it was thought to be a planetary mass object ([Ginski et al., 2018](#)), however, its optical and near-infrared (NIR) spectra have shown that it is possible that CS Cha B is actually an M-dwarf star severely obscured by a highly inclined disk and outflows ([Haffert et al., 2020](#)). Such a circumstellar environment on CS Cha B is also supported by a very high degree of polarization observed with SPHERE and by the detection of a mass accretion rate of  $\dot{M} = 4 \cdot 10^{-11 \pm 0.4} M_{\odot} \text{ yr}^{-1}$  ([Haffert et al., 2020](#)).

If CS Cha B had been a planetary mass companion, it would have become one of the first objects of such class to be detected in their formation stages, back in 2017. This motivated the observations of the system with the ALMA, with the aim of characterizing this newly detected companion. Although the

results about the detection of CS Cha B in millimeter wavelengths are shown in Section 4.4.2, the same ALMA observation also captured the millimeter emission of the circumbinary disk of CS Cha at high angular resolution, which enables the study presented in this chapter.

### 4.3 ALMA Observations

The observation presented in this work provides one of the deepest and highest sensitivity observations available for a Class II circumbinary disk. CS Cha was observed at 0.87 mm with ALMA Band 7 as part of the ALMA project 2017.1.00969.S (PI: M. Benisty) between 26-Nov-2017 and 12-Dec-2017. The correlator was configured to observe four spectral windows: three covered dust continuum emission centered at 334.772 GHz, 336.600 GHz, and 347.471 GHz, with a total bandwidth of 2 GHz; the remaining one was centered at 345.770 GHz to observe the molecular line  $^{12}\text{CO}$  in the J:3-2 transition (from now on referred to as  $^{12}\text{CO}$ ) with a frequency resolution of 122.07 kHz ( $\sim 0.1 \text{ km s}^{-1}$  per channel). The total time on source was 273.1 min, spanning baselines from 15.1 m to 8547.6 m from ALMA antenna configurations C43-8 and C43-7.

I started the data handling from the pipeline calibrated data, which is obtained after executing the `scriptforPI` provided by ALMA. With `CASA 5.6.2`, I extracted the dust continuum emission from the spectral window targeting  $^{12}\text{CO}$ , by flagging the channels located at  $\pm 25 \text{ km s}^{-1}$ . The remaining channels were combined with the other continuum spectral windows to obtain a “pseudo-continuum” dataset, and we averaged them into 125 MHz channels and 6 s bins to reduce data volume. To enhance the signal to noise ratio (S/N), self-calibration was applied on the continuum. A Briggs robust parameter of 0.5 was applied for the imaging of the self-calibration process, and we applied four phase and one amplitude calibrations, using the whole integration time as the solution interval for the amplitude calibration and first phase calibration, while for the remaining phase calibrations, we used 360 s, 150 s, and 60 s.

After self-calibration was complete, I explored different alternative values for the robust parameter to image the data using the `CLEAN` algorithm. For the `multiscale` parameter, I used ( $0\times$ ,  $0.2\times$ ,  $0.5\times$ ,  $1\times$ ) the beam size, which, in combination with a `smallscalebias` of 0.45, returns a smoother model for the emission. This value for `smallscalebias` is smaller than the default

0.6, which leads to the algorithm preferring the extended scales before point sources. To avoid introducing PSF artifacts that could be mistaken for faint emission, we lowered the `gain` parameter to 0.05 (it controls the fraction of the flux that is cleaned in every iteration), and increased the `cyclofactor` to 1.5 (it controls the frequency with which major clean cycles are triggered), both of them chosen for a more conservative imaging compared to the default values. We cleaned down to a  $4\sigma$  threshold, and applied the *JvM correction* to our images, which accounts for the volume ratio  $\epsilon$  between the point spread function (PSF) of the images and the restored Gaussian of the CLEAN beam, as described in [Jorsater & van Moorsel \(1995\)](#) and [Czekala et al. \(2021\)](#).

The calibration tables obtained from the dust continuum self-calibration were applied to the molecular line emission channels, and then the continuum emission was subtracted from them with the `uvcontsub` task. To increase the S/N of the images, we imaged the  $^{12}\text{CO}$  channels with a lowered velocity resolution of  $0.25 \text{ km s}^{-1}$ , centered at  $3.65 \text{ km s}^{-1}$ , which is approximately the velocity at the local standard of rest (VLSR). Different robust parameters ranging from -1.2 to 1.2 were explored to find the best trade-off between angular resolution and sensitivity. Additionally, we also applied visibility tapering

The JvM correction was also applied to the CO channel maps before any analysis was carried out on them. The package `bettermoments` ([Teague & Foreman-Mackey, 2018b](#)) was used to create additional image products from the channel maps. This package fits a quadratic function to find the peak intensity of the line emission in each pixel, and the velocity associated with it, but I also used it to generate the moment 0 and moment 1 of each velocity cube. All the moment images were clipped at 3 sigma and no mask was used.

To accurately analyze the observations, we also applied parametric visibility modeling to the continuum visibilities of the source, as described in Section 4.4.3. To further reduce the data volume after finishing the self-calibration, we averaged the continuum emission into 1 channel per spectral window (as in [Andrews et al., 2021](#)) and 30 s of time binning. We used each binned channel central frequency to convert the visibility coordinates into wavelength units.

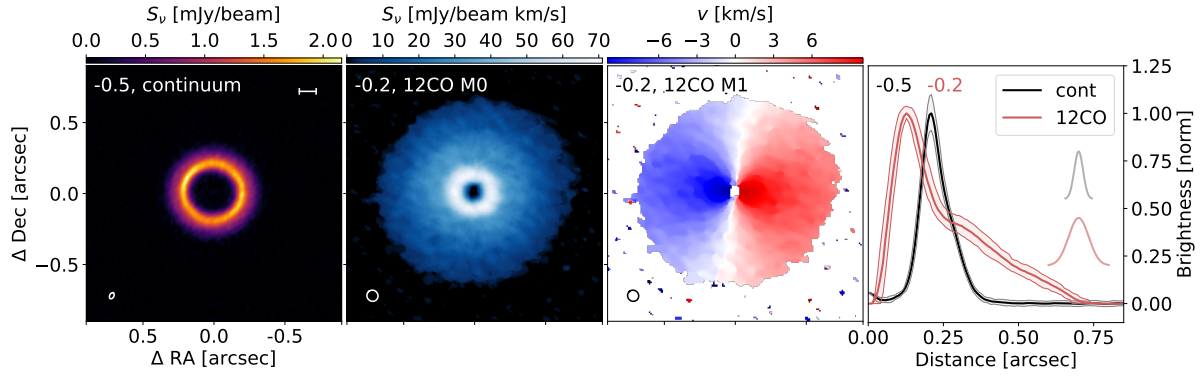


**Figure 4.2:** Reconstructed images of CS Cha dust continuum emission and  $^{12}\text{CO}$ .

From left to right: Dust continuum emission from CS Cha imaged with a robust parameter of -0.5, moment 0 and moment 1 of the  $^{12}\text{CO}$  imaged with a robust of -0.2, and radial profiles for the continuum and  $^{12}\text{CO}$  emission calculated by deprojecting the images with the inclination and position angle of Model 2e (see Section 4.4.3). The ellipse in the left bottom corner of the panels represents the synthesized beam of the images, which is  $30 \times 46$  mas for the dust continuum and  $80 \times 77$  mas for the  $^{12}\text{CO}$ . The scale bar in the top right of the first panel represents 20 au at the distance of the source. The Gaussians in the right panel represent the average radial resolution of the profiles, and in the same panel, the colored region in the profiles represent the  $1\sigma$  dispersion at each radial location.

## 4.4 Observational results

### 4.4.1 Circumbinary disk: Dust continuum emission physical properties

The millimeter emission is resolved into a single disk around the binary stars (a circumbinary disk), as shown in Fig. 4.2 after being imaged with a robust parameter of -0.5, returning an angular resolution of  $30 \times 46$  mas. At a nominal resolution ( $61 \times 87$  mas with a robust parameter of 0.5), the disk appears as a single smooth ring with a central cavity, however, higher angular resolution images resolve the disk radial structure, showing evidence of a radially asymmetric ring (right panel of Fig. 4.2). A gallery with the dust continuum emission reconstructed with different robust parameters ranging from -1 to 1 was shown previously in Figure 2.5. For continuum images with robust parameters larger than 1, the sensitivity changes are negligible, as the beam size increases to an extent less than 10% and the point spread function is poorer due to the sparser visibility coverage at short baselines compared to long baselines, resulting in stronger sidelobes and, thus, stronger structured residuals.

The radial profiles were obtained by deprojecting the images with the geometry parameters obtained in Sect. 4.4.3 (inc=17.86 deg and PA=82.6 deg,

see Tab. 4.1), where we considered multiple Gaussian components and eccentricities to describe the circumbinary disk. We find that the dust continuum ring profile peaks at  $205 \pm 5$  mas from the disk center, which is  $34.6 \pm 0.8$  au at the distance of the source. Since it was calculated from the image, we used 5 mas as a conservative uncertainty (the pixel size), which is consistent with the previous study by [Norfolk et al. \(2021\)](#).

In order to estimate the optical depth  $\tau$  of the emission, we followed the same approach as in [Pinilla et al. \(2021\)](#), assuming that the disk emits as a black body and therefore  $\tau = -\ln(1 - T_B/T_{\text{phys}})$ , where  $T_B$  is the brightness temperature, and  $T_{\text{phys}}$  is the physical temperature of the midplane. We estimated the  $T_B$  from the different dust continuum images by starting from the Rayleigh-Jeans approximation. When the beam size is increased (by using larger robust parameters), the emission becomes more diluted and, so, the peak temperatures decreases. For the image with a robust parameter of 0.5, the peak brightness temperature of the image reaches  $12.3 \pm 0.1$  K (brightness temperature uncertainty given with 3 sigma confidence), while for the image with robust value of -1.0, it reaches  $17.4 \pm 0.4$  K, since the ring is better resolved. For this reason, we decided to use the image generated with robust -0.5 to estimate the optical depth, given it has a high S/N and also high spatial resolution. From this image, we obtained a peak  $T_B$  of  $16.1 \pm 0.3$  K.

For the  $T_{\text{phys}}$ , we need additional assumptions. If we consider the midplane temperature to be at the standard 20 K, then we find a peak optical depth of  $\tau_{\text{peak}} = 1.34$ . On the other hand, if we consider the approximated luminosity-dependent temperature relation from [Andrews et al. \(2013\)](#),  $T = 25(L_{\star}/L_{\odot})^{0.25}$  K, and  $L_{\star} = 1.45 L_{\odot}$  for the stellar luminosity ([Manara et al., 2014](#)), then we can estimate  $T_{\text{phys}} = 27.4$  K and  $\tau_{\text{peak}} = 0.77$ . Both estimates should be considered with caution, as the first assumes a single constant temperature and the latter comes from a luminosity relation for disks with a single stellar host.

We calculated the dust mass of the model by assuming that the flux ( $F_{\nu}$ ) received has a wavelength of 0.87 mm and is being emitted by optically thin dust with a constant temperature of 20 K (as in [Ansdell et al., 2016](#); [Pinilla et al., 2018b](#)), and, alternatively, with a constant temperature of 27.4 K. In both approaches we follow [Hildebrand \(1983\)](#):

$$M_{\text{dust}} = \frac{d^2 F_{\nu}}{\kappa_{\nu} B_{\nu}(T(r))}, \quad (4.1)$$

where  $d$  is the distance to the source,  $\nu$  is the observed frequency,  $B_\nu$  is the Planck function at the frequency  $\nu$ , and  $\kappa_\nu = 2.3(\nu/230\text{ GHz})^{0.4}\text{ cm}^2\text{ g}^{-1}$  is the frequency-dependent mass absorption coefficient (as in [Andrews et al., 2013](#)). The total flux from the source is estimated by taking the weighted average of the baselines shorter than  $28\text{ k}\lambda$ , which gives  $F_\nu = 180.2 \pm 0.5\text{ mJy}$ , not accounting for the 10% uncertainty of ALMA fluxes. We chose to measure it from the visibilities that do not resolve the disk emission to avoid introducing additional uncertainties related to image reconstruction and possible dependence on the mask chosen. Replacing this value in Eq. 4.1, we obtain a dust mass of  $69.0 \pm 0.1 M_\oplus$  when assuming  $T_{phys} = 20\text{ K}$ , and  $44.7 \pm 0.1 M_\oplus$  for  $T_{phys} = 27.4\text{ K}$ . Therefore, the dust mass content is uncertain either because of the temperature assumption and the poor constraints that we have on the dust opacities from the observations.

#### 4.4.2 No detection of emission near CSCha B

We did not detect any significant emitting source at the expected location of CS Cha B, neither in dust continuum emission nor  $^{12}\text{CO}$ , as shown in the upper and lower panels of Fig. 4.3, respectively, where the emission has been saturated to  $5\sigma$  of each image. In the dust continuum, by using our highest sensitivity image (generated with a robust parameter of 1.0) and based on the assumption that CS Cha B is a point source, we can estimate a  $3\sigma$  upper limit for millimeter emission to be  $35.4\mu\text{Jy}$ . This emission translates into a dust mass upper limit of  $M_B < 0.015 M_\oplus$  under the assumption of 20 K and optically thin emission. Even if the disk is not a compact source, the beam size of the robust 1.0 image is  $\approx 18 \times 13\text{ au}$  at the distance of the source, therefore, the dust disk would have been unresolved even if it had a size of 10 au.

In  $^{12}\text{CO}$ , we do not detect any significant emission at the location of CS Cha B either, and this non-detection is independent from the channel map velocity width and synthesized beam size used for image reconstruction. As a final test for the detection of CS Cha B, we generated a cube with a robust parameter of 1.2, no visibility tapering, and a channel width of  $1\text{ km s}^{-1}$ , going from  $-24$  to  $24\text{ km s}^{-1}$  around the rest frame of the  $^{12}\text{CO}$  line. These channels were all stacked and the result is displayed in the lower panel of Fig. 4.3. The peak emission within the square mask does not reach a significance of  $2\sigma$ .

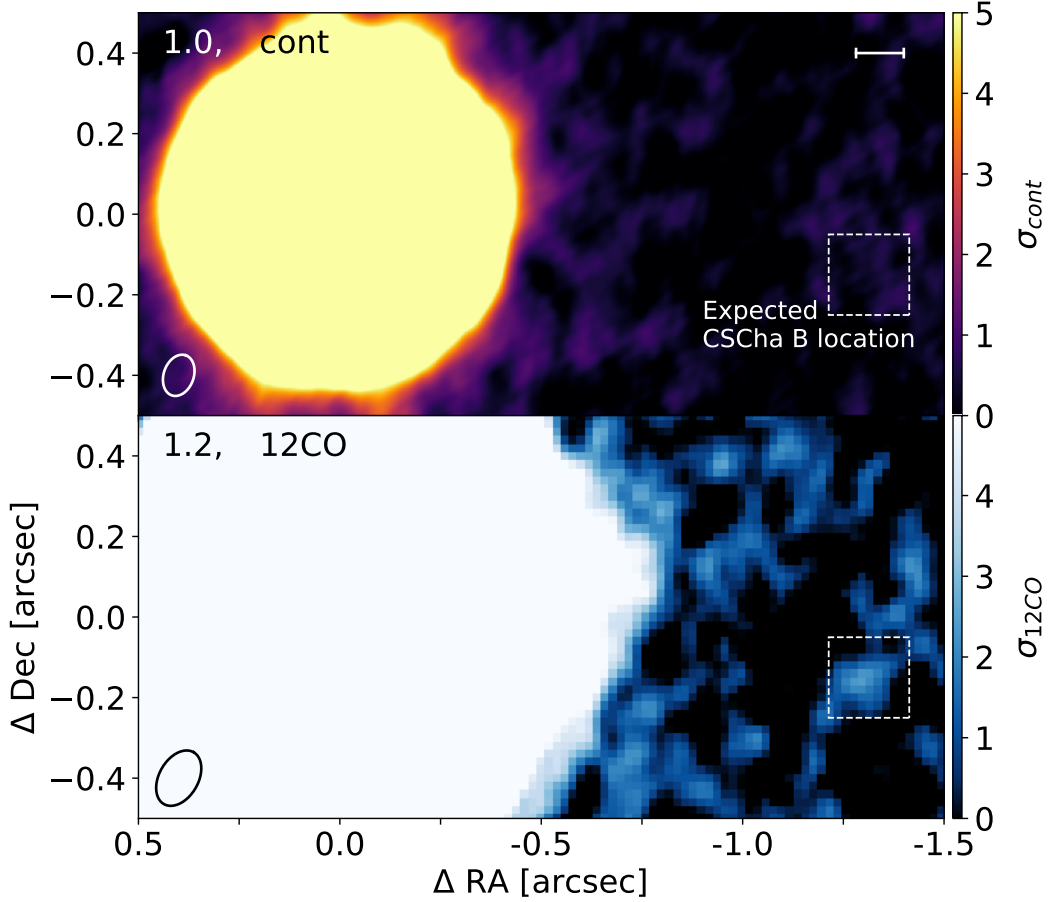


**Figure 4.3:** The non-detection of CS Cha B in the high-sensitivity millimeter emission images of CS Cha.

**Upper panel:** Dust continuum image generated with a robust parameter of 1.0. The color scale is linear and has been saturated to show the emission between 0 and  $5\sigma_{\text{cont}}$ , with  $\sigma_{\text{cont}} = 11.8 \mu\text{Jy}/\text{beam}$  being the rms of this image. A box of  $0.2''$  per side is centered at the expected location of CS Cha B. The beam size is  $105 \times 75 \text{ mas}$ , and is shown in the lower left corner of the figure. The scale bar at the top right represents 20 au. **Lower panel:**  $^{12}\text{CO}$  emission image generated with a robust parameter of 1.2, after stacking all the channel maps between  $-24$  and  $24 \text{ km s}^{-1}$  around the rest frame. The beam size is  $148 \times 97 \text{ mas}$ , and is shown in the lower left corner of the figure. The color scale is linear and has been saturated to show the emission between 0 and  $5\sigma_{12\text{CO}}$ , with  $\sigma_{12\text{CO}} = 1.4 \text{ mJy}/\text{beam}$  being the rms of this image.

#### 4.4.3 Dust morphology from the visibility fitting

To precisely constrain the structure of the dust continuum emission, we applied parametric visibility modeling to the visibilities of the source. In principle, the brightness profile ( $I_r$ ) of an axisymmetric disk would only depend on the radial distance to the center of the disk (given by  $I_r := I_r(r)$ ). However, circumbinary disks are expected to display some eccentricity due to the interaction between the disk material and the binaries (e.g., [Thun et al., 2017](#);

Kley et al., 2019), and so, it is convenient to define the brightness profile not as a function of the radius, but as a function of the semi-major axis instead ( $I_r := I_r(a)$ ). We calculated the eccentric coordinate system by following the same approach that Marino et al. (2019) and Booth et al. (2021):

$$a(r, \phi) = r \frac{1 - e \cos(\phi - \omega)}{1 - e^2}, \quad (4.2)$$

where the semi-major axis  $a$  is a function of the radial distance from the center of mass and the azimuthal angle  $(r, \phi)$ , and it can also be modified by the eccentricity,  $e$ , and the argument of the periastron  $\omega$ . It is pertinent to notice that this coordinate system does allow for the solution  $e = 0.0$ , which returns the standard polar coordinates.

Several models with increasing complexity have been considered to describe the disk around CS Cha, which are composed of a combination of Gaussians shapes by  $I_r = \sum_i g_i$ , where  $g_i$  is the  $i$ th Gaussian. Each subsequent model is motivated by the residuals of the best previous model, but they all share the same basic shape for the disk, described by a bright Gaussian ring ( $g_0$ ) for the inner side of the ring emission, plus a radially asymmetric Gaussian ring ( $g_1$ ) to describe the outer side of the ring emission. This  $g_1$  component has a different width for each side of its peak, also known as broken-Gaussian ( $(\sigma_i, \sigma_o)$  for the inner and outer part, respectively), which was introduced to model the emission of the very low mass stars in Chapter 2. The additional features considered in the more complex models were a centrally peaked Gaussian ( $g_2$ ) and an extended Gaussian ring ( $g_3$ ). All these components are schematized in Figure 4.11 in the additional content section. The components considered in each model are:

1. Model 2g, composed of  $g_0 + g_1$  with eccentricity and argument of the periastron of  $(e_0, \omega_0)$ ;
2. Model 3g, composed of  $g_0 + g_1 + g_2$  with  $(e_0, \omega_0)$ ;
3. Model 4g, composed of  $g_0 + g_1 + g_2 + g_3$  with  $(e_0, \omega_0)$ ;
4. Model 2e, composed of  $g_0 + g_2$  with  $(e_0, \omega_0)$ , and  $g_1 + g_3$  with  $(e_1, \omega_1)$ .

Component		Model 2g	Model 3g	Model 4g	<b>Model 2e</b>	Units
geometry	$\delta_{\text{RA}}$	$-13.17^{+0.04}_{-0.06}$	$-13.28^{+0.09}_{-0.01}$	$-13.18^{+0.06}_{-0.04}$	$-13.16^{+0.08}_{-0.03}$	mas
	$\delta_{\text{Dec}}$	$2.28^{+0.03}_{-0.08}$	$2.07^{+0.01}_{-0.04}$	$2.35^{+0.06}_{-0.05}$	$1.37^{+0.08}_{-0.03}$	mas
	inc	$17.78^{+0.01}_{-0.05}$	$17.95^{+0.01}_{-0.04}$	$17.79^{+0.02}_{-0.03}$	$17.86^{+0.05}_{-0.01}$	deg
	PA	82.6 fixed	82.6 fixed	82.6 fixed	82.6 fixed	deg
eccentricity	$e_0$	$0.023^{+0.001}_{-0.001}$	$0.024^{+0.001}_{-0.001}$	$0.023^{+0.001}_{-0.001}$	$0.039^{+0.001}_{-0.001}$	-
	$\omega_0$	$-5.11^{+0.35}_{-0.55}$	$-5.65^{+0.78}_{-0.12}$	$-5.48^{+0.46}_{-0.43}$	$-1.02^{+0.47}_{-0.28}$	deg
	$e_1$				$0.019^{+0.001}_{-0.001}$	-
	$\omega_1$				$-8.42^{+0.91}_{-0.27}$	deg
$g_0$	$f_0$	$23.05^{+0.02}_{-0.16}$	$24.99^{+0.14}_{-0.03}$	$25.15^{+0.05}_{-0.11}$	$24.61^{+0.09}_{-0.12}$	( $\mu\text{Jy}/\text{pix}$ )
	$r_0$	$203.3^{+0.1}_{-0.1}$	$203.0^{+0.1}_{-0.1}$	$203.7^{+0.1}_{-0.1}$	$202.7^{+0.1}_{-0.1}$	mas
	$\sigma_0$	$16.6^{+0.1}_{-0.3}$	$20.3^{+0.3}_{-0.1}$	$20.0^{+0.1}_{-0.1}$	$18.8^{+0.2}_{-0.1}$	mas
$g_1$	$f_1$	$16.72^{+0.20}_{-0.04}$	$14.46^{+0.02}_{-0.19}$	$14.31^{+0.11}_{-0.07}$	$15.21^{+0.10}_{-0.14}$	( $\mu\text{Jy}/\text{pix}$ )
	$r_1$	$238.7^{+0.3}_{-1.3}$	$255.4^{+0.1}_{-0.1}$	$257.4^{+0.5}_{-0.8}$	$251.1^{+0.9}_{-0.7}$	mas
	$\sigma_{1i}$	$56.8^{+0.2}_{-0.8}$	$58.6^{+0.7}_{-0.1}$	$63.0^{+0.4}_{-0.5}$	$58.8^{+0.5}_{-0.4}$	mas
	$\sigma_{1o}$	$55.9^{+0.4}_{-0.1}$	$46.3^{+0.1}_{-0.5}$	$44.9^{+0.4}_{-0.3}$	$47.8^{+0.4}_{-0.4}$	mas
$g_2$	$f_2$		$0.59^{+0.01}_{-0.01}$	$2.81^{+2.18}_{-0.31}$	$6.10^{+0.03}_{-3.33}$	( $\mu\text{Jy}/\text{pix}$ )
	$\sigma_2$		$262.4^{+2.2}_{-1.2}$	$12.3^{+1.8}_{-4.7}$	$10.2^{+5.5}_{-0.4}$	mas
$g_3$	$f_3$			$0.37^{+0.02}_{-0.02}$	$0.37^{+0.02}_{-0.02}$	( $\mu\text{Jy}/\text{pix}$ )
	$r_3$			$214.2^{+14.9}_{-11.8}$	$161.5^{+16.7}_{-11.1}$	mas
	$\sigma_3$			$179.2^{+5.2}_{-5.9}$	$206.3^{+5.4}_{-8.1}$	mas
	$F_\lambda$	$178.82 \pm 0.02$	$180.70 \pm 0.04$	$180.49 \pm 0.04$	$180.57 \pm 0.05$	mJy

**Table 4.1:** Best parameters from the parametric visibility modeling of CS Cha dust continuum emission. “mas” stands for milliarcsecond.

The CS Cha disk is close to being face-on (as seen in Fig. 4.2) and so, the dust continuum modeling has a strong dependence between the center of the disk ( $x_0, y_0$ ), the inclination ( $\text{inc}$ ), the position angle (PA), and the eccentricity parameters ( $e, \omega$ ). To reduce the number of free parameters, I used the  $^{12}\text{CO}$  observations (which are independent from the dust continuum observations) to constrain the PA of the disk. As explained in Section 4.4.4, the preliminary kinematic fittings to the  $^{12}\text{CO}$  show that it has a position angle of 82.6 deg, and so the value is fixed in the visibility modeling.

To find the best set of parameters for each different model, I used the package `emcee` to sample the parameter space with a Markov chain Monte Carlo (MCMC) Ensemble Sampler (Foreman-Mackey et al., 2013b), using 250 walkers and a flat prior for all the parameters. The visibilities of the model images were computed with `galarío`, and these images were generated with a pixel size of 5 mas, as the images from `tclean`. The total flux of the model is calculated by averaging the real part of the ten shortest baselines (u-v pairs) after convergence, and we picked 5000 MCMC random walkers positions to calculate the uncertainty of the flux.

The best parameters for each model and their uncertainties are summarized in Table 4.1. All the models show consistent results for the disk flux ( $F_\lambda$ ), the location of the radius that includes the 68% and 90% of the flux ( $R_{68}$  and  $R_{90}$ ), and the location of the peak of the ring (given by the parameter  $r_0$ ). The difference between the models can be better observed when the residuals are imaged, as seen in Fig. 4.4 for the Model 2e, and in the Fig. 4.13 for the Models 2g, 3g, and 4g, in the appendix. The simplest model, Model 2g, shows strong structured residuals in the ring region, and also in the cavity, evidence that the cavity is not completely depleted of dust continuum emission. Then, Model 3g takes into account this inner cavity emission with a Gaussian that peaks at the center of the disk ( $g_2$ ), however, this Gaussian is spread over the whole disk in the attempt to account for an extended diffuse emission, rather than only fitting the cavity emission. To fix this behavior, Model 4g includes a new diffuse extended Gaussian for the ring ( $g_3$ ) in addition to the Gaussian for the inner cavity emission ( $g_2$ ). It ultimately succeeds at describing the cavity emission, but still leaves structured residuals in the circumbinary ring.

The residuals from the Model 4g subtracted too much flux from some regions (seen in blue in the residual image), and not enough from others (seen in red in the residual image). The structure of these residuals cannot be explained by any combination of offsets in center ( $\delta_{\text{RA}}, \delta_{\text{Dec}}$ ), nor geometry ( $\text{inc}$ ,

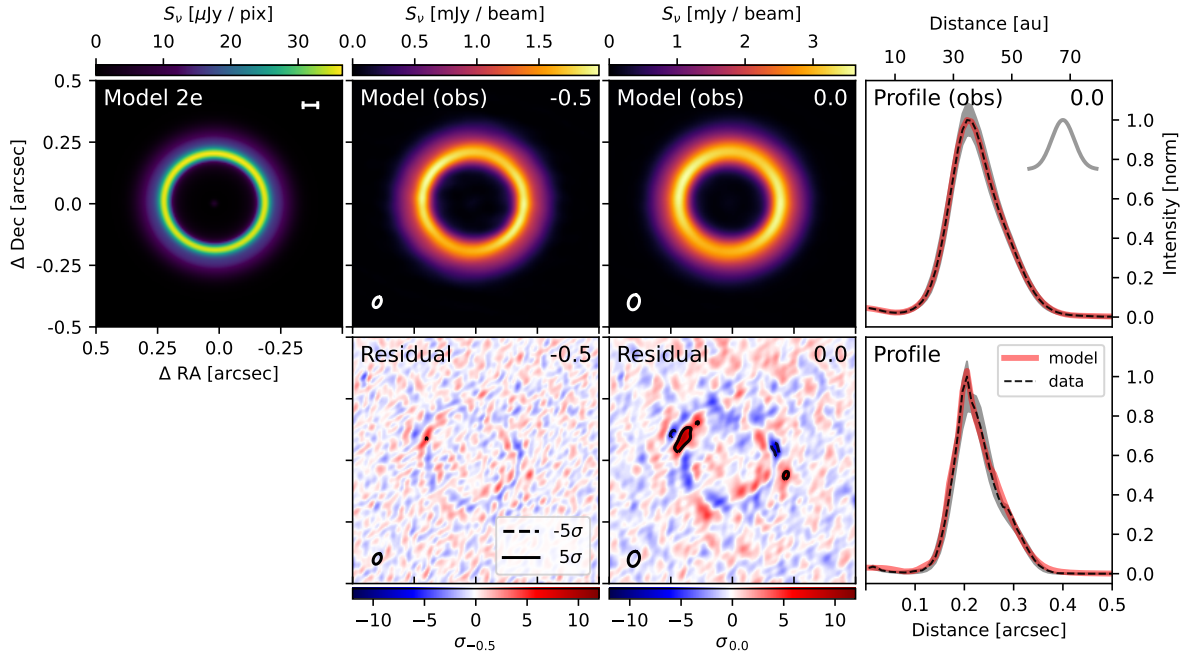


**Figure 4.4:** Best solution for the dust continuum emission generated using the Model 2e, which considers two eccentricities for the disk components.

**Upper row:** Left panel shows the synthetic image of the best model found. Middle panels show how this model would have been observed by ALMA with two different robust parameters, comparable to the images from Fig. 2.5. Right panel shows the radial profile obtained from the beam convolved images generated with a robust parameter of 0.0, and the average beam resolution shown with a Gaussian in gray. **Lower row:** Middle panels show the residuals left by the best model, imaged with two different robust parameters shown in the upper left corner. Right panel shows the intensity profile of the model obtained from `tclean` and the best Model 2e (not convolved by beam).

PA), which is discussed in depth in the Appendix of Andrews et al. (2021). To account for the residuals of Model 4g, two additional models were considered: i) a model where the innermost emission has a different inclination compared to the outer most regions ( $g_0+g_2$  have a inclination  $inc_0$ , while  $g_1+g_3$  have another  $inc_1$ ), but they share the same eccentricity; and ii) a model where those components have the same inclination, but different eccentricities. The model with different inclinations returned residuals that were similar to the ones from Model 4g, and the inclinations ( $inc_0, inc_1$ ) were not disparate from the noise level. On the other hand, the model with two eccentricities (Model 2e) was successful in accounting for the structured residuals observed in the circumbinary ring, as seen in Fig. 4.4.

The best model, Model 2e, found two different eccentricities for the inner most emission and the outermost emission from the circumbinary disk, with

the inner ring eccentricity ( $e_0 = 0.39$ ) being about twice that of the outer disk eccentricity ( $e_1 = 0.19$ ), as shown in Table 4.1. We calculated the mass of the dust in the model by following the same assumptions we took in the dust continuum images: optically thin emission and 0.87 mm, with dust at 20 K. The flux from all components of Model 2e adds up to  $180.57 \pm 0.05$  mJy, which translates into a dust mass of  $69.05 \pm 0.02 M_{\oplus}$  at the distance of this source (not considering the 10% uncertainty of ALMA fluxes). As for central Gaussian,  $g_2$ , alone in the Model 2e, we find a flux of  $150 \pm 16 \mu\text{Jy}$ , or a dust mass of  $0.057 \pm 0.006 M_{\oplus}$  being detected inside the cavity. This dust mass is  $\approx 0.5 M_{\text{Mars}}$ , or  $\approx 5 M_{\text{Moon}}$ , for reference.

#### 4.4.4 The $^{12}\text{CO}$ molecular line emission

##### Emission profile of the $^{12}\text{CO}$ emission

We generated images for the  $^{12}\text{CO}$  emission from CS Cha with different robust parameters to check the emission at a high angular resolution, but also to check the extended structure with high S/N. The channel maps were all generated with the same velocity channels, and their only difference is the robust parameter used. A gallery of the channels generated with robust 0.0 is shown in the appendix (Fig. 4.12).

The  $^{12}\text{CO}$  emission (shown in Figs. 4.2 and 4.5) appears depleted in the central region of the cavity, and the brightness peak is located at 128 mas (or 21.6 au), which is closer to the center of the disk compared to the dust continuum radial profile, which peaks at 34.6 au. The profile recovered from the different moment 0 images consistently show the brightness peak at the same radial location. By using the inclination from the continuum fit, plus the vertical structure and PA traced by a kinematic fit with the `eddy` package (Teague, 2019) (as described in the following Section 4.4.4, and summarized in Table 4.2), we deprojected the  $^{12}\text{CO}$  Moment 0 image and used it to calculate an azimuthally averaged surface brightness profile (shown in Fig. 4.5).

We subtracted the azimuthally averaged surface profile from the  $^{12}\text{CO}$  moment 0, to search for asymmetries. The moment 0 is preferred over the peak intensity map as the later is more affected by the beam size and geometry of the disk, thus creating overbrightness regions along the major axis which are not of physical origin. When an azimuthally symmetric model is subtracted from the moment 0, the disk shows residuals on extended and compact scales, with a typical contrast between the emission and model on the order of  $< 15\%$ .

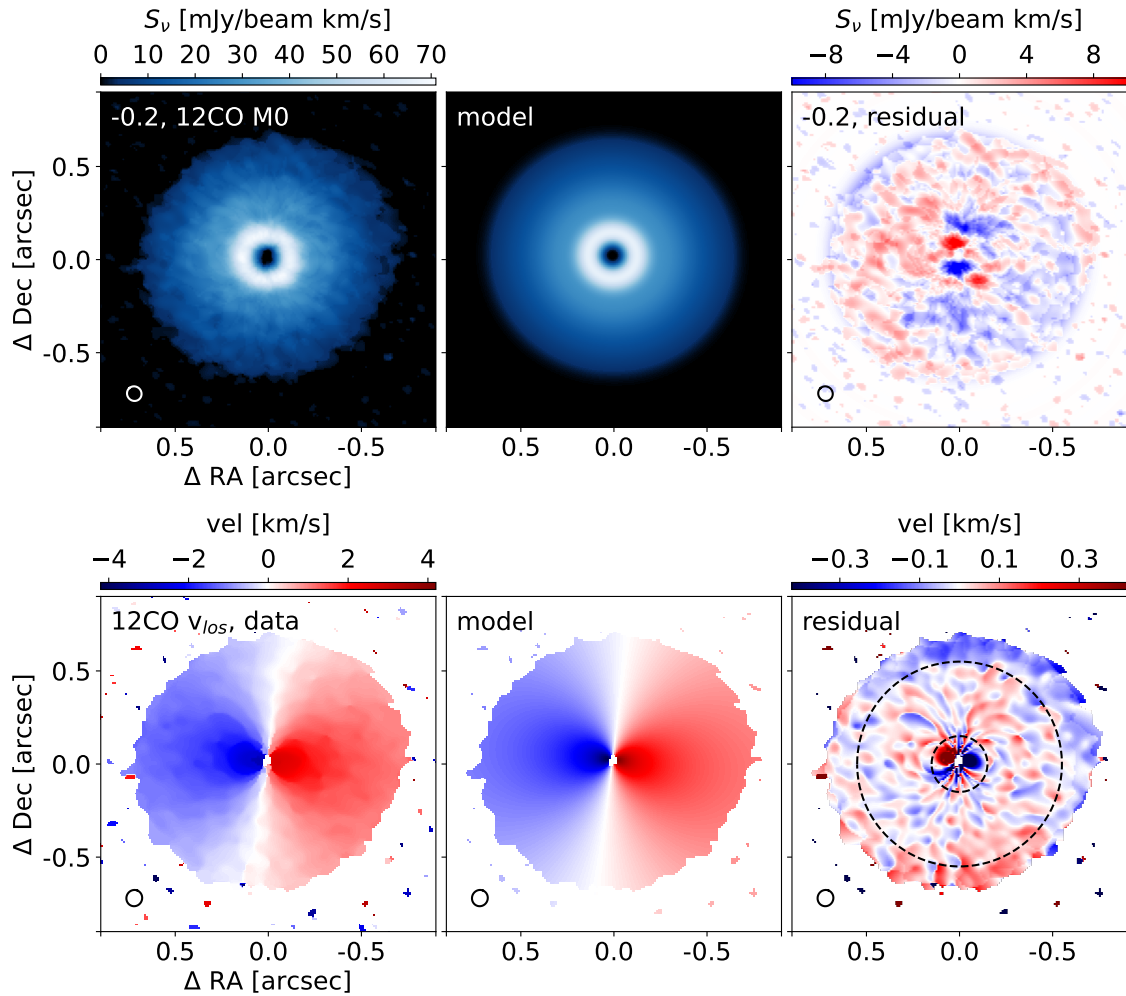


**Figure 4.5:** CS Cha gas emission and kinematics.

**Upper row:**  $^{12}\text{CO}$  moment 0, the best model using the geometry recovered from the kinematic fit, and the residuals. Scale bar represents 20 au at the distance of the source. **Lower row:**  $^{12}\text{CO}$  peak velocity in the line of sight, with the best model calculated with the parameters from Table 4.2, and the residuals. The dashed line shows the mask used for the fit.

The brightness temperature of the  $^{12}\text{CO}$  moment 0 reaches about 120 K at the radial profile peak and decreases towards about 10 K in the outer edge. Due to this temperature range, the emission is possibly more optically thick in some regions than in others and, thus, its brightness traces a combination of temperature and gas density variations at the disk surface layers. These residuals may originate from a combination of small-scale height variations, disk eccentricity and dynamical perturbations, and none are included in the azimuthally averaged surface profile.

### Kinematics of the $^{12}\text{CO}$ emission

We calculated the velocity map of the  $^{12}\text{CO}$  by using the package `bettermoments`, which fits a quadratic function to each pixel over the channel maps cube, allowing us to obtain the velocity corresponding to the peak emission with sub-channel velocity resolution. The velocity map used in the kinematic analysis is shown in Figs. 4.2 and 4.5. Additionally, a careful analysis of the channel maps in Fig. 4.12 allows us to confirm that the southern side of the disk is closer towards us, and so the disk is rotating counter-clockwise from the observers' point of view. This coincides with the projected direction of the proposed orbits for CS Cha B (Ginski et al., 2018), however, its orbital plane has not been accurately constrained and it might not necessarily be coplanar to CS Cha.

As discussed in the Section 4.4.3, with the disk being so close to face-on, there are correlations that are difficult to disentangle without fixing some geometric parameters. In the case of the  $^{12}\text{CO}$  kinematic image, there is a strong correlation between the total mass of the central stars  $M_{\text{total}}$ , the inclination of the disk ( $\text{inc}$ ), and the surface layer geometry from where the  $^{12}\text{CO}$  is being detected, which we describe as a function of the radius from the center of the disk ( $h_{\text{CO}}(r)$ ). Due to the low inclination of the disk, a variable that is mostly independent from the previous unknown parameters is the PA of the disk, and so it is the first value that we constrain.

We used the `eddy` package to fit the  $^{12}\text{CO}$  kinematic map under the assumption of flat disk, to avoid introducing additional free parameters while the inclination and  $M_{\text{total}}$  are still not constrained. We run a MCMC with uniform prior over the six free parameters that include the center of the disk ( $x_0, y_0$ ), the disk geometry ( $\text{inc}$ , PA), the binaries mass ( $M_{\text{total}}$ ), and velocity at the local standard of reference (VLSR), and we recovered a value of  $\text{PA} = 262.6 \pm 0.1$  deg, which is consistent for kinematic maps generated from different robust parameters. This value is higher than 180 deg since the convention used in this kinematic fitting is that the PA is aligned with the red-shifted part of the disk. If we follow the dust continuum emission convention of measuring the PA as the angle between the north and the semi-major axis to the east, we obtain  $\text{PA} = 82.6$  deg (this includes an assumption of a flat dust continuum disk). This value is used in the visibility modeling of the dust continuum (shown in Section 4.4.3), from where we find an inclination of the midplane of  $\text{inc} = 17.86$  deg, which we assume to be the inclination for

the  $^{12}\text{CO}$  emission.

By having the inclination fixed, the degeneracy of the value for  $M_{\text{total}}$  is reduced, enabling us to include as free parameters the description for the vertical height ( $z_{\text{CO}}(r)$ ) of the emitting surface layer. We perform this new fit under the assumption of a single power law, following  $z_{\text{CO}} = z_0 \cdot r^\psi$ , where the free parameters are the pair  $(z_0, \psi)$ , and it is only a function of the distance to the disk center  $r$ . The Keplerian velocity is calculated by including the scale of the height  $^{12}\text{CO}$  in the distance to the center of the disk, based on the following:

$$v_{\text{kep}}(r, z) = \sqrt{\frac{G M_{\text{total}} r^2}{(r^2 + z^2)^{3/2}}}. \quad (4.3)$$

The best parameters obtained after running a MCMC optimizer with the new model are listed in Table 4.2, where we recover the central mass of the stars:  $M_{\text{total}} \approx 1.91 M_{\odot}$ . The kinematic image of the best model, and the residuals, are shown in the bottom-middle and bottom-right panels of Fig. 4.5, respectively, where the mask used to fit the velocity map is shown: an annulus with inner radius of  $0.15''$  and outer radius of  $0.65''$ . Given that our model does not include eccentricity, the inclusion or exclusion of different regions of the disk can change the position of the centroid, which, in turn, also affects the best fit parameters. Depending on the masked region used to fit the velocity map, the mass of the central object can shift between  $1.86 - 1.91 M_{\odot}$ , due to changes in the position of the center. The non-eccentric kinematic model is also the reason for which the values of  $\delta_{\text{RA}}$  and  $\delta_{\text{Dec}}$  do not match between the dust continuum and  $^{12}\text{CO}$  fits.

In principle, the eccentricity is expected to decrease for regions that are located farther away from the binaries. Fitting those regions with a kinematic model should therefore lead to a better determination of the disk barycenter position. In CS Cha, however, there are two issues with including the outer-regions in the velocity fit: i) the S/N is decreased towards the outer edge of the disk, thus not allowing us to distinguish between the emission from the front-side and back-side of the disk; and ii) the line following the zeroth velocity at different radius (in our line of sight), known as the line of nodes, is curved in the outer regions of the disk (as can be better seen in the left panel of Fig. 4.5 and channel map 3.65 in Fig. 4.12). The mechanisms driving the velocity residuals inside and outside of the mask are still a subject to be

Parameter	Best fit	units
$\delta_{\text{RA}}$	$6.9 \pm 0.1$	mas
$\delta_{\text{Dec}}$	$28.8 \pm 0.4$	mas
inc	17.86 fixed	deg
PA	$263.1 \pm 0.2$	deg
$M_{\star}$	$1.911 \pm 0.002$	$M_{\odot}$
VLSR	$3670.1 \pm 0.4$	$\text{m s}^{-1}$
$z_0$	$0.024 \pm 0.002$	arcsec
$\psi$	$0.033 \pm 0.022$	-

**Table 4.2:** Best parameters from the kinematic fitting with `eddy` to the image generated with a robust parameter of 0.0

The vertical profile is calculated following  $z(r) = z_0 \cdot r^{\psi}$ .

studied. In the disk cavity, the residuals could be a combination of eccentric gas flow due to the binaries, and also radial flows of material flowing from the main ring towards the binaries, as described in [Rosenfeld et al. \(2014\)](#). As for the outer disk, the residual velocities could show a combination of eccentricity (which is not accounted in a circular model), and tidal influence from the companion CS Cha B. Such tidal interaction has been observed in other disks in multiple-stellar systems, such as AS 205 and RW Aur ([Kurtovic et al., 2018](#); [Rodriguez et al., 2018](#), respectively).

## 4.5 Hydrodynamical simulations

I compared the ALMA observations to hydrodynamical simulations of circumbinary disks, to test the general conditions that could generate the observable characteristics of CS Cha. The main focus was the comparison between the cavity and ring properties in circumbinary disks that do and those that do not host a single Saturn-like planet, as we describe in the following subsections.

### 4.5.1 Setup: Circumbinary disk with FARGO3D

I ran our simulations in a modified version of the FARGO3D code ([Benítez-Llambay & Masset, 2016](#)) used in [Thun & Kley \(2018\)](#) to simulate a 2D-hydrodynamical model of a circumbinary disk with the stellar properties of CS Cha. This version was handled to me by my coauthor in [Kurtovic et al. \(2022\)](#), Anna Penzlin. As in [Thun & Kley \(2018\)](#) and [Penzlin et al. \(2021\)](#),

I simulated the disk with a cylindrical grid, starting at an inner radius of  $1 a_{\text{bin}}$  up to  $40 a_{\text{bin}}$  (with  $a_{\text{bin}}$  the binary separation), with 684 logarithmically spaced radial cells and 1168 azimuthal cells, which is twice the azimuthal resolution used in the previously mentioned works. This higher resolution is applied to ensure convergence when the planet is included, and the results with half resolution are consistent with the ones shown in the following sections. The total binary mass was obtained from our eddy fit ( $M_{\text{total}} = 1.91 M_{\odot}$ ), and the mass ratio used for the binaries is  $q = 0.7$ , calculated in Ginski et al. (in prep.) by using the R-band and I-band magnitudes of SPHERE ZIMPOL observations (Beuzit et al., 2019; Schmid et al., 2018).

For the surface density, we used a radially dependent profile given by  $\Sigma(r) = f_{\text{gap}} \cdot \Sigma_0 \cdot r^{-3/2}$ , where  $r$  is the radial distance from the disk center,  $\Sigma_0$  is chosen such that the disk mass is  $0.01 M_{\text{total}}$ , and  $f_{\text{gap}}$  is an exponential function that depletes the density profile inside  $2.5 a_{\text{bin}}$ , therefore speeding up the number of orbits needed to reach the steady state. We calculate  $f_{\text{gap}}$  as in Thun et al. (2017), by using  $f_{\text{gap}} = (1 + \exp[-(r - 2.5 a_{\text{bin}})/(0.25 a_{\text{bin}})])^{-1}$ . All our simulations have fixed  $\alpha$  viscosity parameter of  $\alpha = 10^{-4}$  (Shakura & Sunyaev, 1973) for all radii.

Our simulations use a locally isothermal equation of state for the gas, which allows for a faster convergence compared to a viscous heated radiative disk. In the latter, the steady state of the gas is comparable to the isothermal setup for a constant disk aspect ratio  $h/r$ , but it can take over 100 000 orbits to be reached (Kley et al., 2019). We set our binaries such that they are only sensitive to each other (and not to the disk around them).

Due to the long period of their orbit (at least 2482 days, Guenther et al., 2007), the separation of the components and their eccentricity is only constrained to be within a certain parameter range ( $a_{\text{bin}} < 7.5 \text{ au}$  and  $e_{\text{bin}} \lesssim 0.5$ , Ginski et al. in prep.). Given that the simulations can be run with normalized units, the uncertainty in the binary separation can be circumvented by treating distances in terms of the binary separation, but to account for the possible binary eccentricities, we need to run simulations with different values. Therefore, we ran three different binary eccentricities setups:  $e_{\text{bin}} = [0.15, 0.25, 0.35]$ , and we let them evolve for 20 000 binary orbits to reach the steady state. As the circumbinary disks have minimal eccentricity for  $e_{\text{bin}} \approx 0.15$ , we sampled the allowed eccentricity range for  $e_{\text{bin}}$  with increasing eccentricities starting from the smallest (Thun & Kley, 2018; Kley et al., 2019). Additionally, previous works have shown that different aspect ratios

can have an impact in the disk gas morphology (Thun & Kley, 2018; Tiede et al., 2020; Penzlin et al., 2021); therefore, we ran each binary eccentricity with 2 aspect ratios:  $h/r = 0.03$  and  $h/r = 0.05$ .

After 20 000 orbits, we introduced a single planet at a distance of  $6 a_{\text{bin}}$  and we let it migrate inward to its equilibrium orbit. From Kley et al. (2019), we know that the planet ability to open a gap determines its evolution. Planets that are able to open a gap can separate the outer disk from the inner disk, effectively shielding the outer disk from the binaries action, lowering the eccentricity of these regions. Since we are running simulations in a low viscosity scenario, we decided to use a giant planet of low mass  $M_p = 1 M_{\text{Saturn}}$ , which is consistent with the planets detected in P-type orbits (Penzlin et al., 2021).

Previous studies have also found that more massive planets, such as  $1 M_{\text{Jup}}$ , are prone to more unstable orbits and have a higher likelihood of getting excited into a larger distance orbit or even of getting ejected from the system (Pierens & Nelson, 2008). After introducing the planet, we ran each simulation for another 100 000 binary orbits, which is 50 000 orbits after the convergence of five out of six of our migrating planets. For comparison, we also kept running the simulations without a planet for 100 000 additional binary orbits. This leaves us with 12 simulations when taking into account all binary eccentricities, disk aspect ratios, and planet presence. A summary of the setups is found in Table 4.3.

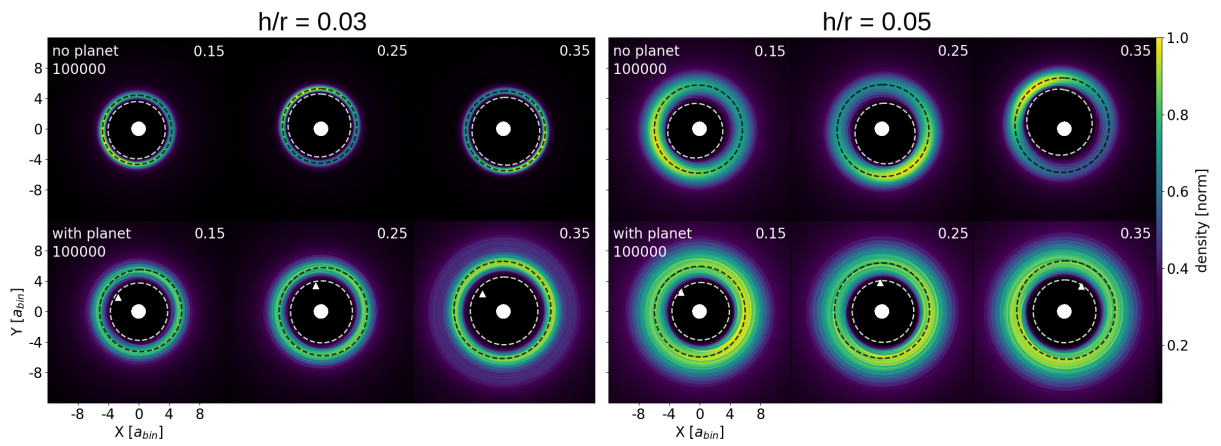


**Figure 4.6:** Gas surface density after 100 000 binary orbits for each simulation. Distance is in binary separations and the color scale is normalized to the maximum of each image. Panels on the left and right show the setups with  $h/r = 0.03$  and  $h/r = 0.05$  respectively. In each panel, the columns show the setups with the same binary eccentricity, being 0.15, 0.25, and 0.35 from left to right. The upper row of each panel contains the setups with no planet, and the lower row the setups with planet. A white dashed line shows the best cavity fit, while the black dashed line shows the best peak ring fit. A white triangle is used to show the position of the planet.

setup	$h/r = 0.03$						$h/r = 0.05$					
	no planet			with planet			no planet			with planet		
	0.15	0.25	0.35	0.15	0.25	0.35	0.15	0.25	0.35	0.15	0.25	0.35
$e_{\text{cav}}$	0.089	0.093	0.122	0.015	0.032	0.027	0.153	0.196	0.206	0.028	0.043	0.044
$a_{\text{cav}}$	3.87	4.25	4.59	3.79	4.09	4.47	3.76	4.13	4.52	3.72	3.90	3.99
$e_{\text{peak}}$	0.061	0.069	0.094	<b>0.049</b>	<b>0.046</b>	<b>0.034</b>	<b>0.028</b>	<b>0.056</b>	0.079	<b>0.049</b>	<b>0.045</b>	<b>0.037</b>
$a_{\text{peak}}$	4.55	4.91	5.24	5.39	5.78	6.39	5.79	6.05	6.22	6.06	6.27	6.57
$q_{\text{peak}}$	1.43	1.44	1.60	<b>1.16</b>	<b>1.16</b>	<b>1.10</b>	1.40	1.60	1.76	<b>1.11</b>	<b>1.18</b>	<b>1.17</b>
$e_{\text{pl}}$				0.019	0.020	0.024				0.016	0.017	0.020
$a_{\text{pl}}$				3.34	3.55	3.74				3.58	3.83	3.99

**Table 4.3:** Disk properties from the hydro-simulations.

Values shown are the eccentricity and semi-major axis of the cavity edge ( $e_{\text{cav}}$ ,  $a_{\text{cav}}$ ), peak density ( $e_{\text{peak}}$ ,  $a_{\text{peak}}$ ), and planetary orbit ( $e_{\text{pl}}$ ,  $a_{\text{pl}}$ ). Values were calculated by taking the median of the last 1000 binary orbits. The ratio between the brightest and dimmest part of the ring peak is shown as  $q_{\text{peak}}$ . The highlighted  $e_{\text{peak}}$  and  $q_{\text{peak}}$  are the values consistent with the observations, as described in Sect. 4.7.

### 4.5.2 Disk evolution with no planet

In the absence of a planet, the disk cavity quickly becomes eccentric, with the size of the cavity and its precession velocity being dependent on the eccentricity of the binaries ( $e_{\text{bin}}$ ) and the disk aspect ratio ( $h/r$ ). In order to measure the cavity properties, we trace the cavity boundary by searching for the radial position at which the density reaches 10% of the peak density, and we repeat for every azimuthal element of the gas density image, thus obtaining 1168 radial positions for each time step. This 10% threshold is chosen to avoid the streamers of material that flow from the circumbinary ring onto the binaries. We fit these points with an eccentric orbit by using the function `curve_fit` from the Python package `scipy.optimize` (Virtanen et al., 2020). The best fit allows us to recover the eccentricity of the cavity ( $e_{\text{cav}}$ ), the semi-major axis ( $a_{\text{cav}}$ ), and the argument of the periastron ( $\omega_{\text{cav}}$ ), which is used to trace the cavity precession.

We show the cavity boundary fit for the binary orbit 100 000 with a white dashed line in Fig. 4.6, and the median value of  $a_{\text{cav}}$  and  $e_{\text{cav}}$  the last 1000 binary orbits is shown in Table 4.3. Alternatively, another approach to recover the eccentricity information of the disk is through the eccentricity vector, which uses the kinematic information and returns the eccentricity of a gas parcel. We find consistent results between both methods (calculating from density compared to eccentricity vector), and we decided to go with the density-based estimation to be consistent with our visibility modeling approach to recover eccentricity.

As expected, the smallest  $e_{\text{cav}}$  and  $a_{\text{cav}}$  are obtained for the binaries with eccentricity of 0.15, which at the end of the simulation have a semi-major axis  $a_{\text{cav}} < 4a_{\text{bin}}$  in both aspect ratio setups. The biggest cavity sizes of all setups are found for the binaries with eccentricity of 0.35, with a final cavity size  $a_{\text{cav}} > 4.5a_{\text{bin}}$ . Overall, the difference between smallest and biggest cavities is only about 15%. We also find that neither  $e_{\text{cav}}$  nor  $a_{\text{cav}}$  are constant in time, as they have an oscillatory behavior with shorter period for smaller binary eccentricity, shown in Fig. 4.7. A quick analysis with a periodogram allowed us to find that the oscillations period in  $e_{\text{cav}}$  and  $a_{\text{cav}}$  are almost identical to the precession period of  $\omega_{\text{cav}}$ , which ranges between 1100 to 2300  $T_{\text{bin}}$  depending on the binary eccentricity and disk aspect ratio. Considering a binary period of 7 yr for CS Cha, a complete precession of the cavity would be observable over a period of at least 7700 yr, considering the shortest precession

#### 4 Planet formation in a circumbinary disk

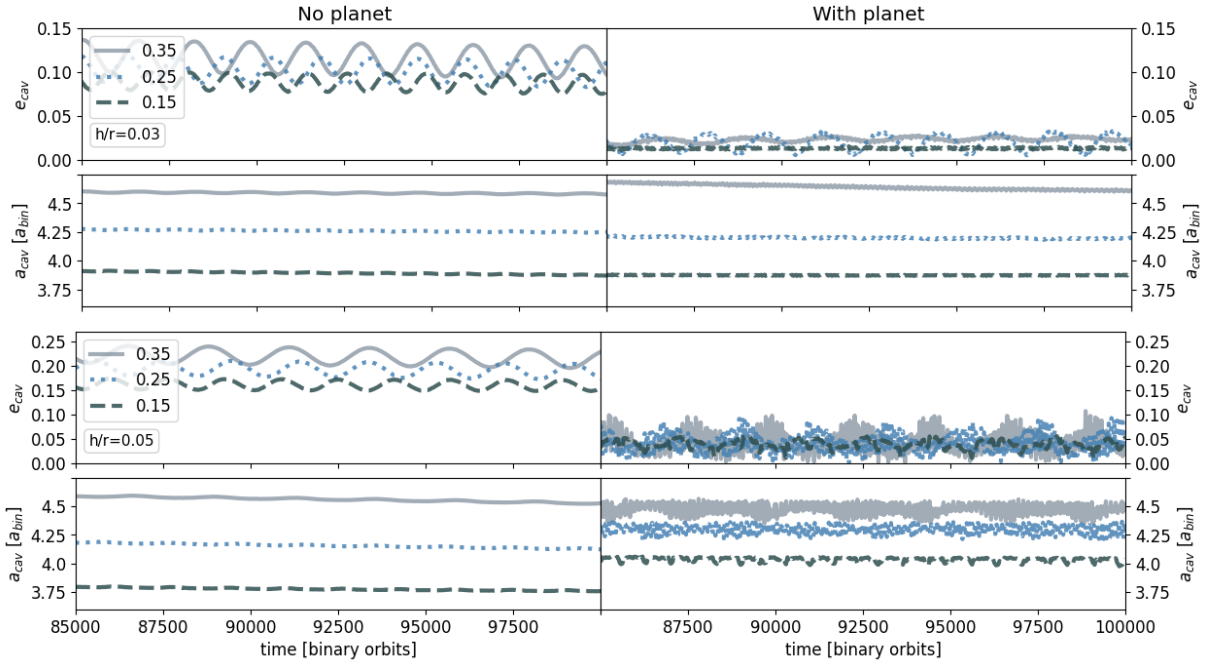


**Figure 4.7:** Eccentricity and semi-major axis for the cavity ( $e_{cav}, a_{cav}$ ) as a function of time in binary orbits.

Each panel contains the simulations of the 3 different  $e_{bin}$  for the binaries, and a single aspect ratio, displayed in the left-side together with the line-style legend.

period of our simulations.

We also traced the radial positions at which the gas density is highest for each azimuthal element (a peak gas density ring), and we fit an eccentric orbit in the same way it was done for the cavity, allowing the recovery of the eccentricity  $e_{peak}$ , semi-major axis  $a_{peak}$ , and argument of the periastron  $\omega_{peak}$ . The best fit to the peak positions is shown in Fig. 4.6 with black dashed lines for the binary orbit 100 000, and the median values for the last 1000 binary orbits for all setups is shown in Table 4.3. In the absence of a planet the values for  $e_{peak}$  can go from 0.03 to almost 0.1, while  $a_{peak}$  ranges between 4.6 and  $6.2 a_{bin}$ . Similar to the cavity, the peak density ring also shows an oscillatory behavior on its parameters, which is shown in Fig. 4.8 for the last 15 000 orbits (in reddish colors).

Another significant feature that can be drawn from the simulations is the azimuthal density variation along the density peaks, which can be better appreciated in Fig. 4.6. Due to the eccentricity of the disks, there is an overdensity at the location of the apoastron of the orbits, which is a product of the slower orbital velocities at that location compared to the periastron orbital velocity. We measure the contrast between the highest density and

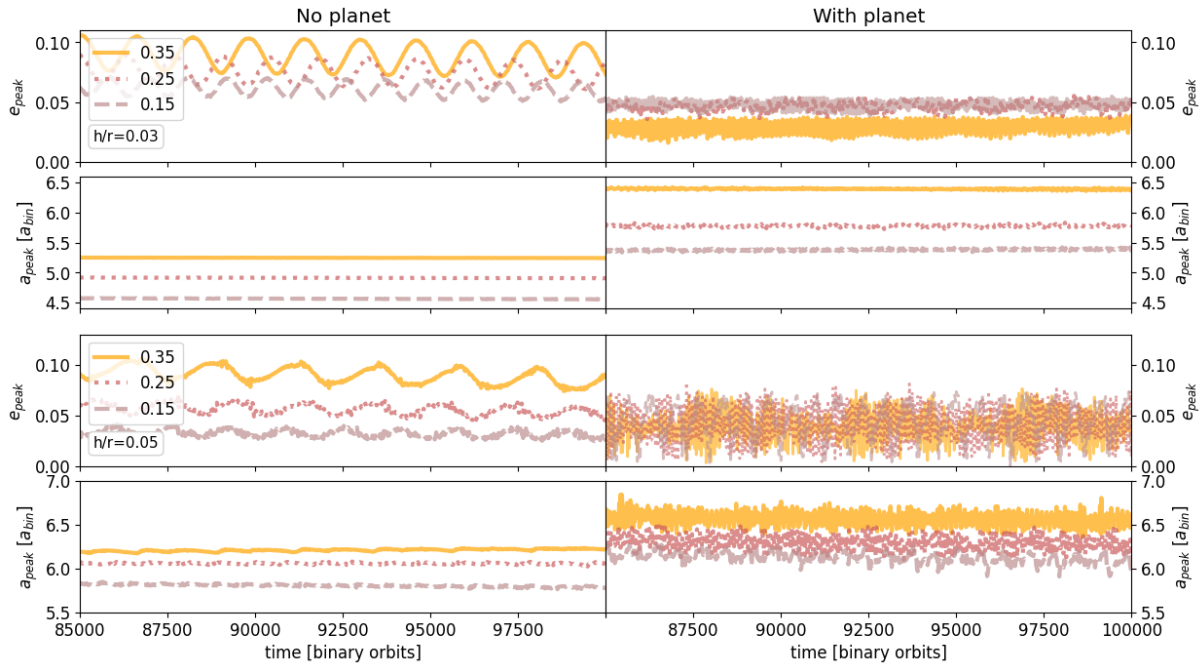


**Figure 4.8:** Eccentricity and semi-major axis for the peak density ring ( $e_{\text{peak}}, a_{\text{peak}}$ ) as a function of time in binary orbits.

Each panel contains the simulations of the three different  $e_{\text{bin}}$  values for the binaries and a single aspect ratio, displayed in the left-side together with the line-style legend.

lower density along the peak density ring by calculating  $q_{\text{peak}} = \rho_{\text{max}}/\rho_{\text{min}}$ , where  $\rho$  is the gas density. This value is reported in Table 4.3, and we find that the binaries with 0.15 of eccentricity have the least asymmetric rings for the no planet setups, with an excess of at least 40% between maximum and minimum density.

### 4.5.3 Disk evolution with a Saturn-like planet

The planet starts migrating inwards and carving a gap as soon as it is introduced into the simulation. The evolution of the planet's eccentricity and semi-major axis is shown in Fig. 4.9. Depending on the binary eccentricity, the planet takes different times to converge to its steady orbit, and the longest time for convergence is obtained for the planet around binaries of eccentricity  $e_{\text{bin}} = 0.15$ . After 50 000 binary orbits, the planet in most of the simulations has converged to its steady semi-major axis ( $a_{\text{pl}}$ ), which ranges between 3.3 to 4.0  $a_{\text{bin}}$ , depending on the binary eccentricity and disk aspect ratio. The only planet that takes more than 50 000 binary orbits to converge to its final position is the planet in the setup  $e_{\text{bin}} = 0.35$  with  $h/r = 0.03$ , as shown in

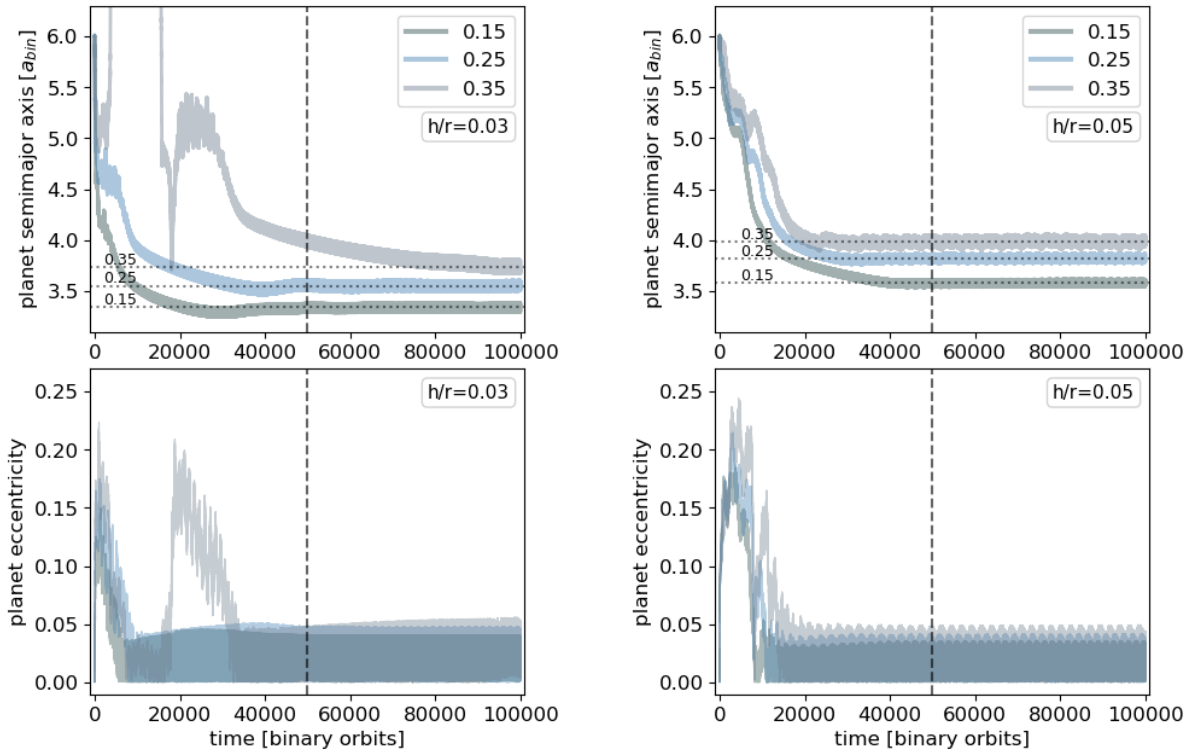


**Figure 4.9:** Planets’ semi-major axis and eccentricity as a function of time (in binary orbits). The upper right number in each plot indicates the eccentricity of the binaries. The dashed vertical curve indicates the position of the 50 000 binary orbits, after which the planet has converged to its equilibrium orbit. The median semi-major axis for the planet orbit after convergence is indicated with a dotted line.

the left panel of Fig. 4.9. As the eccentricity of the binaries is increased, the instability region is pushed farther away, thus the initial position of this planet was more unstable than the others. The planet is initially pushed to a farther orbit, before it starts migrating inwards as the others. Examples of this behavior are also seen in [Penzlin et al. \(2021\)](#), where some of the planets would even get ejected from the system depending on the binary mass ratio, eccentricity and disk aspect ratio, for the same initial planet position. As this planet jumps into a higher orbit, it creates a secondary ring outside the main ring excited by the binaries, with a gap between them located roughly at  $8 a_{\text{bin}}$ . After the planet has migrated inwards into the cavity, the secondary ring remains as a stable structure until the end of our simulations.

The eccentricity of the planet orbit  $e_{\text{pl}}$  is not constant with time, and it oscillates between 0 and 0.05 in both aspect ratio setups (as shown in the lower panel of Fig. 4.9). By analyzing the periodogram of  $e_{\text{pl}}$  (after  $a_{\text{pl}}$  convergence), we find the oscillation period to be consistent with the cavity

oscillations periods, in agreement with the findings of [Penzlin et al. \(2019\)](#), where multiple planets were considered.

The planets modify the structure of the cavity and the overall disk eccentricity. To quantify the difference between the setups with and without planets, we calculated the cavity properties and peak density ring properties following the same procedures explained in Section 4.5.2. The planet presence considerably decreases  $e_{\text{cav}}$ , as shown in Fig. 4.7, where the highest amplitude variations do not reach the minimum  $e_{\text{cav}}$  from the no planet setups, independently from the  $e_{\text{bin}}$  and disk aspect ratio. This oscillations are consistently confined to the range between (0.0, 0.1) for the aspect ratio  $h/r = 0.05$ , and (0.0, 0.03) for the aspect ratio  $h/r = 0.03$ . As in the "no-planet" simulations, the period of the oscillations in  $e_{\text{cav}}$  and  $a_{\text{cav}}$  are consistent with the cavity precession period, and they coincide with the oscillation period of  $e_{\text{pl}}$ .

The decrease in eccentricity due to the planet's presence is extended towards the whole disk. The only case where peak ring eccentricities become comparable between setups with or without a planet is for the aspect ratio  $h/r = 0.05$ , where the setups without planet and  $e_{\text{bin}} = 0.15$  and  $0.25$  have  $e_{\text{peak}}$  in the same eccentricity range of with planet setups (as shown bottom panel-pair in Fig. 4.8). The overall decrease in eccentricity contributes to a decrease in the density asymmetry along the peak density ring, as the gas spends similar amount of time in each azimuthal element. Considering all our simulations, we find the gas density profile to be between three to seven times more axisymmetric when the planet is present, as shown in Table 4.3.

## 4.6 Non-detection of CSCha B

Despite the strong evidence of a highly inclined disk around CS Cha B (high polarization fraction, optical and NIR attenuation, and accretion rate [Ginski et al., 2018](#); [Haffert et al., 2020](#)), our observations are unable to detect such material at 0.87 mm wavelength. For comparison, the  $35.4\mu\text{Jy}$  limit is three times fainter than the detected flux from PDS70c ([Benisty et al., 2021](#)) or the free floating planet OTS 44 ([Bayo et al., 2017](#)) – and it is even lower than the upper limits found for protolunar disk fluxes of directly imaged exoplanets ([Pérez et al., 2019](#)).

The non-detection of CO towards CS Cha B suggests that its emission is either being blocked, or that its CO emitting layer is very compact (or a combination of both). Disks around M-dwarf stars are expected to be smaller

compared to disks around Sun-like stars (Andrews et al., 2013; Tripathi et al., 2017; Hendler et al., 2020), and the tidal interaction of CS Cha B with the main CS Cha system could have further truncated its size (Bate, 2018; Cuello et al., 2019; Manara et al., 2019). Observations at shorter wavelengths (such as ALMA bands 8-10 or JWST instruments MIRI and NIRcam) are needed to fully understand the circumstellar environment of CS Cha B, by connecting the non detection in 0.87 mm to the NIR observations.

Alternatively, CS Cha B could also be a young source located in the background of the Cha I cloud. In such scenario, a disk-less star (or a very small disk) would explain the non-detection at mm wavelengths, while the light would be additionally obscured and polarized by the environment. The  $H\alpha$  emission could be a contribution from accretion and chromospheric activity (e.g. PZ Tel B, Musso Barcucci et al., 2019), and the apparently common proper motion would be due to both systems being on the same cloud. A longer time baseline on the sources astrometry could clarify whether the sources are indeed gravitationally bounded or whether their apparent proximity and similar proper motion is only a temporary coincidence.

## 4.7 A Saturn-like planet is consistent with the morphology of the CSCha disk

Two main properties distinguish the simulated disks that host a Saturn-like planet to the ones that do not: the disk eccentricity and azimuthal density symmetry (or azimuthal contrast). These properties are not independent from each other. In fact, binary disks that do not host a planet have cavities that are consistently more eccentric compared to the planet hosting disks, and a similar behavior is seen for the ring eccentricity. The increased eccentricity produces a higher difference between the orbital velocity at apoastron and periastron, which contributes to the azimuthal asymmetry.

Our simulations are all locally isothermal, and so the gas density maxima will coincide with the gas pressure maxima, where the dust is expected to be trapped more efficiently. As a first approximation, we can compare the eccentricity of the gas density peaks from the simulations to the eccentricity of the dust continuum peaks from our visibility modeling. This assumes that the trapped dust in the pressure bump has the same eccentricity than the gas (as in Ataiee et al., 2013). To quantify how coupled are the dust particles

to the gas, we check the Stokes number of the 1mm-sized particles at the location of the density peak in each simulation, by following the formulas presented in [Birnstiel et al. \(2016\)](#). We find typical values ranging between 0.015 and 0.03 (assuming a volume density of the particles of  $1.2 \text{ g cm}^{-3}$ ). Particles with such Stokes numbers are prompt to be trapped in pressure maxima, in particular when the disk viscosity is low ([Pinilla et al., 2012b](#); [Birnstiel et al., 2013](#); [de Juan Ovelar et al., 2016](#)). Hence, in the framework of our simulations ( $\alpha = 10^{-4}$ ), the assumption of the eccentricity of the gas density peak to be equal to the eccentricity of the dust continuum peak is valid.

The dust continuum observations are better suited than the  $^{12}\text{CO}$  images to be compared with the simulations because the 0.87mm continuum traces the dust density at the midplane (in the optically thin approximation, with a constant temperature at different radii), while the optically thick  $^{12}\text{CO}$  traces temperature in the disk surface layers. Therefore, the peak emission in the  $^{12}\text{CO}$  moment 0 is showing regions of high temperature, and it does not trace gas surface density. In the best parametric model (Model 2e, see Section 4.4.3 and Table 4.1), we find that the eccentricity of the component  $g_0$ , which describes the ring peak (see schematic in Fig. 4.11), is  $e_{g_0} = 0.039$ . In the following discussion, we consider this value as reference to be compared with  $e_{\text{peak}}$ .

In Table 4.3, we highlight the  $e_{\text{peak}}$  that have an eccentricity difference smaller than  $\pm 0.02$  compared to our Model 2e. We find similar eccentricity values for all the disks with a planet, and also for the setups with no planet, with an aspect ratio of  $h/r = 0.05$  and binary eccentricity of 0.15 and 0.25. Previous studies had already determined that the disk eccentricities are the lowest in simulations where the binary eccentricity is  $\approx 0.16$  (e.g., [Kley & Haghighipour, 2014](#)); therefore, it is not surprising that some of the simulation setups with low  $e_{\text{bin}}$  can reach eccentricities comparable to the setups with planet.

Even though our simulations show that low eccentricities can be achieved in circumbinary disks without the need of a planet, the azimuthal asymmetries in gas density are decreased by more than half when a single planet is introduced. This is another quantity that can be directly compared to our observations. The parametric Model 2e does not consider azimuthal variations in the intensity, therefore, we can use the amplitude between the most positive and most negative residuals as a reference approximation for the

ratio between the brightest and dimmest parts of the ring peak. We calculate this value from the residuals imaged with a robust parameter of 0.0, shown in Fig. 4.4. The residual image (after subtracting the best Model 2e) has the advantage that all the emission it contains corresponds to the non-axisymmetric emission from the disk and, therefore, it is better suited to quantify the azimuthal asymmetry. We find the ratio between the peak positive and peak negative residual to be  $q_{2e} = 1.09$ . This a value is obtained from dividing two quantities in  $\text{Jy beam}^{-1}$  units, consequentially, it should not be strongly dependent on the beam size or shape, although the brightness still has a preferred direction, parallel to the major axis of the beam. Any improvement to the parametric model would only result in a decrease in the amplitude of the residuals, which means that  $q_{2e}$  is closer to an upper limit for the ring contrast. This ratio is not a density ratio as in the case of the simulations, since the brightness is also affected by optical depths effects even if we assumed a constant temperature. Nonetheless, this  $q_{2e} = 1.09$  is a reference for the extent to which the observation is axisymmetric, after correcting by eccentricity.

A comparison between the density in the simulated gas and observed dust continuum requires an additional assumption, which is that the dust will have an enhancement in density of the same amplitude as the gas. The asymmetries observed in our simulated disks are not dust traps (e.g., vortex-like structures) and, rather, it is rather akin to a "traffic jam" due to the eccentricity of the disk. In this scenario, [Ataiee et al. \(2013\)](#) found that the azimuthal contrast in the dust can be as high as the contrast in the gas, since the precursor for the local density enhancement is the azimuthal difference in orbital velocities and not an azimuthal dust trap.

The azimuthal contrast along the peak density ring is about three to seven times smaller when a planet is included in the disk, as highlighted in Table 4.3. The combination of low disk eccentricities and low azimuthal variations along the ring could be the key parameters to distinguish between disks that do or do not host a gap-opening planet inside the disk cavity. Observations with good S/N and high spatial resolution of circumbinary disks have been obtained for other systems, such as GG Tau A and AS 205 S, and both show azimuthal brightness variations of higher amplitude compared to the contrast detected in CS Cha. Increasing the sample of circumbinary disks with deep observations is needed to draw a definitive conclusion.

Another constraint that has to be taken into account to estimate the planet

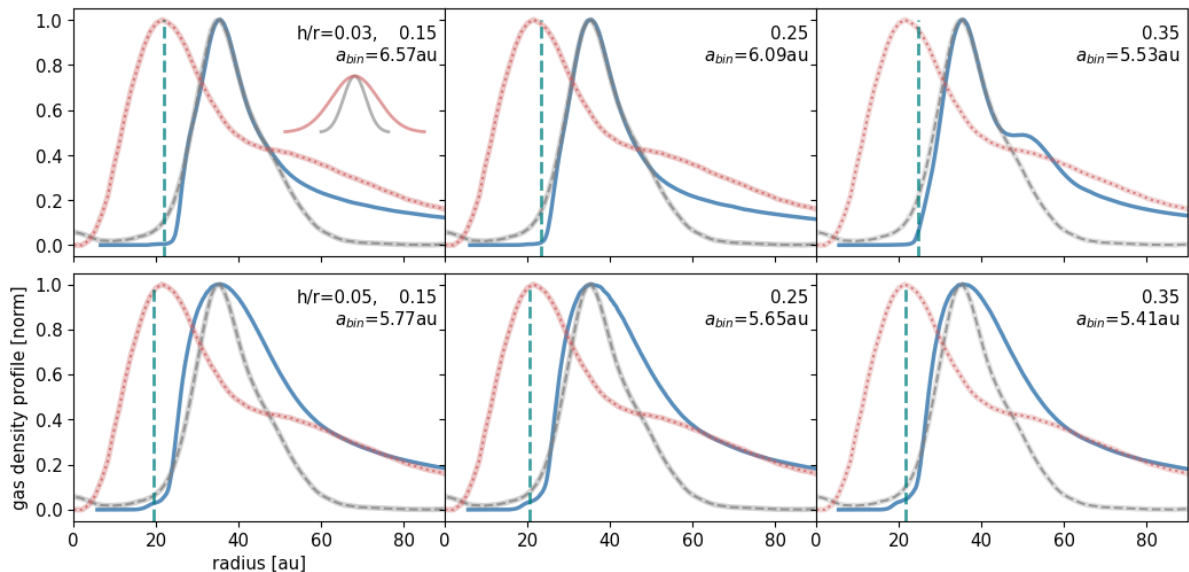


**Figure 4.10:** Comparison of azimuthally averaged radial profiles of CS Cha.

The  $^{12}\text{CO}$  emission is shown in dotted red, the dust continuum emission in dashed gray, and the gas density profile from each simulation setup in solid blue, calculated as the median from the last 1000 orbits. The value of  $a_{\text{bin}}$  is calculated for each simulation to match the peak density position with the peak brightness position of the dust continuum. The values for  $e_{\text{bin}}$  increase from left to right, and each row has a constant disk aspect ratio. The average radial resolution of the  $^{12}\text{CO}$  and dust continuum are shown in the upper left panel, with Gaussians of the same colors. A dashed vertical line marks the position of the simulated planet.

mass is the amount of material that it lets into the cavity through streamers. Our observations detect the presence of dust inside the cavity, which is likely to be part of the circumstellar disk of each star. Due to the faintness of this signal, we do not model it as two individual sources, but we rather use a single Gaussian to describe it. This emission is bright enough not to be neglected, as shown in the residuals from Models 2g and 3g in Fig. 4.13. In the context of circumbinary disks, these individual circumstellar disks seem to be brighter in younger systems such as GG Tau A or IRAS 04158+2805 (Phuong et al., 2020; Ragusa et al., 2021, respectively), and constraining their properties can give more insight into the processes shaping the cavity. High angular resolution observations in shorter wavelengths, such as ALMA Band 9 or Band 10, could have a better chance at detecting, at a higher S/N, the material around the stars and also the circumstellar material of CS Cha B, which is known to be brighter at shorter wavelengths (Haffert et al., 2020).

## 4.8 Cavity edge and ring morphology

As shown in Figs. 4.6 and 4.10, changing  $e_{\text{bin}}$  and disk aspect ratios can induce different rings morphologies, as they differ in eccentricity, azimuthal symmetry, radial extent, and density distribution. Observationally constraining of the orbital parameters of the CS Cha binary stars will greatly reduce the degeneracy of the parameter space, as different binary eccentricities will not need to be sampled and the location of the ring peak and the ring width will also become quantities that can be compared among the observations and simulations. Additional observations of CS Cha in longer wavelengths such as 1.3 mm or 3 mm would allow us to test the azimuthal brightness variation along the ring in optically thinner emission, thus increasing the constraints in the proposed planet.

Observations of the disk in scattered light emission have found the cavity edge (if any) to be hidden by the coronagraph of SPHERE, therefore setting an upper limit of 15.6 au (Ginski et al., 2018). This value differs from the temperature peak at 21.6 au that we observe in the  $^{12}\text{CO}$  emission, which is most likely the location of the gas cavity inner edge. The difference between those measurements is an additional constrain for the possible planet mass, and the disk physical conditions. For the same  $e_{\text{bin}}$ , different disk aspect ratios will also modify the shape of the ring inner edge, depleting the material closer or farther from the star, as shown in Fig. 4.10. To compare the observed profiles to the simulations, we scaled the value of  $a_{\text{bin}}$  such that the peak density position matches with the peak brightness of the dust continuum. This scaling is made under the same assumptions discussed in Sect. 4.7, which is that the brightness peak of the dust continuum will trace the dust density maxima and it will coincide with the gas density maxima of the simulations.

The small  $\mu\text{m}$ -sized grains traced by the scattered light images could be getting through the planet orbit via streamers, which connect the main circumbinary ring to the binaries, and replenish their circumstellar disks. In fact, Fig. 4.10 shows that the simulated gas is not always depleted at the planet location, specially in the setups with  $h/r = 0.05$ . The small grains coupled to the gas at the planet orbit location could contribute to the difference in cavity size when observed with different tracers. Interestingly, when the semi-major axis of the planet is scaled from  $a_{\text{bin}}$  to au, all of our simulations locate the planet almost at the same position as the  $^{12}\text{CO}$  peak brightness, which probably coincides with the cavity edge, where the  $^{12}\text{CO}$  reaches

its highest temperature. Follow-up observations with alternative molecular lines, in combination with the accurate determination of the binaries orbits, would set even stronger constraints over the disk physical conditions and the candidate planet mass.

Finally, our work shows the feasibility of applying visibilities modeling with more than one eccentricity. The problem of analytically describing a coordinate system with variable eccentricity as a function of distance can be solved by approximating the emission with multiple components at different distances and eccentricities. While challenging, a combination of such approach with the visibilities modeling of the  $^{12}\text{CO}$  emission would overcome the limitations related to image reconstruction with synthesized beam convolution and possibly recover a precise description of the cavity inner edge morphology, location, and eccentricity, as we did for the dust continuum emission.

## 4.9 Summary

This chapter presented an analysis of the high angular resolution ( $\approx 30 \times 46$  mas) observations at 0.87 mm of the CS Cha system, composed of a spectroscopic binary (usually referred just as CS Cha) and a co-moving companion at  $1.3''$  known as CS Cha B (Ginski et al., 2018; Haffert et al., 2020). Our observations do not detect any significant emission from the expected position of CS Cha B, neither in the dust continuum emission or  $^{12}\text{CO}$ . We set an upper limit for its disk 0.87 mm continuum emission to be  $35.4 \mu\text{Jy}$ , which is the  $3\sigma$  limit in the image generated with a robust parameter of 1.0.

The circumbinary disk resolves into a single ring, which has a peak in the dust continuum emission at 35 au and 22 au in the  $^{12}\text{CO}$  J:3-2 transition. Both the dust and gas emission show evidence of non-circular orbits, which is expected for circumbinary disks. The eccentricity in the dust continuum is constrained by visibility modeling, and we find the peak of the ring to have an eccentricity of 0.039 and the contrast between the brightest and dimmest part along the peak ring to be at most 9%.

From our simulations of circumbinary disks, we find that including a Saturn-mass planet is in better agreement with the observations compared to the disk with no planet, as it can reproduce the low eccentricity and low azimuthal contrast over the ring. Even though it is possible to achieve low disk eccentricities without the need of a planet, the azimuthal symmetry of the disks is only achieved when a planet is present. Additional deep observa-

tions of other circumbinary disks could reveal if there is a difference within the circumbinary disks population between disks that do or do not host a gap-opening planet within the cavity.

The accurate determination of the orbital parameters of the CS Cha binary would unlock several additional observables that could be directly compared to the simulations, such as the ring location, ring morphology, and outer-disk radius, which are only measured in binary-separation units in the current simulations.

## 4.10 Additional content

Additional images are shown in this Section, complementary to the results shown previously.

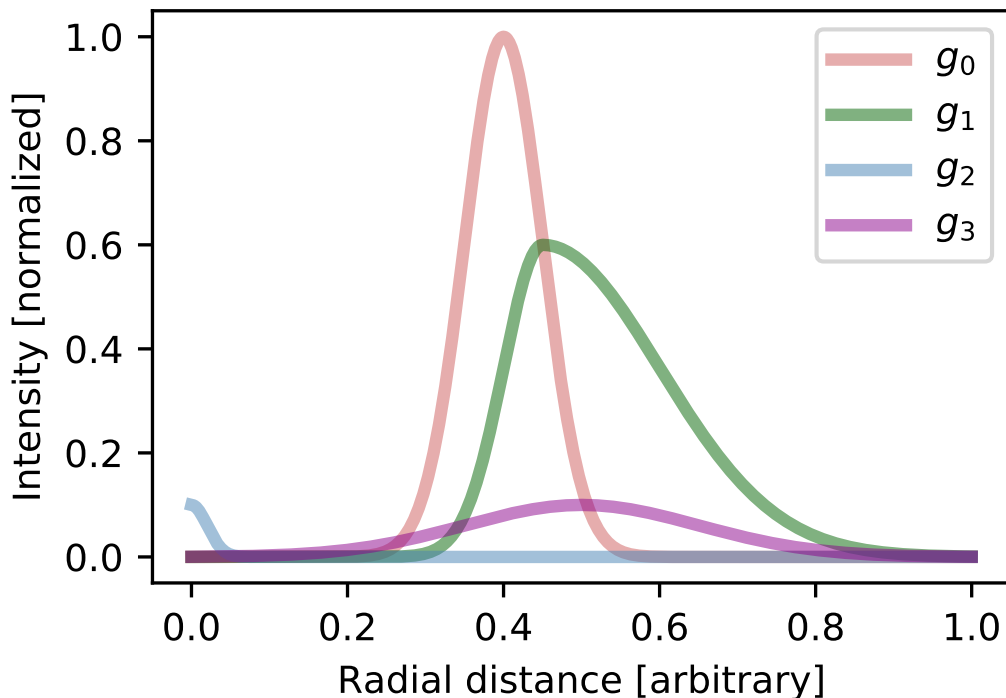


**Figure 4.11:** Schematic profile of the components considered in CS Cha parametric visibility modeling.

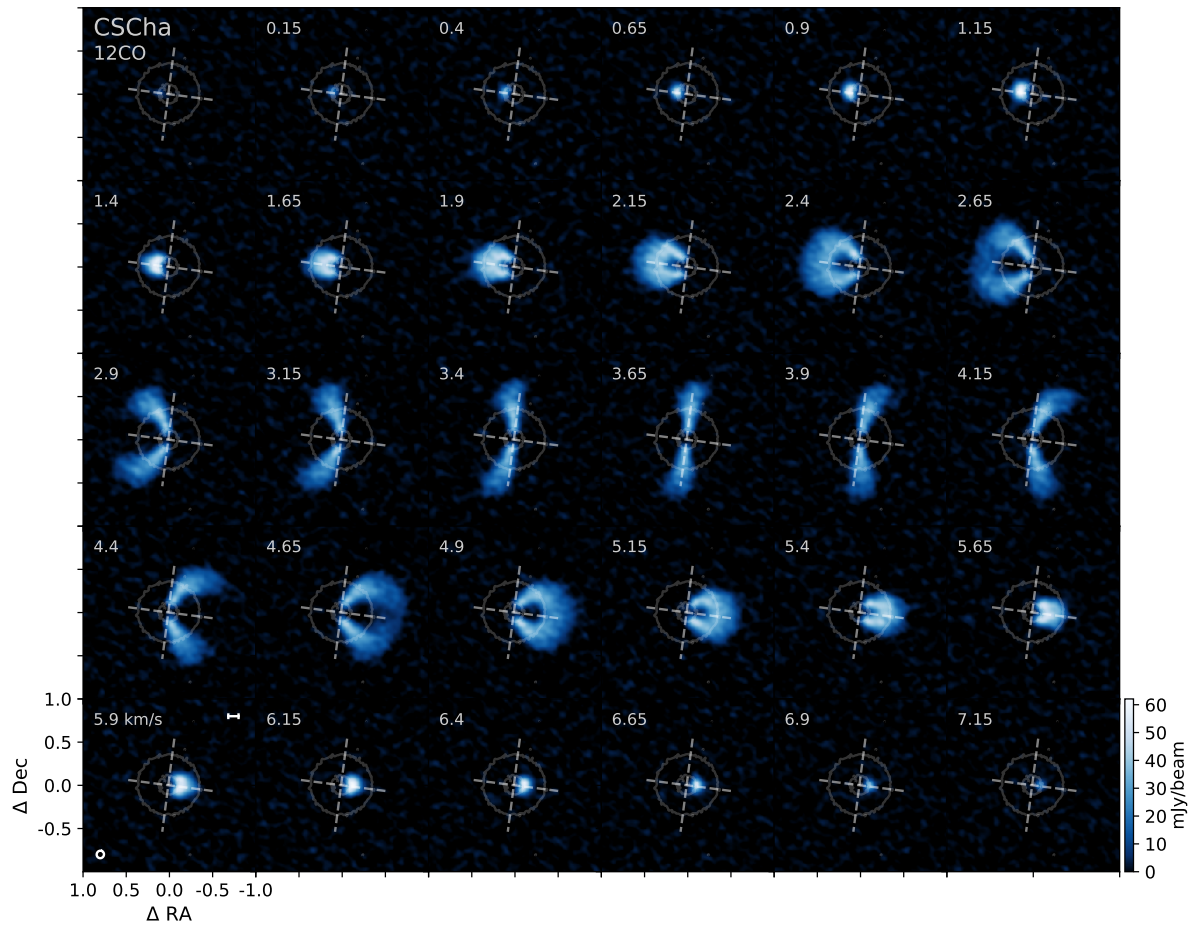


**Figure 4.12:**  $^{12}\text{CO}$  Channel maps of CS Cha, generated with a robust parameter of 0.0. The velocity of each channel is shown in the upper right corner. The contours are the  $5\sigma$  level of the continuum image generated with a robust parameter of 0.0. Lower left panel: Scale bar represents 20 au at the distance of the source, and ellipse represents the beam size for all the images.

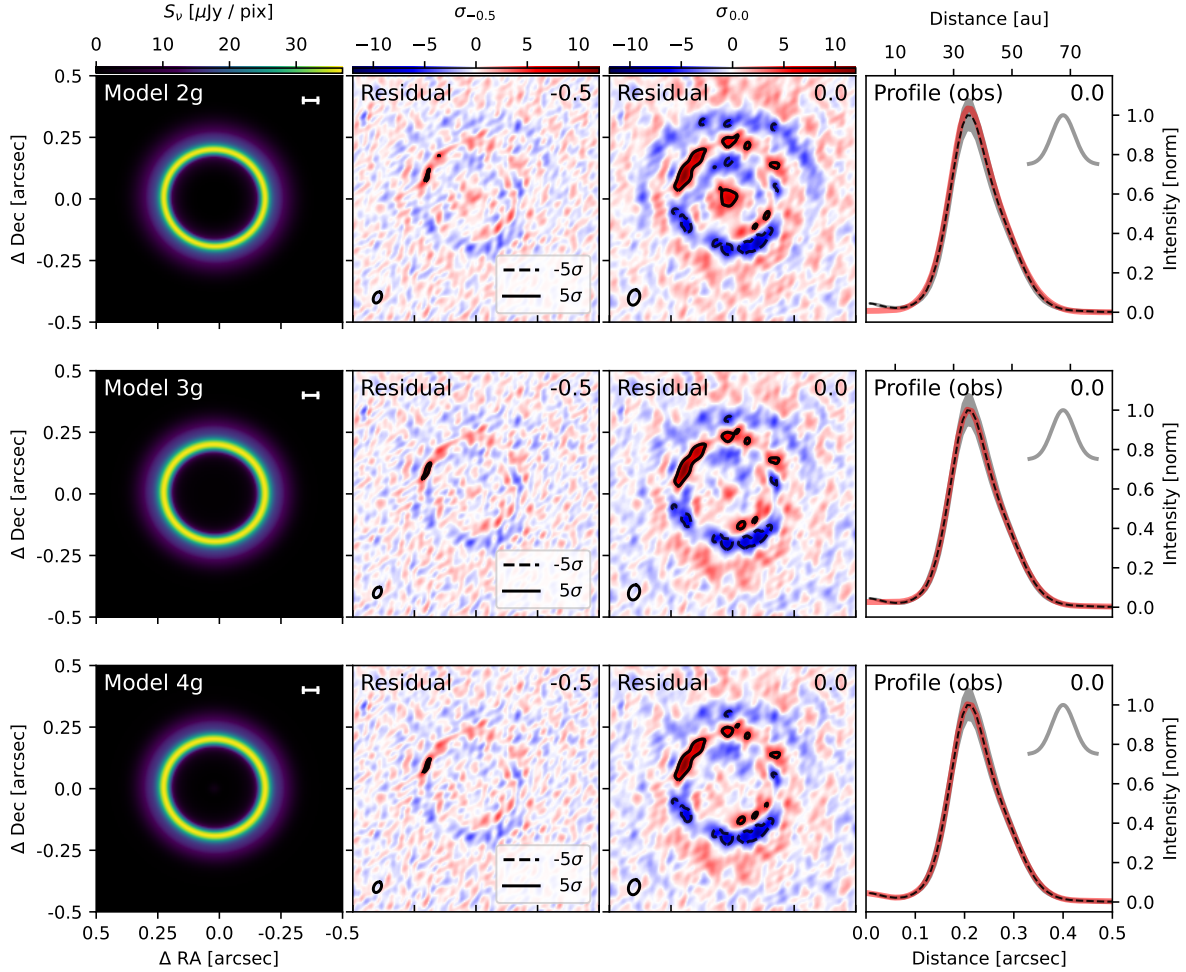


**Figure 4.13:** Best solutions for the dust continuum emission generated with the Models 2g, 3g and 4g.

Left panel shows the best model, and middle panels shows the residuals left by the best model after being imaged with different robust parameters, shown in the upper right corner. Right panel shows the intensity profile of the model obtained from `tclean` (in dashed black) and the best respective model (in red).





# 5

## Planet formation in an interacting multiple stellar system: RW Aur

---

This chapter presents results of a research publication in preparation about the high angular resolution observations of RW Aur (Kurtovic et al., in preparation). I lead the analysis and results interpretation presented in this work. The coauthors of the work in preparation contributed with discussion of the interpretation and methodology.

### 5.1 The impact of dynamical interactions on the disks of young binary disk systems

The impact of external companions on the disk of a star is strongly dependent on the orbital parameters of the perturber relative to the primary star. The orbital parameters of young objects are difficult to constrain, mainly due to the material that is surrounding the stars. For a few bright systems, historical astrometry provides some constraints over the binaries orbit (e.g. Csépany et al., 2017), but additional high accuracy measurements are needed to fully constrain important orbital parameters such as the eccentricity and periastron distance.

A very well studied interacting binary system is RW Aur, which is composed of at least two stars located at 154 pc from us (Gaia Collaboration et al., 2016, 2021), each hosting its own disk (Cabrit et al., 2006; Rodriguez et al., 2018; Long et al., 2019). The stars A and B have luminosities of  $0.88 L_{\odot}$  and  $0.53 L_{\odot}$  respectively (Herczeg & Hillenbrand, 2014, corrected to 154 pc), even though RW Aur A is known for having a variable luminosity and dimming events where the optical brightness can change as much as 2 mag during periods of several months (Chou et al., 2013; Petrov et al., 2015). These variability events have been hypothesized to be related to inner disk dust-winds (Shenavrin et al., 2015; Bozhinova et al., 2016; Koutoulaki et al.,

2019) and tidally disrupted material (Rodriguez et al., 2013; Dai et al., 2015). Evidence of a tidal interaction was directly identified by Cabrit et al. (2006) using the IRAM interferometer, with the detection of an arc-like emission in the  $^{12}\text{CO}$  J:2-1 molecular line. A later follow-up with ALMA by Rodriguez et al. (2018) found multiple additional  $^{12}\text{CO}$  features and suggested the RW Aur system has undergone multiple encounters, an hypothesis that has also been discussed in additional works Dai et al. (e.g., 2015); Dodin et al. (e.g., 2019).

The relation between all the phenomena mentioned above and the circumstellar disk of each binary has remained mostly unclear, as only Rodriguez et al. (2018) barely resolved the dust continuum disk of each source. Thus, the present work aims to study the nature and impact of the binaries interaction in the distribution of the gas and dust emission in their disks.

Project code	Code	PI Name	Obs Date	N antennas	Baselines (m)	Exp Time (min)	Freq (GHz)
2015.1.01506.S	SB1	Rodriguez, Joseph	2016-09-29	39	15 - 3248	32.38	217.5 - 232.6
			2016-09-29	39	15 - 3248	32.38	
			2016-09-30	39	15 - 3144	32.38	
			2016-09-30	39	15 - 3144	32.38	
2016.1.00877.S	SB2	Rodriguez, Joseph	2016-12-08	11	9 - 45	25.54	217.5 - 232.6
			2016-12-08	11	9 - 45	25.54	
			2016-12-08	11	9 - 45	25.54	
2016.1.01164.S	SB3	Herczeg, Gregory	2017-08-31	45	21 - 3697	8.97	217.0 - 234.0
2017.1.01631.S	SB4	Facchini, Stefano	2018-12-02	46	15 - 952	32.92	215.6 - 233.4
			2018-12-05	47	15 - 784	32.92	
2018.1.00973.S	LB1	Facchini, Stefano	2017-10-08	49	41 - 16196	38.73	217.6 - 232.9
			2017-10-09	51	41 - 16196	38.66	
			2017-10-18	51	41 - 16196	39.82	

**Table 5.1:** Observation log of the RW Aur observations by ALMA.

## 5.2 Observations

This work includes 1.3 mm observations of the system RW Aur from several different ALMA projects, listed in Table 5.1, with an approximate timespan of 2 years and 2 months. We name each project with an identification code for the extension of the antenna baselines: SB for the observations performed with compact antenna configurations and LB for extended configurations. The projects SB1 and SB2 were already published in [Rodriguez et al. \(2018\)](#), while SB3 was part of the Taurus survey published in [Long et al. \(2019\)](#) and [Manara et al. \(2019\)](#). The datasets SB4 and LB1, which have not been published before, had the correlator configured to observe 5 and 4 spectral windows, respectively. SB4 contains two spectral windows covering dust continuum emission centered at 218.503 GHz and 232.003 GHz, while the remaining three were centered at the molecular lines  $^{12}\text{CO}$ ,  $^{13}\text{CO}$  and  $\text{C}^{18}\text{O}$  in their transition  $J=2-1$ . The frequency resolution of the continuum is 1128.91 kHz, while for  $^{12}\text{CO}$  is 141.11 kHz and 282.23 kHz for the remaining two lines. The LB1 observation, on the other hand, has three spectral windows for the continuum and one for  $^{12}\text{CO}$  ( $J=2-1$ ). The frequency resolution of all of them is 1128.91 kHz, which is about  $1.3 \text{ km s}^{-1}$  at 230.538 GHz.

We start from the pipeline-calibrated measurement set generated with the `scriptforPI` delivered by ALMA. Using `CASA 5.6.2`, we extract the dust continuum emission from the spectral windows targeting gas emission lines, and we do it by flagging the channels located at  $\pm 25 \text{ km s}^{-1}$  from the system approximate velocity at local standard of rest (VLSR), which is about  $6 \text{ km s}^{-1}$  for RW Aur. The remaining channels are combined with the other continuum spectral windows to obtain a “pseudo-continuum” dataset, and we average into 125 MHz channels and 6 s bins to reduce data volume. Each project has enough signal-to-noise ratio (S/N) to be self-calibrated by itself, and therefore we do not align the different observations to the same phase center prior to self-calibration. Each project was completely observed within days between the first and last observation; therefore, we treat each observation as a single epoch. The imaging for the self-calibration process was done with a Briggs robust parameter of 0.5, except for LB1, where we used 1.0. We combined all the scans and spectral windows for each `gaincal` execution.

The calibration tables obtained from the dust continuum self-calibration of each observation were then applied to the original measurement sets, which contained dust continuum and molecular line emission. We subtract the con-

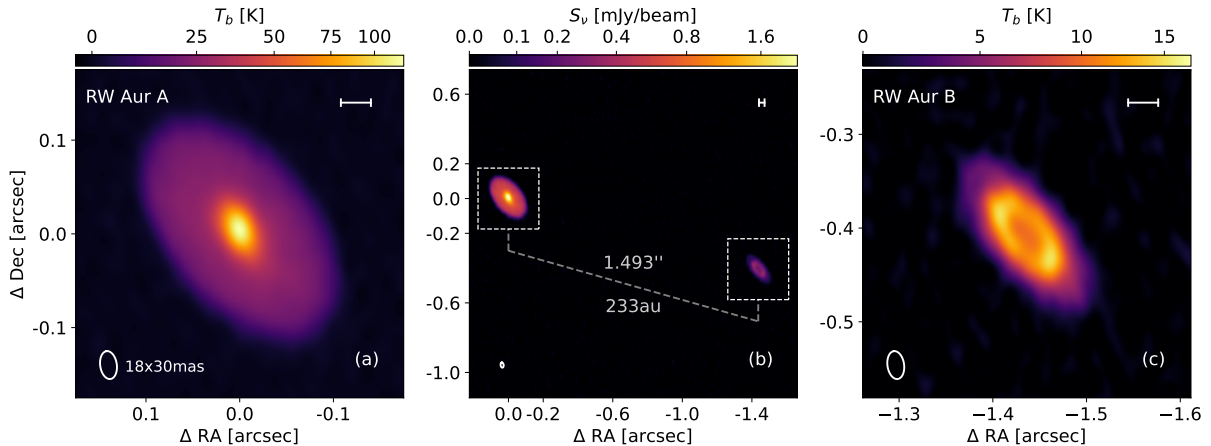


**Figure 5.1:** Dust continuum emission of RW Aur, from the LB1 observation.

Panels (a) and (c) show each disk individually in brightness temperature, while panel (b) shows both disks together in brightness per beam, with the projected distance showed for this epoch. The beam resolution is the same for all the panels, and its size is  $18 \times 30$  mas, as shown in the lower left corner of panel (a). The scale bar is 5 au at the distance of the source.

tinuum emission with the task `uvcontsub` and obtain a measurement set for each molecular line for each epoch. The  $^{12}\text{CO}$  line is present in all the observations except for SB3, while  $^{13}\text{CO}$  and  $\text{C}^{18}\text{O}$  are present in SB1, SB2, SB3 and SB4. We combine the visibilities of different epochs to generate the gas images of each tracer under the assumption that spatial movement is negligible at the scales covered by the angular resolution of the gas observations. The  $^{12}\text{CO}$  line, the brightest gas emission line available in our data, was imaged twice. The first image combined the observations SB1, SB2, and SB4 to optimize sensitivity to large spatial scales (which we call SB  $^{12}\text{CO}$  image), and the second image combined all observations to maximize sensitivity at high angular resolution (which we call LB  $^{12}\text{CO}$  image). When combining with the LB1 dataset, the maximum velocity resolution allowed is  $1.3 \text{ km s}^{-1}$ , while the SB  $^{12}\text{CO}$  image is imaged with  $0.5 \text{ km s}^{-1}$  to optimize the sensitivity/velocity resolution ratio. The  $^{13}\text{CO}$  and  $\text{C}^{18}\text{O}$  have the same imaging setup as SB  $^{12}\text{CO}$  image, but including SB3.

Both gas and continuum emission are imaged using the task `tclean`. To avoid introducing PSF artifacts that could be mistaken for faint emission, we lower the `gain` parameter to 0.05 and increase the `cyclefactor` to 1.5, for more conservative imaging compared to the default values, and we cleaned down to the  $4\sigma$  threshold. We apply the JvM correction to all our images, which accounts for the volume ratio  $\epsilon$  between the PSF of the images and the restored Gaussian of the CLEAN beam, as described in [Jorsater & van](#)

Moorsel (1995) and Czekala et al. (2021). We use the package `bettermoments` (Teague & Foreman-Mackey, 2018b; Teague et al., 2019) to create additional image products from the channel maps. We calculate the peak intensity image by fitting a quadratic function in each pixel along the velocity axis, which also gives us the velocity associated with the peak flux. The same package is also used to generate the moment 0 and moment 1 of each velocity cube. All the moment images were clipped at 0 sigma (negative emission is removed), and no mask was used. An additional clipped image is generated from the LB  $^{12}\text{CO}$  image, where we only consider pixels with emission over  $1.3 \text{ mJy beam}^{-1} \text{ km s}^{-1}$ , with the aim of filtering extended gas emission and recover the bright localized emission from the disks.

We apply visibility modeling to the continuum visibilities of each epoch. To further reduce the data volume after finishing the self-calibration, we averaged the continuum emission into one channel per spectral window and 24 s. We used each binned channel central frequency to convert the visibility coordinates into wavelength units, and we did not combine the visibility tables of different epochs.

### 5.3 Dust continuum emission of RWAur

The dust continuum observations resolve into two independent disks (as it had been observed before in Cabrit et al., 2006; Rodriguez et al., 2018; Long et al., 2019; Manara et al., 2019), one around each source of the system, as shown in Fig. 5.1. When imaged at very high angular resolution, RW Aur A resolves into a compact ( $R_{90\%} = 0.124''$ , being  $R_{90\%}$  the radii that enclose 90% of the dust continuum emission) centrally peaked disk, with no evidence of annular ring-like structure with the  $3 \times 5 \text{ au}$  beam resolution. Located about 233 au in projected distance to the southwest is RW Aur B, also a compact disk ( $R_{90\%} = 0.093''$ ) with evidence of a dust continuum ring. The sizes were constrained through visibility modeling of the dust continuum emission visibilities, as described in Sect. 5.3.1.

We constrain the flux of each source from the visibility modeling. RW Aur A dust continuum is almost eight times brighter than its companion RW Aur B, with 34.5 mJy, and 4.4 mJy of integrated flux, respectively. RW Aur A is also considerably hotter in brightness temperature, with a peak  $T_b = 120 \text{ K}$  in the disk center. RW Aur A has a monotonically decreasing temperature profile remains higher than 20 K until a radius of 107 mas (or 17 au). As a contrast,

RW Aur B maximum brightness temperature at any radii is 15 K.

For an estimate of the dust mass, we follow [Hildebrand \(1983\)](#), as we also did in chapters 2 and 3:

$$M_{\text{dust}} = \frac{d^2 F_\nu}{\kappa_\nu B_\nu(T(r))}, \quad (5.1)$$

where  $d$  is the distance to the source,  $\nu$  is the observed frequency,  $B_\nu$  is the Planck function at the frequency  $\nu$ , and  $\kappa_\nu = 2.3(\nu/230 \text{ GHz})^{0.4} \text{ cm}^2 \text{ g}^{-1}$  is the frequency-dependent mass absorption coefficient (as in [Andrews et al., 2013](#)). The additional assumption for this calculation is that the dust emission at 1.3 mm is being emitted by optically thin dust with a known temperature, commonly set to 20 K for standard reference (as in [Ansdell et al., 2016](#); [Cieza et al., 2019](#)). As the brightness temperature is higher than 20 K for about 75% of the emitting area of RW Aur A, the assumption of optically thin emission fails, and thus we can only provide a lower limit to its dust mass. If we assume the midplane temperature of 20 K (for comparison with other surveys and observations), we obtain  $11.885 \pm 0.003 M_\oplus$  and  $1.525 \pm 0.002 M_\oplus$ . These small uncertainties are representative of the sensitivity obtained when combining our multiple ALMA observations, and they do not take into account the 10% uncertainty of ALMA flux calibration.

### 5.3.1 Parametric visibility modeling

To determine the dust continuum emission morphology and properties, we use the packages `galario` ([Tazzari et al., 2017](#)) and `emcee` ([Foreman-Mackey et al., 2013b](#)) to fit a parametric visibility model to the data. We generate one independent image for each source and calculate each model image's visibilities separately. Due to the additive properties of the Fourier Transform, we can add the visibilities of each source and compare that combination to the observations.

We fit all the epochs at the same time with the same intensity models. However, we allow the disk centers to be different in each observation, with the underlying assumption that each disk brightness distribution is constant during the two years covered by our data, and the only possible difference between epochs are the disk's relative positions.

Additionally, it is known that the ALMA flux calibration can have uncertainties ranging up to 10%, and even higher in particular cases (as in some

	Property	Best value $\pm 1\sigma$	unit
RW Aur B position relative to RW Aur A	$r_{AB}(SB1)$	$1491.49 \pm 0.15$	mas
	$r_{AB}(SB3)$	$1493.49 \pm 0.64$	mas
	$r_{AB}(SB4)$	$1499.50 \pm 0.60$	mas
	$r_{AB}(LB1)$	$1493.56 \pm 0.15$	mas
	$\theta_{AB}(SB1)$	$254.1546 \pm 0.0084$	deg
	$\theta_{AB}(SB3)$	$254.0475 \pm 0.0264$	deg
	$\theta_{AB}(SB4)$	$254.0415 \pm 0.0335$	deg
	$\theta_{AB}(LB1)$	$254.0553 \pm 0.0059$	deg
Disks Geometry	$\text{inc}_A$	$54.93 \pm 0.04$	deg
	$\text{PA}_A$	$39.35 \pm 0.05$	deg
	$\text{inc}_B$	$63.98 \pm 0.16$	deg
	$\text{PA}_B$	$39.65 \pm 0.24$	deg
Disks Continuum Properties	$R_{B,\text{ring}}$	$41.49 \pm 0.29$	mas
	$R_{A,68\%}$	$101.37 \pm 0.13$	mas
	$R_{B,68\%}$	$68.55 \pm 0.23$	mas
	$R_{A,90\%}$	$123.77 \pm 0.12$	mas
	$R_{B,90\%}$	$92.95 \pm 0.14$	mas
	$F_{A,mm}$	$34.504 \pm 0.010$	mJy
	$F_{B,mm}$	$4.427 \pm 0.006$	mJy

**Table 5.2:** Dust continuum emission properties obtained with parametric visibility modeling. Relative position of RW Aur B respect to A and disks geometries are free parameters in the MCMC, while the disks continuum properties are products of the fit. The remaining free parameters of our model are in Table 5.5.

of the DSHARP sources, Andrews et al., 2018), therefore we add an extra free parameter for each epoch, a scalar  $i_{obs} \approx 1$  which multiplies the whole intensity model, and scales the possible flux difference. As the flux reference, we use the observation SB4, which has a fixed  $i_{SB4} = 1$ , and thus all the remaining  $i_{obs}$  scale the models to match SB4 flux. This epoch was chosen because it has the highest sensitivity in short baselines and is neither the brightest nor dimmest observation, as confirmed by the scaling factors  $i_{obs}$  in Table 5.5.

We fit azimuthally symmetric models to RW Aur A, and RW Aur B, taking the morphology of the CLEAN model as a guideline. For RW Aur A, the function used to describe its brightness profile is the following:

$$I_A(r) = f_{A0} + G(r, f_{A1}, \sigma_{A1}) + TP(r, f_{A2}, r_{A2}, \alpha, \beta), \quad (5.2)$$

where  $f_{A0}$  is the flux of a point source at the disk center,  $G$  is a centrally

peaked Gaussian of peak flux  $f_{A1}$  and standard deviation  $\sigma_{A1}$ , and  $TP$  is a power law tapered with an exponential decay, described in Section 5.7.1. The point and Gaussian components are needed to describe the inner emission of the disk, while the tapered power law is used to describe the monotonically decreasing brightness decay with the possibility of a sharp outer edge, if needed.

For RW Aur B, the disk is very inclined, and therefore the information of its cavity is limited. A possible parametrization for the dust continuum ring could have been done with a broken Gaussian (i.e. a Gaussian ring with different widths for each side of its peak). However, that model returns a very steep inner edge to try to compensate for the slow decrease of its outer edge, similar to the inclined disk MHO 6 chapter 3. This problem with the broken Gaussian description can be overcome by slightly increasing the complexity of the model to two Gaussian rings. These Gaussians can become a centrally peaked emission while allowing the model to fit radially asymmetric rings. The equation that described the model of RW Aur B as a function of radii is:

$$I_B(r) = G(r - r_{B1}, f_{B1}, \sigma_{B1}) + G(r - r_{B2}, f_{B2}, \sigma_{B2}), \quad (5.3)$$

where  $f_{B1}$  and  $f_{B2}$  are the peak intensity of each ring, centered at  $r_{B1}$  and  $r_{B2}$  with a Gaussian width of  $\sigma_{B1}$  and  $\sigma_{B2}$ , respectively.

We run a MCMC fitting all 5 epochs at the same time, therefore achieving complete visibility coverage starting from the ACA array baselines from SB2, until the longest baselines from ALMA antenna configuration C43-10 with LB1. We use a flat prior over the allowed parameter space, and the boundaries for each free parameter are wide enough such that walkers never interact with them. The pixel size for the model images was initially 4 mas, and we also tested the stability of the fit by running the same models with a pixel size of 2 mas, obtaining consistent results. A summary of the main results is given in Table 5.2, while the remaining free parameters of the MCMC are shown in Table 5.5.

The best profile for each disk is shown in Fig. 5.2, where we compare the best visibility model profile with the azimuthally averaged radial profiles of the dust continuum and  $^{12}\text{CO}$  moment 0 images. By construction, the emission from RW Aur A is centrally peaked, and our model described the disk emission as a monotonically decreasing profile. When the residual visibilities

are imaged (see Fig. 5.3), we find our flat disk model describes most of the structure detected in the observation LB1, as the highest peak residual is only  $6\sigma$  (compared to  $> 300\sigma$  of the dust continuum image). Even though the residuals are of low contrast, their structure suggests that our description of a Gaussian with a point source for the central emission is incomplete.

Our model for RW Aur B, on the other side, completely describes the disk emission to the noise level, and no structured residual is detected at the position of the source (see Fig. 5.3). We find that RW Aur B ring peaks at about 42 mas, which is 6.5 au from the disk center. Interestingly, both disks show similar geometry in our line of sight, with their position angles being the same to the uncertainty level. RW Aur B is slightly more inclined than A, as it was also estimated by [Rodríguez et al. \(2018\)](#) and [Manara et al. \(2019\)](#). Under the assumption that both disks have their angular momentum vector pointing in the same direction, we find a misalignment of 9.15 deg, or 118.8 deg if they point in different directions.

### 5.3.2 RW Aur B orbit: With ALMA astrometry

Our visibility model allows the disk centers to be in different locations for each epoch, except for SB2, where the angular resolution is not high enough to resolve the disks. For SB2, we repeat the same disk positions from the closest observation in time, SB1. If we consider the central position of RW Aur A as the origin of the coordinate system, we can study the coordinates of RW Aur B disk center relative to A as a function of time. Those results are shown in Table 5.2 in polar coordinates (separation and position angle) and also shown in panel (a) of Fig. 5.4, with confidence contour levels. Observations SB1 and LB1 have the highest position accuracy, which is a combination of the extended integration time and high angular resolution. The observation SB3, even though it has longer baselines than SB1, is only 9 min long, limiting the positional accuracy due to lower sensitivity. Finally, observation SB4 achieves a similar uncertainty region to SB3 due to the higher sensitivity, despite the more compact baseline configuration. RW Aur B shows a consistent trend moving toward the southwest as a function of time. Under the assumption that the central position of the disks coincides with the location of the star, we can use our visibility-modeled disk center as a precise astrometric measurement for each system. We combine our ALMA astrometry with the historical separation between RW Aur A and B as compiled by [Csépany et al.](#)

(2017), which has epochs ranging from 1944 to 2013, and are shown in panel (b) of Fig. 5.4.

In order to recover the orbit of RW Aur B around RW Aur A, we use the function `kepler.calc_orbit` from the python package `orbitize!` to calculate the orbital positions starting from a set of orbital elements. We exclude two outliers measurements from the historical astrometric positions, which are the 1944 and 1991 observations from Joy & van Biesbroeck (1944) and Leinert et al. (1993), respectively. These observations deviate from the positional trend, and the 1991 observation is inconsistent by about  $0.1''$  in separation and more than  $2\text{ deg}$  in position angle with measurements from 1990 and 1994. We included a single radial velocity measurement, using the relative line of sight velocity obtained with ALMA, and assigned an average epoch considering our four ALMA observations. This radial velocity is assigned to RW Aur B with a value of  $-0.954\text{ km s}^{-1}$  (where negative means coming closer to us), relative to the rest reference frame of RW Aur A. Due to the high S/N of the emission of each disk in the  $^{12}\text{CO}$  channel maps, the integrated velocity images such as moment 1 and velocity at peak brightness show a “channelization problem”, where the low frequency resolution produces a discrete velocity distribution, instead of a continuous rotation map, as seen in Figure 5.7. Such effect makes it challenging to obtain a meaningful uncertainty from the ALMA cube, and thus we set a conservative  $1\sigma$  dispersion to  $100\text{ m s}^{-1}$  for the fitting.

The function `kepler.calc_orbit` has eight free parameters, including the orbit semi-major axis (`sma`), eccentricity (`ecc`), inclination (`inc`), argument of periastron (`aop`), longitude of ascending node (`pan`), epoch of periastron (`tau`), distance to the system (`plx`), and the system total mass (`mtot`). We found the parameters “`aop`” and “`pan`” to be strongly linearly correlated in our MCMC runs, thus we define a new parameter “`hal`” with the experimentally determined relation:

$$\text{pan} = \text{hal} + (0.996 \cdot \text{aop}) + 48 \text{ [deg]}, \quad (5.4)$$

thus decorrelating to first order the two parameters.

We found the Affine-invariant MCMC algorithm from `emcee` within `orbitize!` would not converge over reasonable amounts of time, due to the strong non-linear correlation of the parameters. Instead, we used the python package `zeus` (Karamanis et al., 2021), which has an Slice-Sampling MCMC

implementation (Karamanis & Beutler, 2020), allowing for a more efficient sampling of the parameter space. We use a flat prior over the allowed parameter space for the first six parameters, while for “plx” and “mtot” we used Gaussian priors with the GAIA DR3 distance and uncertainty and the mass recovered from the fit to the 12CO emission as described in Sect. 5.4, respectively. We assume the total mass is contained in RW Aur A, and RW Aur B is a massless point source, thus solving the orbital equation with RW Aur A at the origin of the coordinate system. For the mass Gaussian prior, we considered a  $1\sigma$  uncertainty of  $0.05 M_{\odot}$  for each star, and thus a  $1\sigma = 0.05 \cdot \sqrt{2} M_{\odot}$  for the total system mass. The number of walkers was set equal to eight times the number of free parameters, as recommended in Karamanis et al. (2021).

Even with the **zeus** MCMC and the implementation of the “hal” parameter, we do not achieve convergence for each walker for each parameter after running for over  $1 \cdot 10^6$  steps. To alleviate this problem, we ran five independent MCMCs with the same priors, boundaries and number of walkers. Each MCMC has a burning stage of  $4 \cdot 10^6$  steps at minimum, and then we use additional  $4 \cdot 10^6$  steps for each walker to sample the parameter space. To reduce the data volume, we only record 1 out of every 20 steps, thus accumulating  $2 \cdot 10^5$  positions for each walker. We find the resulting distribution of each parameter is consistent among the different MCMC runs, and we take the average of all of them to calculate the final distributions, thus combining  $1 \cdot 10^6$  measurements for each parameter.

The results for the RW Aur B orbit relative to RW Aur A are displayed in the panels (b) and (c) of Fig. 5.4, where the colored regions show the  $1\sigma$ ,  $2\sigma$ , and  $3\sigma$  confidence levels, calculated from the distribution of orbital positions for each angle. The orbital parameters’ distribution is shown in blue in Fig. 5.5 for all the possible orbits allowed by the astrometric measurements, as covered by the MCMC walkers. The eccentricity solutions are well constrained to be  $< 1$ , which suggests that the RW Aur system is in a bound orbit. Therefore, the fit to the historical astrometry combined with ALMA astrometry suggests their last interaction was not an hyperbolic fly-by. By combining the periastron distance and the semi-major axis, we can use the vis-viva equation to estimate the velocity of RW Aur B relative to RW Aur A at periastron, which is  $\text{vel}_{B,per} = 14.04 \pm 0.83 \text{ km s}^{-1}$ .

Parameter	Astrometry	units
semi-major axis (sma)	$224.9^{+69.2}_{-4.6}$	mas
eccentricity (ecc)	$0.814^{+0.089}_{-0.098}$	-
inclination (inc)	$137.1^{+22.8}_{-11.5}$	deg
argument of periastron (aop)	$27.5^{+100.8}_{-2.1}$	deg
hal	$-6.0^{+7.5}_{-6.2}$	deg
epoch of periastron (tau)	$0.871^{+0.035}_{-0.007}$	-
period	$2254.6^{+811.6}_{-210.5}$	years
last periastron	$1728.3^{+20.9}_{-74.4}$	year UTC
periastron distance	$267.8^{+293.3}_{-106.5}$	mas
angle of periastron	$27.5^{+75.0}_{-7.6}$	deg
line of nodes	$69.4^{+90.2}_{-9.9}$	deg

**Table 5.3:** Highest likelihood orbital solution, and  $1\sigma$  deviation for the orbital parameters of RW Aur B around RW Aur A.

### 5.3.3 RW Aur B orbit: Excluding ALMA astrometry

Additional tests were run excluding the ALMA astrometry from the orbital fit, to test the robustness of the result. We fit the orbital parameters for three different scenarios: (i) Only using the historical astrometry from [Csépany et al. \(2017\)](#), (ii) historical astrometry and ALMA radial velocity, and (iii) historical astrometry, ALMA radial velocity, and GAIA DR3 astrometry. The results for the orbital parameters of these tests are shown in Figure 5.9. We find that the historical astrometry with the ALMA radial velocity are not able to constrain the eccentricity of the orbit. However, including the astrometry from GAIA DR3 narrows the allowed eccentricity range to  $\text{ecc} < 1$ , suggesting bound orbital solutions. Thus, ALMA astrometry and GAIA astrometry

	Property	Best value $\pm 1\sigma$	unit
RW Aur A Geometry	$\text{inc}_{\text{out}}$	$54.83 \pm 0.04$	deg
	$\text{PA}_{\text{out}}$	$39.43 \pm 0.05$	deg
	$\text{inc}_{\text{inn}}$	$60.82 \pm 0.39$	deg
	$\text{PA}_{\text{inn}}$	$35.55 \pm 0.57$	deg
RW Aur A inner disk	$f_{A1}$	$12.81 \pm 0.30$	$\mu\text{Jy}/\text{pix}$
	$\sigma_{A1}$	$16.45 \pm 0.23$	mas

**Table 5.4:** Geometry and inner disk properties of RW Aur A, as measured by an MCMC fitting described in Sect. 5.3.4.

independently suggest the interaction between the stars was not an hyperbolic fly-by. The astrometry of both instruments was not combined in a single fit, due to a non-negligible difference in astrometry between ALMA and GAIA of about 6mas, which is further discussed in Sect. 5.5.

### 5.3.4 RWAur A inner disk geometry

After subtracting the best visibility model in Sect. 5.3.1, the residuals in RW Aur A inner disk show a dipole-like structure, which could be due to a slightly different inclination for this region. On the other hand, the timescale for the binary’s latest interaction suggested by our orbital fitting was only a few hundred years ago. Thus, inner and outer disk geometry could still be misaligned. Motivated by these results, we ran an additional visibility model for the dust continuum emission in the same way described in Sect. 5.3.1. We allowed the central Gaussian component describing the inner disk emission of RW Aur A to have a different inclination and position angle ( $\text{inc}_{\text{inn}}$ ,  $\text{PA}_{\text{inn}}$ ) relative to the outer disk ( $\text{inc}_{\text{out}}$ ,  $\text{PA}_{\text{out}}$ ). The results of the MCMC are shown in Table 5.4 and Fig. 5.6.

The central Gaussian finds a higher inclination than the outer disk, with a relative difference of  $6.0 \pm 0.4$  deg between inner and outer disk. The Gaussian width at half maximum is 3 au, indicating the extent of the tentative inner disk warp. When reconstructing an image with the residual visibilities between the observation and the best model, we find the highest amplitude residual is  $5\sigma$ , smaller than for the non-warped disk model. Nonetheless, low contrast residuals from non-axisymmetric structures are observed along the whole disk extension. The remaining parameters describing RW Aur A outer disk, and RW Aur B remained consistent.

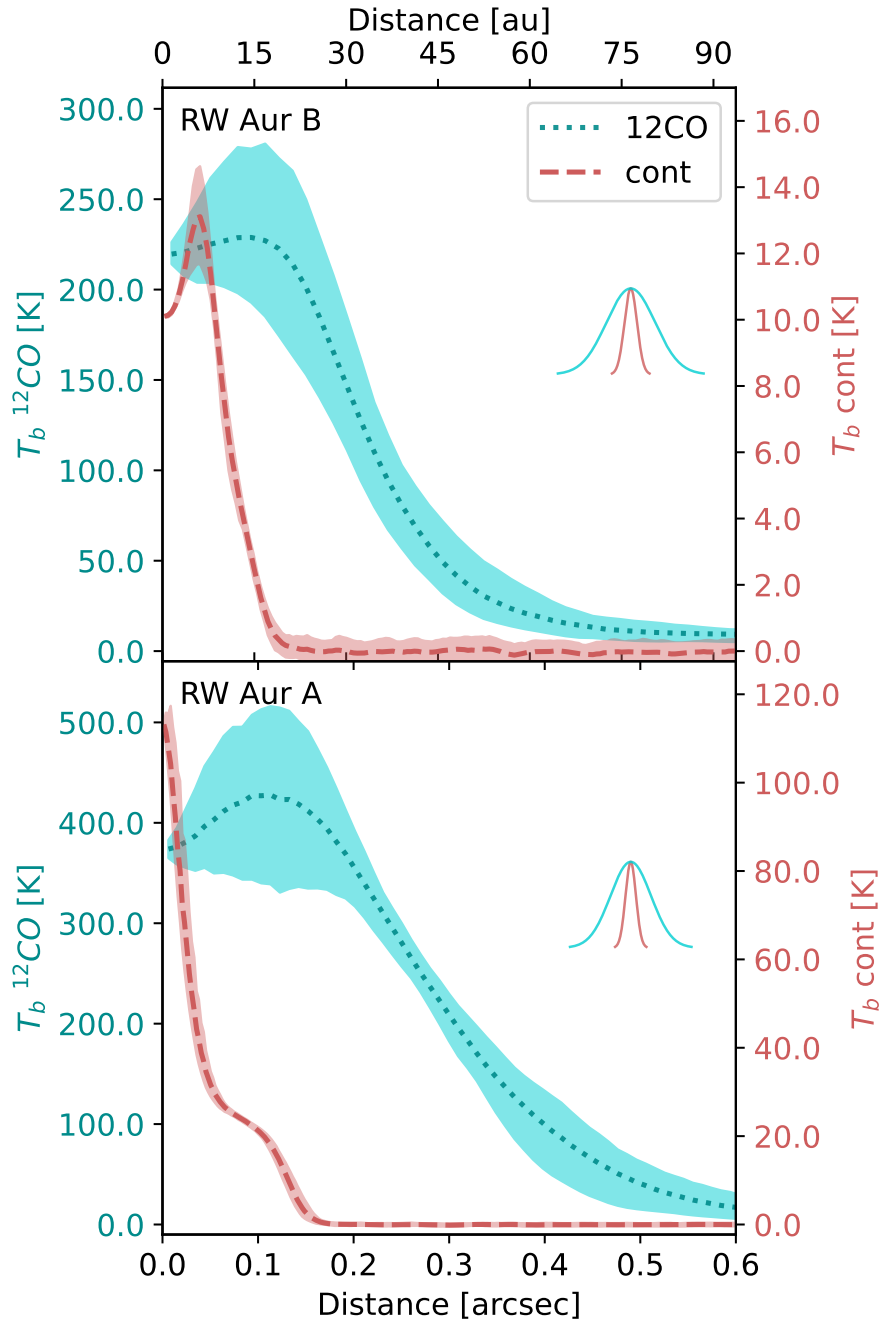


**Figure 5.2:** Dust continuum and  $^{12}\text{CO}$  azimuthally averaged profiles from the CLEAN images.

The dust continuum is shown in red, and the  $^{12}\text{CO}$  in blue, as measured from the moment 0. The colored regions show the  $1\sigma$  dispersion at each location. The Gaussians in the right of each panel represent the average radial resolution of the dust continuum image and LB  $^{12}\text{CO}$  moment 0.

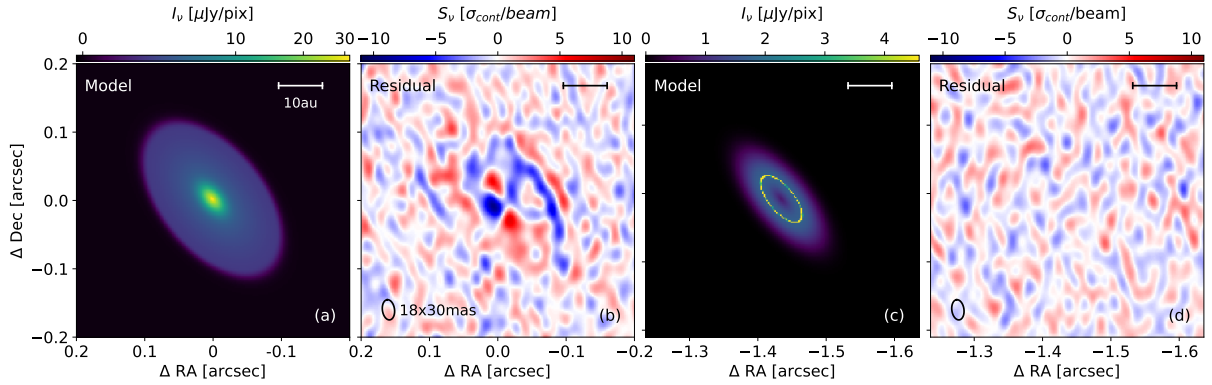


**Figure 5.3:** Best parametric models and residuals for the dust continuum emission. **Panels (a) and (c)** show the best parametric models for RW Aur A and B, respectively. **Panels (b) and (d)** show the image of the residual visibilities, not JvM corrected, in units of the image sensitivity. The scale bar is 10 au at the distance of the source, and the beam size in the residual images is shown in the lower left corner.

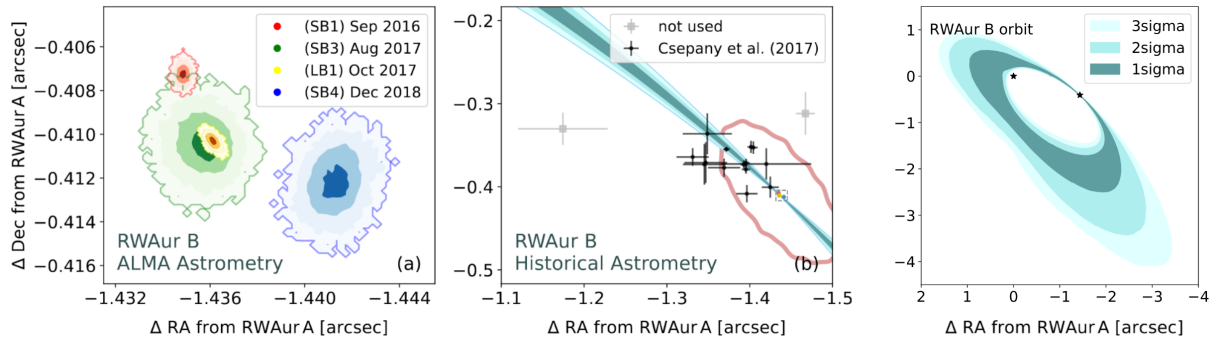


**Figure 5.4:** Orbital solutions found from ALMA and historical astrometry.

**Panel (a)** shows the density maps for RW Aur B central position relative to RW Aur A center, represented with different colors as a function of epoch. The exact date of each observation is shown in Table 5.1, as here we only show months, for reference. The darkest color shows the region where 68% of the walkers are contained ( $1\sigma$ ), and the subsequent regions show the  $2\sigma$ ,  $3\sigma$ , and  $5\sigma$  level, over which an outer contour is drawn. **Panel (b)** shows the literature astrometry of RW Aur B with respect to A, compiled by Csépany et al. (2017). The ALMA astrometry is shown inside a dashed rectangle, which represents the spatial extent of panel (a). **Panel (c)** shows the  $1\sigma$ ,  $2\sigma$ , and  $3\sigma$  regions of the allowed orbits for RW Aur B. The position of the stars is shown with a black star-marker.

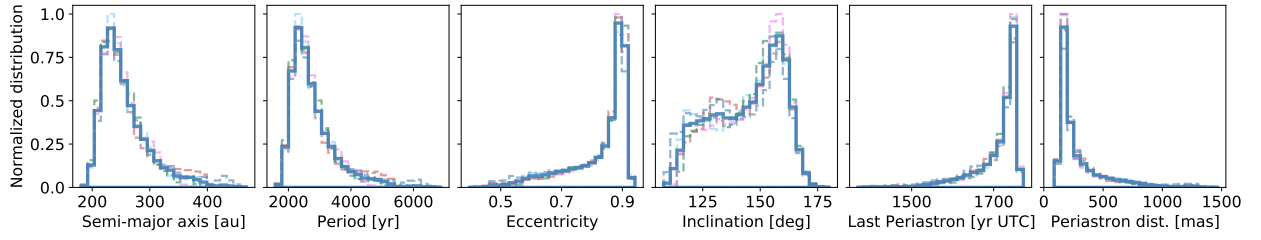


**Figure 5.5:** Normalized probability density distribution for some of the orbital parameters of RW Aur B around RW Aur A.

In solid blue, we show the distribution of all walker’s positions combined, while the dashed curves show the distribution of each MCMC, as described in Sect. 5.3.2. The last periastron year is shown in Universal Time Coordinated (UTC).

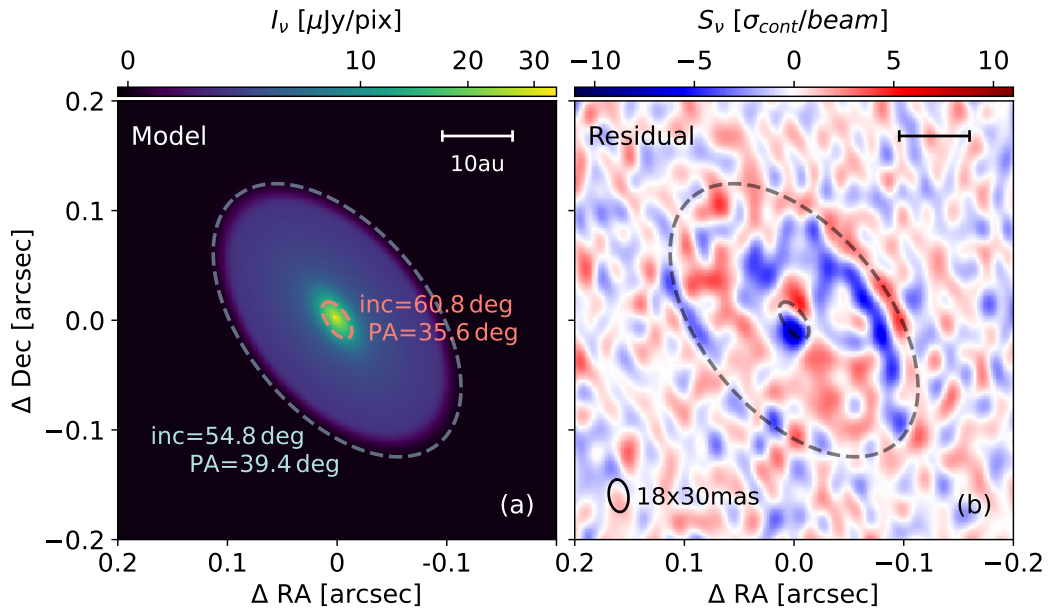


**Figure 5.6:** Warped visibility model for RW Aur A dust continuum emission. The inner disk ellipse in Panel **a)** shows the full width at half maximum size of the central Gaussian, with the geometry from Table 5.4.

## 5.4 Molecular $^{12}\text{CO}$ line emission of RWAur

Our  $^{12}\text{CO}$  observation re-detects the same features previously reported in Cabrit et al. (2006) and Rodriguez et al. (2018). Our increased sensitivity allows us to connect the clumps of emission detected in Rodriguez et al. (2018) into an intricate system of tidal arcs, filaments, and extended faint emission, which extends farther than 2000 au in projected distance from RW Aur A, as shown in panel (a) from Fig. 5.7. This panel also shows the whole field of view of the SB  $^{12}\text{CO}$  image, which combines the observations with short baseline configurations (SB1, SB2, and SB4), thus maximizing the sensitivity over extended spatial scales. The LB  $^{12}\text{CO}$  image is shown in panel (b), and its increased angular resolution allows us to resolve the disk emission and kinematics, shown in panels (c) to (f). The component “RW Aur C”, proposed in Rodriguez et al. (2018), does not resolve into a disk-like emission or coherent rotating structure. As the LB1 observation has a lower frequency resolution than the other observations, the LB  $^{12}\text{CO}$  image is limited to a velocity resolution of  $1.3 \text{ km s}^{-1}$ , which hides kinematic structures with smaller velocity amplitude.

We use the package `eddy` (Teague, 2019) to fit the keplerian rotation of each disk and estimate the mass of the central object. We do not downsample the velocity image pixels, which have a size of 4 mas. The emission was masked with an elliptical mask of size  $0.4''$  and  $0.28''$  for A and B, respectively, to avoid including non-keplerian emission surrounding each object. Due to the compact nature of the sources and the low-frequency resolution, our images cannot disentangle between upper-lower emission surfaces. Therefore, we fit them with a flat keplerian disk. The disk center, inclination, and position angle are fixed values from the dust continuum modeling. The only free parameters for each disk are the stellar mass and the central velocity in the line of sight. For RW Aur A, we obtain  $M_A = 1.238 M_\odot$  and  $VLSR_A = 6172.44 \text{ m s}^{-1}$ , while for RW Aur B we obtain  $M_B = 0.995 M_\odot$  and  $VLSR_B = 5218.24 \text{ m s}^{-1}$ . The estimation of uncertainties from `eddy` suggests the standard deviations are a fraction of a percent for the masses and velocity in the local standard of rest. Those small uncertainties come from the combination of very high sensitivity per channel and low-velocity resolution, which produces a “channelization” effect, as described in the second paragraph of Sect. 5.3.2, and seen in panels (c) to (f) from Fig. 5.7. A possible solution to this problem is to do a forward-modeling of the image cube (e.g., Izquierdo et al., 2021),

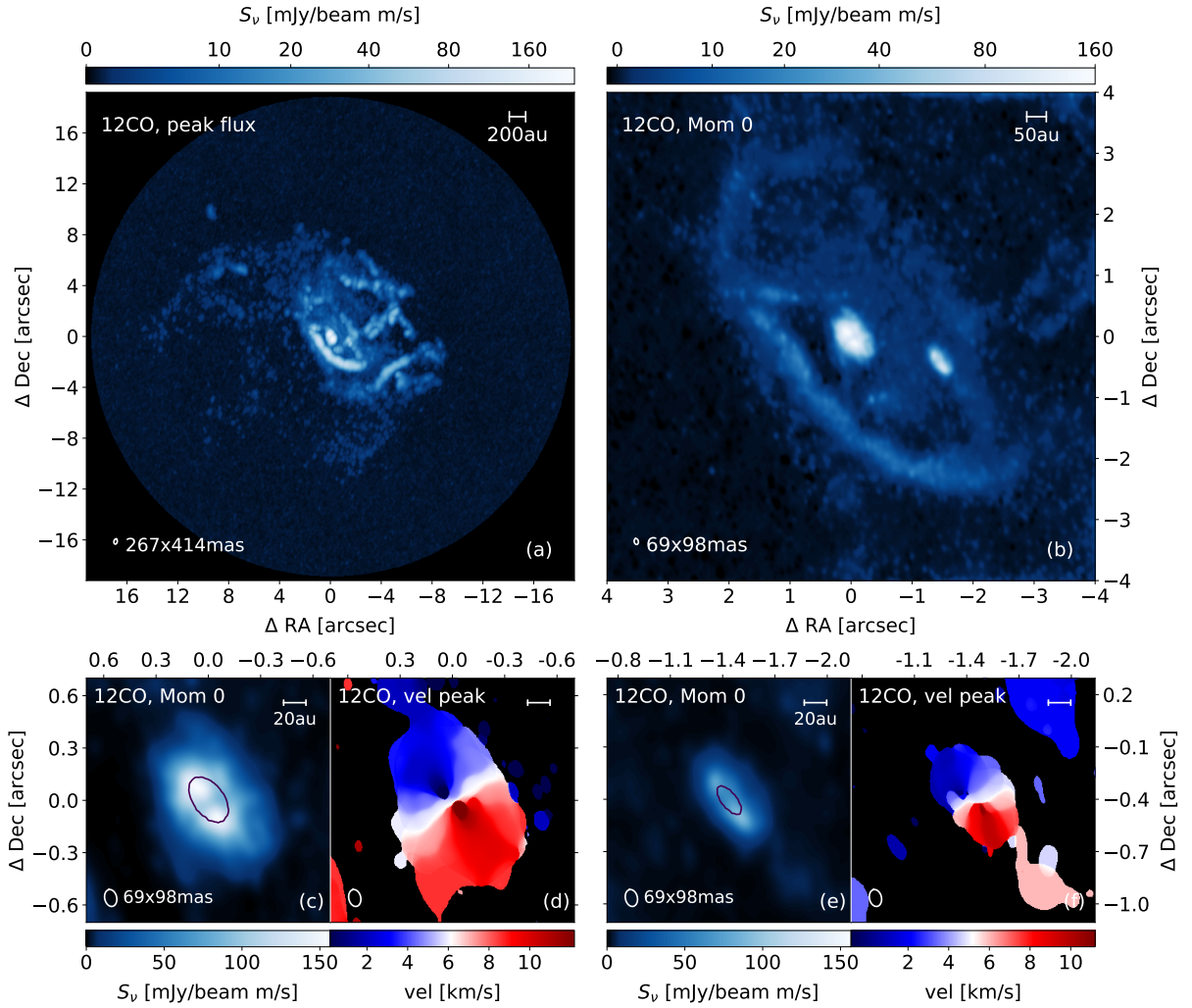


**Figure 5.7:**  $^{12}\text{CO}$  emission images at different spatial scales.

**Panel (a)** shows the peak emission of each pixel, imaged by combining the observations SB1, SB2, and SB4. **Panel (b)** shows the Moment 0 image generated by combining all the existing datasets. The elliptical lines are the contours for the  $1\sigma$ ,  $2\sigma$ , and  $3\sigma$  confidence levels for the allowed orbits, also shown in Fig. 5.4. **Panels (c) to (f)** were generated by clipping the emission at  $1.3 \text{ mJy beam}^{-1} \text{ m s}^{-1}$ . **Panels (d) and (f)** show the velocity of the peak brightness emission. The black contour in panels (c) and (e) show the  $5\sigma$  dust continuum contours.

or the visibilities (e.g., Long et al., 2021). For both approaches, a better understanding of the gas disk structure is needed.

The detected emission structures span thousands of astronomical units in spatial scales and about  $40 \text{ km s}^{-1}$  in velocity. Over this extended range, many pixels in the image are part of different  $^{12}\text{CO}$  kinematic structures, such that a single image of velocity at peak emission or moment one does not represent the kinematic richness of the gas. To alleviate this problem, we separate the channels between the blueshifted and redshifted emission relative

to RW Aur A, and calculate their peak brightness and velocities, as shown in Fig. 5.10. Most of the redshifted emission is connected to the bright southern arc, while the blueshifted emission has a semi-circle shape, with most of the emission being northwest to RW Aur A. Under the assumption that these structures are getting farther away from the RW Aur disks, then the north-western emission would be closer towards us in the line of sight direction, and the redshifted south-eastern emission would be farther away.

The high angular resolution  $^{12}\text{CO}$  image shows that neither of the disks is centrally peaked, as seen in the azimuthally averaged radial profiles in Fig. 5.2. The peak emission for  $^{12}\text{CO}$  in RW Aur A is obtained at  $113 \pm 4$  mas (about 18 au), and  $93 \pm 4$  mas (about 15 au) for RW Aur B, roughly at the locations of their outer radii in dust continuum emission. As the disks are surrounded by material from the interaction, the definition of outer radii for the gas is not as simple as in isolated disks. To avoid including emission from the surrounding material, we integrate the disk radii over an elliptical aperture of radius  $0.6''$  and  $0.45''$  for RW Aur A and B, respectively. The radius enclosing the 68% and 90% of the flux for RW Aur A are  $R_{A,CO,68\%} = 327 \pm 25$  mas and  $R_{A,CO,90\%} = 0.456 \pm 64$  mas, while for RW Aur B we obtain  $R_{B,CO,68\%} = 238 \pm 29$  mas and  $R_{B,CO,90\%} = 0.343 \pm 60$  mas. When compared to the R90% of the continuum radius, both disks have a dust to gas size ratio of 3.7, although this value should be considered as an upper limit, given that the gas radius was measured from a beam convolved  $^{12}\text{CO}$  profile.

We combined all the compact antenna observations (SB1, SB2, SB3, and SB4) to produce images for the  $^{13}\text{CO}$  and  $\text{C}^{18}\text{O}$ , using the same imaging parameters as the  $^{12}\text{CO}$ . We calculated their velocity integrated maps after clipping by  $3\sigma$ , and the results are shown in Fig. 5.11. In the  $^{13}\text{CO}$  image, the sensitivity is high enough to detect emission from the southern arc, while in  $\text{C}^{18}\text{O}$ , we only have a detection of RW Aur A disk. These images have angular resolutions similar to the SB  $^{12}\text{CO}$  image, and therefore we cannot resolve the cavities or structures, if they existed.

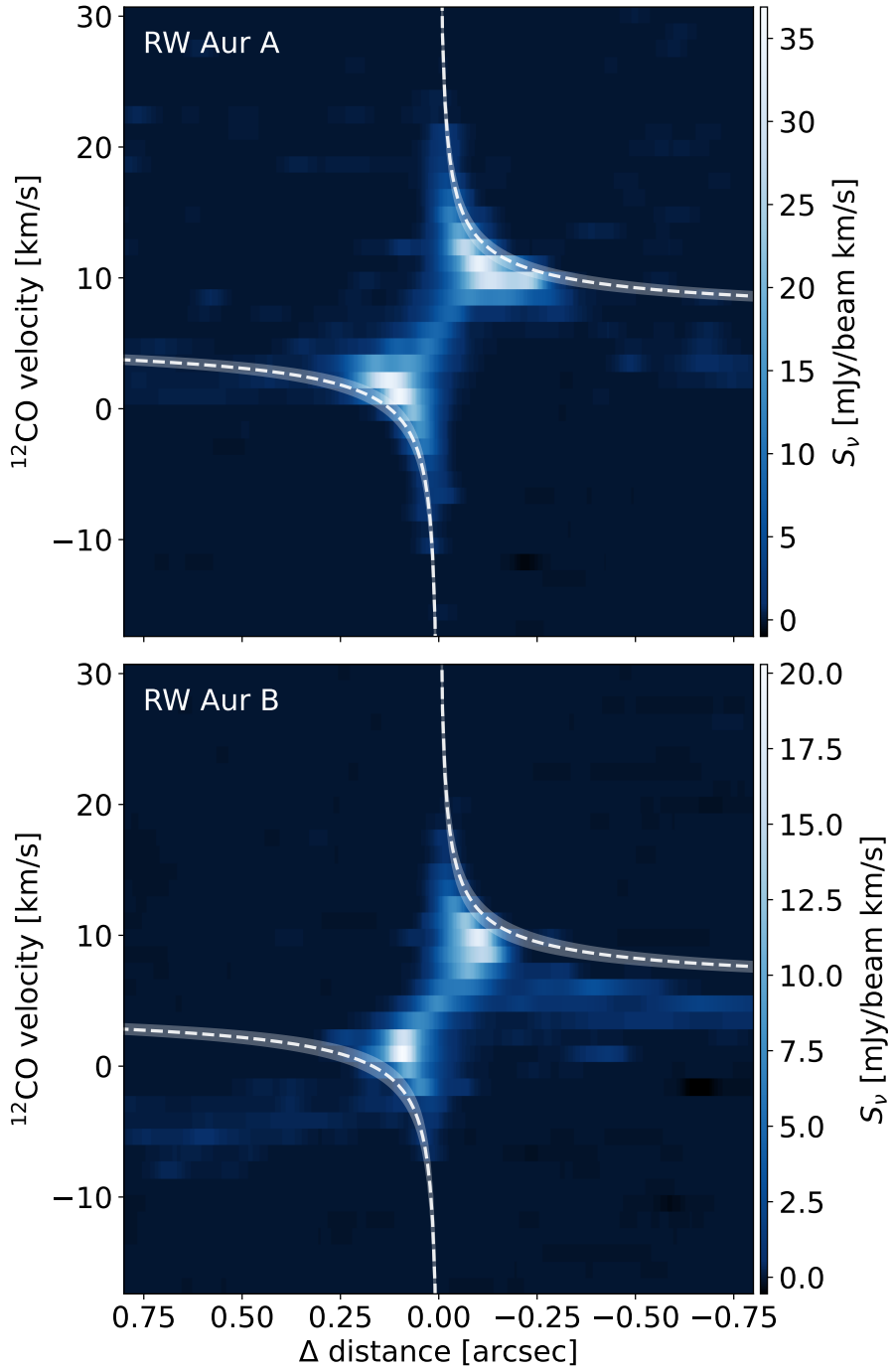


**Figure 5.8:** Position velocity diagram along the major axis of the disks, calculated from the LB  $^{12}\text{CO}$  cube.

The inclination and position angle were obtained with the dust continuum visibility modeling. The dashed rotation curve shows the best solution obtained with eddy, while the shaded region shows the  $3\sigma$  confidence region of the rotation curve by changing the stellar mass and disk systemic velocity, as discussed in 5.4.

## 5.5 The RWAur system is in a gravitationally bound orbit

The eccentricity distribution for the allowed orbital solutions suggests a gravitationally bound system with ALMA or GAIA astrometry, sharing consistent solutions for the remaining parameters. Starting from this result, we can speculate about its relation to the emission structures.

### Structure of the $^{12}\text{CO}$ emission

Previous simulations of a close encounter in RW Aur had already shown that such interactions could excite tidally stripped arcs of material, such as the one observed in the  $^{12}\text{CO}$  emission (Dai et al., 2015). The additional clumps of  $^{12}\text{CO}$  detected in Rodriguez et al. (2018) and re-detected in this work at higher sensitivity (see panel (a) in Fig. 5.7) could have been produced as tidal arcs in previous interactions of this bound system. If the orbital plane of the binaries is not aligned with the plane of their disks, a warp can be excited during the close interactions (e.g., Cuello et al., 2019). As the perturber’s gravitational influence decreases over time after periastron, the warp can smooth out towards coplanarity (Rowther et al., 2022), changing the disk-plane during this process. During the next close stellar interaction, the circumstellar material will have changed their relative disk-binary inclination, thus the next tidally stripped arc of material could be ejected in a different direction. Such an effect, added to possible temperature differences due to stellar illumination (e.g. Weber et al., 2023), are tentative explanations for the  $^{12}\text{CO}$  emission structure.

When the LB1 observation is included, both disks are spatially resolved in  $^{12}\text{CO}$ , allowing us to analyze their Keplerian rotation. Due to the low frequency resolution, we are unable to confirm or exclude warped or tidally induced velocity structures, as it has been observed in other systems (e.g., Kurtovic et al., 2018; Mayama et al., 2018). Future high angular resolution observations towards RW Aur could explore this kinematic aspect of the interaction by observing at a higher frequency resolution. Additionally, this would also allow for a more robust estimate of each stellar mass.

Neither disk is centrally peaked in the  $^{12}\text{CO}$  integrated velocity map, as shown in Fig. 5.2 and also in panels c) and e) from Fig. 5.7. In RW Aur B, a cavity is also observed in the dust continuum emission. In RW Aur A, however, the dust continuum emission is centrally peaked, and thus a cavity in the gas emission is puzzling. As the peak emission of the  $^{12}\text{CO}$  in RW Aur A

is detected at a similar distance compared to the outer disk continuum radius, an optically thick dust continuum emission could be contributing to the observed cavity. However, it remains an open question what is the role of the accretion events, inner disk misalignment, and the possible asymmetry in the morphology of the  $^{12}\text{CO}$ . Observations at similar angular resolution to LB1 but higher frequency resolution should be able to characterize the disk's gas morphology, which would also allow determining the disk's orientation.

### Structure of the dust continuum emission

We confirm the compact nature of the dust continuum disk sizes as it was also observed by [Rodriguez et al. \(2018\)](#) and [Manara et al. \(2019\)](#). Although RW Aur A dust continuum image (as reconstructed by CLEAN) seems to be a featureless disk, the residuals from our visibility modeling shows that it is rich in low contrast small scale structure. A flat disk model describes most of the emission of the disk, and it only leaves a strong structured residual in the inner disk region, suggesting a different inclination for inner and outer disk. From an additional visibility modeling, allowing the inner disk region emission to have different inclination, we find a difference of  $6.0 \pm 0.4$  deg between inner and outer disk. This tilt could have origin in the last close encounter between both stars. Additional structure is observed in the residual map after subtracting the model with a misaligned inner disk (see Fig. 5.6), suggesting that the inner disk of RW Aur A could have an azimuthally asymmetric structure. Higher angular resolution observations are needed to confirm this geometry and morphology, making RW Aur A an ideal candidate to be targeted with the near-infrared interferometric capabilities of the Very Large Telescope.

The misalignment we observe in RW Aur A is likely to be smaller than the initial tilt induced by RW Aur B during the last periastron. With SPH simulations, [Rowther et al. \(2022\)](#) showed that the timescale for smoothing out a misalignment can be as short as a couple of orbits of the outer disk edge, which is consistent with the time since last periastron recovered with our orbital fitting. In [Rowther et al. \(2022\)](#), it is also shown that the difference in the velocity field between inner and outer warped disk can produce work and dissipate energy as heat. Under the assumption of optically thick dust continuum emission, the misalignment could be contributing to the high brightness temperature observed in the midplane of RW Aur A. This could

be tested with additional observations at different wavelengths.

Considering the results of our orbital fitting, we can speculate about the origin of the dust structures in the disk of RW Aur B. From the distribution of solutions for the binaries periastron distance, we observe that the peak likelihood is comparable to the dust continuum outer radii of RW Aur A, and over 90% of the solutions are smaller than its outer gas radius. If the periastron distance is smaller than the disk radii, RW Aur B could have crossed the disk of RW Aur A during the last interaction. Such a close encounter would have induced a warp in RW Aur A, while RW Aur B could have captured some material into its own disk. Such material capture has been observed in SPH simulations of fly-by encounters (e.g., [Dai et al., 2015](#); [Cuello et al., 2019](#)), and it would also explain the ring-like structure of RW Aur B, as capturing material in outer-disk orbits is easier compared to the high-velocity inner disk orbits. The lower surface density of captured grains could translate into a lower optical depth, which is consistent with the low brightness temperature of RW Aur B. The captured material scenario also explains the similar geometry observed in both disks.

Our speculative interpretation of the disk structures would benefit from additional observations at high angular resolution. A follow-up with ALMA starting from cycle 10 would increase the time baseline of the ALMA astrometry by a factor of four compared to this work, and it would allow for a more robust determination of the time and distance at periastron. Similarly, a follow-up in longer millimeter wavelengths will enable accurate measurements of spectral index and optical depth, which could support or exclude our explanations for the origin of the substructures.

### Origin of the close-interactions

Tidal interactions are expected to truncate the disk's sizes, and both simulations and analytical studies have found that disks in multiple stellar systems are truncated to a fraction of the binary separation (e.g., [Pichardo et al., 2005](#); [Harris et al., 2012](#); [Rosotti et al., 2014](#)). In RW Aur, the orbital fitting suggests that the distance at the closest interaction could be smaller than the disk size, which is in tension with the tidal truncation scenario, especially considering that the orbital period would allow for over ten interactions in the last  $10^5$  yr.

A speculative scenario is that the RW Aur binaries have only recently

been induced into this high eccentricity orbit, possibly by an interaction with a third body. The dissolution of triple stellar systems commonly results in the formation of a single and binary stellar system (e.g., [Toonen et al., 2022](#)), and interactions with external gravitational potentials (such as a third companion) can change the eccentricity of the bound binary (e.g., [Monaghan, 1976](#); [Stone & Leigh, 2019](#); [Ginat & Perets, 2021](#)). By analyzing GAIA DR3 proper motion and parallax, [Shuai et al. \(2022\)](#) found that Gaia DR3 156431440590447744 could have had a close interaction with RW Aur about  $6 \cdot 10^3$  yrs ago, making it a candidate for gravitational interaction. It is important to consider this scenario as tentative, as both RW Aur A and RW Aur B have GAIA RUWE values over 1 (1.5 and 16.), and thus their parallax and proper motion should be reanalyzed in future works considering their binarity and variability. Observations over a longer time baseline with high precision parallax measurements could test this third companion hypothesis, and confirm if the RW Aur binaries have indeed only interacted very few times, thus not yet fully truncating the disks.

### 5.5.1 Astrometry with ALMA

Due to their compact emitting surface, stars are usually undetected in millimeter wavelength observations. As stars cannot be directly observed with instruments such as ALMA, finding a reference for high precision astrometry is challenging. When binary disks are detected, as in RW Aur, high precision astrometry can be done in a relative coordinate system, by fixing the origin in the center of one of the disks, and calculating their relative distance.

The center of each disk can be recovered with MCMC approaches such as parametric visibility modeling. To translate disks astrometry to stellar astrometry, we need the additional assumption that the stars are in the center of the disks. Even though this is a safe assumption for most of the study cases, ALMA is sensible to very low contrast asymmetries and eccentricity structures (e.g., [Andrews et al., 2021](#); [Kurtovic et al., 2022](#)), which could shift a disk center by a few milliarcseconds. Thus, any attempt to recover stellar astrometry from modeling the disk’s position must use a model which describes as much of the emission morphology as possible.

In RW Aur A, our parametric model for the dust continuum does not consider azimuthal asymmetries at any radii, which leaves low contrast structure in the residuals image (see Fig. 5.6). These residuals are problematic, as an

asymmetry in the inner disk region could slightly shift the center of the disk. For example, at the distance of RW Aur, an asymmetry located at 1 au from the star would appear at about 6 mas from the disk center. Thus, over the span of one orbit, this asymmetry could shift as much as 12 mas in position, modifying the recovered disk center by a fraction of this distance, compared to an axisymmetric model. Such effect is a possible explanation for the difference in relative astrometry between the observations SB1-LB1 and LB1-SB4, which despite having a comparable time-baseline, do not show the same relative movement between the fitted disk centers. Longer time-baselines for astrometry should be less sensible to asymmetries rotation.

In addition to carefully describing the disks' morphology, additional considerations should be taken when recovering disks' relative astrometry from ALMA data. For example, observations from different ALMA cycles should have their visibility weights standardized with tools such as `statwt` from `CASA` before they are compared with an MCMC based approach. As the flux calibration of ALMA can have variations of up to 10%, a flux scaling factor should always be fitted as part of the analysis process. Finally, if astrometry is the goal of an observation, it should be planned to have enough S/N to be self-calibrated by itself, without the need of combining it with another observation taken at a different epoch.

For RW Aur, all of our observations were taken at almost the same frequency range (see Tab. 5.1), and thus we could assume that the emission morphology was the same for every observation (neglecting possible changes due to inner disk rotation discussed in the previous paragraphs). Attempts to obtain relative astrometry with parametric models from observations taken at different wavelengths should consider the wavelength-dependence of emission morphology, as structures can change in optical depth, and thus different regions of the disks do not necessarily have the same spectral index. In such scenario, a single flux-scaling factor will not work properly.

ALMA relative binary motion has conflicting values when compared to those from GAIA DR3, which does not allow them to be fitted at the same time. A likely explanation for their difference are the systematics from GAIA when analyzing stars with circumstellar material and variable brightness (quantified by the high RUWE values, [Fitton et al., 2022](#)), and the possible shifts due to asymmetries in the inner disk region. Additional observations with ALMA and re-analysis of the GAIA data should alleviate this issue.

When a high S/N observation with ALMA antenna configuration C43-10

is analyzed, we obtain binary relative distances with accuracy comparable to that of GAIA DR3. Thus, ALMA observations arise as an alternative to study binary motion in those young star-forming regions where optical wavelengths are completely extinguished by cloud contamination. Dedicated continuum observations at high angular resolution of regions such as Ophiuchus would allow us to study the impact of binarity and interaction in the very early stages of planet's and star's formation.

## 5.6 Summary

This work analyzed the 1.3 mm emission of the RW Aur system, as observed by ALMA over a span of two years, with angular scales ranging from the ACA-7m array to ALMA C43-10 antenna configuration. We resolve the disks in continuum and in  $^{12}\text{CO}$  emission, confirming their compact nature. When analyzed in the visibility plane, RW Aur A shows evidence of low contrast non-axisymmetric structures, and tentatively the inner 3 au of the disk are misaligned by 6 deg relative to the outer disk. RW Aur B is well described by a single ring in the dust continuum emission and shows a very low brightness temperature compared to RW Aur A.

By analyzing the disk's relative distance as a function of time, and combining ALMA with historical astrometry, we constrain the allowed orbital parameter space for the RW Aur binaries. Fitting the orbit with ALMA astrometry or GAIA astrometry finds independently that the RW Aur system is in a gravitationally bound orbit. Thus, their last interaction was not a hyperbolic fly-by. Based on the recovered periastron distances, there is a high likelihood for RW Aur B having crossed the disk of RW Aur A during their last close encounter. The tentative warp of RW Aur A, and the brightness temperature structure of both disks are consistent with the disk-collision scenario. Additional observations are needed to confirm this hypothesis, mainly focused on getting a better constraint of the orbital parameter space and the physical properties of each disk.

The gas emission of RW Aur is resolved into an intricate system of extended emission and filamentary structures, which could be evidence of several close interactions, as previously proposed by [Rodriguez et al. \(2018\)](#) and suggested by our orbital fitting. Due to the limited frequency resolution of our observations, we are unable to confirm warped structures in gas emission.

Multiple epoch observations of binary systems with ALMA are a viable

alternative to recover the stellar orbital parameters, which are crucial to understanding the impact of multiplicity in the planet formation potential of each disk. Even though careful visibility modeling is needed to recover robust disk astrometry, ALMA observations can be used as an alternative to GAIA in those systems where optical emission is entirely extinct, thus positioning ALMA as an ideal tool to follow young binary disks over the long term.

## 5.7 Additional content

### 5.7.1 Dust continuum parametric models

The dust continuum emission of RW Aur A is described with a point source, a centrally peaked Gaussian and a tapered power law function. The tapered power law is shown in Eq. 5.5, where the free parameters are the flux amplitude  $f_{A2}$ , a critical radius  $R_{A2}$ , and two exponents  $(\alpha, \beta)$ . The best values and  $1\sigma$  uncertainty obtained from the visibility model are shown in Tab. 5.5

$$TP(r, f_{A2}, R_{A2}, \alpha, \beta) = f_{A2} \left( \frac{r}{R_{A2}} \right)^\alpha \left( 1 - \exp \left[ - \left( \frac{r}{R_{A2}} \right)^\beta \right] \right) \quad (5.5)$$

### 5.7.2 Orbital solutions excluding the ALMA data

We executed the same orbital fitting described in Sect. 5.3.2 for three additional scenarios: Only historical astrometry from Csépany et al. (2017), historical astrometry and ALMA radial velocity, and GAIA DR3 with historical astrometry and ALMA radial velocity. The results for those fits are shown in Fig. 5.9 and compared with the best orbital solution from the ALMA astrometry. The best orbital fit to the ALMA astrometry is shown in Tab. 5.3. Fitting historical astrometry does not constrain the eccentricity of the system, however, both ALMA and GAIA DR3 astrometry constrain the eccentricity to be  $\text{ecc} < 1$ .

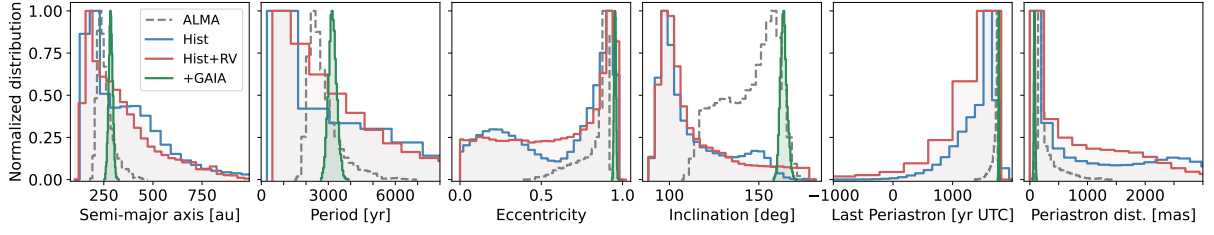


**Figure 5.9:** Same as Figure 5.5, but showing the solutions when excluding the ALMA astrometry.

For comparison, orbital solutions including ALMA astrometry are shown with a gray dashed line. Fit to historical astrometry is shown in blue, including the ALMA radial velocity to the fit is shown in red, and including GAIA DR3 is shown in green.

	Property	Best value	unit
RW Aur A position relative to phasecenter	$\Delta\text{RA (SB1)}$	$0.65 \pm 0.02$	mas
	$\Delta\text{Dec (SB1)}$	$-0.14 \pm 0.01$	mas
	$\Delta\text{RA (SB3)}$	$0.44 \pm 0.04$	mas
	$\Delta\text{Dec (SB3)}$	$0.18 \pm 0.12$	mas
	$\Delta\text{RA (SB4)}$	$1.41 \pm 0.09$	mas
	$\Delta\text{Dec (SB4)}$	$0.41 \pm 0.07$	mas
	$\Delta\text{RA (LB1)}$	$0.12 \pm 0.05$	mas
	$\Delta\text{Dec (LB1)}$	$3.16 \pm 0.06$	mas
Flux Amplitude Scaling	$i_{SB1}$	$1.063 \pm 0.001$	-
	$i_{SB2}$	$1.055 \pm 0.006$	-
	$i_{SB3}$	$1.006 \pm 0.002$	-
	$i_{LB1}$	$0.970 \pm 0.001$	-
RW Aur A profile	$f_{A0}$	$522.08^{+25.39}_{-28.29}$	$\mu\text{Jy/pix}$
	$f_{A1}$	$14.19 \pm 0.41$	$\mu\text{Jy/pix}$
	$\sigma_{A1}$	$14.48 \pm 0.38$	mas
	$f_{A2}$	$1.27 \pm 0.02$	$\mu\text{Jy/pix}$
	$r_{A2}$	$129.46 \pm 0.25$	mas
	$\alpha_A$	$-0.44 \pm 0.01$	-
	$\beta_A$	$-22.07 \pm 0.62$	-
RW Aur B profile	$f_{B1}$	$9.91^{+1.38}_{-1.80}$	$\mu\text{Jy/pix}$
	$r_{B1}$	$41.49 \pm 0.40$	mas
	$\sigma_{B1}$	$0.68 \pm 0.31$	mas
	$f_{B2}$	$1.73^{+0.03}_{-0.03}$	$\mu\text{Jy/pix}$
	$r_{B2}$	$40.07 \pm 1.32$	mas
	$\sigma_{B2}$	$30.81 \pm 0.93$	mas

**Table 5.5:** Best fit parameters for the visibility modeling of the dust continuum emission. The pixel size was 4 mas.

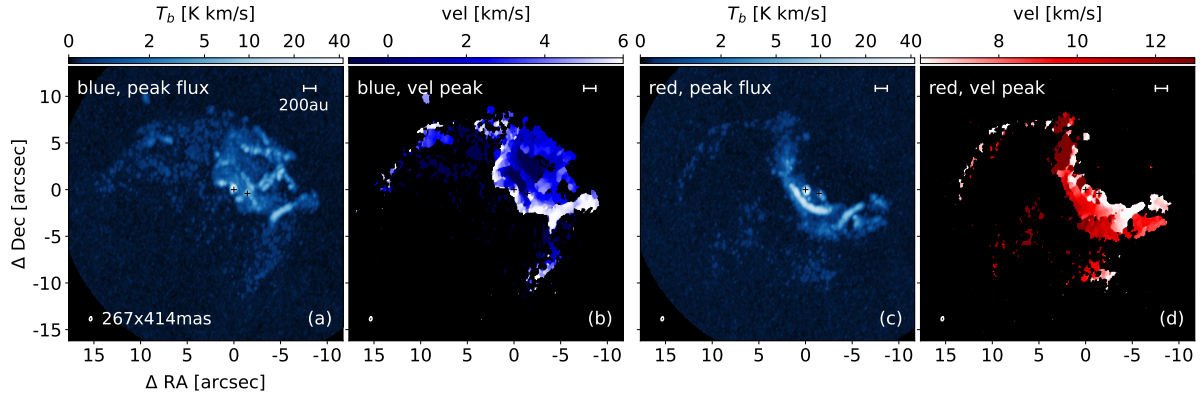


**Figure 5.10:** Blueshifted and redshifted molecular line emission of  $^{12}\text{CO}$ , relative to RW Aur A systemic velocity.

The beam size in the lower left corner and the scale bar in the upper right are the same for all the panels. The centers of the 2 disks are shown with black + symbols.

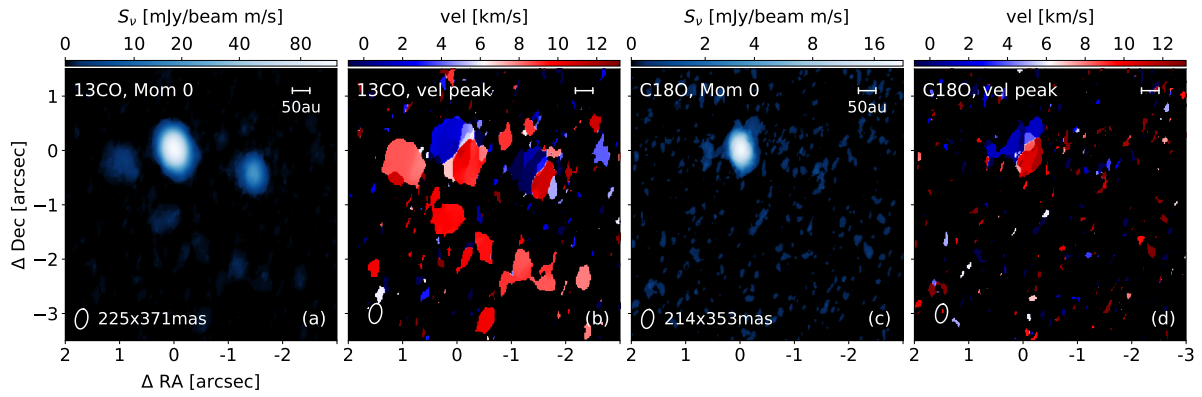


**Figure 5.11:** Integrated maps of  $^{13}\text{CO}$  and  $\text{C}^{18}\text{O}$  molecular line emission.

Moment 0 and velocity at peak flux of  $^{13}\text{CO}$  are shown in panels (a) and (b), while the same images for  $\text{C}^{18}\text{O}$  are shown in panels (c) and (d). Beam sizes are shown in lower left corner, and a scale bar of 20 au is shown in the upper right corner.

### 5.7.3 RWAur CO isotopologues emission

The kinematical map of RW Aur CO isotopologues are shown in Fig. 5.10 and Fig. 5.11. The  $^{13}\text{CO}$  J:2-1 emission is detected in both disks, and the bright tidal arm to the south of RW Aur A is detected too. In  $\text{C}^{18}\text{O}$  J:2-1 emission, only RW Aur A is detected. Due to the moderate angular resolution of these detections, it is not possible to explore the radial morphology of the emission with the same detail as the dust continuum or  $^{12}\text{CO}$  J:2-1 emission.





# 6

## Summary and Future Prospects

---

### 6.1 Summary of my thesis

Planets are formed from the gas and dust content in planet-forming disks around young stars. By studying a disk's density, temperature, and chemical structure, we can gain insight into its potential for planet formation and the existing newborn planets that could shape the disk morphology. In this thesis, I have studied the structures of disks around those stars that are the most common in our galaxy: Very low mass stars and stars that are part of multiple stellar systems.

In the case of very low mass stars, the high angular resolution observations have found substructured emission in the disks that are spatially resolved, showing evidence of tentative unresolved substructures in some of the most compact disks. These findings support the idea that disk substructures, which could be related to planet formation, can be generated in the disks of very low mass stars, despite the additional challenges they could have compared to circumstellar disks around solar-type objects, such as the strong radial drift.

By studying the circumbinary disk around CS Cha, I showed that the morphology of the disk could be used as an indirect tracer of newborn planets. Due to the presence of the binary stars at the center of the disk, we can use the deviations from the expected disk morphology to differentiate between systems that host Saturn-like planets and those which do not.

The impact of companion-disk interaction in a circumstellar disk is strongly dependent on the mass of the perturber and its orbit around the primary star. By studying the gas and dust emission from the RW Aur system, I showed the feasibility of recovering the orbital motion of the binaries with millimeter interferometric observations. The analysis suggests the binaries

are in a gravitationally bound orbit and could undergo close interactions every few thousand years. The last close interaction is the most likely responsible for all the substructures we observe at millimeter wavelengths.

The detection of structures like rings, asymmetries, and spirals in planet-forming disks provides initial clues about ongoing planet formation processes. Understanding the mechanisms originating these features requires a detailed study of their morphology, as shown in this thesis. As a wide range of mechanisms can affect planet formation, it remains crucial to conduct in-depth investigations of individual sources. Future research should prioritize the development of analysis techniques that can extract maximum information from observations, and accurately describing emission structures.

## 6.2 Future Prospects

### 6.2.1 Maximizing information recovery from gas observations through visibility modeling

Building kilometer-sized single-dish telescopes is unfeasible on Earth’s surface. Therefore, increasing the angular resolution of astronomical observations can only be done with interferometers. Several interferometric facilities are pushing upgrades or building new capabilities (e.g., ALMA 2030, ngVLA, SKA), meaning that understanding how to maximize the information recovery from interferometric data will continue to be crucial in the upcoming decades.

The quality of images generated from large interferometers such as ALMA is high enough to analyze the dust and gas emission structure of planet-forming disks in the image plane. However, the limitations and assumptions of the image reconstruction process can reduce the information recovery compared to direct analysis of the visibility domain. The works in this thesis exemplify that visibility-based analysis informed by prior parametric models is key to describing subtle emission structures.

Currently, most of the analysis of gas emission observations is done in the image plane due to the challenges of doing frequency-dependent intensity models. Due to the limitations explained in Section 1.5.1, we are currently restricted to studying the structure of the gas emission in extended bright disks, observed with deep integration times. However, most of the disks do not meet those requirements, and thus an alternative approach is needed. In Section 3.11, I showed a proof of concept for modeling the visibilities of gas emission. Improving this method’s complexity and efficiency will allow us to extend the studies of gas substructures into moderate and low resolution and sensitivity observations.

### 6.2.2 Astrometry of binary disks with ALMA

Constraining the orbital parameters of binaries is needed to recover the distance and epoch of the last periastron, which is essential to understand the structures (or lack of) observed in their disks and the impact of interactions in the planet-formation potential of each system. Recovering the binary orbits from optical astrometry is challenging, as young stellar objects are commonly obscured by their natal cloud and show variable optical brightness. Instead,

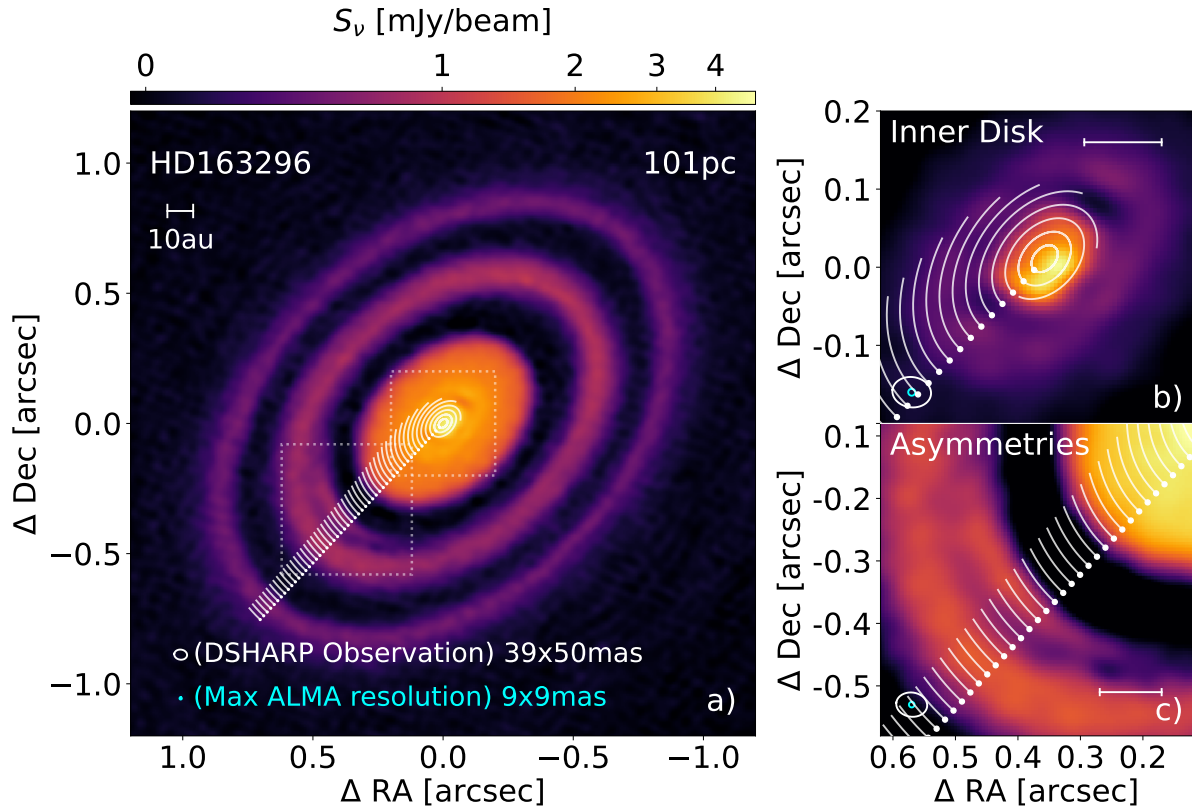


**Figure 6.1:** Expected Keplerian motion at different radii over HD163296, in a period of 10 yrs. Panel a) shows the dust continuum emission of HD 163296 at 1.25 mm, as observed by DSHARP (Isella et al., 2018). The white lines are radially-spaced every 3 au, and show the clockwise movement due to Keplerian rotation over a period of 10 yr. Dotted squares show the area covered by panels b) and c). Changes can be appreciated both in the disk’s inner and outer regions, with displacements larger than the angular resolution of DSHARP. Currently, ALMA can achieve angular resolutions  $\times 4$  higher than in this observation, increasing the need for time-domain considerations.

we can use time-domain analysis of interferometric observations to recover the stellar astrometry by following the position of the disks. The feasibility of obtaining (sub-)milliarcsec accuracy in relative astrometry with ALMA has been demonstrated in the work shown in Chapter 5, and ongoing work on the binary systems presented in Kurtovic et al. (2018) has shown that the same approach is reproducible in other multiple stellar systems.

Analyzing the disk’s relative distance as a function of time opens an alternative path to recover the orbital motion of very young binary systems and explore their impact on the planet formation potential of their disks. Future studies focused on larger samples from the nearby SFR could provide unprecedented orbital information on those young binary systems.

### 6.2.3 Disks rotation as a probe for the origin of substructures

In Chapter 5, I showed the capabilities of ALMA for detecting the Keplerian motion of binary disks. However, the disks also rotate around the central star near Keplerian speeds. Even though the Keplerian movement expected for planet-forming disks in nearby SFR is only a few milliarcseconds per year, ALMA has enough sensitivity and angular resolution to detect it, as shown in Figure 6.1. It has been predicted that some substructures should have a time-domain evolution, and the most accessible examples are asymmetries and spirals.

In the case of brightness asymmetries in the azimuthal profile, if produced by an eccentricity “traffic-jam” effect (see discussion in Section 4.7), then it would remain stationary at the location of an eccentric ring apoastron. This is different from co-rotational asymmetries or vortices, which would rotate at near Keplerian speeds. Checking the movement of the central asymmetry in RW Aur A over the time domain could help differentiate over those scenarios (as shown in Figure 6.2), and even for asymmetries located at tens of astronomical units, their movement over a few years is large enough to be detectable (see Figure 6.1).

Unveiling the origin of spiral density waves is another promising future work. With information over the time domain, it is easier to disentangle the origin of spirals between internal disk perturbers, external disk perturbers, and gravitational instabilities, as they all have different time behaviors (see discussion by Ren et al., 2020, and references therein). Follow-up observations of the disks with spirals detected in the DSHARP sources are the ideal sample to test this variability due to the extended period since the DSHARP observations.

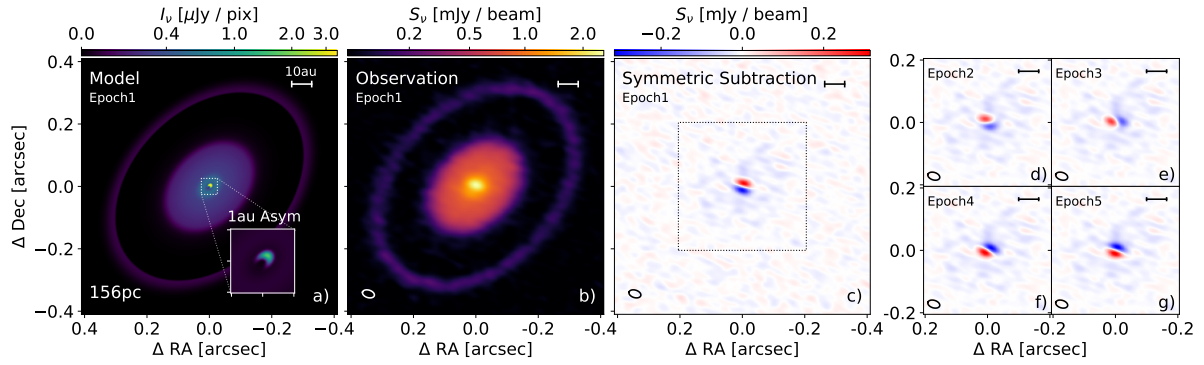


**Figure 6.2:** A synthetic dust model of a disk has an asymmetry at 1 au from the star in (a), which is not detected in the 1.3mm image of its simulated observation in (b), with the same sensitivity and angular resolution of DSHARP (Andrews et al., 2018). However, when a visibility model for the axisymmetric structure is subtracted, the residuals show that the disk is not-axisymmetric at its center (see c). We cannot see structures smaller than the angular resolution, but we can detect if it changes as a function of time (c-g), revealing the asymmetry Keplerian rotation. Synthetic observations were generated with my software package [SIMIO](#), presented in Chapter 2.

## List of first-author publications included in this thesis

These scientific publications have been published during my doctoral studies, or are in preparation for publication within this year.

1. **N.T. Kurtovic**, in prep, “Recovering the gas properties of a planet-forming disk through parametric visibility-modeling”.
2. **N.T. Kurtovic**, in prep, “RW Aur at high angular resolution, with ALMA”.
3. **N.T. Kurtovic**, 2022, “SIMIO-continuum: Connecting simulations to interferometric observations”, JOSS, in review.
4. **N.T. Kurtovic**, P. Pinilla, A. B. T. Penzlin, et al., 2022, “The morphology of CS Cha circumbinary disk suggesting the existence of a Saturn-mass planet”, A&A, 645, A139.
5. **N.T. Kurtovic**, P. Pinilla, M. Benisty, et al., 2021, “Size and Structures of Disks around Very Low Mass Stars in the Taurus Star-Forming Region”, A&A, 645, A139.

## List of publications not included in this thesis

In this list, I compile all my publications where I have lead or contributed to the projects. The results of these publications are not included as part of this thesis, although some of them are briefly mentioned in the context of the presented works.

1. **N.T. Kurtovic**, L.M. Pérez, M. Benisty, et al., 2018, “The Disk Substructures at High Angular Resolution Project (DSHARP). IV. Characterizing Substructures and Interactions in Disks around Multiple Star Systems”, ApJL, 869, L44.
2. L. Flores-Rivera, M. Flock, **N.T. Kurtovic**, et al., “Forbidden emission lines in protoplanetary disks with MUSE”, A&A, in review.
3. P. Pinilla, M. Benisty, **N.T. Kurtovic**, et al., 2022, “Distributions of gas and small and large grains in the LkHa330 disk trace a young planetary system”, A&A, 665, A128.

4. C. Bergez-Casalou, B. Bitsch, **N.T. Kurtovic**, P. Pinilla, 2022, “Constraining giant planet formation with synthetic ALMA images of the Solar System’s natal protoplanetary disk”, *A&A*, 659, A6.
5. M. Ackerman Pyerin, T. N. Delage, **N.T. Kurtovic**, et al., 2021, “Constraining the properties of the potential embedded planets in the disk around HD 100546”, *A&A*, 656, A150.
6. P. Pinilla, **N.T. Kurtovic**, M. Benisty, et al., 2021, “A bright inner disk and structures in the transition disk around the very low-mass star CIDA 1”, *A&A*, 649, A122.
7. L. Wölfer, S. Facchini, **N.T. Kurtovic**, et al., 2021, “A highly non-Keplerian protoplanetary disc. Spiral structure in the gas disc of CQ Tau”, *A&A*, 648, A19.
8. J. S. Jenkins, M. R. Diaz, **N.T. Kurtovic**, et al., 2020, “An ultrahot Neptune in the Neptune desert”, *Nature Astronomy*, 4, 1148.
9. P. Weber, et al. (including **N.T. Kurtovic**), 2022, “The SPHERE view of three interacting twin disc systems in polarised light”, in review.
10. C. Ginski, et al. (including **N.T. Kurtovic**), 2022, “A polarimetric scattered light survey of planet-forming disks in Chamaeleon-I”, in review.
11. J. Dietrich, et al. (including **N.T. Kurtovic**), 2022, “EDEN Survey: Small Transiting Planet Detection Limits and Constraints on the Occurrence Rates for Late M Dwarfs within 15 pc”, in review.
12. M. Gárate, et al. (including **N.T. Kurtovic**), 2022, “Millimeter emission in photoevaporating disks is determined by early substructures”, in review.
13. J. Bae, et al. (including **N.T. Kurtovic**), 2022, “Molecules with ALMA at Planet-forming Scales (MAPS): A Circumplanetary Disk Candidate in Molecular-line Emission in the AS 209 Disk”, *ApJL*, 934, L20.
14. P. Curone, et al. (including **N.T. Kurtovic**), 2022, “A giant planet shaping the disk around the very low-mass star CIDA 1”, *A&A*, 665, A25.

15. I. Czekala, et al. (including **N.T. Kurtovic**), 2021, “Molecules with ALMA at Planet-forming Scales (MAPS). II. CLEAN Strategies for Synthesizing Images of Molecular Line Emission in Protoplanetary Disks”, *ApJS*, 257, 2.
16. K. Öberg, et al. (including **N.T. Kurtovic**), 2021, “Molecules with ALMA at Planet-forming Scales (MAPS). I. Program Overview and Highlights”, *ApJS*, 257, 1.
17. S.B. Brown-Sevilla, et al. (including **N.T. Kurtovic**), 2021, “Multi-wavelength analysis of the protoplanetary disk around WaOph 6”, *A&A*, 629, A111.
18. M. Benisty, et al. (including **N.T. Kurtovic**), 2021, “ A Circumplanetary Disk around PDS70c ”, *ApJL*, 916, L2.
19. S.M. Andrews, et al. (including **N.T. Kurtovic**), 2021, “Limits on Millimeter Continuum Emission from Circumplanetary Material in the DSHARP Disks”, *ApJ*, 916, 51.
20. S. Jorquera, et al. (including **N.T. Kurtovic**), 2021, “A Search for Companions via Direct Imaging in the DSHARP Planet-forming Disks”, *AJ*, 161, 146.
21. R.C. Challener, et al. (including **N.T. Kurtovic**), 2021, “Identification and Mitigation of a Vibrational Telescope Systematic with Application to Spitzer”, *The Planetary Science Journal*, 2, 9.
22. L. Cieza, et al. (including **N.T. Kurtovic**), 2021, “The Ophiuchus DIsc Survey Employing ALMA (ODISEA) - III. The evolution of substructures in massive discs at 3-5 au resolution”, *MNRAS*, 501, 2934.
23. L. D. Nielsen, et al. (including **N.T. Kurtovic**), 2020, “Mass determinations of the three mini-Neptunes transiting TOI-125”, *MNRAS*, 492, 5399.
24. R. Cloutier, et al. (including **N.T. Kurtovic**), 2019, “Characterization of the L 98-59 multi-planetary system with HARPS. Mass characterization of a hot super-Earth, a sub-Neptune, and a mass upper limit on the third planet”, *A&A*, 629, A111.
25. J.S. Jenkins, et al. (including **N.T. Kurtovic**), 2019, “Proxima Centauri b is not a transiting exoplanet”, *MNRAS*, 487, 268.

26. M.G. Ubeira, et al. (including **N.T. Kurtovic**), 2019, “A dust and gas cavity in the disc around CQ Tau revealed by ALMA”, MNRAS, 486, 4638.
27. L.M. Pérez, et al. (including **N.T. Kurtovic**), 2018, “The Disk Substructures at High Angular Resolution Project: X. Multiple rings, a misaligned inner disk, and a bright arc in the disk around T Tauri star HD 143006”, ApJL, 869, L50.
28. C.P. Dullemond, et al. (including **N.T. Kurtovic**), 2018, “The Disk Substructures at High Angular Resolution Project: VI. Dust trapping in thin-ringed protoplanetary disks”, ApJL, 869, L46.
29. S.M. Andrews, et al. (including **N.T. Kurtovic**), 2018, “The Disk Substructures at High Angular Resolution Project: I. Motivation, Sample, Calibration, and Overview”, ApJL, 869, L41.

## Bibliography

---

- Adachi, I., Hayashi, C., & Nakazawa, K. 1976, *Progress of Theoretical Physics*, 56, 1756 [18](#)
- Alexander, R., Pascucci, I., Andrews, S., Armitage, P., & Cieza, L. 2014, in *Protostars and Planets VI*, ed. H. Beuther, R. S. Klessen, C. P. Dullemond, & T. Henning, 475–496 [22](#)
- Alexander, R. D., & Armitage, P. J. 2007, *MNRAS*, 375, 500 [78](#)
- ALMA Partnership, Brogan, C. L., Pérez, L. M., et al. 2015, *ApJ*, 808, L3 [23](#)
- Alves, F. O., Caselli, P., Girart, J. M., et al. 2019, *Science*, 366, 90 [38](#)
- Andrews, S. M. 2020, *ARA&A*, 58, 483 [15](#), [17](#), [19](#), [35](#)
- Andrews, S. M., Rosenfeld, K. A., Kraus, A. L., & Wilner, D. J. 2013, *ApJ*, 771, 129 [26](#), [59](#), [70](#), [71](#), [73](#), [80](#), [109](#), [110](#), [130](#), [147](#)
- Andrews, S. M., Terrell, M., Tripathi, A., et al. 2018a, *ApJ*, 865, 157 [81](#)
- Andrews, S. M., & Williams, J. P. 2005, *ApJ*, 631, 1134 [26](#)
- Andrews, S. M., Wilner, D. J., Zhu, Z., et al. 2016, *ApJ*, 820, L40 [23](#)
- Andrews, S. M., Huang, J., Pérez, L. M., et al. 2018, *ApJ*, 869, L41 [23](#), [49](#), [58](#), [74](#), [148](#)
- Andrews, S. M., Elder, W., Zhang, S., et al. 2021, arXiv e-prints, arXiv:2105.08821 [54](#), [107](#), [115](#), [165](#)
- Ansdell, M., Williams, J. P., van der Marel, N., et al. 2016, *ApJ*, 828, 46 [70](#), [109](#), [147](#)

Ansdell, M., Williams, J. P., Trapman, L., et al. 2018, *ApJ*, 859, 21 [19](#), [84](#), [85](#)

Arlt, R., & Urpin, V. 2004, *A&A*, 426, 755 [22](#)

Armstrong, D. J., Osborn, H. P., Brown, D. J. A., et al. 2014, *MNRAS*, 444, 1873 [103](#)

Artymowicz, P., Clarke, C. J., Lubow, S. H., & Pringle, J. E. 1991, *ApJ*, 370, L35 [36](#)

Artymowicz, P., & Lubow, S. H. 1994, *ApJ*, 421, 651 [22](#), [36](#), [37](#), [78](#), [103](#)

Ataiee, S., Pinilla, P., Zsom, A., et al. 2013, *A&A*, 553, L3 [130](#), [132](#)

Bae, J., Hartmann, L., & Zhu, Z. 2015, *ApJ*, 805, 15 [22](#)

Bae, J., Isella, A., Zhu, Z., et al. 2022, arXiv e-prints, arXiv:2210.13314 [5](#), [20](#), [22](#), [24](#), [28](#)

Bae, J., Teague, R., & Zhu, Z. 2021, *ApJ*, 912, 56 [51](#)

Bae, J., & Zhu, Z. 2018a, *ApJ*, 859, 118 [22](#)

—. 2018b, *ApJ*, 859, 119 [22](#)

Balbus, S. A., & Hawley, J. F. 1991, *ApJ*, 376, 214 [22](#)

Barranco, J. A., & Marcus, P. S. 2005, *ApJ*, 623, 1157 [22](#)

Barraza-Alfaro, M., Flock, M., Marino, S., & Pérez, S. 2021, *A&A*, 653, A113 [22](#), [51](#)

Bate, M. R. 2018, *MNRAS*, 475, 5618 [36](#), [37](#), [130](#)

Bayo, A., Joergens, V., Liu, Y., et al. 2017, *ApJ*, 841, L11 [129](#)

Beckwith, S. V. W., & Sargent, A. I. 1993, *ApJ*, 402, 280 [29](#)

Beckwith, S. V. W., Sargent, A. I., Chini, R. S., & Guesten, R. 1990, *AJ*, 99, 924 [15](#)

Benisty, M., Bae, J., Facchini, S., et al. 2021, *ApJ*, 916, L2 [21](#), [129](#)

Benítez-Llambay, P., & Masset, F. S. 2016, *ApJS*, 223, 11 [120](#)

Beuzit, J. L., Vigan, A., Mouillet, D., et al. 2019, *A&A*, 631, A155 [121](#)

Birnstiel, T., Dullemond, C. P., & Pinilla, P. 2013, *A&A*, 550, L8 [131](#)

Birnstiel, T., Fang, M., & Johansen, A. 2016, *Space Sci.Rev.*, 205, 41 [131](#)

Birnstiel, T., Dullemond, C. P., Zhu, Z., et al. 2018, *ApJ*, 869, L45 [27](#)

Bolton, J. G., & Slee, O. B. 1953, *Australian Journal of Physics*, 6, 420 [43](#)

Booth, M., Schulz, M., Krivov, A. V., et al. 2021, *MNRAS*, 500, 1604 [112](#)

Bozhinova, I., Scholz, A., Costigan, G., et al. 2016, *MNRAS*, 463, 4459 [141](#)

Briceño, C., Hartmann, L., Stauffer, J., & Martín, E. 1998, *AJ*, 115, 2074 [79](#)

Brown-Sevilla, S. B., Keppler, M., Barraza-Alfaro, M., et al. 2021, *A&A*, 654, A35 [21](#), [23](#)

Cabrit, S., Pety, J., Pesenti, N., & Dougados, C. 2006, *A&A*, 452, 897 [141](#), [142](#), [146](#), [158](#)

Calvet, N., D'Alessio, P., Hartmann, L., et al. 2002, *ApJ*, 568, 1008 [19](#)

Casassus, S., & Pérez, S. 2019, *ApJ*, 883, L41 [32](#)

Casassus, S., Wright, C. M., Marino, S., et al. 2015, *ApJ*, 812, 126 [23](#)

Chou, M.-Y., Takami, M., Manset, N., et al. 2013, *AJ*, 145, 108 [141](#)

Cieza, L. A., Ruíz-Rodríguez, D., Hales, A., et al. 2019, *MNRAS*, 482, 698 [147](#)

Cieza, L. A., González-Ruilova, C., Hales, A. S., et al. 2021, *MNRAS*, 501, 2934 [23](#), [58](#), [74](#)

Clark, B. G. 1980, *A&A*, 89, 377 [45](#)

Clarke, C. J., Gendrin, A., & Sotomayor, M. 2001, *MNRAS*, 328, 485 [22](#)

Clarke, C. J., & Pringle, J. E. 1993, *MNRAS*, 261, 190 [36](#)

Coradini, A., Magni, G., & Federico, C. 1981, *A&A*, 98, 173 [15](#)

Crida, A., Morbidelli, A., & Masset, F. 2006, *Icarus*, 181, 587 [79](#)

Cs ep any, G., van den Ancker, M.,  brah am, P., et al. 2017, A&A, 603, A74  
[141](#), [150](#), [153](#), [156](#), [168](#)

Cuello, N., Dipierro, G., Mentiplay, D., et al. 2019, MNRAS, 483, 4114 [22](#),  
[37](#), [38](#), [130](#), [162](#), [164](#)

Czekala, I., Andrews, S. M., Jensen, E. L. N., et al. 2015, ApJ, 806, 154 [87](#)

Czekala, I., Loomis, R. A., Teague, R., et al. 2021, ApJS, 257, 2 [46](#), [47](#), [107](#),  
[146](#)

Daemgen, S., Natta, A., Scholz, A., et al. 2016, A&A, 594, A83 [35](#)

Dai, F., Facchini, S., Clarke, C. J., & Haworth, T. J. 2015, MNRAS, 449,  
1996 [142](#), [162](#), [164](#)

Dartois, E., Dutrey, A., & Guilloteau, S. 2003, A&A, 399, 773 [29](#)

de Juan Ovelar, M., Pinilla, P., Min, M., Dominik, C., & Birnstiel, T. 2016,  
MNRAS, 459, L85 [131](#)

Dodin, A., Grankin, K., Lamzin, S., et al. 2019, MNRAS, 482, 5524 [142](#)

Dodson-Robinson, S. E., & Salyk, C. 2011, ApJ, 738, 131 [77](#), [78](#)

Dong, R., Liu, S.-y., Eisner, J., et al. 2018, ApJ, 860, 124 [23](#)

Dong, R., Liu, H. B., Cuello, N., et al. 2022, Nature Astronomy, 6, 331 [38](#)

Doyle, L. R., Carter, J. A., Fabrycky, D. C., et al. 2011, Science, 333, 1602  
[103](#)

Dullemond, C. P., & Dominik, C. 2004, A&A, 417, 159 [75](#)

Dullemond, C. P., Juhasz, A., Pohl, A., et al. 2012, RADMC-3D: A multi-  
purpose radiative transfer tool, Astrophysics Source Code Library, record  
ascl:1202.015, ascl:1202.015 [52](#)

Dullemond, C. P., Birnstiel, T., Huang, J., et al. 2018, ApJ, 869, L46 [58](#)

Dutrey, A., Guilloteau, S., Duvert, G., et al. 1996, A&A, 309, 493 [15](#)

Dutrey, A., Guilloteau, S., Prato, L., et al. 1998, A&A, 338, L63 [29](#)

Dutrey, A., Guilloteau, S., & Simon, M. 1994, A&A, 286, 149 [29](#)

- Dutrey, A., Semenov, D., Chapillon, E., et al. 2014, in *Protostars and Planets VI*, ed. H. Beuther, R. S. Klessen, C. P. Dullemond, & T. Henning, 317–338 [28](#), [29](#)
- Dvorak, R. 1986, *A&A*, 167, 379 [103](#)
- Espaillet, C., Furlan, E., D’Alessio, P., et al. 2011, *ApJ*, 728, 49 [104](#)
- Espaillet, C., Calvet, N., D’Alessio, P., et al. 2007, *ApJ*, 664, L111 [104](#)
- Espaillet, C., Muzerolle, J., Najita, J., et al. 2014, in *Protostars and Planets VI*, ed. H. Beuther, R. S. Klessen, C. P. Dullemond, & T. Henning, 497–520 [15](#)
- Facchini, S., van Dishoeck, E. F., Manara, C. F., et al. 2019, *A&A*, 626, L2 [19](#), [83](#), [84](#)
- Fernández-López, M., Zapata, L. A., & Gabbasov, R. 2017, *ApJ*, 845, 10 [38](#)
- Fitton, S., Tofflemire, B. M., & Kraus, A. L. 2022, *Research Notes of the American Astronomical Society*, 6, 18 [166](#)
- Flaherty, K., Hughes, A. M., Simon, J. B., et al. 2020, *ApJ*, 895, 109 [19](#)
- Flock, M., Ruge, J. P., Dzyurkevich, N., et al. 2015, *A&A*, 574, A68 [22](#), [78](#), [79](#)
- Foreman-Mackey, D., Hogg, D. W., Lang, D., & Goodman, J. 2013a, *PASP*, 125, 306 [68](#)
- . 2013b, *PASP*, 125, 306 [114](#), [147](#)
- Fung, J., Shi, J.-M., & Chiang, E. 2014, *ApJ*, 782, 88 [77](#)
- Gaia Collaboration, Prusti, T., de Bruijne, J. H. J., et al. 2016, *A&A*, 595, A1 [104](#), [141](#)
- Gaia Collaboration, Brown, A. G. A., Vallenari, A., et al. 2018, *A&A*, 616, A1 [59](#), [60](#)
- . 2021, *A&A*, 649, A1 [41](#), [60](#), [104](#), [141](#)
- Gammie, C. F. 1996, *ApJ*, 457, 355 [22](#)
- Gárate, M., Delage, T. N., Stadler, J., et al. 2021, *A&A*, 655, A18 [22](#), [51](#)

- Garrido-Deutelmoser, J., Petrovich, C., Charalambous, C., Guzmán, V. V., & Zhang, K. 2023, *ApJ*, 945, L37 [55](#)
- Gauvin, L. S., & Strom, K. M. 1992, *ApJ*, 385, 217 [104](#)
- Ginat, Y. B., & Perets, H. B. 2021, *MNRAS*, 508, 190 [165](#)
- Ginski, C., Benisty, M., van Holstein, R. G., et al. 2018, *A&A*, 616, A79 [105](#), [118](#), [129](#), [134](#), [135](#)
- Goldreich, P., & Sari, R. 2003, *ApJ*, 585, 1024 [36](#)
- Goldreich, P., & Tremaine, S. 1979, *ApJ*, 233, 857 [36](#)
- Gonzalez, J. F., Laibe, G., & Maddison, S. T. 2017, *MNRAS*, 467, 1984 [22](#)
- Guenther, E. W., Esposito, M., Mundt, R., et al. 2007, *A&A*, 467, 1147 [104](#), [121](#)
- Haffert, S. Y., van Holstein, R. G., Ginski, C., et al. 2020, *A&A*, 640, L12 [105](#), [129](#), [133](#), [135](#)
- Hardegree-Ullman, K. K., Cushing, M. C., Muirhead, P. S., & Christiansen, J. L. 2019, *AJ*, 158, 75 [57](#)
- Harris, R. J., Andrews, S. M., Wilner, D. J., & Kraus, A. L. 2012, *ApJ*, 751, 115 [164](#)
- Hashimoto, J., Dong, R., & Muto, T. 2021, *AJ*, 161, 264 [35](#)
- Hendler, N., Pascucci, I., Pinilla, P., et al. 2020, *ApJ*, 895, 126 [35](#), [81](#), [82](#), [91](#), [130](#)
- Hendler, N. P., Mulders, G. D., Pascucci, I., et al. 2017, *ApJ*, 841, 116 [35](#)
- Henning, T., Pfau, W., Zinnecker, H., & Prusti, T. 1993, *A&A*, 276, 129 [28](#), [104](#)
- Herczeg, G. J., & Hillenbrand, L. A. 2008, *ApJ*, 681, 594 [78](#)
- . 2014, *ApJ*, 786, 97 [59](#), [60](#), [79](#), [87](#), [141](#)
- Hildebrand, R. H. 1983, *QJRAS*, 24, 267 [70](#), [109](#), [147](#)

Hirsh, K., Price, D. J., Gonzalez, J.-F., Ubeira-Gabellini, M. G., & Ragusa, E. 2020, MNRAS, 498, 2936 [37](#), [104](#)

Högbom, J. A. 1974, A&AS, 15, 417 [45](#)

Holman, M. J., & Wiegert, P. A. 1999, AJ, 117, 621 [103](#)

Horne, K., & Marsh, T. R. 1986, MNRAS, 218, 761 [29](#)

Huang, J., Andrews, S. M., Cleeves, L. I., et al. 2018a, ApJ, 852, 122 [53](#)

Huang, J., Andrews, S. M., Dullemond, C. P., et al. 2018b, ApJ, 869, L42 [74](#)

—. 2020, ApJ, 891, 48 [65](#)

Isella, A., Testi, L., Natta, A., et al. 2007, A&A, 469, 213 [29](#)

Isella, A., Guidi, G., Testi, L., et al. 2016, Phys.Rev.Lett, 117, 251101 [29](#)

Isella, A., Huang, J., Andrews, S. M., et al. 2018, ApJ, 869, L49 [29](#)

Izquierdo, A. F., Testi, L., Facchini, S., Rosotti, G. P., & van Dishoeck, E. F. 2021, A&A, 650, A179 [158](#)

Jäger, C., Mutschke, H., Henning, T., & Huisken, F. 2008, ApJ, 689, 249 [25](#)

Jennings, J., Booth, R. A., Tazzari, M., Rosotti, G. P., & Clarke, C. J. 2020, MNRAS, 495, 3209 [63](#)

Johansen, A., & Youdin, A. 2007, ApJ, 662, 627 [22](#)

Johansen, A., Youdin, A., & Klahr, H. 2009, ApJ, 697, 1269 [22](#)

Jorsater, S., & van Moorsel, G. A. 1995, AJ, 110, 2037 [107](#), [145](#)

Joy, A. H., & van Biesbroeck, G. 1944, PASP, 56, 123 [151](#)

Kanagawa, K. D., Muto, T., Tanaka, H., et al. 2015, ApJ, 806, L15 [77](#)

Karamanis, M., & Beutler, F. 2020, arXiv e-prints, arXiv:2002.06212 [152](#)

Karamanis, M., Beutler, F., & Peacock, J. A. 2021, MNRAS, 508, 3589 [151](#), [152](#)

Kataoka, A., Okuzumi, S., Tanaka, H., & Nomura, H. 2014, A&A, 568, A42 [83](#)

Kataoka, A., Tanaka, H., Okuzumi, S., & Wada, K. 2013, *A&A*, 557, L4 [83](#)

Keller, L. D., Sloan, G. C., Forrest, W. J., et al. 2008, *ApJ*, 684, 411 [25](#)

Kelly, B. C. 2007, *ApJ*, 665, 1489 [82](#)

Kenyon, S. J., & Hartmann, L. 1987, *ApJ*, 323, 714 [75](#)

Kim, K. H., Watson, D. M., Manoj, P., et al. 2009, *ApJ*, 700, 1017 [104](#)

Klahr, H., & Hubbard, A. 2014, *ApJ*, 788, 21 [22](#)

Klein, R., Apai, D., Pascucci, I., Henning, T., & Waters, L. B. F. M. 2003, *ApJ*, 593, L57 [35](#)

Kley, W., & Haghighipour, N. 2014, *A&A*, 564, A72 [104](#), [131](#)

Kley, W., Thun, D., & Penzlin, A. B. T. 2019, *A&A*, 627, A91 [104](#), [112](#), [121](#), [122](#)

Kostov, V. B., Orosz, J. A., Feinstein, A. D., et al. 2020, *AJ*, 159, 253 [103](#)

Koutoulaki, M., Facchini, S., Manara, C. F., et al. 2019, *A&A*, 625, A49 [141](#)

Kratter, K., & Lodato, G. 2016, *ARA&A*, 54, 271 [22](#)

Kraus, A. L., & Hillenbrand, L. A. 2007, *ApJ*, 662, 413 [79](#)

—. 2009, *ApJ*, 704, 531 [87](#)

Kurtovic, N. T., Pérez, L. M., Benisty, M., et al. 2018, *ApJ*, 869, L44 [21](#), [37](#), [38](#), [120](#), [162](#), [176](#)

Kurtovic, N. T., Pinilla, P., Long, F., et al. 2021, *A&A*, 645, A139 [57](#), [58](#), [59](#), [60](#), [77](#), [84](#), [201](#)

Kurtovic, N. T., Pinilla, P., Penzlin, A. B. T., et al. 2022, *A&A*, 664, A151 [21](#), [103](#), [120](#), [165](#), [201](#)

Kuznetsova, A., Bae, J., Hartmann, L., & Mac Low, M.-M. 2022, *ApJ*, 928, 92 [22](#)

Law, C. J., Teague, R., Loomis, R. A., et al. 2021, *ApJS*, 257, 4 [31](#), [88](#), [89](#)

Law, C. J., Crystian, S., Teague, R., et al. 2022a, *ApJ*, 932, 114 [31](#), [88](#), [89](#)

- Law, C. J., Teague, R., Öberg, K. I., et al. 2022b, arXiv e-prints, arXiv:2212.08667 [31](#), [88](#), [89](#)
- Leinert, C., Zinnecker, H., Weitzel, N., et al. 1993, A&A, 278, 129 [151](#)
- Lesur, G., Ercolano, B., Flock, M., et al. 2022, arXiv e-prints, arXiv:2203.09821 [20](#), [22](#)
- Liu, B., Lambrechts, M., Johansen, A., Pascucci, I., & Henning, T. 2020, A&A, 638, A88 [35](#)
- Long, F., Pinilla, P., Herczeg, G. J., et al. 2018, ApJ, 869, 17 [23](#), [74](#), [75](#), [76](#), [77](#)
- Long, F., Herczeg, G. J., Harsono, D., et al. 2019, ApJ, 882, 49 [85](#), [141](#), [144](#), [146](#)
- Long, F., Andrews, S. M., Vega, J., et al. 2021, ApJ, 915, 131 [37](#), [159](#)
- Long, F., Andrews, S. M., Rosotti, G., et al. 2022, ApJ, 931, 6 [19](#), [35](#), [85](#)
- Lovelace, R. V. E., Li, H., Colgate, S. A., & Nelson, A. F. 1999, ApJ, 513, 805 [22](#)
- Lubow, S. H. 1991, ApJ, 381, 259 [22](#), [37](#), [104](#)
- Luhman, K. L. 2006, ApJ, 645, 676 [35](#)
- . 2007, ApJS, 173, 104 [104](#)
- MacFadyen, A. I., & Milosavljević, M. 2008, ApJ, 672, 83 [37](#), [104](#)
- MacGregor, M. A., Weinberger, A. J., Wilner, D. J., Kowalski, A. F., & Cranmer, S. R. 2018, ApJ, 855, L2 [81](#)
- Macías, E., Guerra-Alvarado, O., Carrasco-González, C., et al. 2021, A&A, 648, A33 [19](#)
- Manara, C. F., Testi, L., Natta, A., et al. 2014, A&A, 568, A18 [104](#), [109](#)
- Manara, C. F., Tazzari, M., Long, F., et al. 2019, A&A, 628, A95 [37](#), [130](#), [144](#), [146](#), [150](#), [163](#)
- Mannings, V., & Sargent, A. I. 1997, ApJ, 490, 792 [15](#)

- Marino, S., Yelverton, B., Booth, M., et al. 2019, MNRAS, 484, 1257 [112](#)
- Martin, D. V. 2019, MNRAS, 488, 3482 [103](#)
- Martin, D. V., & Triaud, A. H. M. J. 2014, A&A, 570, A91 [103](#)
- Martinez-Brunner, R., Casassus, S., Pérez, S., et al. 2022, MNRAS, 510, 1248 [19](#)
- Mayama, S., Tamura, M., Hanawa, T., et al. 2010, Science, 327, 306 [38](#)
- Mayama, S., Akiyama, E., Panić, O., et al. 2018, ApJ, 868, L3 [162](#)
- McMullin, J. P., Waters, B., Schiebel, D., Young, W., & Golap, K. 2007, in Astronomical Society of the Pacific Conference Series, Vol. 376, Astronomical Data Analysis Software and Systems XVI, ed. R. A. Shaw, F. Hill, & D. J. Bell, 127 [47](#), [60](#)
- Mercer, A., & Stamatellos, D. 2020, A&A, 633, A116 [58](#)
- Meschiari, S. 2012, ApJ, 752, 71 [104](#)
- Meyers, J. 2015, linmix, <https://github.com/jmeyers314/linmix> [82](#)
- Miotello, A., Kamp, I., Birnstiel, T., Cleeves, L. I., & Kataoka, A. 2022, arXiv e-prints, arXiv:2203.09818 [27](#)
- Miranda, R., & Lai, D. 2015, MNRAS, 452, 2396 [22](#), [36](#), [103](#)
- Miranda, R., Muñoz, D. J., & Lai, D. 2017, MNRAS, 466, 1170 [79](#)
- Mizuno, H., Markiewicz, W. J., & Voelk, H. J. 1988, A&A, 195, 183 [15](#)
- Monaghan, J. J. 1976, MNRAS, 176, 63 [165](#)
- Morales, J. C., Mustill, A. J., Ribas, I., et al. 2019, Science, 365, 1441 [35](#), [57](#), [79](#)
- Muñoz, D. J., & Lai, D. 2016, ApJ, 827, 43 [79](#)
- Muñoz, D. J., & Lithwick, Y. 2020, ApJ, 905, 106 [37](#), [104](#)
- Mulders, G. D., Pascucci, I., & Apai, D. 2015, ApJ, 814, 130 [57](#)
- Musso Barucci, A., Cugno, G., Launhardt, R., et al. 2019, A&A, 631, A84 [130](#)

Mužić, K., Scholz, A., Peña Ramírez, K., et al. 2019, *ApJ*, 881, 79 [35](#), [57](#)

Nakagawa, Y., Nakazawa, K., & Hayashi, C. 1981, *Icarus*, 45, 517 [18](#)

Nealon, R., Cuello, N., & Alexander, R. 2020, *MNRAS*, 491, 4108 [37](#)

Nelson, R. P., Gressel, O., & Umurhan, O. M. 2013, *MNRAS*, 435, 2610 [22](#)

Nguyen, D. C., Brandeker, A., van Kerkwijk, M. H., & Jayawardhana, R. 2012, *ApJ*, 745, 119 [104](#)

Norfolk, B. J., Maddison, S. T., Pinte, C., et al. 2021, *MNRAS*, 502, 5779 [105](#), [109](#)

Öberg, K. I., & Bergin, E. A. 2021, *Physics Reports*, 893, 1 [5](#), [15](#), [16](#)

Öberg, K. I., Murray-Clay, R., & Bergin, E. A. 2011, *ApJ*, 743, L16 [75](#)

Öberg, K. I., Guzmán, V. V., Walsh, C., et al. 2021, *ApJS*, 257, 1 [31](#)

Okuzumi, S., Momose, M., Sirono, S.-i., Kobayashi, H., & Tanaka, H. 2016, *ApJ*, 821, 82 [75](#)

Owen, J. E., Clarke, C. J., & Ercolano, B. 2012, *MNRAS*, 422, 1880 [78](#)

Owen, J. E., & Kollmeier, J. A. 2019, *MNRAS*, 487, 3702 [78](#)

Paardekooper, S.-J., Leinhardt, Z. M., Thébault, P., & Baruteau, C. 2012, *ApJ*, 754, L16 [103](#)

Paneque-Carreño, T., Miotello, A., van Dishoeck, E. F., et al. 2022, *A&A*, 666, A168 [31](#)

Papaloizou, J., & Pringle, J. E. 1977, *MNRAS*, 181, 441 [37](#)

Papaloizou, J. C. B., & Terquem, C. 2006, *Reports on Progress in Physics*, 69, 119 [15](#)

Pascucci, I., Testi, L., Herczeg, G. J., et al. 2016, *ApJ*, 831, 125 [59](#), [60](#)

Penzlin, A. B. T., Ataiee, S., & Kley, W. 2019, *A&A*, 630, L1 [129](#)

Penzlin, A. B. T., Kley, W., & Nelson, R. P. 2021, *A&A*, 645, A68 [104](#), [120](#), [122](#), [128](#)

Pérez, L. M., Carpenter, J. M., Andrews, S. M., et al. 2016, *Science*, 353, 1519 [23](#)

Pérez, S., Marino, S., Casassus, S., et al. 2019, *MNRAS*, 488, 1005 [51](#), [129](#)

Petrov, P. P., Gahm, G. F., Djupvik, A. A., et al. 2015, *A&A*, 577, A73 [141](#)

Pfalzner, S., & Kaczmarek, T. 2013, *A&A*, 555, A135 [37](#)

Phuong, N. T., Dutrey, A., Diep, P. N., et al. 2020, *A&A*, 635, A12 [133](#)

Pichardo, B., Sparke, L. S., & Aguilar, L. A. 2005, *MNRAS*, 359, 521 [164](#)

Pierens, A., McNally, C. P., & Nelson, R. P. 2020, *MNRAS*, 496, 2849 [103](#)

Pierens, A., & Nelson, R. P. 2007, *A&A*, 472, 993 [104](#)

—. 2008, *A&A*, 483, 633 [122](#)

Pinilla, P. 2022, *European Physical Journal Plus*, 137, 1206 [35](#), [36](#), [88](#)

Pinilla, P., Benisty, M., & Birnstiel, T. 2012a, *A&A*, 545, A81 [22](#), [78](#)

Pinilla, P., Birnstiel, T., Benisty, M., et al. 2013, *A&A*, 554, A95 [34](#), [35](#), [85](#)

Pinilla, P., Birnstiel, T., Ricci, L., et al. 2012b, *A&A*, 538, A114 [19](#), [131](#)

Pinilla, P., Flock, M., Ovelar, M. d. J., & Birnstiel, T. 2016, *A&A*, 596, A81 [79](#), [80](#)

Pinilla, P., Garufi, A., & Gárate, M. 2022a, *A&A*, 662, L8 [34](#)

Pinilla, P., Natta, A., Manara, C. F., et al. 2018b, *A&A*, 615, A95 [58](#), [59](#), [60](#), [65](#), [70](#), [77](#), [90](#), [109](#)

Pinilla, P., Pascucci, I., & Marino, S. 2020, *A&A*, 635, A105 [59](#)

Pinilla, P., Pohl, A., Stammler, S. M., & Birnstiel, T. 2017a, *ApJ*, 845, 68 [76](#)

Pinilla, P., & Youdin, A. 2017, *Astrophysics and Space Science Library*, Vol. 445, *Particle Trapping in Protoplanetary Disks: Models vs. Observations* (Springer Cham), 91 [35](#)

Pinilla, P., van der Marel, N., Pérez, L. M., et al. 2015, *A&A*, 584, A16 [65](#)

Pinilla, P., Pérez, L. M., Andrews, S., et al. 2017b, *ApJ*, 839, 99 [65](#), [77](#)

- Pinilla, P., Quiroga-Nuñez, L. H., Benisty, M., et al. 2017c, *ApJ*, 846, 70 [34](#), [35](#), [58](#), [76](#), [83](#)
- Pinilla, P., Tazzari, M., Pascucci, I., et al. 2018, *ApJ*, 859, 32 [65](#)
- Pinilla, P., Kurtovic, N. T., Benisty, M., et al. 2021, *A&A*, 649, A122 [21](#), [77](#), [109](#)
- Pinilla, P., Benisty, M., Kurtovic, N. T., et al. 2022b, *A&A*, 665, A128 [21](#), [34](#), [55](#)
- Pinte, C., Teague, R., Flaherty, K., et al. 2022, arXiv e-prints, arXiv:2203.09528 [29](#)
- Pinte, C., Ménard, F., Duchêne, G., et al. 2018, *A&A*, 609, A47 [31](#)
- Pinte, C., van der Plas, G., Ménard, F., et al. 2019, *Nature Astronomy*, 419 [87](#)
- Price, D. J., Cuello, N., Pinte, C., et al. 2018, *MNRAS*, 477, 1270 [78](#)
- Pyerin, M. A., Delage, T. N., Kurtovic, N. T., et al. 2021, *A&A*, 656, A150 [21](#)
- Ragusa, E., Alexander, R., Calcino, J., Hirsh, K., & Price, D. J. 2020, *MNRAS*, 499, 3362 [37](#), [104](#)
- Ragusa, E., Dipierro, G., Lodato, G., Laibe, G., & Price, D. J. 2017, *MNRAS*, 464, 1449 [79](#)
- Ragusa, E., Fasano, D., Toci, C., et al. 2021, *MNRAS*, 507, 1157 [133](#)
- Regály, Z., Juhász, A., Sándor, Z., & Dullemond, C. P. 2012, *MNRAS*, 419, 1701 [79](#)
- Ren, B., Dong, R., van Holstein, R. G., et al. 2020, *ApJ*, 898, L38 [177](#)
- Ribas, Á., Bouy, H., Merín, B., et al. 2016, *MNRAS*, 458, 1029 [104](#)
- Ricci, L., Rome, H., Pinilla, P., et al. 2017a, *ApJ*, 846, 19 [35](#)
- Ricci, L., Testi, L., Natta, A., et al. 2010, *A&A*, 512, A15 [27](#)
- Ricci, L., Testi, L., Natta, A., Scholz, A., & de Gregorio-Monsalvo, I. 2012, *ApJ*, 761, L20 [35](#)

- Ricci, L., Testi, L., Natta, A., et al. 2014, *ApJ*, 791, 20 [35](#)
- Ricci, L., Cazzoletti, P., Czekala, I., et al. 2017b, *AJ*, 154, 24 [35](#)
- Rice, W. K. M., Armitage, P. J., Wood, K., & Lodato, G. 2006, *MNRAS*, 373, 1619 [78](#)
- Rodriguez, J. E., Pepper, J., Stassun, K. G., et al. 2013, *AJ*, 146, 112 [142](#)
- Rodriguez, J. E., Loomis, R., Cabrit, S., et al. 2018, *ApJ*, 859, 150 [37](#), [38](#), [120](#), [141](#), [142](#), [144](#), [146](#), [150](#), [158](#), [162](#), [163](#), [167](#)
- Rosenfeld, K. A., Andrews, S. M., Hughes, A. M., Wilner, D. J., & Qi, C. 2013, *ApJ*, 774, 16 [29](#)
- Rosenfeld, K. A., Chiang, E., & Andrews, S. M. 2014, *ApJ*, 782, 62 [120](#)
- Rosotti, G. P., Dale, J. E., de Juan Ovelar, M., et al. 2014, *MNRAS*, 441, 2094 [164](#)
- Rosotti, G. P., Juhasz, A., Booth, R. A., & Clarke, C. J. 2016, *MNRAS*, 459, 2790 [77](#)
- Rota, A. A., Manara, C. F., Miotello, A., et al. 2022, *A&A*, 662, A121 [37](#)
- Rowther, S., Nealon, R., & Meru, F. 2022, *ApJ*, 925, 163 [162](#), [163](#)
- Ruden, S. P. 1999, in NATO Advanced Study Institute (ASI) Series C, Vol. 540, *The Origin of Stars and Planetary Systems*, ed. C. J. Lada & N. D. Kylafis, 643 [15](#)
- Safronov, V. S. 1972, *Evolution of the protoplanetary cloud and formation of the earth and planets*. (Keter Publishing House) [15](#)
- Sanchis, E., Testi, L., Natta, A., et al. 2020, *A&A*, 633, A114 [35](#)
- Sandford, S. A. 1996, *Meteoritics & Planetary Science*, 31, 449 [25](#)
- Schlafly, E. F., Green, G., Finkbeiner, D. P., et al. 2014, *ApJ*, 789, 15 [5](#), [60](#), [62](#)
- Schmid, H. M., Bazzon, A., Roelfsema, R., et al. 2018, *A&A*, 619, A9 [121](#)
- Scholz, A., Jayawardhana, R., & Wood, K. 2006, *ApJ*, 645, 1498 [35](#)

- Scholz, A., Jayawardhana, R., Wood, K., et al. 2007, *ApJ*, 660, 1517 [35](#)
- Scholz, A., Muzic, K., Geers, V., et al. 2012, *ApJ*, 744, 6 [35](#), [57](#)
- Schwarz, U. J. 1978, *A&A*, 65, 345 [47](#)
- Shakura, N. I., & Sunyaev, R. A. 1973, *A&A*, 500, 33 [121](#)
- Shenavrin, V. I., Petrov, P. P., & Grankin, K. N. 2015, *Information Bulletin on Variable Stars*, 6143, 1 [141](#)
- Shuai, L., Ren, B. B., Dong, R., et al. 2022, *ApJS*, 263, 31 [165](#)
- Sinclair, C. A., Rosotti, G. P., Juhasz, A., & Clarke, C. J. 2020, *MNRAS*, 493, 3535 [58](#)
- Skrutskie, M. F., Dutkevitch, D., Strom, S. E., et al. 1990, *AJ*, 99, 1187 [15](#)
- Smallwood, J. L., Nealon, R., Chen, C., et al. 2021, *MNRAS*, 508, 392 [37](#)
- Stone, N. C., & Leigh, N. W. C. 2019, *Nature*, 576, 406 [165](#)
- Strom, K. M., Strom, S. E., Edwards, S., Cabrit, S., & Skrutskie, M. F. 1989, *AJ*, 97, 1451 [15](#)
- Takami, M., Fu, G., Liu, H. B., et al. 2018, *ApJ*, 864, 20 [38](#)
- Takeuchi, T., & Lin, D. N. C. 2002, *ApJ*, 581, 1344 [18](#)
- Tanaka, H., Himeno, Y., & Ida, S. 2005, *ApJ*, 625, 414 [17](#)
- Tazzari, M., Beaujean, F., & Testi, L. 2018, *MNRAS*, 476, 4527 [65](#)
- Tazzari, M., Testi, L., Natta, A., et al. 2017, *A&A*, 606, A88 [147](#)
- Teague, R. 2019, *The Journal of Open Source Software*, 4, 1220 [32](#), [87](#), [116](#), [158](#)
- Teague, R., Bae, J., & Bergin, E. A. 2019, *Nature*, 574, 378 [87](#), [146](#)
- Teague, R., & Foreman-Mackey, D. 2018a, *Research Notes of the American Astronomical Society*, 2, 173 [31](#)
- . 2018b, *Research Notes of the American Astronomical Society*, 2, 173 [86](#), [107](#), [146](#)

- Testi, L., Birnstiel, T., Ricci, L., et al. 2014, in *Protostars and Planets VI*, ed. H. Beuther, R. S. Klessen, C. P. Dullemond, & T. Henning, 339–361 [17](#)
- Thompson, A. R., Moran, J. M., & Swenson, George W., J. 2017, *Interferometry and Synthesis in Radio Astronomy*, 3rd Edition (Springer Cham), doi:10.1007/978-3-319-44431-4 [44](#)
- Thun, D., & Kley, W. 2018, *A&A*, 616, A47 [104](#), [120](#), [121](#), [122](#)
- Thun, D., Kley, W., & Picogna, G. 2017, *A&A*, 604, A102 [37](#), [104](#), [111](#), [121](#)
- Tiede, C., Zrake, J., MacFadyen, A., & Haiman, Z. 2020, *ApJ*, 900, 43 [122](#)
- Toomre, A. 1964, *ApJ*, 139, 1217 [22](#)
- Toonen, S., Boekholt, T. C. N., & Portegies Zwart, S. 2022, *A&A*, 661, A61 [165](#)
- Trapman, L., Ansdell, M., Hogerheijde, M. R., et al. 2020, arXiv e-prints, arXiv:2004.07257 [85](#)
- Trapman, L., Facchini, S., Hogerheijde, M. R., van Dishoeck, E. F., & Bruderer, S. 2019, *A&A*, 629, A79 [19](#), [58](#), [85](#), [86](#), [91](#)
- Tripathi, A., Andrews, S. M., Birnstiel, T., & Wilner, D. J. 2017, *ApJ*, 845, 44 [71](#), [81](#), [82](#), [130](#)
- Urpin, V., & Brandenburg, A. 1998, *MNRAS*, 294, 399 [22](#)
- van der Marel, N., Williams, J. P., & Bruderer, S. 2018, *ApJ*, 867, L14 [76](#)
- van der Marel, N., van Dishoeck, E. F., Bruderer, S., et al. 2013, *Science*, 340, 1199 [23](#)
- van der Plas, G., Ménard, F., Ward-Duong, K., et al. 2016, *ApJ*, 819, 102 [35](#)
- Virtanen, P., Gommers, R., Oliphant, T. E., et al. 2020, *Nature Methods*, 17, 261 [125](#)
- Ward-Duong, K., Patience, J., Bulger, J., et al. 2018, *AJ*, 155, 54 [35](#), [59](#), [71](#), [87](#)
- Watson, D. M., Leisenring, J. M., Furlan, E., et al. 2009, *ApJS*, 180, 84 [25](#)
- Weber, P., Pérez, S., Guidi, G., et al. 2023, *MNRAS*, 518, 5620 [38](#), [162](#)

- Weidenschilling, S. J. 1977, MNRAS, 180, 57 [18](#)
- . 2000, Space Sci.Rev., 92, 295 [15](#)
- Whipple, F. L. 1972, in From Plasma to Planet, ed. A. Elvius, 211 [18](#)
- Williams, I. P., & Cremin, A. W. 1968, QJRAS, 9, 40 [15](#)
- Winter, A. J., Booth, R. A., & Clarke, C. J. 2018, MNRAS, 479, 5522 [38](#)
- Wölfer, L., Facchini, S., Kurtovic, N. T., et al. 2021, A&A, 648, A19 [21](#)
- Youdin, A. N., & Goodman, J. 2005, ApJ, 620, 459 [22](#)
- Zapata, L. A., Rodríguez, L. F., Fernández-López, M., et al. 2020, ApJ, 896, 132 [37](#), [38](#)
- Zhang, K., Blake, G. A., & Bergin, E. A. 2015, ApJ, 806, L7 [22](#), [75](#)
- Zhang, S., Zhu, Z., Huang, J., et al. 2018, ApJ, 869, L47 [51](#)
- Zhu, Z., Andrews, S. M., & Isella, A. 2018, MNRAS, 479, 1850 [85](#)
- Zhu, Z., Nelson, R. P., Hartmann, L., Espaillat, C., & Calvet, N. 2011, ApJ, 729, 47 [78](#)



## Acknowledgements

---

This work has been made possible by the kind mentorship of my advisor Paola Pinilla, and I am thankful of her multi-dimensional support and guidance. Working as part of Paola's group has been a privilege, allowing me to grow as a researcher and as a person. Her dedication and passion for research, and for the well-being of researchers, are a role-model for the advisor I would like to be. Thank you.

I would like to acknowledge the work of the developers of the *freely available* tools used during this thesis. In particular, Dan Foreman-Mackey (`emcee`), R. Teague (`bettermoments`, `eddy`, `simple-disk`), and the developers of FARGO3D.

The hydro-simulations presented in this thesis were run in the on the HPC system RAVEN at MPCDF (Max Planck Computing and Data Facility). Simulation tests, MCMCs, and simulated observations were run on the MPIA computing facilities.

I acknowledge the support provided by the Alexander von Humboldt Foundation in the framework of the Sofja Kovalevskaja Award endowed by the Federal Ministry of Education and Research.

In Chapters 3, 4 and 5, I showed the results from Kurtovic et al. (2021, 2022) and Kurtovic et al. (in prep), which make use of the following ALMA data:

ADS/JAO.ALMA#2012.1.00743.S, ADS/JAO.ALMA#2015.1.00934.S,  
ADS/JAO.ALMA#2016.1.01511.S, ADS/JAO.ALMA#2018.1.00310.S,  
ADS/JAO.ALMA#2017.1.00969.S, ADS/JAO.ALMA#2015.1.01506.S,  
ADS/JAO.ALMA#2016.1.00877.S, ADS/JAO.ALMA#2016.1.01164.S,  
ADS/JAO.ALMA#2017.1.01631.S, ADS/JAO.ALMA#2018.1.00973.S.

ALMA is a partnership of ESO (representing its member states), NSF (USA) and NINS (Japan), together with NRC (Canada), MOST and ASIAA (Taiwan), and KASI (Republic of Korea), in cooperation with the Republic of Chile. The Joint ALMA Observatory is operated by ESO, AUI/NRAO and NAOJ.



# Declaration of Originality

---

## **Declaration of Originality**

I hereby declare that this thesis is my own work and that I have used no other than the stated sources and aids.

## **Erklärung zur Originalität der Arbeit**

Ich versichere, dass ich diese Arbeit selbstständig verfasst habe und keine anderen als die angegebenen Quellen und Hilfsmittel benutzt habe.

Heidelberg, der 4. Mai 2023

Nicolas Kurtovic

